School of Electrical Engineering, Computing, and Mathematical Sciences

Scattering from Diatomic Molecules in the Spheroidal Convergent Close-Coupling Formalism

Jeremy Stephen Savage

This thesis is presented for the Degree of
Doctor of Philosophy
of
Curtin University

September 2018

Declaration

To the best of my knowledge and belief this thesis contains no material previously published by any other person except where due acknowledgement has been made.

This thesis contains no material which has been accepted for the award of any other degree or diploma in any university.

Signature: .....

Date: 19/09/19

Abstract

The study of electron and positron collisions with molecules is not only important for improving our fundamental understanding of the physics of the scattering process, but also in providing data for numerous and varied applications both in industry and other scientific fields. With the advancement of computational power and techniques over the past few decades, theoretical close-coupling methods have led the way in obtaining comprehensive sets of collision data. For the most part this progress has belonged to scattering on atomic targets, but the past few years have seen the successful application of the Convergent Close-Coupling (CCC) method to electron and positron scattering from the simplest molecules.

Calculations of molecular collisions require significantly more computer power than atoms and so the efficiency of theoretical methods becomes critically important. The recent spherical formulation of the CCC method proved to be the technique that allowed for a major breakthrough in the field. However, it also experienced significant difficulties in performing accurate calculations as the internuclear distance of the molecule increased beyond the bond length of molecular hydrogen ($\sim$ 1.4 atomic units), which renders it unable to study processes in which nuclear motion is involved.

This work details the formulation of the CCC method in prolate spheroidal coordinates—the natural coordinate system for describing diatomic molecules—and its application to positron and electron scattering from molecular hydrogen. The aim is to demonstrate that, despite the mathematical complexities, this spheroidal formulation is superior to the spherical in both accuracy and efficiency, and includes the ability to account for nuclear motion within the adiabatic-nuclei approximation. Ultimately, it is the only theory able to calculate comprehensive data sets for diatomic molecules.

The milestones of this work are:

- A detailed derivation of the CCC method for electron and positron scattering on diatomic molecules in spherical coordinates, and the algorithmic and

mathematical changes required for the formulation in prolate spheroidal coordinates. This theory was developed under the Born-Oppenheimer and fixed-nuclei approximations and extended to adiabatic-nuclei calculations.

- Comparisons between the spherical and spheroidal structure calculations of H_2 electronic energies, oscillator strengths, and polarisabilities. The spheroidal formulation is demonstrated to be more accurate while also requiring a smaller basis expansion. In particular, it is able to remain accurate for all values of the internuclear distance required for studying vibrational states and the processes that involve them.

- Calculations of positron scattering on H_2, as well as grand total, ionisation, and excitation cross sections for electron-H_2 scattering. These calculations were compared to previous results from the spherical formulation with generally good agreement, and stronger agreement with experiment for the elastic scattering of e^--H_2.

- The calculation of results that were too computationally expensive or difficult in the spherical formulation—elastic differential and $v = 0 \rightarrow 1$ vibrational excitation cross sections, as well as scattering from the metastable $c\,^3\Pi_u$ state of H_2. We also note how the advantages of the spheroidal formulation has been used to supplement larger calculations investigating complex processes such as molecular dissociation.

This success gives us confidence that the spheroidal formulation of the CCC method will be an effective means for providing data of electron and positron collisions with molecules, starting with H_2 and eventually extending to other important diatomics.

Statement of contributions by others

The content of Chapter 2, "General theory", is a combination of established molecular scattering theory concepts, my own work in this general context, as well as important principles underlying convergent close-coupling methods as established by I. Bray and I.E. McCarthy and further developed by D.V. Fursa and M.C. Zammit. These elements were summarised and arranged by myself to construct a concise but general framework for the following specific formulations.

The content of Chapter 3, "Spherical MCCC", is heavily based on the two-electron atomic convergent close-coupling method devised by D.V. Fursa and I. Bray and its extension to molecular targets by D.V. Fursa, M.C. Zammit, and myself. In particular, the equations given for the V-matrix elements were reformulated by myself to be consistent with those in the following chapter.

The content of Chapter 4, "Spheroidal MCCC", is wholly my own work with the exception of Subsection 4.3.2, "Vibrational energies", which relies on developments by M.C. Zammit and L.H. Scarlett.

The content of Chapter 5, "Results", contains calculations labelled "spheroidal" that are published or in the process of publication. These results were produced with code developed by myself and built upon elements developed by D.V. Fursa, M.C. Zammit, I. Bray, and L.H. Scarlett. The results labelled "spherical" were obtained by M.C. Zammit and published in several papers as cited by the text. Figure 5.16 in Section 5.9, "Further work", was created by J.K. Tapley and L.H. Scarlett for the paper cited in the text.

Signature of Candidate: .....

Signature of Supervisor: .....

List of publications

The following results that are presented in this thesis are in the process of being published:

- Jeremy S. Savage, Jonathan K. Tapley, Dmitry V. Fursa, Liam H. Scarlett, and Igor Bray. Electron scattering on the metastable $c\,^3\Pi_u$ state of H_2 in the spheroidal convergent close-coupling formalism. Unpublished.

- Jeremy S. Savage, Dmitry V. Fursa, Liam H. Scarlett, Mark C. Zammit, and Igor Bray. Adiabatic-nuclei calculations of the elastic differential, integrated, and vibrational excitation cross sections of e^-–H_2. Unpublished.

In addition, I have contributed to several articles during my time working on this project, including:

- Mark C. Zammit, Jeremy S. Savage, Dmitry V. Fursa, and Igor Bray. Complete solution of electronic excitation and ionization in electron-hydrogen molecule scattering. *Phys. Rev. Lett.* **116**(23): 233201, June 2016.

- Mark C. Zammit, Jeremy S. Savage, Dmitry V. Fursa, and Igor Bray. Electron-impact excitation of molecular hydrogen. *Phys. Rev. A* **95**(2): 022708, February 2017.

- Mark C. Zammit, Dmitry V. Fursa, Jeremy S. Savage, and Igor Bray. Electron- and positron-molecule scattering: development of the molecular convergent close-coupling method. *J. Phys. B* **50**(12): 123001, May 2017.

- Liam H. Scarlett, Jonathan K. Tapley, Dmitry V. Fursa, Mark C. Zammit, Jeremy S. Savage, and Igor Bray. Low-energy electron-impact dissociative excitation of molecular hydrogen and its isotopologues. *Phys. Rev. A* **96**(6): 062708, December 2017.

- Liam H. Scarlett, Jonathan K. Tapley, Dmitry V. Fursa, Mark C. Zammit, Jeremy S. Savage, and Igor Bray. Electron-impact dissociation of molecular hydrogen into neutral fragments. *Eur. J. Phys. D* **72**(2): 34, February 2018.

- Jonathan K. Tapley, Liam H. Scarlett, Jeremy S. Savage, Mark C. Zammit, Dmitry V. Fursa, and Igor Bray. Vibrationally resolved electron-impact excitation cross sections for singlet states of molecular hydrogen. *J. Phys. B* **51**: 144007, June 2018.

- Jonathan K. Tapley, Liam H. Scarlett, Jeremy S. Savage, Dmitry V. Fursa, Mark C. Zammit, and Igor Bray. Electron-impact dissociative excitation cross sections for singlet states of molecular hydrogen. *Phys. Rev. A* **98**: 032701, September 2018.

Acknowledgements

This work would not have been possible without the endless support of my beloved fiancée Annmaree, the inspiration from my delightful son Leo, as well as my loving and devoted family.

I owe tremendous gratitude to my supervisors Dmitry Fursa and Igor Bray for their continued patience and tutelage. I also wish to thank the members—past and present—of the Institute of Theoretical Physics at Curtin University for providing me with a place of belonging. I am particularly grateful to Mark Zammit for his part in our shared journey.

Finally, I am appreciative of Curtin University and the Australian Government for the financial support and research facilities—namely the Pawsey Supercomputing Centre and National Computational Infrastructure—that enabled this research.

Contents

List of Figures

"A physicist is just an atom's way of looking at itself."

— Unknown; often attributed to Niels Bohr

Chapter 1

Introduction

At the quantum scale, a scattering event is the interaction between an incident projectile and a target of interest, resulting in collision products that may have changed in energy and possibly composition. Such interactions can be between photons, atomic particles (of both matter and antimatter), atoms, and molecules, and are the driving force behind chemical reactions. The study of scattering systems not only increases our fundamental understanding of the reactants involved and temporary states created, but also provides important results for a vast and varied range of fields. Data sets obtained are used in other disciplines including fusion research [1, 2] and astrophysics [3–5], as well as in practical applications within the laser, lighting, materials, and medical industries [6].

Experiments are important for generating scattering data but are usually unable to provide a comprehensive set due to practical limitations. This can be the result of collision processes that cannot be resolved or data that are difficult to normalise on an absolute scale. On the other hand, theoretical methods do have the potential to calculate comprehensive sets of collision data within their range of applicability. With the ever-increasing computational power available these scattering problems may be "solved" fairly cheaply in comparison to experiment. For complex scattering systems and processes that require more computing resources than are currently available, certain assumptions are carefully chosen to minimise the loss of accuracy.

The simplest electron-atom scattering problems were considered effectively "solved" in the early 1990's by theories. The Convergent Close-Coupling (CCC) formalism was at the forefront with the studies of atomic hydrogen by Bray & Stelbovics [7] and atomic helium by Fursa & Bray [8]. In the case of these atoms, the available computational power had become sufficient for the new and

comprehensive methods to generate results in contradiction to the established experimental data of the time, and eventually lead to revised experiments that were in agreement with calculations.

The success of the CCC theory stems from the ability to include a large yet finite close-coupling expansion that is used to account for all relevant scattering channels and thus gives accurate results at all energies of interest. Following this, the steadily increasing computational power has allowed theories to expand this idea to other projectiles and more complex targets, with the CCC, R-matrix with pseudostates (RMPS) [9], and time-dependent close-coupling (TDCC) [10] methods leading the way. Such calculations have been performed for positron, photon, and heavy-projectile collisions on targets such as helium, alkali and alkaline earth metals, noble gases, and simple molecules.

It is the aim of this project to develop an accurate and efficient formulation of the CCC method to serve as the foundation for further work in obtaining comprehensive data sets for electron and positron scattering on diatomic molecules.

1.1 Molecular scattering

As opposed to atoms, molecular targets have additional complexity due to the lack of spherical symmetry, as well as an increase in the number of interaction channels (including dissociation into fragments) and degrees of freedom (vibration and rotation of the nuclei) [11]. In addition to electronic states, the finely-spaced vibrational and rotational spectra make it computationally infeasible to include all states in close-coupling calculations. In developing theoretical methods, the typical first step of approaching the molecular problem is to invoke the Born-Oppenheimer approximation [6, 12] to separate electronic and nuclear motion. This starting point allows theories such as CCC to perform calculations for just the electronic states before subsequently re-incorporating nuclear effects [13].

With the recent advances in computing, the molecular field is in a similar position as atomic scattering was in the mid-1990's. The CCC method for molecules has been applied successfully to antiproton scattering on molecular hydrogen [14], as well as positron and electron scattering on the hydrogen molecular ion H_2^+ and its isotopologues (D_2^+, T_2^+, HD^+, HT^+, and TD^+) and the hydrogen molecule H_2 (see [13] and references therein). However, even for the relatively simple H_2 there has been difficulty in modelling the spheroidally-shaped orbitals of this two-centre molecule using the standard spherical coordinates — particularly for calculations

at internuclear separations larger than equilibrium, which are important for modelling vibrational processes. For this reason, any comprehensive set of theoretical data for H_2 and heavier diatomic molecules suggest a reformulation of the theory in spheroidal coordinates.

The applications for electron and positron scattering data from molecules is as varied as it is for atoms. Physics disciplines that would benefit include the study of star formation and the interstellar medium [15–18], fusion research [1, 2], as well as atmospheric science (most notably for H_2 and N_2) for both particle collisions [19, 20] and rocket re-entry [5, 21]. In industry, the data will be useful in the production of nanomaterials [22], the generation of magnetohydrodynamic power, and electron lasers such as the CO_2 laser [6]. There are also potential biological applications in the study of electron-impact damage to biomolecules [23] and the preparation of biomass for conversion to biofuels [24, 25].

1.2 Overview of scattering theories

We can describe the various scattering theories as either perturbative or non-perturbaive. A perturbative theory finds a solution to a complex problem by first solving a known (approximate) form and then adding progressively smaller "corrective" perturbation terms until convergence is achieved. On the other hand, non-perturbative methods approach the problem more directly and are generally based on solving the Schrödinger equation using a close-coupling expansion or grid-based technique.

Perturbative methods

Perturbative theories are typically only accurate at high projectile energies or for highly-ionised targets. For instance, the first Born approximation (FBA) essentially replaces the target atom or molecules with a perturbative field in free space, and this is most appropriate when the field is relatively small compared to that of the incident particle.

Beyond the FBA, the distorted-wave Born approximation (DWBA) replaces the incident plane-wave with one that has been influenced by a simple distorting potential [26]. This has been successfully implemented for calculating electron-impact excitation, ionisation, and fully differential cross sections for both orientation-averaged molecules [27] and aligned molecules [28].

Of particular note is the independent-atom model (IAM) which uses an opti-

cal potential consisting of static, exchange, and polarisation terms and is applicable to high-energy (roughly 100–10000 eV) scattering. The quasi-free absorption model adds a complex term and was used in electron scattering on helium, neon, and argon to calculate absorption and elastic differential cross sections [29] as well as inelastic cross sections [30]. The inclusion of relativistic and many-body effects [31] and an addivity rule for screening effects [32] permitted electron scattering on molecules such as N_2, CO, CO_2, and benzene. This improved method (named IAM-SCAR) produces accurate cross sections down to 30 eV and scales well to large polyatomic molecules including CF_4 and C_3F_8 [33] that would be too difficult to model in close-coupling calculations. Recent advantages that account for rotational [34] and interference contributions [35] allow accurate integrated and differential cross sections down to 1 eV and has found success in studying electron and positron scattering from biomolecules such as pyrimidine ($C_4H_4N_2$).

The following methods described are generally non-perturbative.

Low-energy close-coupling methods

There is currently no ab initio theory that can include the immense number of electronic and nuclear states in a full close-coupling calculation. Using the Born-Oppenheimer approximation and phenomenological potentials, there have been calculations of vibrational [36], rotational [37], and ro-vibrational [38] close-coupling for near-threshold scattering.

The multi-channel quantum defect theory (MQDT) divides the electronic and nuclear coordinates into three regions depending on the dominant interactions present within, then solves the Lippmann-Schwinger equations perturbatively for the inner region before propagating the scattering wave outwards using frame transformations [39]. Nuclear states are coupled in one of these regions, so various molecular processes can be accounted for but only at low projectile energies [40]. The MQDT is only applicable to ionic targets and has been used to calculate dissociative excitation and recombination for H_2^+ and its isotopologues [41].

Schwinger variational methods

The Schwinger variational principle is a method for finding a stable T-matrix and thus solving the corresponding Lippmann-Schwinger equation [42]. The Schwinger multi-channel (SMC) method builds on this by instead solving for the K-matrix in the multichannel case and accounting for exchange and polarisation effects. This method is relatively computer-intensive and is therefore limited

in the number of channels that can be included and is restricted to low scattering energies. The recent review paper by da Costa *et al.* [43] details the numerous variations of this theory.

This method has been used to obtain elastic scattering and excitation cross sections of electron scattering on the diatomic molecules H_2 [44] and N_2 [45], positron scattering on the same molecules [46, 47], as well as triatomic and polyatomic molecules [43]. The results have been in generally good agreement with experiment, with the exception of electron-impact excitation of H_2 and N_2.

Kohn variational methods

The Kohn variational method is similar to the aforementioned Schwinger method, except that the Kohn principle [48] changes the objective to instead find the stationary phase shifts $\tan \delta_\ell$. This has the advantage of not requiring the intense calculation of matrix elements VG_0V, but causes the appearance of so-called Kohn singularities that until recently have proven difficult to deal with [49]. The complex Kohn variational method [50] modifies the Coulomb function basis to have the correct (real) boundary conditions, transforming the phase shifts into the T-matrix, and has demonstrated the removal of singularities whilst agreeing with the original Kohn method [49].

For diatomic molecules, the complex Kohn variational method has been used to obtain electron-impact excitation cross sections from H_2 [51], but results were in disagreement with experimental data. The Kohn variational method was applied to positron-impact scattering on H_2 [52] and N_2 [53] and the results were somewhat in agreement with older experiments. As with the Schwinger method, the complex Kohn method has also been used for polyatomic organic molecules with some success.

R-matrix methods

The R-matrix (RM) method, recently reviewed by Tennyson [9], partitions configuration space into an inner "core" region containing the molecular electrons while taking into account electron exchange and short-range correlations, and then an outer "potential-field" region for just the long-range interactions (without exchange). The total scattering wavefunction is obtained via diagonalisation in the inner region and is then propagated through the outer region where it is simpler to deal with. The R-matrix facilitates in the transition between the solutions in each region, and the boundary between them must be carefully determined by a

largely trial-and-error procedure [6].

The molecular R-matrix method with pseudostates (MRMPS) allows the diagonalisation basis to construct functions to represent the continuum, which is important for polarisation effects and ionisation channels. The R-matrix method using a B-spline basis has been successful for atomic targets [54] but the extension to molecular scattering [55] has experienced difficulties with two-electron targets [9].

For diatomic hydrogen, the RM method has been used to calculate low-energy elastic differential and integral cross sections [56] and the resulting dissociation rates of H_2 and its isotopologues [57, 58], while electron-impact ionisation cross sections were calculated with MRMPS [59]. The RM method has additionally investigated vibrational excitation for e^+-HF scattering [60], rotational excitation for e^--HCl scattering [61], and resonances of e^--N_2 caused by the coupling of electronic resonances with nuclear motion [62]. Other theoretical work for electron and positron scattering has been compiled by Tennyson [9]. As with the above variational methods, agreement with experiment is mixed. For H_2, the electron-impact excitation cross sections exhibit a particularly notable discrepancy.

Time-dependent close-coupling method

As its name suggests, the time-dependent close-coupling (TDCC) method solves the time-dependent Schrödinger equation. The projectile wavefunction is initially taken to be a Gaussian wavepacket and iterated from $t = 0$ to the collision region, and then to $t \to \infty$ to obtain scattering probabilities and hence cross sections. This method also allows the calculation of ionisation and photoionisation cross sections, as well as single, double, triple, and fully differential cross sections. Decreasing the grid spacing and time step increases the accuracy of the calculation but exacerbates the computationally demanding nature of this method.

Reviewed by Pindzola *et al.* [10], the TDCC method has been used to obtain electron-impact ionisation cross sections from H_2^+ [63], H_2 [64], and Li_2 [65]. In addition, their results for triple [66] and fully [67] differential cross sections of H_2 agree well with experiment, as did their predictions of the double-photoionisation of H_2 [68].

Convergent close-coupling methods

The spherical formulation of the molecular CCC method, as detailed in Chapter 3 and Zammit *et al.* [13], largely follows the original atomic formulation as reviewed

by Bray *et al.* [69]. In the first step, the CCC code diagonalises the target Hamiltonian in a Sturmian (Laguerre) basis to obtain both negative-energy and positive-energy pseudostates, with the latter being a discrete representation of the continuum. These pseudostates are then used to solve the Lippmann-Schwinger equation for the T-matrix and ultimately cross sections. An adiabatic-nuclei (AN) approximation may then be used to re-introduce nuclear dynamics.

The AN CCC method has already been applied successfully to electron scattering from H_2^+ and its isotopologues [70–72] in addition to positron scattering from H_2 [73, 74]. In contrast, electron-impact excitation of H_2 cross sections [75–77] showed notable discrepancies with previous calculations and somewhat better agreement with experiment.

Most significantly, the spherical formulation of the CCC method proved to be inefficient and inaccurate in performing the AN calculations that are required for vibrationally excited transitions. This was a large driving force behind the development of the molecular CCC theory in prolate spheroidal coordinates. This new formulation takes advantage of the spatial configuration of diatomic molecules and will allow us to obtain a comprehensive set of electronic and ro-vibrational data for electron and positron scattering.

Chapter 2

General theory

This chapter contains the background theory required for the problem of electron- and positron-molecule scattering, and specifically for a time-independent and non-relativistic approach. The aim is to calculate cross section data over a wide range of energies for comparison with experiment and use in plasma modelling.

Section 2.1 describes the scattering problem in general terms and what differences there are to atomic targets. In Section 2.2 we look at various approximations used to reduce the problem to a manageable size, before narrowing our attention to diatomic molecules in Section 2.3. Section 2.4 contains the T-matrix formalism and how it relates to observable cross sections. Finally, Section 2.5 describes additional techniques used in molecular scattering to account for nuclear processes or reduce the size and complexity of calculations.

Atomic units are used throughout this work unless otherwise specified.

2.1 Scattering problem

In this work we consider the scattering problem of a projectile (electron or positron) with wavefunction $F(x_0)$ interacting with a molecular target and subsequently being measured at an asymptotic distance well outside the interaction region. Because molecules will have an orientation that is independent of incoming projectile beam and detector angle, we can separate the system into two frames of reference: the *body frame* relative to the target and the *lab frame* relative to the experiment. The projectile-target interaction is calculated in the body frame and resulting scattering cross sections then transformed into the lab frame.

Inside the interaction region, the projectile and target are coupled in the total wavefunction $\Psi(\bar{x}, \bar{X})$ where the lower-case $\bar{x} = \{x_a, a = 0, 1, \ldots, n\}$ represents

the spatial ($\bar{\mathbf{r}}$) and spin ($\bar{\sigma}$) coordinates of both the projectile (index 0) and the n molecular electrons, while the upper-case $\bar{X} = \{X_A, A = 1, \ldots, N\}$ represents the same for the N molecular nuclei where the spatial components are $\bar{\mathbf{R}}$. The total wavefunction is subject to the time-independent Schrödinger equation

$$\hat{H}\Psi(\bar{x}, \bar{X}) = E\Psi(\bar{x}, \bar{X}) \tag{2.1}$$

where $\hat{H}$ is the interaction Hamiltonian and $\Psi(\bar{x}, \bar{X})$ is the (antisymmetric) total wavefunction.

The projectile-molecule Hamiltonian for an arbitrary molecule is

$$\hat{H} = \sum_a \hat{K}_a + \sum_A \hat{K}_A + \sum_{ab} V_{ab} + \sum_{a,A} V_{aA} + \sum_{A \neq B} V_{AB} \tag{2.2}$$

with kinetic operators $\hat{K}$ and Coulombic interaction potentials V. For electron scattering, the Pauli principle and hence requirement of antisymmetry gives rise to an "exchange" potential to be discussed later. The second and fifth terms of (2.2) represent nuclear motion and interaction that are not present for atomic targets, and lead to vibrational and rotational quantum states.

The energy separations of these additional states are small relative to electronically excited states, with vibrational in the order of 10^{-1} eV and rotational states in the order of 10^{-5} eV [78]. Due to the small energy separations of these states, many are accessible even at very low incident energies and therefore should be accounted for in scattering calculations.

In the convergent close-coupling (CCC) theory we do not solve the Schrödinger equation (2.1) directly for the wavefunction. It is more convenient to transform the problem and instead solve for the T-matrix and scattering amplitudes; the theoretical details of this are contained in Section 2.4. The scattering amplitudes quantify the interaction between projectile and target, and the square of their absolute values yield the cross sections which are the most convenient interface theory has with experiment. For molecular collisions, experimental energy resolution is sensitive enough to produce vibrationally resolved cross sections, but the small energy spacing of rotational states means that they are usually averaged over.

2.2 Molecular approximations

Solving the molecular scattering problem with the total wavefunction $\Psi(\bar{\mathbf{r}}, \bar{\mathbf{R}})$ means taking into account the vast number of electronic, vibrational, and rotational states. As a result the size of the calculations is far beyond that of atomic

scattering and the ability of contemporary computers. Instead, we must consider the following approximations to reduce the number of reaction channels in order to make the calculations possible.

2.2.1 The Born-Oppenheimer approximation

The usual first step in dealing with molecules is given by Born & Oppenheimer [12] as separating the electronic and nuclear components of the wavefunction

$$\Psi(\bar{\mathbf{r}}, \bar{\mathbf{R}}) \approx \Psi^{\mathrm{E}}(\bar{\mathbf{r}}; \bar{\mathbf{R}})\Psi^{\mathrm{N}}(\bar{\mathbf{R}}) \tag{2.3}$$

to enable us to solve for them separately. The electronic component $\Psi^{\mathrm{E}}(\bar{\mathbf{r}}; \bar{\mathbf{R}})$ depends only parametrically on the nuclei positions $\bar{\mathbf{R}}$ and the nuclear component $\Psi^{\mathrm{N}}(\bar{\mathbf{R}})$ is the product of rotational and vibrational wavefunctions. We may use this approximation to solve the electronic Hamiltonian

$$\begin{aligned}\hat{H}^{\mathrm{E}} &= \sum_{a} \hat{K}_a + \sum_{a<b} V_{ab} + \sum_{a,A} V_{aA} \\ &= -\sum_{a=0}^{n} \frac{\hat{\nabla}_a^2}{2} + \sum_{a=0}^{n}\sum_{a<b}^{n} \frac{z_a z_b}{|\mathbf{r}_a - \mathbf{r}_b|} - \sum_{a=0}^{n}\sum_{A=1}^{N} \frac{z_a Z_A}{|\mathbf{r}_a - \mathbf{R}_A|}\end{aligned} \tag{2.4}$$

where z_a and Z_A are the charges of electron a and nuclei A respectively, and m is the mass of an electron. Solutions of the nuclear Hamiltonian

$$\begin{aligned}\hat{H}^{\mathrm{N}} &= \sum_{A} \hat{K}_A + \sum_{A<B} \hat{V}_{AB} \\ &= -\sum_{A=1}^{N} \frac{\hat{\nabla}_A^2}{2M_A} + \sum_{A=1}^{N}\sum_{A<B}^{N} \frac{Z_A Z_B}{|\mathbf{R}_A - \mathbf{R}_B|}\end{aligned} \tag{2.5}$$

are now separate from the molecular electrons. To approximate the interaction between nuclei and electron, one may replace the nuclei-nuclei potential by the *energy surface* as defined by

$$\epsilon_{ji}(\bar{\mathbf{R}}) = \left\langle \Psi_j^{\mathrm{E}}(\bar{\mathbf{r}}; \bar{\mathbf{R}}) \left| \sum_{A=1}^{N}\sum_{B>A}^{N} \frac{Z_A Z_B}{|\mathbf{R}_A - \mathbf{R}_B|} + \hat{H}^{\mathrm{E}} \right| \Psi_i^{\mathrm{E}}(\bar{\mathbf{r}}; \bar{\mathbf{R}}) \right\rangle \tag{2.6}$$

and where the integral is over $\mathbf{r}$. The ro-vibrational states are now solutions of the Hamiltonian

$$\hat{H}^{\mathrm{N(BO)}} = -\sum_{A=1}^{N} \frac{\hat{\nabla}_A^2}{2M_A} + \epsilon_{ji}(\bar{\mathbf{R}}). \tag{2.7}$$

If we discretise (2.6) in internuclear distance and solve for electronic wavefunctions for each fixed $\bar{\mathbf{R}}$, the problem is diagonal in i and j and we may then obtain nuclear wavefunctions by diagonalising (2.7). However, this is a classical approximation that neglects the explicit coupling between electronic and nuclear states and in some circumstances may affect the accuracy of the calculation.

From a physical standpoint, the Born-Oppenheimer approximation assumes that electrons and positrons are so small and fast that they respond instantaneously to changes of nuclei position. This simplified picture breaks down in the cases of highly excited electronic or vibrational states, where electrons are slow or nuclei are fast respectively [6].

2.2.2 Fixed-nuclei approximation

Within the Born-Oppenheimer approximation we can even further simplify and suppose that the nuclei remain fixed relative to one another. In this fixed-nuclei (FN) approximation the nuclear Hamiltonian (2.5) becomes trivial as the first term vanishes, leaving only the (constant) internuclear repulsion

$$\hat{H}^{\mathrm{N(FN)}} = \sum_{A=1}^{N} \sum_{A<B}^{N} \frac{Z_A Z_B}{|\mathbf{R}_A - \mathbf{R}_B|} \tag{2.8}$$

with no spectra of rotational or vibrational states. The electronic wavefunctions Ψ_j^{E} only need to be calculated at the particular arrangement $\bar{\mathbf{R}}$.

Neglecting the nuclear states of the molecule drastically simplifies the problem but may not be applicable in certain cases. It is most valid in the region near the molecule where interaction is predominantly due to molecular electrons instead of the nuclei. The FN approximation should be valid for "fast collisions" where the collision time is significantly less than the periods for nuclear rotation ($\sim 10^{-12}$ s) and excitation ($\sim 10^{-14}$ s) such that these can be safely ignored [6]. The classical collision time is slower for incident energies near thresholds and resonances, or when long-range interactions dominate [6].

For this approximation we must choose the most appropriate length of the internuclear axis. Historically, calculations are usually performed at the equilibrium distance $R_0 = 1.4$, which corresponds to the minimum energy of the ground electronic state. Zhang & Mitroy [79] point out that the mean internuclear distance of the ground vibrational state $R_m = 1.448$ provides a better approximation to the (more accurate) adiabatic-nuclei (AN) theory that is detailed in the next section. However, AN calculations are several times more computationally expensive and will only be used where it is necessary to account for nuclear processes.

2.2.3 Adiabatic-nuclei approximation

The adiabatic-nuclei (AN) approximation allows us to obtain information about the nuclear processes without the expense of directly coupling electronic and nuclear states together. This lets us account for vibrational excitation channels and investigate processes such as dissociative excitation that result from these. From a physical standpoint we are allowing the electrons to respond adiabatically to the instantaneous positions (but not motion) of the nuclei.

In this approximation the electronic wavefunctions (2.4) are determined for a series of fixed-nuclei molecular arrangements, as are the nuclear wavefunctions (2.5) in the $\mathbf{R}$ region of interest. We may then obtain AN scattering quantities, such as the T-matrix (Section 2.4.2) and scattering amplitudes (Section 2.4.3), from integrating the FN quantities in $\mathbf{R}$-space in the presence of initial and final vibrational waves. This results in vibrationally resolved cross sections; the final vibrational state is often summed over to allow comparison with experiments that are unable to resolve the fine energy spacing of vibrational levels.

As this method is built upon performing multiple fixed-nuclei calculations, it relies on the same assumptions and can be expected to have similar weaknesses. The AN approximation should be an improvement in energy regions around vibrational thresholds, which are typically within a few eV of electronic thresholds. However, because we are not explicitly coupling vibrational states, cross sections involving vibrational transitions violate energy conservation and the true thresholds must be accounted for in order to obtain accurate results near-threshold [36].

The adiabatic-nuclei approximation was first tested by Peek & Green [80] for the $1s\sigma_g$–$2p\sigma_u$ excitation cross section of e^-–H_2^+ scattering in the first Born approximation. The authors' calculation without the Born-Oppenheimer (or FN and AN) approximations matched previous AN results except those involving highly excited vibrational states. Recently, the CCC calculations of electron-H_2^+ [71] and positron-H_2 [74] scattering show excellent agreement between FN and AN approximations.

2.3 Diatomic molecules

We now focus the discussion on molecules with two nuclei Z_1 and Z_2 separated by a single internuclear axis $\mathbf{R}$. For convenience we align the $\mathbf{R}$ with the z-axis of the body frame. Vibrational states are functions of the internuclear distance

$R = |R|$ and rotational states are functions of the angle $\hat{\mathbf{R}}$.

In the Born-Oppenheimer (Section 2.2.1) and fixed-nuclei (Section 2.2.2) approximations, scattering from diatomic molecules is nearly as straightforward as for atoms. By separating the nuclear and electronic states, the constant nuclear energy

$$E^{\mathrm{N(FN)}} = \frac{Z_A Z_B}{R} \tag{2.9}$$

is simply summed with electronic energy to give the total energy of the molecule. Although we initially neglect the rotational and vibrational degrees of freedom they can be restored in the AN approximation.

With two nuclei there is no definitive central point for the origin of the spherical coordinate system. The most sensible location would be along the internuclear axis, resulting in the single-centre approach (Section 2.3.1). Alternatively, by adopting the spheroidal coordinate system and placing each of the two foci at the nuclei we get the double-centre approach (Section 2.3.2) and achieve greater accuracy. Note that this terminology should not be confused with the one-centre and two-centre methods of positron scattering, which refer to the exclusion or inclusion (respectively) of explicit positronium states.

In the following two sections we will describe the mathematical details of the one-electron Hamiltonian for both single-centre and double-centre coordinate approaches.

2.3.1 Single-centre (spherical) approach

In this approach we must choose where the origin is in relation to the two nuclei. For the sake of generality let $\mathbf{R}_1$ and $\mathbf{R}_2$ be vectors from the origin to each nuclei, such that $\mathbf{R} = \mathbf{R}_1 - \mathbf{R}_2$. This gives us the one-electron Hamiltonian

$$\hat{H}_1 = \hat{K}_1 + V_1 \tag{2.10}$$

which comprised of the kinetic energy operator

$$\hat{K_1} = \frac{-1}{2r^2}\left[\frac{\partial}{\partial r}\left(r^2\frac{\partial}{\partial r}\right) + \frac{1}{\sin\theta}\frac{\partial}{\partial\theta}\left(\sin\theta\frac{\partial}{\partial\theta}\right) + \frac{1}{\sin^2\theta}\frac{\partial^2}{\partial\phi^2}\right] \tag{2.11}$$

and the nuclear potential with general form

$$V_1 = \frac{zZ_1}{|\mathbf{r}+\mathbf{R}_1|} + \frac{zZ_2}{|\mathbf{r}+\mathbf{R}_2|}. \tag{2.12}$$

We may use the Laplace expansion (F.1) and the fact that $\mathbf{R}$ lies along the z-axis to rewrite the potential in terms of the partial waves

$$V_1 = z \sum_{L=0}^{\infty} \left[Z_1 \frac{\min(r, R_1)^L}{\max(r, R_1)^{L+1}} + (-1)^L Z_2 \frac{\min(r, R_2)^L}{\max(r, R_2)^{L+1}} \right] P_L(\cos\theta). \tag{2.13}$$

If the nuclei are equidistant ($R_1 = R_2$), then (2.13) simplifies to

$$V_1 = z \sum_{L=0}^{\infty} \left[Z_1 + (-1)^L Z_2 \right] \frac{r_<^L}{r_>^{L+1}} P_L(\cos\theta) \tag{2.14}$$

with $r_< = \min(r, \frac{R}{2})$ and $r_> = \max(r, \frac{R}{2})$. It is straightforward to show that in the homogeneous case ($Z_1 = Z_2$) the sum takes only even L values, thereby introducing molecular parity, and that in the atomic limit $r_<^L = \delta_{L0}$ and therefore $V_1 = (Z_1 + Z_2)/r$ as expected. For heterogenerous diatomics ($Z_1 \neq Z_2$) it may be more convenient to locate the origin closer to one of the two nuclei ($R_1 \neq R_2$) in (2.13).

2.3.2 Double-centre (spheroidal) approach

Rather than needing to choose the position of the origin, the foci of the spheroidal coordinates can naturally coincide with the two nuclei of the diatomic molecules. In terms of spherical coordinates with equidistant nuclei, we define the distance to a point from each centre by $r_1 = |\mathbf{r} + \frac{1}{2}\mathbf{R}|$ and $r_2 = |\mathbf{r} - \frac{1}{2}\mathbf{R}|$. With these definitions we can write the prolate spheroidal coordinates (ξ, η, ϕ) as

$$\begin{aligned} \xi &= \frac{r_1 + r_2}{R} \in [1, \infty) \\ \eta &= \frac{r_1 - r_2}{R} \in (-1, 1] \\ \phi &\in [0, 2\pi) \end{aligned} \tag{2.15}$$

where the azimuthal variable ϕ is the same as its spherical coordinate counterpart. As the focal points come together ($R \to 0$) it is clear that $\lim_{R\to 0} r_1 = \lim_{R\to 0} r_2 = r$ and therefore

$$\lim_{R\to 0} \xi = \frac{2r}{R} \tag{2.16}$$

by our definitions and

$$\lim_{R\to 0} \eta = \cos\theta \tag{2.17}$$

from trigonometry.

The prolate spheroidal volume element (A.19)

$$\mathrm{d}V = \tfrac{R^3}{8}(\xi^2 - \eta^2)\mathrm{d}\xi\mathrm{d}\eta\mathrm{d}\phi \tag{2.18}$$

and Laplacian (A.21) are derived in Appendix A.1; the latter gives the kinetic energy operator as

$$\hat{K}_1 = \frac{-2/R^2}{\xi^2 - \eta^2}\left\{\frac{\partial}{\partial\xi}\left[(\xi^2-1)\frac{\partial}{\partial\xi}\right] + \frac{\partial}{\partial\eta}\left[(1-\eta^2)\frac{\partial}{\partial\eta}\right] + \left(\frac{1}{\xi^2-1} + \frac{1}{1-\eta^2}\right)\frac{\partial^2}{\partial\phi^2}\right\} \tag{2.19}$$

and the nuclear potential given in (2.12) rearranges into the spheroidal form

$$V_1 = \frac{2/R^2}{\xi^2 - \eta^2}\Big\{z(Z_1 + Z_2)R\xi - z(Z_1 - Z_2)R\eta\Big\}. \tag{2.20}$$

Consider the Schrödinger equation for a particle of charge z in the presence of a fixed Coulombic potential $V(\xi, \eta)$,

$$[\hat{K} + V(\xi,\eta)]\psi(\xi,\eta,\phi) = E\psi(\xi,\eta,\phi), \tag{2.21}$$

such that the potential is of form

$$V(\xi,\eta) = \frac{2/R^2}{\xi^2 - \eta^2}\Big\{V_\xi(\xi) + V_\eta(\eta)\Big\}, \tag{2.22}$$

which has the same multiplicative factor as the kinetic energy operator (2.19). Then (2.21) can be rearranged into

$$\begin{aligned}\Bigg\{&\frac{\partial}{\partial\xi}\left[(\xi^2-1)\frac{\partial}{\partial\xi}\right] + \frac{1}{\xi^2-1}\frac{\partial^2}{\partial\phi^2} - V_\xi(\xi) + \frac{1}{2}ER^2\xi^2 \\ &+\frac{\partial}{\partial\eta}\left[(1-\eta^2)\frac{\partial}{\partial\eta}\right] + \frac{1}{1-\eta^2}\frac{\partial^2}{\partial\phi^2} - V_\eta(\eta) - \frac{1}{2}ER^2\eta^2\Bigg\}\psi(\xi,\eta,\phi) = 0.\end{aligned} \tag{2.23}$$

Following Burrau [81] we presume that the wavefunction is separable as the product

$$\psi(\xi,\eta,\phi) = \Xi(\xi)\mathrm{H}(\eta)\Phi(\phi) \tag{2.24}$$

and then apply the familiar separation of variables technique to discern the behaviour of each individual function. The azimuthal coordinate resolves identically to the spherical case, with

$$\frac{\mathrm{d}^2}{\mathrm{d}\phi^2}\Phi(\phi) = -m^2\Phi(\phi) \tag{2.25}$$

for constant m. As such, we define

$$\Phi(\phi) = \exp(\mathrm{i}m\phi). \tag{2.26}$$

Substituting this back into (2.23) and separating again results in

$$\frac{1}{\Xi(\xi)}\left\{\frac{\mathrm{d}}{\mathrm{d}\xi}\left[(\xi^2-1)\frac{\mathrm{d}}{\mathrm{d}\xi}\right]-\frac{m^2}{\xi^2-1}-V_\xi(\xi)+c^2\xi^2\right\}\Xi(\xi)$$
$$=\frac{-1}{\mathrm{H}(\eta)}\left\{\frac{\mathrm{d}}{\mathrm{d}\eta}\left[(1-\eta^2)\frac{\mathrm{d}}{\mathrm{d}\eta}\right]-\frac{m^2}{1-\eta^2}-V_\eta(\eta)-c^2\eta^2\right\}H(\eta)=a \quad (2.27)$$

for constant a and the quantity $c^2=\frac{1}{2}ER^2$. Rearrangement yields the radial equation

$$\left\{\frac{\mathrm{d}}{\mathrm{d}\xi}\left[(\xi^2-1)\frac{\mathrm{d}}{\mathrm{d}\xi}\right]-\frac{m^2}{\xi^2-1}-V_\xi(\xi)+c^2(\xi^2-1)-A\right\}\Xi(\xi)=0 \quad (2.28)$$

and, after combining $\Upsilon(\eta,\phi)=\mathrm{H}(\eta)\exp(\mathrm{i}m\phi)$, the angular equation

$$\left\{\frac{\partial}{\partial\eta}\left[(1-\eta^2)\frac{\partial}{\partial\eta}\right]-\frac{m^2}{1-\eta^2}-V_\eta(\eta)+c^2(1-\eta^2)+A\right\}\Upsilon(\eta,\phi)=0 \quad (2.29)$$

where we define the *spheroidal separation constant* as $A=a-c^2$. Some authors do not include the c^2 term into their definition, and some have different sign conventions, so care must be taken when making comparisons between works.

The above radial (2.28) and angular (2.29) equations can be used to generate spheroidal partial waves for particles in free space or short-ranged distorting potentials, as will be done in Chapter 4.1.2. If the potential is a fixed pair of charges, such as in a diatomic molecule, comparison of (2.20) with (2.22) gives us the potentials as

$$V_\xi(\xi)=Z_+R\xi \qquad \text{and} \qquad V_\eta(\eta)=-Z_-R\eta \quad (2.30)$$

with $Z_\pm=z(Z_1\pm Z_2)$.

The above typifies the difference between the spherical and spheroidal approaches to diatomic molecules. The spheroidal volume element (2.18) results in somewhat more complicated integrations, but because the coordinate system is better suited to diatomic molecules, the potential terms (2.30) are simpler and do not require an angular expansion as in the spherical case (2.13).

2.4 Formal scattering theory

The time-independent Schrödinger equation for a projectile incident on a two-electron diatomic molecule is

$$(E-\hat{H})\Psi_i(\mathbf{r}_0,\mathbf{r}_1,\mathbf{r}_2)=0, \quad (2.31)$$

which has the Hamiltonian

$$\hat{H} = \hat{K}_0 + \hat{V}_0 + \hat{V}_{01} + \hat{V}_{02} + \hat{H}_1 + \hat{H}_2 + \hat{V}_{12} + \tfrac{Z^2}{R}, \tag{2.32}$$

where $\hat{K}_0$ is the kinetic energy of the projectile;
$\hat{V}_0$ is the projectile-target-nuclei potential;
$\hat{V}_{01}$ and $\hat{V}_{02}$ are the projectile-target-electron potentials; and
$\hat{H}_1 + \hat{H}_2 + \hat{V}_{12} + \frac{Z^2}{R} \equiv \hat{H}_{12}$ is the target Hamiltonian.

Instead of directly solving for the total scattering wavefunction $\Psi_i(\mathbf{r}_0, \mathbf{r}_1, \mathbf{r}_2) \equiv \langle \mathbf{r}_0, \mathbf{r}_1, \mathbf{r}_2 | \Psi_i \rangle$ we will now derive the Lippmann-Schwinger formalism to obtain scattering amplitudes.

While molecular electron states will be constructed as antisymmetric, the total scattering wavefunction must be antisymmetrised in the case of an electron projectile. We may define it in terms of an antisymmetrising operator acting on a more general scattering wavefunction

$$|\Psi_i\rangle = (1 - \hat{P}_{01} - \hat{P}_{02})|\psi_i\rangle, \tag{2.33}$$

where $\hat{P}_{ij}$ is a space-exchange operator that switches the coordinates and spin of electrons i and j. The multichannel expansion with our set of target states $\Phi_n(x_1, x_2)$ gives

$$\begin{aligned} |\Psi_i\rangle &= (1 - \hat{P}_{01} - \hat{P}_{02}) \sum_{n=1}^{N} |\Phi_n\rangle\langle\Phi_n|\psi_i\rangle \\ &= (1 - \hat{P}_{01} - \hat{P}_{02}) \sum_{n=1}^{N} |F_n^{(i)}\Phi_n\rangle \end{aligned} \tag{2.34}$$

with the projectile functions $|F_n^{(i)}\rangle = \langle\Phi_n|\psi_i\rangle$. As the target states are antisymmetric by construction, both

$$\hat{P}_{01}[F_n^{(i)}(x_0)\Phi_n(x_1, x_2)] = F_n^{(i)}(x_1)\Phi_n(x_0, x_2) \tag{2.35}$$

and

$$\begin{aligned} \hat{P}_{02}[F_n^{(i)}(x_0)\Phi_n(x_1, x_2)] &= -\hat{P}_{02}[F_n^{(i)}(x_0)\Phi_n(x_2, x_1)] \\ &= -F_n^{(i)}(x_1)\Phi_n(x_2, x_0) \\ &= F_n^{(i)}(x_1)\Phi_n(x_0, x_2) \end{aligned} \tag{2.36}$$

are equivalent, so we can rewrite $-\hat{P}_{01} - \hat{P}_{02} = -2\hat{P}_{01}$ in (2.34). A similar argument allows us to rewrite $\hat{V}_{01} + \hat{V}_{02} = 2\hat{V}_{01}$ in (2.32).

Combining the Schrödinger equation (2.31) with the antisymmetry condition (2.33), and rearranging the Hamiltonian (2.32) to give molecular interaction terms on the left and asymptotic terms on the right, we obtain

$$\left[\hat{V}_0 + 2\hat{V}_{01} + 2(E - \hat{H})\hat{P}_{01}\right] |\psi_i\rangle = (E - \hat{K}_0 - \hat{H}_{12})|\psi_i\rangle. \tag{2.37}$$

At this point one may introduce a distorting potential $\hat{U}_0$, which is a common mathematical technique used to increase the efficiency of scattering calculations. This potential must be short-ranged and its influence removed before scattering amplitudes can be extracted. Subtracting the distorting potential (which can be 0) from both sides yields our equation for the three-electron scattering states $|\psi_i\rangle = \psi_i(x_0, x_1, x_2)$

$$\hat{V}_U|\psi_i\rangle = (E - \hat{H}_{\rm asym})|\psi_i\rangle \tag{2.38}$$

with the (distorted) interaction potential

$$V_U = V_0 - U_0 + 2V_{01} + 2(E - \hat{H})\hat{P}_{01} \tag{2.39}$$

and asymptotic Hamiltonian $\hat{H}_{\rm asym} = \hat{K}_0 + \hat{U}_0 + \hat{H}_{12}$.

If we consider an individual channel n and pre-multiply (2.38) by the target state $\langle\Phi_n|$ we obtain

$$\begin{aligned}\langle\Phi_n|\hat{V}_U|\psi_i\rangle &= \sum_{n'=1}^{N}\langle\Phi_n|E - \hat{H}_{12} - \hat{K}_0 - \hat{U}_0|\Phi_{n'}F_{n'}^{(i)}\rangle \\ &= (E - \epsilon_n - \hat{K}_0 - \hat{U}_0)|F_n^{(i)}\rangle \end{aligned}\tag{2.40}$$

with state energy ϵ_n and channel functions $F_n^{(i)}(x_0)$. In the non-interacting ($\hat{V}_U = 0$) case the solution is

$$(E - \epsilon_n - \epsilon_{k_n})|\Phi_n\mathbf{k}_n^{(+)}\rangle = 0, \tag{2.41}$$

where the (outgoing) distorted waves $|\mathbf{k}_n^{(+)}\rangle$ have on-shell energy $\epsilon_{k_n} = \frac{k_n^2}{2} = E - \epsilon_n$ corresponding to channel n.

2.4.1 Green's functions

In the CCC approach we solve for the channel functions (2.40) by invoking the theory of Green's functions. The Green's function of the linear operator $E - \epsilon_n - \hat{K}_0 - \hat{U}_0$ is essentially its reciprocal. Projecting into momentum space yields

$$\hat{G}_n = \frac{1}{E - \epsilon_n - \hat{K}_0 - \hat{U}_0} = \int \frac{|\mathbf{k}^{(-)}\rangle\langle\mathbf{k}^{(-)}|}{E - \epsilon_n - \frac{k^2}{2}}\mathrm{d}^3\mathbf{k} \tag{2.42}$$

where we have used (2.41). This Green's function is singular at the on-shell momentum $k = k_n$ so we offset the denominator by an imaginary amount and let it approach zero ($\pm \mathrm{i}0 \equiv \lim_{\epsilon \to 0^\pm} \mathrm{i}\epsilon$), giving

$$\hat{G}_n^{(\pm)} = \int \frac{|\mathbf{k}^{(-)}\rangle\langle\mathbf{k}^{(-)}|}{\frac{k_n^2}{2} - \frac{k^2}{2} \pm \mathrm{i}0} \mathrm{d}^3\mathbf{k}. \tag{2.43}$$

Projecting this into coordinate space

$$\langle \mathbf{x}|\hat{G}_n^{(\pm)}|\mathbf{x}'\rangle = -2 \int \frac{\langle \mathbf{x}|\mathbf{k}^{(-)}\rangle\langle\mathbf{k}^{(-)}|\mathbf{x}'\rangle}{k^2 - k_n^2 \mp \mathrm{i}0} \mathrm{d}^3\mathbf{k} \tag{2.44}$$

gives the functional form of the Green's function as

$$G_n^{(\pm)}(\mathbf{x}, \mathbf{x}') = \frac{-1}{4\pi^3} \int \frac{\mathrm{e}^{-\mathrm{i}\mathbf{k}\cdot\mathbf{x}} \mathrm{e}^{\mathrm{i}\mathbf{k}\cdot\mathbf{x}'}}{k^2 - k_n^2 \mp \mathrm{i}0} \mathrm{d}^3\mathbf{k}, \tag{2.45}$$

where we have used

$$\langle \mathbf{x}|\mathbf{k}\rangle = \exp(-\mathrm{i}\mathbf{k}\cdot\mathbf{x}) \tag{2.46}$$

as the definition of plane waves. For convenience these waves are normalised

$$\langle \mathbf{k}'|\mathbf{k}\rangle = \int \mathrm{e}^{-\mathrm{i}(\mathbf{k}-\mathbf{k}')\cdot\mathbf{x}} \mathrm{d}\mathbf{k} = (2\pi)^3 \delta(\mathbf{k} - \mathbf{k}') \tag{2.47}$$

in momentum space. Now we let $\mathbf{r} = \mathbf{x}' - \mathbf{x}$ and align the z-axis with $\hat{\mathbf{r}}$ to simplify the integration of $\hat{\mathbf{k}}$:

$$\begin{aligned} G_n^{(\pm)}(r) &= \frac{-1}{4\pi^3} \iiint \frac{\mathrm{e}^{\mathrm{i}kr\cos\theta}}{k^2 - k_n^2 \mp \mathrm{i}0} k^2 \sin\theta \mathrm{d}k\mathrm{d}\theta\mathrm{d}\phi \\ &= \frac{-1}{4\pi^3} \left(\int_0^\infty \frac{\mathrm{e}^{\mathrm{i}kr}}{k^2 - k_n^2 \mp \mathrm{i}0} \frac{2\pi k^2}{\mathrm{i}kr} \mathrm{d}k - \int_0^\infty \frac{\mathrm{e}^{-\mathrm{i}kr}}{k^2 - k_n^2 \mp \mathrm{i}0} \frac{2\pi k^2}{\mathrm{i}kr} \mathrm{d}k \right) \\ &= \frac{-1}{2\pi^2 \mathrm{i}r} \int_{-\infty}^\infty \frac{\mathrm{e}^{\mathrm{i}kr}}{k^2 - k_n^2 \mp \mathrm{i}0} k \mathrm{d}k. \end{aligned} \tag{2.48}$$

Reorganising the denominator to $(k - k_n \mp \mathrm{i}0)(k + k_n \pm \mathrm{i}0)$ slightly shifts the singularities to $k = k_n \pm \mathrm{i}0$ and $k = -k_n \mp \mathrm{i}0$.

We now employ residue theory by considering a semicircular contour $\mathcal{C} = \mathcal{C}_1 \cup \mathcal{C}_2$ with its base $\mathcal{C}_1$ extending to the infinities on the real axis and arc $\mathcal{C}_2$ joining the ends in the top half of the complex plane, enclosing the pole at $k = \pm k_n + \mathrm{i}0$. Since $r = |\mathbf{x} - \mathbf{x}'| > 0$, the positive imaginary component of k ensures $\mathrm{e}^{\mathrm{i}kr} \to 0$

for $\mathcal{C}_2$, and so the integration in (2.48) is equivalent to

$$\begin{aligned}\int_{-\infty}^{\infty} \frac{\mathrm{e}^{\mathrm{i}kr}}{k^2 - k_n^2 \mp \mathrm{i}0} k\mathrm{d}k &= \oint_{\mathcal{C}} \frac{\mathrm{e}^{\mathrm{i}kr}}{(k - k_n \mp \mathrm{i}0)(k + k_n \pm \mathrm{i}0)} k\mathrm{d}k \\ &= 2\pi\mathrm{i} \lim_{k \to \pm k_n + \mathrm{i}0} (k \mp k_n - \mathrm{i}0) \frac{k\mathrm{e}^{\mathrm{i}kr}}{(k - k_n \mp \mathrm{i}0)(k + k_n \pm \mathrm{i}0)} \\ &= \pi\mathrm{i}\mathrm{e}^{\pm \mathrm{i}k_n r}. \end{aligned} \tag{2.49}$$

Hence the operational Green's functions (2.42) with complex component

$$\hat{G}_n^{(\pm)} = \frac{1}{E - \epsilon_n - \hat{K}_0 - \hat{U}_0 \pm \mathrm{i}0} \tag{2.50}$$

have the functional forms

$$G_n^{(\pm)}(\mathbf{x}, \mathbf{x}') = \frac{-1}{2\pi} \frac{\mathrm{e}^{\pm \mathrm{i}k_n |\mathbf{x}' - \mathbf{x}|}}{|\mathbf{x}' - \mathbf{x}|}, \tag{2.51}$$

and the $(+)$ and $(-)$ cases represent outgoing and incoming spherical wave respectively. Only the outgoing wave matches the boundary conditions of our scattering problem, so henceforth we shall consider only $G_n^{(+)}(\mathbf{x}', \mathbf{x})$.

2.4.2 The T-matrix

Using the Green's function (2.50) we may recast the differential Schrödinger equations into integral Lippmann-Schwinger equations for individual channel functions (2.40)

$$|F_n^{(i)}\rangle = \delta_{ni} |\mathbf{k}_i^{(+)}\rangle + \int \frac{|\mathbf{k}^{(-)}\rangle \langle \mathbf{k}^{(-)} \Phi_n | \hat{V}_U | \psi_i \rangle}{E - \epsilon_n - \epsilon_k + \mathrm{i}0} \mathrm{d}^3\mathbf{k}. \tag{2.52}$$

Multiplying by $|\Phi_n\rangle$ and summing over n recovers the expression for the three-electron scattering wavefunction

$$|\psi_i\rangle = |\Phi_i \mathbf{k}_i^{(+)}\rangle + \sum_{n=1}^{N} \int \frac{|\Phi_n \mathbf{k}^{(-)}\rangle \langle \mathbf{k}^{(-)} \Phi_n | \hat{V}_U | \psi_i \rangle}{E - \epsilon_n - \epsilon_k + \mathrm{i}0} \mathrm{d}^3\mathbf{k}, \tag{2.53}$$

while the unscattered (distorted) wave can be written as

$$|\Phi_i \mathbf{k}_i^{(+)}\rangle = |\Phi_i \mathbf{k}_i\rangle + \frac{1}{E - \epsilon_n - \epsilon_{k_i} + \mathrm{i}0} U_0 |\Phi_n \mathbf{k}_i^{(+)}\rangle \tag{2.54}$$

in terms of plane waves. The scattering wavefunction (2.53) can be written in the short-hand notation

$$|\psi\rangle = |\psi_1\rangle + \hat{G}\hat{V}|\psi\rangle, \tag{2.55}$$

where we may think of $|\psi\rangle$ and $|\psi_0\rangle = |\Phi_0 \mathbf{k}_0\rangle$ as the scattered and unscattered waves respectively, $\hat{V}$ as the interaction between projectile and molecule, and $\hat{G}$ as the emanation of a spherical wave (2.51) that results from this interaction.

If we assume that the scattering V is weak, the scattered wave is simply

$$|\psi\rangle \approx |\psi_0\rangle, \tag{2.56}$$

giving us what is known as the first Born approximation. The Born series is perturbative, and we can obtain the next term by using (2.56) as the unknown wavefunction on the right-hand side of (2.55), thereby obtaining

$$|\psi_1\rangle \approx |\psi_0\rangle + \hat{G}\hat{V}|\psi_0\rangle \tag{2.57}$$

or the second Born approximation. Physically, this represents an incoming projectile $|\psi_0\rangle$ either not interacting (first term) or scattering once from $\hat{V}$ and causing an outgoing spherical wave $\hat{G}$ (second term). The resulting wave $|\psi_1\rangle$ can be again substituted into the second term of (2.55) for the third term

$$|\psi_2\rangle \approx |\psi_0\rangle + \hat{G}\hat{V}|\psi_0\rangle + \hat{G}\hat{V}\hat{G}\hat{V}|\psi_0\rangle, \tag{2.58}$$

which represents 0, 1, or 2 scattering events. By repeating this process ad infinitum and rearrange we get

$$\begin{aligned} |\psi\rangle &= |\psi_0\rangle + \hat{G}\hat{V}|\psi_0\rangle + \hat{G}\hat{V}\hat{G}\hat{V}|\psi_0\rangle + \hat{G}\hat{V}\hat{G}\hat{V}\hat{G}\hat{V}|\psi_0\rangle + \ldots \\ &= |\psi_0\rangle + \hat{G}(\hat{V} + \hat{V}\hat{G}\hat{V} + \hat{V}\hat{G}\hat{V}\hat{G}\hat{V} + \ldots)|\psi_0\rangle \\ &= |\psi_0\rangle + \hat{G}\hat{T}|\psi_0\rangle, \end{aligned} \tag{2.59}$$

where this new operator $\hat{T}$ contains all possible scattering event combinations. In our original long-hand notation (2.59) looks like

$$|\psi_i\rangle = |\Phi_i \mathbf{k}_i^{(+)}\rangle + \sum_{n=1}^{N} \int \frac{|\Phi_n \mathbf{k}^{(-)}\rangle\langle \mathbf{k}^{(-)}\Phi_n|T_U|\Phi_i \mathbf{k}_i^{(+)}\rangle}{E - \epsilon_n - \epsilon_k + \mathrm{i}0} \mathrm{d}^3\mathbf{k} \tag{2.60}$$

and hence we define the (distorted) T-matrix as

$$\langle \mathbf{k}_f^{(-)}\Phi_f|T_U|\Phi_i \mathbf{k}_i^{(+)}\rangle = \langle \mathbf{k}_f^{(-)}\Phi_f|\hat{V}_U|\psi_i^{(+)}\rangle. \tag{2.61}$$

Rather than trying to calculate the scattering wavefunction from (2.60), we premultiply it by $\langle \mathbf{k}_f^{(-)}\Phi_f|V_U$ to obtain the coupled Lippmann-Schwinger equations

$$\begin{aligned} \langle \mathbf{k}_f^{(-)}\Phi_f|T_U|\Phi_i \mathbf{k}_i^{(+)}\rangle &= \langle \mathbf{k}_f^{(-)}\Phi_f|V_U|\Phi_i \mathbf{k}_i^{(+)}\rangle \\ &\quad + \sum_{n=1}^{N} \int \frac{\langle \mathbf{k}_f^{(-)}\Phi_f|V_U|\Phi_n \mathbf{k}^{(-)}\rangle\langle \mathbf{k}^{(-)}\Phi_n|T_U|\Phi_i \mathbf{k}_i^{(+)}\rangle}{E - \epsilon_n - \frac{k^2}{2} + \mathrm{i}0} \mathrm{d}^3\mathbf{k} \end{aligned} \tag{2.62}$$

for this scattering system. The recursive character of (2.62) means that it will be solved as a simultaneous system of equations. This will be discussed in detail in Section 3.6.3 after detailing how the projectile waves (Section 3.1) and target states (Sections 3.2–3.4) will be represented in spherical coordinates. The equivalent representations in prolate spheroidal coordinates are given in Section 4.1.

Finally, to remove the effects of the distorting potential we must first rearrange (2.54) to

$$\langle \mathbf{k}_f \Phi_f| = \langle \mathbf{k}_f^{(-)} \Phi_f| - \frac{1}{E - \epsilon_f - \epsilon_{k_f} + \mathrm{i}0} \langle \mathbf{k}_f^{(-)} \Phi_f | U_0 \tag{2.63}$$

and then similarly obtain the undistorted formula

$$\frac{1}{E - \epsilon_f - \hat{K}_0 + \mathrm{i}0} \langle \Phi_f | V | \psi_i \rangle = \langle \Phi_f | \psi_i \rangle - \delta_{fi} | \mathbf{k}_i \rangle \tag{2.64}$$

and combine both to yield an expression for the physical T-matrix

$$\begin{aligned} \langle \mathbf{k}_f \Phi_f | T | \Phi_i \mathbf{k}_i \rangle &= \langle \mathbf{k}_f \Phi_f | V | \psi_i \rangle \\ &= \langle \mathbf{k}_f^{(-)} \Phi_f | T_U | \Phi_i \mathbf{k}_i^{(+)} \rangle + \delta_{fi} \langle \mathbf{k}_f^{(-)} | U | \mathbf{k}_i \rangle \end{aligned} \tag{2.65}$$

in terms of (2.61) and a numerical overlap involving the distorting potential.

2.4.3 Scattering amplitude

The T-matrix has a qualitative relevance to scattering experiments, but it is more convenient to go a step further and examine the projectile function $\langle \mathbf{r} | F_n^{(i)} \rangle \equiv F_n^{(i)}(\mathbf{r})$ in the asymptotic region $|\mathbf{r}| \to \infty$ where the experimental detector will receive it.

Following the functional form of the Green's function (2.51), the channel functions (2.52) may be rewritten as

$$F_n^{(i)}(\mathbf{x}) = \frac{\delta_{ni}}{(2\pi)^{3/2}} \mathrm{e}^{\mathrm{i}\mathbf{k}_n \cdot \mathbf{x}} - \int \frac{\mathrm{e}^{\mathrm{i}k_n |\mathbf{x}' - \mathbf{x}|}}{2\pi |\mathbf{x}' - \mathbf{x}|} V^{(n,i)}(\mathbf{x}') \mathrm{d}^3 \mathbf{x}'. \tag{2.66}$$

The interaction potential $V^{(n,i)}(\mathbf{x}') = \langle \mathbf{x}' \Phi_n | V | \psi_i \rangle$ is only nonzero in the vicinity of the molecule, so in the experimental detector region $\mathbf{x} \gg \mathbf{x}'$ we have $r \simeq |\mathbf{x}|$ and can safely make the approximation

$$|\mathbf{x}' - \mathbf{x}| = \sqrt{|\mathbf{x}'|^2 - 2\mathbf{x}' \cdot \mathbf{x} + |\mathbf{x}|^2} \simeq r \sqrt{1 - \tfrac{2\mathbf{x}' \cdot \mathbf{x}}{r^2}} \simeq r - \tfrac{\mathbf{x}' \cdot \mathbf{x}}{r} \tag{2.67}$$

and use it to write

$$F_n^{(i)}(\mathbf{x}) = \frac{\delta_{ni}}{(2\pi)^{3/2}} \mathrm{e}^{\mathrm{i}\mathbf{k}_n \cdot \mathbf{x}} - \frac{\mathrm{e}^{\mathrm{i}k_n r}}{2\pi r} \int \mathrm{e}^{-\mathrm{i}\frac{k_n}{r} \mathbf{x}' \cdot \mathbf{x}} V^{(n,i)}(\mathbf{x}') \mathrm{d}^3 \mathbf{x}'. \tag{2.68}$$

With $\mathbf{k}'_n = \frac{k_n}{r}\mathbf{x}$, $|\mathbf{k}'_n| = k_n$, (2.46), and

$$\int \mathrm{e}^{-\mathrm{i}\mathbf{k}'_n\cdot\mathbf{x}'} V^{(n,i)}(\mathbf{x}')\mathrm{d}^3\mathbf{x}' = (2\pi)^{3/2}\langle \mathbf{k}'_n\Phi_n|V|\psi_i\rangle, \tag{2.69}$$

we arrive at the form

$$F_n^{(i)}(\mathbf{x}) = \frac{1}{(2\pi)^{3/2}}\left(\delta_{ni}\mathrm{e}^{\mathrm{i}\mathbf{k}_n\cdot\mathbf{x}} + f_{ni}(\mathbf{k}_n,\mathbf{k}'_n)\frac{\mathrm{e}^{\mathrm{i}k_n r}}{r}\right) \tag{2.70}$$

with the scattering amplitude defined as

$$f_{ni}(\mathbf{k}_n,\mathbf{k}'_n) = -(2\pi)^2\langle \mathbf{k}'_n\Phi_n|V|\psi_i\rangle. \tag{2.71}$$

Using our definition of the T-matrix (2.65), we can transform these expressions into the more standard spherical coordinates

$$F_n^{(i)}(\mathbf{r}) = \frac{1}{(2\pi)^{3/2}}\left(\delta_{ni}\mathrm{e}^{\mathrm{i}k_n z} + f(\theta)\frac{\mathrm{e}^{\mathrm{i}k_n r}}{r}\right) \tag{2.72}$$

where θ is the angle between the incident beam $\mathbf{k}_n$ and detector position $\mathbf{k}'_n$ and (2.71) becomes

$$f_{ni}^S(\theta) = -(2\pi)^2\langle \mathbf{k}\Phi_n|T|\Phi_i\mathbf{k}_i\rangle. \tag{2.73}$$

Here S is the spin coupling between projectile and target.

2.4.4 Cross sections

Physically, the scattering amplitude represents a probability for an incoming projectile $\mathbf{k}_i$ scattering off a target state Φ_i before departing as an outgoing wave $\mathbf{k}_n$ emanating away from the resultant target state Φ_n. By conservation of energy we must have

$$\tfrac{1}{2}k_i^2 + E_i = \tfrac{1}{2}k_n^2 + E_n. \tag{2.74}$$

Therefore, a final state Φ_n is only energetically accessible when

$$k_n^2 = k_i^2 - 2(E_n - E_i) \geq 0 \tag{2.75}$$

or equivalently

$$k_i^2 \geq 2(E_n - E_i). \tag{2.76}$$

The energy difference in brackets is the excitation energy of state n from state i. For a particular incident energy $\frac{1}{2}k_i^2$, target states are "open" if they satisfy (2.76) and "closed" otherwise.

The scattering amplitude of the $i \to n$ transition can be related to the experimentally observable cross sections $\frac{\mathrm{d}\sigma_{ni}}{\mathrm{d}\Omega}$. The latter represents a ratio of scattered particle flux through a given solid angle to the incident particle flux, i.e.

$$\frac{\mathrm{d}\sigma}{\mathrm{d}\Omega}\mathrm{d}\Omega = \frac{|\mathbf{j}_{\mathrm{scat}}|}{|\mathbf{j}_{\mathrm{inc}}|} r^2 \mathrm{d}\Omega. \tag{2.77}$$

This results in (spin-resolved) differential cross sections (DCS) defined as

$$\frac{\mathrm{d}\sigma^S_{ni}}{\mathrm{d}\Omega} = \frac{k_n}{k_i} \left| f^S_{ni}(\theta) \right|^2 \tag{2.78}$$

for transition $i \to n$ and scattering angle θ. Often the fine spacing of rotational and vibrational energy levels make it difficult to resolve individual ro-vibrational states, and so sums over certain initial and final states are taken. Averaging over all possible spin levels of the projectile and target gives the spin-averaged DCS as

$$\frac{\mathrm{d}\sigma_{ni}}{\mathrm{d}\Omega} = \frac{1}{2(2S_i+1)} \sum_S (2S+1) \frac{\mathrm{d}\sigma^S_{ni}}{\mathrm{d}\Omega}. \tag{2.79}$$

Integrating the DCS (2.78) over the ejection angle θ gives the integrated cross section (ICS)

$$\sigma_{ni} = \frac{k_n}{k_i} \iint \left| f^S_{ni}(\theta) \right|^2 \sin\theta \mathrm{d}\theta \mathrm{d}\phi, \tag{2.80}$$

which quantifies all scattered particles for a particular incident energy. Another quantity, the momentum-transfer cross section (MTCS)

$$\sigma^{\mathrm{MT}}_{i\to n} = \frac{k_n}{k_i} \iint |f_{ni}(\theta)|^2 (1 - \cos\theta) \sin\theta \mathrm{d}\theta \mathrm{d}\phi \tag{2.81}$$

is of particularly importance to "swarm" experiments which measure transport properties of materials.

2.5 Molecular cross sections

The above cross-sections are calculated at a given internuclear separation R with the fixed-nuclei approximation. We now return to the underlying Born-Oppenheimer approximation, which separates electronic and nuclear motion, and express the nuclear wavefunctions

$$\Psi^{\mathrm{N}}_{n v_n J_n m_{J_n}}(\mathbf{R}) = \nu_{n v_n}(R) \mu_{n J_n m_{J_n}}(\hat{\mathbf{R}}) \tag{2.82}$$

as a product of vibrational $\nu_{nv_n}(R)$ and rotational $\mu_{nJ_nm_{J_n}}(\hat{\mathbf{R}})$ function. Here J_n is the rotational angular momentum and m_{J_n} is its projection. In the adiabatic-nuclei approximation, nuclear wavefunctions are obtained using the energy surface method discussed in Section 2.2.1 and positive-energy (continuum) ro-vibrational levels correspond to the dissociation of the molecule.

The rotational wavefunctions may be represented by the non-vibrating (rigid rotor) approximation

$$\mu_{nJ_nm_{J_n}}(\hat{\mathbf{R}}) = Y_{J_n}^{m_{J_n}}(\hat{\mathbf{R}}) \tag{2.83}$$

in terms of spherical harmonics (Appendix C.1) or the vibrating (symmetric-top) approximation

$$\mu_{nJ_nm_{J_n}}(\hat{\mathbf{R}}) = \sqrt{\frac{2J_n+1}{8\pi^2}}\mathcal{D}^{J_n}_{m_{J_n}m_n}(\hat{\mathbf{R}}) \tag{2.84}$$

in terms of Wigner D-matrices (Appendix D.2).

2.5.1 Analytic Born cross sections

In the Born approximation ($T = V$) we write

$$\langle \mathbf{k}_f\Phi_f|V|\psi_i\rangle = \langle \mathbf{k}_f\Phi_f|T|\mathbf{k}_i\Phi_i\rangle \approx \langle \mathbf{k}_f\Phi_f|V|\mathbf{k}_i\Phi_i\rangle \tag{2.85}$$

and neglect the exchange potential arising from the Pauli exclusion principle so that $|\Psi_i\rangle = |\psi_i\rangle$. This uncouples the total scattering wavefunction (2.33) into

$$\Psi_i(x_0, x_1, x_2) \approx \Phi_{k_i}(x_0)\Phi_i(x_1, x_2), \tag{2.86}$$

where the incident projectile momentum is $k_i = \sqrt{2(E-\epsilon_i)}$.

With this, the molecular potential (without distortion) is significantly simpler and without loss of generality (with respect to coordinate systems) evaluates to

$$\begin{aligned} V_{fi}^{(\mathrm{AB})} &= z\left\langle \Psi_f\left|\frac{Z_1}{|\mathbf{r}_0-\frac{1}{2}\mathbf{R}|}+\frac{Z_2}{|\mathbf{r}_0+\frac{1}{2}\mathbf{R}|}-\sum_j^{N_e}\frac{1}{|\mathbf{r}_0-\mathbf{r}_j|}\right|\Psi_i\right\rangle \\ &= z\delta_{fi}\left\langle \mathbf{k}_f\left|\frac{Z_1}{|\mathbf{r}_0-\frac{1}{2}\mathbf{R}|}+\frac{Z_2}{|\mathbf{r}_0+\frac{1}{2}\mathbf{R}|}\right|\mathbf{k}_i\right\rangle - z\left\langle \Psi_f\left|\frac{N_e}{|\mathbf{r}_0-\mathbf{r}_1|}\right|\Psi_i\right\rangle, \end{aligned} \tag{2.87}$$

where we have used the antisymmetry of $\Phi_i(x_1, x_2)$ in the second term (2.87). In the body frame the internuclear axis $\mathbf{R}$ is aligned with the z-axis. For convenience we also suppose that the same is true for the initial wavevector $\mathbf{k}_i = (k_i, 0, 0)$ and denote the angle between it and and final wavevector $\mathbf{k}_f = (k_f, \theta_f, \phi_f)$ as $\theta = \theta_f$. With this in mind, we define the momentum transfer vector

$$\mathbf{q} = \mathbf{k}_i - \mathbf{k}_f \tag{2.88}$$

which has the components (q, θ_q, ϕ_q) given by

$$\begin{aligned} q &= \sqrt{k_i^2 + k_f^2 - 2k_i k_f \cos\theta_f} \\ \cos\theta_q &= \frac{k_i - k_f \cos\theta_f}{q} \\ \phi_q &= \phi_f. \end{aligned} \tag{2.89}$$

Using these, along with (F.2), the first (elastic) term in (2.87) reduces to

$$\begin{aligned} \left\langle \mathbf{k}_f \middle| \frac{Z_1}{|\mathbf{r}_0 - \frac{1}{2}\mathbf{R}|} + \frac{Z_2}{|\mathbf{r}_0 + \frac{1}{2}\mathbf{R}|} \middle| \mathbf{k}_i \right\rangle &= \frac{1}{(2\pi)^3} \int Z_1 \frac{\exp(\mathrm{i}\mathbf{q}\cdot\mathbf{r}_0)}{|\mathbf{r}_0 - \frac{1}{2}\mathbf{R}|} + Z_2 \frac{\exp(\mathrm{i}\mathbf{q}\cdot\mathbf{r}_0)}{|\mathbf{r}_0 + \frac{1}{2}\mathbf{R}|} \mathrm{d}\mathbf{r}_0 \\ &= \frac{1}{2\pi^2 q^2} \left[Z_1 \exp\left(\tfrac{\mathrm{i}}{2}\mathbf{q}\cdot\mathbf{R}\right) + Z_2 \exp\left(-\tfrac{\mathrm{i}}{2}\mathbf{q}\cdot\mathbf{R}\right) \right], \end{aligned} \tag{2.90}$$

and the second (general) term of (2.87) can be expressed as

$$\begin{aligned} \left\langle \Psi_f \middle| \frac{N_e}{|\mathbf{r}_0 - \mathbf{r}_1|} \middle| \Psi_i \right\rangle &= \frac{N_e}{(2\pi)^3} \left\langle \Phi_f \middle| \int \frac{\exp(\mathrm{i}\mathbf{q}\cdot\mathbf{r}_0)}{|\mathbf{r}_0 - \mathbf{r}_1|} \mathrm{d}\mathbf{r}_0 \middle| \Phi_i \right\rangle \\ &= \frac{N_e}{2\pi^2 q^2} \langle \Phi_f | \exp(\mathrm{i}\mathbf{q}\cdot\mathbf{r}_1) | \Phi_i \rangle. \end{aligned} \tag{2.91}$$

The plane wave can be expanded in a series of spherical (3.4) or spheroidal (4.36) partial waves and the resulting expressions for Analytic Born matrix elements will be given in Sections 3.5 and 4.2.3 respectively.

The analytical Born technique is useful in performing convergence checks. For molecular scattering, the conserved quantum numbers of the projectile-target system are total angular momentum projection M and spin S, as well as parity Π for homogeneous diatomics (as opposed to angular momentum L in atomic scattering). This allows us to divide our calculations by partial waves, and increase the number of M partial waves until we achieve convergence. All combinations of Π and S are included for each M partial wave.

The sum of partial wave cross sections calculated in the Born approximation $\sigma_{i\to f}^{M(BA)}$ will converge towards the corresponding analytical Born cross sections $\sigma_{i\to f}^{(\mathrm{AB})}$, i.e.

$$\lim_{M_{\max}\to\infty} \sum_{M=0}^{M_{\max}} \sigma_{i\to f}^{M(\mathrm{BA})} \approx \sigma_{i\to f}^{(\mathrm{AB})}. \tag{2.92}$$

This allows us to estimate the degree of convergence in $M_{\max}$ achieved by our close-coupling cross sections $\sigma_{i\to f}^{\mathrm{M(CC)}}$.

Analytical Born Completion

The analytical Born matrix elements are also useful because they become more accurate as the angular momentum of the partial wave increases. As they are relatively cheap to calculate, we can take the analytical Born cross section, remove the partial-wave Born approximation contributions where they are not converged, and replace them with the accurate close-coupling solution partial waves, i.e.

$$\sigma_{i\to f}^{(\mathrm{ABC})} = \sigma_{i\to f}^{(AB)} + \sum_{M=0}^{M_{\max}} \left[\sigma_{i\to f}^{M(\mathrm{CC})} - \sigma_{i\to f}^{M(\mathrm{BA})}\right]. \tag{2.93}$$

This effectively tops-up, or *completes* the cross-section for partial waves $M > M_{\max}$. This allows us to achieve convergence faster because we need fewer resource-intensive calculations.

Orientation averaging

V-matrix elements and resulting T-matrix elements such as those from the Analytical Born approximation (3.76) and close-coupling (Section 3.6) are said to be calculated in the *body frame*, where the orientation of the molecule is fixed. However, the experimental cross sections we are to compare to are measured in the *lab frame*, where only the incoming particle beam has a known orientation.

For convenience we align the incident projectile momentum with the z-axis and the declare the arbitrary molecule orientation as $\hat{\mathbf{R}} \equiv (R, \theta_R, \phi_R)$. Mathematically, this involves taking the partial-wave expansion of the body frame matrix elements $V_{fi,Lm_L}(\mathbf{q})$ and rotating the direction of the momentum vector $\hat{\mathbf{q}}$ around the internuclear axis (which is fixed in this frame) by an arbitrary set of angles. More specifically, we convert the direction of the spherical harmonics from the body-frame ($\hat{\mathbf{q}}$) to the lab-frame ($\hat{\mathbf{Q}}$) by using

$$Y_L^{m_L}(\hat{\mathbf{q}}) = \sum_{\mu=-L}^{L} \mathcal{D}^L_{m_L\mu_L}(\boldsymbol{\beta}) Y_L^{\mu_L}(\hat{\mathbf{Q}}) \tag{2.94}$$

with the Wigner D-matrices $\mathcal{D}^L_{m_L\mu_L}(\boldsymbol{\beta})$ and Euler angles $\boldsymbol{\beta} = (\phi_R, \theta_R, 0)$ in the z-y'-z'' form. (2.94) represents first a rotation of angle ϕ_R around the z-axis followed by a second rotation of angle θ_R around the new y'-axis.

In classical orientation averaging we assume all molecule orientations are equally likely and do not respond to the projectile, which amounts to neglecting the rotational quantum states of the molecule. In this model we average over the

Euler angles (D.7) to obtain the differential cross sections (2.78) to be

$$\begin{aligned}
\left.\frac{\mathrm{d}\sigma(\theta)}{\mathrm{d}\Omega}\right|_{i\to f} &= \frac{k_f}{k_i}\int |f_{i\to f}(\theta_f,\boldsymbol{\beta})|^2 \frac{\mathrm{d}\boldsymbol{\beta}}{8\pi^2} \\
&= (2\pi)^4 \frac{k_f}{k_i} \sum_{L',L} \mathrm{i}^{L-L'} V_{fi,L'm'_L}(Q) V_{fi,Lm_L}(Q) \\
&\quad \times \sum_{\mu'_L,\mu_L} Y_{L'}^{\mu'_L}(\hat{\mathbf{Q}}) \overline{Y}_{L}^{\mu_L}(\hat{\mathbf{Q}}) \int \mathcal{D}^{L'}_{m'_L\mu'_L}(\boldsymbol{\beta}) \overline{\mathcal{D}}^{L}_{m_L\mu_L}(\boldsymbol{\beta}) \frac{\mathrm{d}\boldsymbol{\beta}}{8\pi^2} \\
&= (2\pi)^4 \frac{k_f}{k_i} \sum_{L} V_{fi,Lm_L}(Q) V_{fi,Lm_L}(Q) \sum_{\mu_L=-L}^{L} Y_L^{\mu_L}(\hat{\mathbf{Q}}) \overline{Y}_L^{\mu_L}(\hat{\mathbf{Q}}) \frac{1}{2\ell+1} \\
&= 4\pi^3 \frac{k_f}{k_i} \sum_{L} |V_{fi,Lm_L}(Q)|^2
\end{aligned} \tag{2.95}$$

using (D.8) and (C.9). This allows us to calculate differential cross sections directly from partial V-matrix elements.

2.5.2 Adiabatic-nuclei cross sections

In this section we bring together the concepts of the adiabatic-nuclei approximation (Section 2.2.3), T-matrices (Section 2.4.2), scattering amplitudes (Section 2.4.3), cross sections (Section 2.4.4), and nuclear wavefunctions (Section 2.5) to calculate AN cross sections. After making many FN calculations over a range of internuclear distances R that spans the vibrational wavefunctions of interest, we can take **R**-space integrals of the parametric T-matrix elements

$$T_{fi}^{(\mathrm{FN})}(\mathbf{k}_f,\mathbf{k}_i;R) \equiv \langle \mathbf{k}_f \Phi_f | T | \Phi_i \mathbf{k}_i \rangle \tag{2.96}$$

to obtain AN scattering amplitudes

$$f^{\mathrm{AN}}_{fv_fJ_fm_{J_f},iv_iJ_im_{J_i}}(\mathbf{k}_f,\mathbf{k}_i) = -(2\pi)^2 \langle \nu_{fv_f}\mu_{fJ_fm_{J_f}} | T_{fi}^{(\mathrm{FN})}(\mathbf{k}_f,\mathbf{k}_i;R) | \mu_{iJ_im_{J_i}}\nu_{iv_i}\rangle \tag{2.97}$$

for calculating various cross sections including those that are vibrationally and rotationally resolved.

If we treat the rotational wavefunctions as rigid rotors (2.83) we may calculate the vibrationally-resolved differential cross section for the transition $iv_i \to fv_f$ of a molecule that is initially in the rotational ground state $J_i = 0$ and then summed over final rotational states J_f. To do this, we substitute the rigid rotors into (2.97), rotate them into the lab frame as in Section 2.5.1, and classically

average over all molecular orientations to obtain

$$\frac{\mathrm{d}\sigma^{(\mathrm{AN})}_{f\nu_f,i\nu_i}}{\mathrm{d}\Omega} = \frac{1}{4\pi}\frac{k_f}{k_i}\int \left| f^{(\mathrm{FN})}_{f\nu_f,i\nu_i}(k_f,k_i;R)\right|^2 \mathrm{d}\Omega. \tag{2.98}$$

The expression for this in terms of T-matrix elements is not straightforward [13], but reduces nicely to the vibrationally-resolved integrated cross section

$$\sigma^{(\mathrm{AN})}_{f\nu_f,i\nu_i} = \frac{1}{4\pi}\frac{k_f}{k_i}\sum_{\ell_f,m_f}\sum_{\ell_i,m_i}\left|\langle\nu_{f\nu_f}|A^{(\mathrm{FN})}_{f\ell_f m_f,i\ell_i m_i}(\mathbf{k}_f,\mathbf{k}_i;R)|\nu_{i\nu_i}\rangle\right|^2, \tag{2.99}$$

where we define

$$A^{(\mathrm{FN})}_{f\ell_f m_f,i\ell_i m_i}(\mathbf{k}_f,\mathbf{k}_i;R) = -(2\pi)^2(k_f k_i)^{-1}\mathrm{i}^{\ell_i-\ell_f}\mathrm{e}^{\mathrm{i}(\sigma_{\ell_f}+\sigma_{\ell_i})}T^{(\mathrm{FN})}_{fl_f m_f,il_i m_i}(\mathbf{k}_f,\mathbf{k}_i;R) \tag{2.100}$$

in terms of partial T-matrix elements and their corresponding phase shifts σ_ℓ.

An alternate method of calculating the vibrationally resolved ICS (2.99) is to employ the approximate technique of Ghazaly *et al.* [82] and integrate the fixed-nuclei integrated cross sections (2.80)

$$\sigma^{\mathrm{AN}}_{f\nu_f,i\nu_i} \approx \left|\langle\nu_{f\nu_f}|\sqrt{\sigma^{\mathrm{FN}}_{fi}(R)}|\nu_{i\nu_i}\rangle\right|^2 \tag{2.101}$$

for many different FN calculations over an appropriate R-grid. This method has proven to be efficient and sufficiently accurate most cases, including electron-impact dissociation of the hydrogen and deuterium molecule ions [82] as well as positron scattering from molecular hydrogen [74].

Chapter 3

Spherical MCCC

This Chapter contains the details of the spherical formulation for the Molecular Convergent Close-Coupling method. It is based on the overall procedure of two-electron atomic CCC as established for electron-helium scattering [8] but with several changes owing to the complexities of molecular targets. Indeed, this spherical approach transforms into the atomic formalism in the combined nuclei limit ($R = 0$). Despite non-spherical molecular potentials, the relative straightforwardness of this coordinate system means that it is also appealing for extension to larger, more complicated molecular targets.

The aim is to calculate the T-matrices (2.62) required for cross sections describing collisions between the incident particle and the target molecule. The projectile function is expanded in a series of spherical waves with given angular momenta (Section 3.1) while the target electron wavefunctions are determined by a configuration interaction (CI) expansion constructed from a square-integrable Laguerre basis (Sections 3.2–3.4). The spherical waves and target states are coupled through angular momenta and spin channels. T-matrices are calculated with the analytic Born approximation (Section 3.5) or through the Lippmann-Schwinger close-coupling approach (Section 3.6).

This formulation is specific to two-electron diatomic molecules with nuclei charges Z_1 and Z_2. The expressions for one-electron targets can be recovered by using the corresponding target states and ignoring terms involving the second electron in the scattering sections. Both homogeneous ($Z_1 = Z_2$) and heterogeneous ($Z_1 \neq Z_2$) diatomics are covered. For the sake of simplicity we choose the coordinate origin to be at the geometric centre of our nuclei, eve though this may not be the best choice for heterogeneous diatomics. Electron scattering (projectile charge $z = -1$) is assumed, but a single-centre approximation to

positron scattering is readily available by setting $z = +1$ and dropping exchange V-matrix elements. These methods can be extended to many-electron targets with quasi-one- or quasi-two-electron behaviour by introducing a core potential. The conventions used in the spherical coordinate system are given in Appendix A.

3.1 Projectile waves

An incident projectile with asymptotic momentum k and charge z in the presence of a molecule with total (protons and electrons) asymptotic charge Z_{asym} is represented by the wave vector $|\mathbf{k}^{(\pm)}\rangle$. The subscript represents either incoming $(+)$ or outgoing $(-)$ waves. In the most general case we generate waves as the solution of

$$\left(\epsilon_k - \hat{K} - U + \tfrac{zZ_{\text{asym}}}{r}\right)|\mathbf{k}^{(\pm)}\rangle = 0 \tag{3.1}$$

where $\epsilon_k = k^2/2$ is the projectile energy, $\hat{K}$ is the kinetic energy operator, U is an arbitrary short-ranged distorting potential, and Z_{asym} is the asymptotic molecular charge. The form of the distorting potential will be discussed later. When there is no distortion ($U = 0$) or asymptotic charge (Z_{asym}) the solutions are simple plane waves $|\mathbf{k}\rangle$. In the asymptotic region, projectile waves are given the momentum space normalisation of plane waves

$$\langle \mathbf{r}|\mathbf{k}\rangle = \frac{\mathrm{e}^{\mathrm{i}\mathbf{k}\cdot\mathbf{r}}}{(2\pi)^{3/2}} \tag{3.2}$$

which satisfies

$$\langle \mathbf{k}'|\mathbf{k}\rangle = \frac{1}{(2\pi)^3}\int \mathrm{e}^{\mathrm{i}(\mathbf{k}-\mathbf{k}')\cdot\mathbf{r}}\mathrm{d}^3\mathbf{k} = \delta^3(\mathbf{k}-\mathbf{k}'). \tag{3.3}$$

We can represent the projectile wave function (3.1) as a series of spherical waves in the partial-wave expansion

$$|\mathbf{k}^{(\pm)}\rangle = \sqrt{\frac{2}{\pi}}k^{-1}\sum_{L=0}^{\infty}\sum_{m_L=-L}^{L}\mathrm{i}^L\mathrm{e}^{\pm\mathrm{i}\theta_L}|kLm_L\rangle\overline{Y}_L^{m_L}(\hat{\mathbf{k}}) \tag{3.4}$$

with phase shift θ_L and

$$\langle \mathbf{r}|kLm_L\rangle = R_L(r;k)Y_L^{m_L}(\hat{\mathbf{r}}). \tag{3.5}$$

Both the radial functions and spherical harmonics are orthonormal in their respective coordinates. Substituting the partial waves (3.4) into (3.1) and using the orthonormality of spherical harmonics (C.4), we find that

$$\left[k^2 + \frac{\partial}{\partial r}\left(r^2\frac{\partial}{\partial r}\right) - \frac{L(L+1)}{r^2} + 2U(r) - \frac{2zZ_{\text{asym}}}{r}\right]R_L(r;k)Y_L^{m_L}(\hat{\mathbf{r}}) = 0. \tag{3.6}$$

With the substitutions $x = kr$, $\eta = zZ_{\text{asym}}/k$, $u_L(x;\eta) = rR_L(r;k)$, and again invoking spherical harmonic orthonormality, this rearranges to

$$\left[\frac{\mathrm{d}^2}{\mathrm{d}x^2} + 1 - \frac{2\eta}{x} - \frac{L(L+1)}{x^2} + \frac{U(x)}{E}\right] u_L(x;\eta) = 0, \tag{3.7}$$

and the partial projectile functions are now expressed as

$$\langle \mathbf{r}|kLm_L\rangle = r^{-1}u_L(kr)Y_L^{m_L}(\hat{\mathbf{r}}). \tag{3.8}$$

The r^{-1} factor is useful in cancelling out the r^2 factor in an integral involving two such functions.

Asymptotically, the partial radial functions are sinusoidal

$$u_L(x;\eta) \xrightarrow[x\to\infty]{} \sin[x - \theta_L(x;\eta)] \tag{3.9}$$

with phase shift

$$\theta_L(x;\eta) = L\tfrac{\pi}{2} - \eta\ln(2x) + \sigma_L(\eta) + \delta_L. \tag{3.10}$$

The Coulomb phase shift

$$\sigma_L(\eta) = \arctan\left(\frac{\mathrm{Im}\{\Gamma(L+1+\mathrm{i}\eta)\}}{\mathrm{Re}\{\Gamma(L+1+\mathrm{i}\eta)\}}\right) \tag{3.11}$$

can be calculated analytically through the gamma function $\Gamma(z)$ while the distorting phase shift δ_L is determined through matching against undistorted ($U = 0$) functions. With no distortion the radial functions $u_L(x;\eta)$ are related to spherical Bessel functions by $u_L(x;0) = xj_L(x)$ for neutral molecules ($\eta = 0$) and Coulomb functions of the first kind $u_L(x;\eta) = F_L(\eta, x)$ for charged molecules ($\eta > 0$). In the plane wave case ($U = Z_{\text{asym}} = 0$) both of these phase shifts are zero.

3.2 Configuration interaction

A given Hamiltonian $\hat{H}$ has eigenstates $|\Phi_i\rangle$ and corresponding eigenenergies E_i that are solutions to the time-independent Schrödinger equation

$$\hat{H}|\Phi_i\rangle = E_i|\Phi_i\rangle. \tag{3.12}$$

The configuration interaction (CI) procedure is a method of approximating these true eigenstates by reconstructing them as expansions of appropriate basis functions. These so-called pseudostates $|\Phi_i^{(N)}\rangle$ diagonalise the Hamiltonian

$$\langle\Phi_f^{(N)}|\hat{H}|\Phi_i^{(N)}\rangle = \epsilon_i^{(N)}\delta_{fi} \tag{3.13}$$

and include both positive energy (continuum) and negative energy (bound) states. The diagonalisation condition (3.13) is weaker than the Schrödinger equation (3.12), and so eigenstates will diagonalise the Hamiltonian but pseudostates will not necessarily be solutions. As the basis size N increases, the pseudostates with negative energy converge to the true eigenstates of (3.12):

$$\lim_{N\to\infty} |\Phi_i^{(N)}\rangle = |\Phi_i\rangle \tag{3.14}$$

$$\lim_{N\to\infty} \epsilon_i^{(N)} = E_i \tag{3.15}$$

as per the variational principle, while those with positive energy provide an increasingly dense discretisation of the continuum. The overall accuracy of the scattering calculations is largely dependent on the accuracy of the target states. Those of negative energy are important to excitation channels, and the degree to which positive energy pseudostates span the continuum will affect ionisation channels.

The pseudostates are represented through the expansion

$$|\Phi_i^{(N)}\rangle = \sum_{\alpha=1}^{N} C_\alpha^{(i)} |\alpha\rangle \tag{3.16}$$

with CI coefficients $C_\alpha^{(i)}$ and one-electron functions $|\alpha\rangle$. In the Convergent Close-Coupling (CCC) formalism we typically use Laguerre polynomials, as the radial functions of our basis as their tunable exponential decay allows us to accurately replicate bound states, while their square-integrability guarantees that all integrals required for scattering calculations will not be divergent. Spherical harmonics are used as the angular functions, as we can use the well established angular momentum algebra to analytically evaluate all angular integrals.

Target states are characterised by their energy as well as a "symmetry" or set of good quantum numbers. For atoms this includes the angular momentum ℓ, its projection m, parity π, and spin s. Diatomic molecules do not have ℓ as a good quantum number, and heterogeneous diatomics do not have π either.

To calculate the CI coefficients we consider a pseudostate $|\Phi_i^{(N)}\rangle$ with a given symmetry, and expand it in a set of N configurations $|\alpha\rangle$ and premultiply by $\langle\beta|$ to yield a set of equations

$$\sum_{\alpha=1}^{N} \langle\beta|\hat{H}|\alpha\rangle\langle\alpha|\Phi_i^{(N)}\rangle = \epsilon_i^{(N)} \sum_{\alpha=1}^{N} \langle\beta|\alpha\rangle\langle\alpha|\Phi_i^{(N)}\rangle \tag{3.17}$$

for $\beta = 1, \ldots, N$. These equations can be rewritten as the matrix problem

$$\begin{bmatrix} H_{11} & H_{12} & \cdots & H_{1N} \\ H_{21} & H_{22} & \cdots & H_{2N} \\ \vdots & \vdots & \ddots & \vdots \\ H_{N1} & H_{N2} & \cdots & H_{NN} \end{bmatrix} \begin{bmatrix} C_1^{(i)} \\ C_2^{(i)} \\ \vdots \\ C_N^{(i)} \end{bmatrix} = \epsilon_i^{(N)} \begin{bmatrix} b_{11} & b_{12} & \cdots & b_{1N} \\ b_{21} & b_{22} & \cdots & b_{2N} \\ \vdots & \vdots & \ddots & \vdots \\ b_{N1} & b_{N2} & \cdots & b_{NN} \end{bmatrix} \begin{bmatrix} C_1^{(i)} \\ C_2^{(i)} \\ \vdots \\ C_N^{(i)} \end{bmatrix} \tag{3.18}$$

where $H_{\beta\alpha} = \langle\beta|\hat{H}|\alpha\rangle$ are the Hamiltonian matrix elements, $b_{\beta\alpha} = \langle\beta|\alpha\rangle$ are the overlap matrix elements, and $C_\alpha^{(i)} = \langle\alpha|\Psi_i\rangle$ are the CI coefficients. Now (3.18) can be solved as a generalised eigenvalue problem, which results in $i = 1, \ldots, N$ eigenvectors $\{C_\alpha^{(i)}\}$ with corresponding eigenenergies $\epsilon_i^{(N)}$. These describe N pseudostates (3.16) that form an orthonormal set

$$\langle\Phi_f^{(N)}|\Phi_i^{(N)}\rangle = \delta_{fi} \tag{3.19}$$

and diagonalise the electronic Hamiltonian as per (3.13).

3.3 One-electron states

We use the CI procedure for the one-electron Hamiltonian (2.10) to construct the one-electron pseudostates $\langle x|\Phi_i^{\pi_i m_i s_i}\rangle = \Phi_i^{\pi_i m_i s_i}(x)$ of the target diatomic molecule, where $x \equiv (r, \theta, \phi, \sigma)$ represents the combined coordinate and spin spaces. These pseudostates have a symmetry consisting of parity π_i (for homogeneous diatomics only), angular momentum projection m_i, and spin s_i. In the non-relativistic approach taken in this work the one-electron functions have $s_i = \frac{1}{2}$; for brevity we separate spin out as $\Phi_i^{\pi_i m_i s_i}(x) = \Phi_i^{\pi_i m_i}(\mathbf{r})\chi^{s_i}(\sigma)$ and only consider coordinate space in this Section.

While we are interested in a theoretical method for scattering from two-electron diatomics, it is useful to build up from the one-electron case as a means of introducing our basis and deriving the one-electron matrix elements. In addition, the one-electron ground state energy is used to determine accurate ionisation energies, and we may also reuse pseudostates calculated here as orbitals in our two-electron diagonalisation procedure.

3.3.1 Spherical coordinate basis

As with atomic CCC we define our spherical basis functions $|\alpha\rangle = |k\ell m\rangle$, with $\langle\mathbf{r}|k\ell m\rangle \equiv \varphi_{k\ell m}(r, \theta, \phi; \lambda_\ell)$, as

$$\varphi_{k\ell m}(r, \theta, \phi; \lambda_\ell) = r^{-1}\Lambda_{k\ell}(r; \lambda_\ell)Y_\ell^m(\cos\theta, \phi), \tag{3.20}$$

which has the radial function

$$\Lambda_{k\ell}(r;\lambda_\ell) = \sqrt{\frac{\lambda_\ell}{2(k+\ell)}\frac{(k-1)!}{(k+2\ell)!}}(\lambda_\ell r)^{\ell+1}\exp(-\lambda_\ell r/2)L_{k-1}^{2\ell+1}(\lambda_\ell r), \tag{3.21}$$

where $L_a^b(x)$ is an associated Laguerre polynomial, and the adjustable exponential fall-off parameters λ_m affect the rate of convergence. Note that here the domains of the spherical harmonics are $\theta \in [0,\pi]$ and $\phi \in [0,2\pi)$ (see Appendix A). In an integral involving two basis functions, the r^{-1} factors of (3.20) cancel with the r^2 of the spherical integration weight.

The normalisation is chosen such that the self-overlap is

$$\begin{aligned}\langle k\ell m|k\ell m\rangle &= \frac{\lambda_\ell}{2(k+\ell)}\frac{(k-1)!}{(k+2\ell)!}\int_0^\infty (\lambda_\ell r)^{2\ell+2}\exp(-\lambda_\ell r)\left[L_{k-1}^{2\ell+1}(\lambda_\ell r)\right]^2 \mathrm{d}r \\ &= 1\end{aligned} \tag{3.22}$$

using (B.4). We also have orthogonality with a r^{-1} weight

$$\begin{aligned}\langle k'\ell'm'|r^{-1}|k\ell m\rangle &= \delta_{\ell'\ell}\delta_{m'm}\frac{\lambda_\ell^2}{2}\sqrt{\frac{1}{(k'+\ell)(k+\ell)}\frac{(k'-1)!}{(k'+2\ell)!}\frac{(k-1)!}{(k+2\ell)!}} \\ &\quad\times\int_0^\infty (\lambda_\ell r)^{2\ell+1}\exp(-\lambda_\ell r)L_{k'-1}^{2\ell+1}(\lambda_\ell r)L_{k-1}^{2\ell+1}(\lambda_\ell r)\mathrm{d}r \\ &= \delta_{k'k}\delta_{\ell'\ell}\delta_{m'm}\frac{\lambda_\ell}{2(k+\ell)},\end{aligned} \tag{3.23}$$

due to (B.2).

3.3.2 Overlap matrix elements

For the spherical basis the overlap between two functions

$$\langle k'\ell'm'|\mathbf{r}\rangle \equiv \overline{\varphi}_{k'\ell'm'}(r,\theta,\phi;\lambda'_\ell) \quad \text{and} \quad \langle \mathbf{r}|k\ell m\rangle \equiv \varphi_{k\ell m}(r,\theta,\phi;\lambda_\ell)$$

is calculated analytically by

$$\begin{aligned}\langle k'\ell'm'|k\ell m\rangle &= \delta_{\ell'\ell}\delta_{m'm}\int_0^\infty \Lambda_{k'\ell'}(r;\lambda'_\ell)\Lambda_{k\ell}(r;\lambda_\ell)\mathrm{d}r \\ &= \delta_{\ell'\ell}\delta_{m'm}b^\ell_{k'k}\end{aligned} \tag{3.24}$$

where

$$b^{\ell}_{k'k} = \begin{cases} -\frac{1}{2}\sqrt{\frac{k(k+1+2\ell)}{(k+\ell)(k+1+\ell)}} & k' = k+1 \\ 1 & k' = k \\ -\frac{1}{2}\sqrt{\frac{(k-1)(k+2\ell)}{(k-1+\ell)(k+\ell)}} & k' = k-1 \\ 0 & \text{otherwise.} \end{cases} \tag{3.25}$$

3.3.3 One-electron Hamiltonian matrix elements

The one-electron Hamiltonian $\hat{H}_1 = \hat{K}_1 + V_1$ matrix elements can be partitioned into kinetic and potential components as

$$\langle k'\ell'm'|\hat{H}_1|k\ell m\rangle = \langle k'\ell'm'|\hat{K}_1|k\ell m\rangle + \langle k'\ell'm'|V_1|k\ell m\rangle, \tag{3.26}$$

which we shall consider separately.

Applying the spherical kinetic energy operator (2.11)

$$\hat{K}_1 = \frac{-1/2}{r^2}\left[\frac{\partial}{\partial r}\left(r^2\frac{\partial}{\partial r}\right) + \frac{1}{\sin\theta}\frac{\partial}{\partial\theta}\left(\sin\theta\frac{\partial}{\partial\theta}\right) + \frac{1}{\sin^2\theta}\frac{\partial^2}{\partial\phi^2}\right]$$

to our basis function (3.20) gives

$$\begin{aligned}\hat{K}_1 &\left[r^{-1}\Lambda_{k\ell}(r;\lambda_\ell)Y^m_\ell(\cos\theta,\phi)\right] \\ &= \frac{-1/2}{r^2}\left[\frac{\partial}{\partial r}\left(r^2\frac{\partial}{\partial r}\right) - \ell(\ell+1)\right]\left[r^{-1}\Lambda_{k\ell}(r;\lambda_\ell)Y^m_\ell(\cos\theta,\phi)\right]\end{aligned} \tag{3.27}$$

using the definition of spherical harmonics (C.3). Utilising (B.5) and (B.6) the radial derivative evaluates to

$$\frac{\partial}{\partial r}\left(r^2\frac{\partial}{\partial r}\right)\left[r^{-1}\Lambda_{k\ell}(r;\lambda_\ell)\right] = \left[\tfrac{1}{4}\lambda^2_\ell r^2 - (k+\ell)\lambda r + \ell(\ell+1)\right] r^{-1}\Lambda_{k\ell}(r;\lambda_\ell). \tag{3.28}$$

Inserting this into (3.27) and taking the overlap with another basis function $\langle k'\ell'm'|$ yields

$$\begin{aligned}\langle k'\ell'm'|\hat{K}_1|k\ell m\rangle &= -\tfrac{1}{2}\delta_{\ell'\ell}\delta_{m'm}\int_0^\infty \Lambda_{k'\ell'}(r;\lambda_\ell)\left[\tfrac{1}{4}\lambda^2_\ell - (k+\ell)\lambda_\ell r^{-1}\right]\Lambda_{k\ell}(r;\lambda_\ell)\mathrm{d}r \\ &= -\tfrac{1}{4}\lambda^2_\ell\delta_{\ell'\ell}\delta_{m'm}\left(\tfrac{1}{2}b^\ell_{k'k} + \delta_{k'k}\right)\end{aligned} \tag{3.29}$$

using (3.23), (3.24) and with $b^\ell_{k'k}$ defined in (3.25).

When the origin is at the midpoint of the nuclear axis, the matrix elements due to interaction with the nuclei (2.14) are

$$\langle k'\ell'm'|V_1|k\ell m\rangle = z\sum_{L=0}^{\infty}[Z_1+(-1)^L Z_2]\int_0^{\infty}\Lambda_{k'\ell'}(r;\lambda_{\ell'})\frac{r_<^L}{r_>^{L+1}}\Lambda_{k\ell}(r;\lambda_\ell)\mathrm{d}r \\ \times\iint_{4\pi}Y_{\ell'}^{m'}(\cos\theta,\phi)P_L(\cos\theta)Y_\ell^m(\cos\theta,\phi)\sin\theta\mathrm{d}\theta\mathrm{d}\phi \quad (3.30)$$

with $r_< = \min(r, \frac{R}{2})$ and $r_> = \max(r, \frac{R}{2})$. We define the nuclear potential function piecewise as

$$V_L(r,\tfrac{R}{2}) = \begin{cases} \dfrac{r^L}{(\frac{R}{2})^{L+1}} & r \le \frac{R}{2} \\ \dfrac{(\frac{R}{2})^L}{r^{L+1}} & r > \frac{R}{2} \end{cases} \quad (3.31)$$

and resolve the angular integral through (C.3) and (D.1) as

$$\int_{\theta=0}^{\pi}\int_{\phi=0}^{2\pi}Y_{\ell'}^{m'}(\cos\theta,\phi)P_L(\cos\theta)Y_\ell^m(\cos\theta,\phi)\sin\theta\mathrm{d}\theta\mathrm{d}\phi = (-1)^L C^{\ell'\ L\ \ell}_{0\ 0\ 0}C^{\ell\ L\ \ell'}_{m\ 0\ m'}. \quad (3.32)$$

The selection rules of these Clebsch-Gordan coefficients (D.2) limit the non-zero terms in the sum to those for which L satisfies

$$\begin{aligned}(-1)^L &= (-1)^{\ell'+\ell} \\ L_{\min} &= |\ell'-\ell| \\ L_{\max} &= \ell'+\ell\end{aligned} \quad (3.33)$$

and so the matrix elements can be evaluated as

$$\langle k'\ell'm'|V_1|k\ell m\rangle \\ = z\sum_{L=L_{\min}}^{L_{\max}}{}' [(-1)^L Z_1+Z_2]C^{\ell'\ L\ \ell}_{0\ 0\ 0}C^{\ell\ L\ \ell'}_{m\ 0\ m'}\int_0^{\infty}\Lambda_{k'\ell'}(r;\lambda_{\ell'})V_L(r,\tfrac{R}{2})\Lambda_{k\ell}(r;\lambda_\ell)\mathrm{d}r \quad (3.34)$$

with the primed sum indicating that L takes every second value. Furthermore, the term in square brackets is zero for homogeneous diatomics ($Z_1 = Z_2$) when L is odd, i.e. when $(-1)^{\ell'} \neq (-1)^{\ell}$. In this case, therefore, only functions of similar parity will result in non-zero matrix elements. This, along with the $\ell' = \ell$

condition for overlap (3.24) and kinetic energy (3.29) matrix elements, is the mathematical justification that parity is a good quantum number for homogeneous diatomics. For heterogeneous diatomics where parity does not exist, it may make more sense to not place the coordinate origin at the geometric mean of the nuclei.

For the combined nuclei case ($R = 0$) we have $r_< = 0$ and $r_> = r$, and so $V_L(r, 0) = \frac{\delta_{L0}}{r^{L+1}}$. Therefore the sum will collapse to only the $L = 0$ term and the Clebsch-Gordan coefficients (along with the other matrix elements which are unchanged) would enforce $\ell' = \ell$. This results in the familiar atomic case where the angular momentum ℓ is a good quantum number.

Solving the generalised eigenvalue problem (3.18) with the overlap (3.24) and Hamiltonian (3.26) matrix elements yields N pseudostates as an expansion of our basis functions

$$\Phi_i^{\pi_i m_i}(r, \theta, \phi) = \sum_{\ell=0}^{\ell_{\max}} \sum_{k=1}^{N_\ell} C_{k\ell m_i}^{(i)} \varphi_{k\ell m_i}(r, \theta, \phi; \lambda_\ell), \tag{3.35}$$

where the sum over ℓ is restricted by $(-1)^\ell = \pi_i$ and a given maximum target angular momentum $\ell_{\max}$. It is usually convenient to combine the radial parts of each ℓ to give us a form similar to the original basis functions (3.20)

$$\Phi_i^{\pi_i m_i}(r, \theta, \phi) = r^{-1} \sum_{\ell=0}^{\ell_{\max}} X_\ell^{(i)}(r) Y_\ell^{m_i}(\cos\theta, \phi) \tag{3.36}$$

with the rearranged radial functions

$$X_\ell^{(i)}(r) = \sum_{k=1}^{N_\ell} C_{k\ell m_i}^{(i)} \Lambda_{k\ell}(r; \lambda_\ell). \tag{3.37}$$

Ultimately our aim in constructing these pseudostates is to maximise their accuracy (convergence) whilst maintaining a manageable expansion size (small N_ℓ and $\ell_{\max}$), as a larger expansion means more terms to evaluate.

3.4 Two-electron states

We now apply the Configuration Interaction procedure to construct the pseudostates $\langle x_1, x_2 | \Phi_i^{\Pi MS} \rangle = \Phi_i^{\Pi MS}(x_1, x_2)$ of the two-electron Hamiltonian

$$\hat{H}_{12} = \hat{H}_1 + \hat{H}_2 + V_{12} \tag{3.38}$$

consisting of two one-electron Hamtiltonians (2.10) and the electron-electron potential V_{12}. These pseudostates are characterised by energy ϵ_i and have the quantum numbers of parity Π, angular momentum projection M, and spin S. The two-electron spin, as being a combination of two $\frac{1}{2}$ spins, can either be $S = 0$ (singlet) or $S = 1$ (triplet). As with the one-electron case, parity is only a good quantum number for homogeneous diatomics and should be ignored throughout this Section for the heterogeneous case.

The pseudostates diagonalise the target Hamiltonian (3.38)

$$\langle \Phi_f^{\Pi' M' S'} | \hat{H}_{12} | \Phi_i^{\Pi M S} \rangle = \delta_{fi} \epsilon_i \tag{3.39}$$

and must be antisymmetric

$$\Phi_i^{\Pi M S}(x_2, x_1) = -\Phi_i^{\Pi M S}(x_1, x_2) \tag{3.40}$$

due to the Pauli exclusion principle. If we separate the coordinate and spin components

$$\Phi_i^{\Pi M S}(x_1, x_2) = \Phi_i^{\Pi M S}(\mathbf{r}_1, \mathbf{r}_2) X_i^S(\sigma_1, \sigma_2), \tag{3.41}$$

they individually obey

$$\Phi_i^{\Pi M S}(\mathbf{r}_2, \mathbf{r}_1) = (-1)^S \Phi_i^{\Pi M S}(\mathbf{r}_1, \mathbf{r}_2) \tag{3.42}$$

and

$$X_i^S(\sigma_2, \sigma_1) = -(-1)^S X_i^S(\sigma_1, \sigma_2). \tag{3.43}$$

3.4.1 Antisymmetry

In order to build antisymmetric pseudostates we use configurations that have been antisymmetrised. Two-electron configurations consist of one-electron orbitals

$$\varphi_\alpha^{\pi_\alpha m_\alpha}(x) = \varphi_\alpha^{\pi_\alpha m_\alpha}(\mathbf{r}) \chi(\sigma), \tag{3.44}$$

which may either be Laguerre basis function (3.20) or one-electron pseudostates (3.36). Note that the spin quantum number will be suppressed for one-electron orbitals, as it is clear that $s_\alpha = \frac{1}{2}$.

For a combination of two one-electron orbitals we couple their spins through angular momentum algebra to give

$$\varphi_{\alpha,\beta}^{\pi_\alpha m_\alpha, \pi_\beta m_\beta}(x_1, x_2) = \varphi_\alpha^{\pi_\alpha m_\alpha}(\mathbf{r}_1) \varphi_\beta^{\pi_\beta m_\beta}(\mathbf{r}_2) \sum_{\sigma_1, \sigma_2} C^{\frac{1}{2}\ \frac{1}{2}\ S}_{\sigma_1\ \sigma_2\ m_S} \chi(\sigma_1) \chi(\sigma_2) \tag{3.45}$$

for a total spin of $S \in \{0, 1\}$. Applying the (coordinate and spin) antisymmetriser operator $(1 - \hat{P}_{12})$ on this yields the two-electron configurations

$$\varphi_{\alpha\beta}^{\Pi MS}(x_1, x_2) = \frac{1}{\sqrt{2(1+\delta_{\alpha\beta})}} \Big[\varphi_\alpha^{m_\alpha \pi_\alpha}(\mathbf{r}_1) \varphi_\beta^{m_\beta \pi_\beta}(\mathbf{r}_2) \sum_{\sigma_1,\sigma_2} C^{\frac{1}{2}\,\frac{1}{2}\,S}_{\sigma_1\,\sigma_2\,m_S} \chi(\sigma_1)\chi(\sigma_2) - \varphi_\alpha^{m_\alpha \pi_\alpha}(\mathbf{r}_2) \varphi_\beta^{m_\beta \pi_\beta}(\mathbf{r}_1) \sum_{\sigma_1,\sigma_2} C^{\frac{1}{2}\,\frac{1}{2}\,S}_{\sigma_1\,\sigma_2\,m_S} \chi(\sigma_2)\chi(\sigma_1) \Big], \tag{3.46}$$

which are characterised by two-electron parity $\Pi = \pi_\alpha \pi_\beta$ and orbital angular momentum projection $M = m_\alpha + m_\beta$. From symmetry relations of the Clebsch-Gordan coefficients (D.4) we can rewrite the second sum over spin functions as

$$\begin{aligned} \sum_{\sigma_1,\sigma_2} C^{\frac{1}{2}\,\frac{1}{2}\,S}_{\sigma_1\,\sigma_2\,m_S} \chi(\sigma_2)\chi(\sigma_1) &= (-1)^{1-S} \sum_{\sigma_1,\sigma_2} C^{\frac{1}{2}\,\frac{1}{2}\,S}_{\sigma_2\,\sigma_1\,m_S} \chi(\sigma_2)\chi(\sigma_1) \\ &= -(-1)^S \sum_{\sigma_1,\sigma_2} C^{\frac{1}{2}\,\frac{1}{2}\,S}_{\sigma_1\,\sigma_2\,m_S} \chi(\sigma_1)\chi(\sigma_2), \end{aligned} \tag{3.47}$$

where we have switched the dummy indices in the second line. This is a more explicit form of the spin antisymmetry condition (3.43). With it, (3.46) can be rewritten as

$$\varphi_{\alpha\beta}^{\Pi MS}(x_1, x_2) = \frac{1}{\sqrt{2(1+\delta_{\alpha\beta})}} \Big[1 + (-1)^S \hat{P}_{\alpha\beta}\Big] \Big[\varphi_\alpha^{\pi_\alpha m_\alpha}(\mathbf{r}_1) \varphi_\beta^{\pi_\beta m_\beta}(\mathbf{r}_2)\Big] \times \sum_{\sigma_1,\sigma_2} C^{\frac{1}{2}\,\frac{1}{2}\,S}_{\sigma_1\,\sigma_2\,m_S} \chi(\sigma_1)\chi(\sigma_2) \tag{3.48}$$

with the coordinate space exchange operator $\hat{P}_{\alpha\beta}$. A more compact notation is

$$|\varphi_i^{\Pi MS}\rangle = \hat{\mathcal{A}}^S |\alpha\beta\rangle |S m_S\rangle \tag{3.49}$$

$$\langle \varphi_f^{\Pi' M' S'}| = \langle S' m'_S| \langle \gamma\delta| \hat{\mathcal{A}}^{S'} \tag{3.50}$$

where the coordinate antisymmetriser

$$\hat{\mathcal{A}}^S = \frac{1}{\sqrt{2(1+\delta_{\alpha\beta})}} \Big[1 + (-1)^S \hat{P}_{\alpha\beta}\Big] \tag{3.51}$$

acts to the right on $|\alpha\beta\rangle = \varphi_\alpha^{\pi_\alpha m_\alpha}(\mathbf{r}_1)\varphi_\beta^{\pi_\beta m_\beta}(\mathbf{r}_2)$ and to the left on $\langle\gamma\delta| = \overline{\varphi}_\gamma^{\pi_\gamma m_\gamma}(\mathbf{r}_1)\overline{\varphi}_\delta^{\pi_\delta m_\delta}(\mathbf{r}_2)$. As with their one-electron counterparts, the two-electron spin functions

$$\langle \sigma_1, \sigma_2 | S m_S \rangle = \sum_{\sigma_1\,\sigma_2} C^{\frac{1}{2}\,\frac{1}{2}\,S}_{\sigma_1\,\sigma_2\,m_S} \chi(\sigma_1)\chi(\sigma_2) \tag{3.52}$$

are orthonormal, i.e. $\langle S' m'_S | S m_S \rangle = \delta_{S'S} \delta_{m'_S m_S}$.

The overlap matrix elements are calculated as

$$\langle \varphi_{\gamma\delta}^{\Pi' M' S'} | \varphi_{\alpha\beta}^{\Pi M S} \rangle = \frac{\delta_{S'S} \delta_{m'_S m_S}}{\sqrt{(1+\delta_{\gamma\delta})(1+\delta_{\alpha\beta})}} \Big[\langle \gamma\delta | \alpha\beta \rangle + (-1)^S \langle \gamma\delta | \beta\alpha \rangle \Big], \tag{3.53}$$

where $\langle \gamma\delta | \alpha\beta \rangle = \langle \delta\gamma | \beta\alpha \rangle = \langle \gamma | \alpha \rangle \langle \delta | \beta \rangle$ can be determined through one-electron overlaps (see Section 3.3.2). In addition, the two-electron Hamiltonian matrix elements

$$\langle \varphi_{\gamma\delta}^{\Pi' M' S'} | \hat{H}_{12} | \varphi_{\alpha\beta}^{\Pi M S} \rangle = \frac{\delta_{S'S} \delta_{m'_S m_S}}{\sqrt{(1+\delta_{\gamma\delta})(1+\delta_{\alpha\beta})}} \Big[\langle \gamma\delta | \hat{H}_{12} | \alpha\beta \rangle + (-1)^s \langle \gamma\delta | \hat{H}_{12} | \beta\alpha \rangle \Big] \tag{3.54}$$

require the quantity

$$\langle \gamma\delta | \hat{H}_{12} | \alpha\beta \rangle = \langle \gamma | \hat{H}_1 | \alpha \rangle \langle \delta | \beta \rangle + \langle \gamma | \alpha \rangle \langle \delta | \hat{H}_2 | \beta \rangle + \langle \gamma\delta | \hat{V}_{12} | \alpha\beta \rangle, \tag{3.55}$$

which includes one-electron Hamiltonian matrix elements (Section 3.3.3) together with two-electron $\hat{V}_{12}$ matrix elements (Section 3.4.2). Examination of these matrix elements will reveal the conservation of two-electron parity $\Pi' = \Pi$ and angular momentum projection $M' = M$, in addition to total spin $S' = S$.

As in the one-electron case, we may now use our (antisymmetrised) two-electron configurations to solve the generalised eigenvalue problem (3.18) and obtain the two-electron pseudostates as the CI expansion

$$\Phi_i^{\Pi M S}(x_1, x_2) = \sum_{\alpha \geq \beta} c_{\alpha\beta}^{(i)} \varphi_{\alpha\beta}^{\Pi M S}(x_1, x_2) \tag{3.56}$$

in terms of configurations (3.48). Expanding these and dropping the spin component gives us an expression for the coordinate part of our two-electron states

$$\Phi_i^{\Pi M S}(\mathbf{r}_1, \mathbf{r}_2) = \sum_{\alpha,\beta} C_{\alpha\beta}^{(i)} \varphi_\alpha^{\pi_\alpha m_\alpha}(\mathbf{r}_1) \varphi_\beta^{\pi_\beta m_\beta}(\mathbf{r}_2), \tag{3.57}$$

where the new expansion coefficients are

$$C_{\alpha\beta}^{(i)} = \frac{1}{\sqrt{2(1+\delta_{\alpha\beta})}} c_{\alpha\beta}^{(i)} \tag{3.58}$$

and satisfy

$$C_{\beta\alpha}^{(i)} = (-1)^S C_{\alpha\beta}^{(i)}, \tag{3.59}$$

which is reminiscent of the coordinate space antisymmetry condition (3.42).

3.4.2 Electron-electron potential

For the two-electron Hamiltonian matrix elements (3.55) we must calculate the electron-electron potential term $\langle\gamma\delta|V_{12}|\alpha\beta\rangle \equiv \langle\gamma\delta : \Pi' M'|V_{12}|\alpha\beta : \Pi M\rangle$ between four one-electron orbitals, e.g. $\langle\mathbf{r}_1|\alpha\rangle \equiv \varphi_\alpha^{\pi_\alpha m_\alpha}(\mathbf{r}_1)$, which are in the general form

$$\varphi_\alpha^{\pi_\alpha m_\alpha}(\mathbf{r}_1) = r_1^{-1} \sum_{\ell_\alpha} X_{\ell_\alpha}^{(\alpha)}(r_1) Y_{\ell_\alpha}^{m_\alpha}(\hat{\mathbf{r}}_1). \tag{3.60}$$

Here $\Pi' = \pi_\gamma \pi_\delta$, $M' = m_\gamma + m_\delta$, $\Pi = \pi_\alpha \pi_\beta$, and $M = m_\alpha + m_\beta$. The potential is expanded in spherical harmonics by

$$V_{12} = \sum_{L=0}^{\infty} \sum_{m_L=-L}^{L} (-1)^{m_L} \frac{4\pi}{2L+1} \frac{r_<^L}{r_>^{L+1}} Y_L^{-m_L}(\hat{\mathbf{r}}_1) Y_L^{m_L}(\hat{\mathbf{r}}_2) \tag{3.61}$$

with $r_< = \min\{r_1, r_2\}$ and $r_> = \max\{r_1, r_2\}$.

The angular integrals are straightforward to evaluate using angular momentum algebra. They become

$$\int_{4\pi} \overline{Y}_{\ell_\gamma}^{m_\gamma}(\hat{\mathbf{r}}_1) Y_L^{-m_L}(\hat{\mathbf{r}}_1) Y_{\ell_\alpha}^{m_\alpha}(\hat{\mathbf{r}}_1) \mathrm{d}\hat{\mathbf{r}}_1 = (-1)^L \sqrt{\frac{2\ell+1}{4\pi}} C^{\ell_\gamma\, L\, \ell_\alpha}_{0\ 0\ 0} C^{\ell_\alpha\ \ L\ \ \ell_\gamma}_{m_\alpha\, -m_L\, m_\gamma} \tag{3.62}$$

and

$$\int_{4\pi} \overline{Y}_{\ell_\delta}^{m_\delta}(\hat{\mathbf{r}}_2) Y_L^{m_L}(\hat{\mathbf{r}}_2) Y_{\ell_\beta}^{m_\beta}(\hat{\mathbf{r}}_2) \mathrm{d}\hat{\mathbf{r}}_2 = (-1)^L \sqrt{\frac{2\ell+1}{4\pi}} C^{\ell_\delta\, L\, \ell_\beta}_{0\ 0\ 0} C^{\ell_\beta\ \ L\ \ \ell_\delta}_{m_\beta\, m_L\, m_\delta} \tag{3.63}$$

in the spaces of $\mathrm{d}\hat{\mathbf{r}}_1$ and $\mathrm{d}\hat{\mathbf{r}}_2$ respectively. From the selection rules of the Clebsch-Gordan coefficients (D.2) we can restrict the values of ℓ and m to

$$\begin{gathered} L_{\min} \le L \le L_{\max}, \\ L_{\min} = \max\{|\ell_\gamma - \ell_\alpha|, |\ell_\delta - \ell_\beta|\}, \\ L_{\max} = \min\{\ell_\gamma + \ell_\alpha, \ell_\delta + \ell_\beta\}, \\ (-1)^{\ell_\gamma + \ell_\alpha} = (-1)^L = (-1)^{\ell_\delta + \ell_\beta}, \text{ and} \\ m_\gamma - m_\alpha = m_L = m_\beta - m_\delta. \end{gathered} \tag{3.64}$$

Therefore, for each quadruplet of orbitals, L is always even or always odd, m_L is a single value, and two-electron parity $\Pi' = \Pi$ and orbital angular momentum projection $M' = M$ are conserved.

We now turn our attention to the radial integrals, which can be written as

$$\int_0^\infty \int_0^\infty X_{\ell_\gamma}^{(\gamma)}(r_1) X_{\ell_\delta}^{(\delta)}(r_2) \frac{r_<^L}{r_>^{L+1}} X_{\ell_\alpha}^{(\alpha)}(r_1) X_{\ell_\beta}^{(\beta)}(r_2) \mathrm{d}r_1 \mathrm{d}r_2$$

$$= \int_0^\infty X_{\ell_\gamma}^{(\gamma)}(r_1) f_{\ell_\delta,L,\ell_\beta}^{(\delta,\beta)}(r_1) X_{\ell_\alpha}^{(\alpha)}(r_1) \mathrm{d}r_1, \quad (3.65)$$

where we have defined the function

$$f_{\ell_\delta,L,\ell_\beta}^{(\delta,\beta)}(r_1) = \int_0^{r_1} X_{\ell_\delta}^{(\delta)}(r_2) \frac{r_2^L}{r_1^{L+1}} X_{\ell_\beta}^{(\beta)}(r_2) \mathrm{d}r_2 + \int_{r_1}^\infty X_{\ell_\delta}^{(\delta)}(r_2) \frac{r_1^L}{r_2^{L+1}} X_{\ell_\beta}^{(\beta)}(r_2) \mathrm{d}r_2. \quad (3.66)$$

Putting all of this together, the electron-electron matrix elements are

$$\langle \gamma\delta | V_{12} | \alpha\beta \rangle = \delta_{M'M} \delta_{\Pi'\Pi} \sum_{\substack{\ell_\gamma,\ell_\delta \\ \ell_\alpha,\ell_\beta}} \sum_{L=L_{\min}}^{L_{\min}} (-1)^{m_L} C^{\ell_\gamma\ L\ \ell_\alpha}_{0\ 0\ 0} C^{\ell_\alpha\ \ L\ \ \ell_\gamma}_{m_\alpha\ -m_L\ m_\gamma} C^{\ell_\delta\ L\ \ell_\beta}_{0\ 0\ 0} C^{\ell_\beta\ \ L\ \ \ell_\delta}_{m_\beta\ m_L\ m_\delta}$$

$$\times \int_0^\infty X_{\ell_\gamma}^{(\gamma)}(r_1) X_{\ell_\alpha}^{(\alpha)}(r_1) f_{\ell_\delta,L,\ell_\beta}^{(\delta,\beta)}(r_1) \mathrm{d}r_1 \quad (3.67)$$

subject to the restrictions on L given by (3.64).

3.5 Analytic Born

In this Section we will determine the spherical expressions for the Analytic Born matrix elements used in the convergence testing and top-up procedures of Section 2.5.1. The V-matrix elements (2.87)

$$V_{fi}^{(\mathrm{AB})} = z\delta_{fi} \left\langle \mathbf{k}_f \middle| \frac{Z_1}{|\mathbf{r}_0 - \frac{1}{2}\mathbf{R}|} + \frac{Z_2}{|\mathbf{r}_0 + \frac{1}{2}\mathbf{R}|} \middle| \mathbf{k}_i \right\rangle - z \left\langle \Psi_f \middle| \frac{N_e}{|\mathbf{r}_0 - \mathbf{r}_1|} \middle| \Psi_i \right\rangle \quad (3.68)$$

are split into an elastic term (2.90) and general term (2.91).

In spherical coordinates the plane waves are expanded as

$$\exp(\mathrm{i}\mathbf{q}\cdot\mathbf{r}) = 4\pi \sum_{L=0}^\infty \sum_{m_L=-L}^{L} \mathrm{i}^L \overline{Y}_L^{m_L}(\hat{\mathbf{q}}) j_L(qr) Y_L^{m_L}(\hat{\mathbf{r}}) \quad (3.69)$$

in terms of spherical Bessel functions $j_L(qr)$. The elastic term becomes

$$\left\langle \mathbf{k}_f \middle| \frac{Z_1}{|\mathbf{r}_0 - \frac{1}{2}\mathbf{R}|} + \frac{Z_2}{|\mathbf{r}_0 + \frac{1}{2}\mathbf{R}|} \middle| \mathbf{k}_i \right\rangle$$

$$= \frac{4\pi}{2\pi^2 q^2} \sum_{L=0}^\infty \mathrm{i}^L \overline{Y}_L^{m_L}(\hat{\mathbf{q}}) \left[Z_1 + (-1)^L Z_2 \right] j_L(\tfrac{R}{2}q) \sqrt{\tfrac{2L+1}{4\pi}} \delta_{m_L 0} \quad (3.70)$$

where we have used the fact that $\mathbf{R}$ lies along the z-axis, (C.5) as well as the reflection formula (C.7) for the Z_2 term.

For the general term we apply the Born approximation (2.86) to separate the total scattering wavefunctions Ψ and represent the resulting target states as

$$\Phi_i(x_1, x_2) = \sum_{\alpha,\beta} C^{(i)}_{\alpha,\beta} \varphi_\alpha(\mathbf{r}_1)\varphi_\beta(\mathbf{r}_2) X_i^{S_i}(\sigma_1, \sigma_2) \tag{3.71}$$

with constituent one-electron orbitals

$$\varphi_\alpha(\mathbf{r}_1) = r^{-1} \sum_{\ell_\alpha} X^{(\alpha)}_{\ell_\alpha}(r_1) Y^{m_\alpha}_{\ell_\alpha}(\hat{\mathbf{r}}_1), \tag{3.72}$$

where spin resolves trivially. In the two-electron case these matrix elements become

$$\begin{aligned}\left\langle \Psi_f \left| \frac{N_e}{|\mathbf{r}_0 - \mathbf{r}_1|} \right| \Psi_i \right\rangle &= 4\pi\delta_{S_f S_i} \sum_L \mathrm{i}^L \overline{Y}^{m_L}_L(\hat{\mathbf{q}}) \sum_{\gamma,\delta} \sum_{\alpha,\beta} C^{(f)}_{\gamma,\delta} C^{(i)}_{\alpha,\beta} \langle\delta|\beta\rangle \\ &\times \sum_{\ell_\gamma,\ell_\alpha} (-1)^L \sqrt{\frac{2L+1}{4\pi}} C^{\ell_\gamma\ L\ \ell_\alpha}_{0\ 0\ 0} C^{\ell_\alpha\ \ L\ \ \ell_\gamma}_{m_\alpha\ m_L\ m_\gamma} \int_0^\infty X^{(\gamma)}_{\ell_\gamma}(r_1) j_L(q r_1) X^{(\alpha)}_{\ell_\alpha}(r_1) \mathrm{d}r_1, \end{aligned} \tag{3.73}$$

where $\langle\delta|\beta\rangle$ is simply the overlap of these two orbitals, and therefore $\pi_\delta = \pi_\beta$ and $m_\delta = m_\beta$. With the selection rules of the Clebsch-Gordan coefficients (D.2) this means that $m_L = m_\gamma - m_\alpha = m_f - m_i$, and in addition $(-1)^L = (-1)^{\ell_\gamma + \ell_\alpha} = \Pi_f \Pi_i$ for homogeneous diatomics. By defining the function

$$\begin{aligned} F^{(\mathrm{AB})}_{fi,Lm_L}(r_1) &= \delta_{S_f S_i} N_e (-1)^L \sqrt{2L+1} \\ &\times \sum_{\gamma,\delta} \sum_{\alpha,\beta} C^{(f)}_{\gamma,\delta} C^{(i)}_{\alpha,\beta} \langle\delta|\beta\rangle \sum_{\ell_\gamma,\ell_\alpha} C^{\ell_\gamma\ L\ \ell_\alpha}_{0\ 0\ 0} C^{\ell_\alpha\ \ L\ \ \ell_\gamma}_{m_\alpha\ m_L\ m_\gamma} X^{(\gamma)}_{\ell_\gamma}(r_1) X^{(\alpha)}_{\ell_\alpha}(r_1) \end{aligned} \tag{3.74}$$

the final form of (2.91) is

$$\left\langle \Psi_f \left| \frac{N_e}{|\mathbf{r}_0 - \mathbf{r}_1|} \right| \Psi_i \right\rangle = \frac{\sqrt{\pi}}{\pi^2 q^2} \sum_{L=0}^\infty \mathrm{i}^L \overline{Y}^{m_L}_L(\hat{\mathbf{q}}) \int_0^\infty F^{(\mathrm{AB})}_{fi,Lm_L}(r_1) j_L(q r_1) \mathrm{d}r_1. \tag{3.75}$$

Using (3.70) and (3.75) we can rewrite the Analytical Born matrix elements (2.87) as

$$V^{(\mathrm{AB})}_{fi}(\mathbf{q}) = \sum_{L=0}^\infty \mathrm{i}^L V^{(\mathrm{AB})}_{fi,Lm_L}(q) \overline{Y}^{m_L}_L(\hat{\mathbf{q}}) \tag{3.76}$$

with the partial matrix elements

$$V^{(\mathrm{AB})}_{fi,Lm_L}(q) = \frac{z\sqrt{\pi}}{\pi^2 q^2} \left[\delta_{fi} J_L(q) - \int_0^\infty F^{(\mathrm{AB})}_{fi,Lm_L}(r_1) j_L(q r_1) \mathrm{d}r_1 \right]. \tag{3.77}$$

Here we have defined

$$J_L(q) = \left[Z_1 + (-1)^L Z_2\right] \sqrt{2L+1} j_L(\tfrac{R}{2}q). \tag{3.78}$$

For homogeneous diatomics both (3.74) and (3.78), and hence (3.77), are zero for odd values of L.

3.5.1 Elastic singularity

Our expression for the partial matrix elements (3.77) appears to be singular when the momentum transfer $q = 0$. According to the definitions (2.89) this occurs when $k_i = k_f$ and $\theta_f = 0$, and therefore occurs in elastic scattering. To resolve the singularity we look closer at (3.77) when $f = i$ and $q \to 0$.

The small q behaviour of the spherical Bessel functions yields the Taylor series expansions

$$\begin{aligned} \lim_{q\to 0} j_0(qr_1) &= \lim_{q\to 0} \frac{\sin(qr_1)}{qr_1} \\ &= 1 - \frac{(qr_1)^2}{6} + \mathcal{O}(q^4) \end{aligned} \tag{3.79}$$

for $L = 0$ and

$$\begin{aligned} \lim_{q\to 0} j_2(qr_1) &= \lim_{q\to 0} \frac{-\sin(qr_1)}{qr_1} - \frac{3\cos(qr_1)}{(qr_1)^2} + \frac{3\sin(qr_1)}{(qr_1)^3} \\ &= \frac{(qr_1)^2}{15} + \mathcal{O}(q^4) \end{aligned} \tag{3.80}$$

for $L = 2$. Only these two spherical Bessels are relevant, because L is restricted to even numbers in the elastic case of homogeneous diatomics, and all terms with q^3 or a higher power will not be completely cancelled by the q^{-2} factor and therefore vanish at $q = 0$. Ignoring the heterogeneous diatomic case, (3.78) now simplifies to

$$J_0(q)|_{q\to 0} \approx 2Z\left(1 - \frac{R^2q^2}{24}\right) \tag{3.81}$$

and

$$J_2(q)|_{q\to 0} \approx 2Z\frac{\sqrt{5}R^2q^2}{60}. \tag{3.82}$$

We can also compare the elastic $L = 0$ term of (3.74) to the self-overlap

$$\langle\Phi_i|\Phi_i\rangle = \delta_{S_iS_i} \sum_{\gamma,\delta}\sum_{\alpha,\beta} C^{(i)}_{\gamma,\delta} C^{(i)}_{\alpha,\beta} \langle\delta|\beta\rangle \sum_{\ell_\gamma,\ell_\alpha} \delta_{\ell_\gamma\ell_\alpha}\delta_{m_\gamma m_\alpha} \int_0^\infty X^{(\gamma)}_{\ell_\gamma}(r_1) X^{(\alpha)}_{\ell_\alpha}(r_1)\mathrm{d}r_1 \tag{3.83}$$

and conclude that

$$\int_0^\infty F_{ii,00}^{(\mathrm{AB})}(r_1)\mathrm{d}r_1 \equiv N_e\langle\Phi_i|\Phi_i\rangle = N_e \tag{3.84}$$

using the degeneracy of the Clebsch-Gordan coefficients (D.3).

From this behaviour we may write the first $i \to i$ term of (3.77) explicitly as

$$\begin{aligned} V_{ii,00}^{(\mathrm{AB})}(q)\Big|_{q=0} &= \frac{z\sqrt{\pi}}{\pi^2 q^2}\left[2Z\left(1-\frac{R^2q^2}{24}\right) - \int_0^\infty F_{ii,00}(r_1)\left(1-\frac{q^2r_1^2}{6}\right)\mathrm{d}r_1\right] \\ &= \frac{z}{\pi^{3/2}}\left[\frac{2Z-N_e}{q^2} - \frac{ZR^2}{12} + \frac{1}{6}\int_0^\infty F_{ii,00}(r_1)r_1^2\mathrm{d}r_1\right] \end{aligned} \tag{3.85}$$

and the second term as

$$V_{ii,20}^{(\mathrm{AB})}(q)\Big|_{q=0} = \frac{z}{\pi^{3/2}}\left[\frac{\sqrt{5}ZR^2}{30} - \frac{1}{15}\int_0^\infty F_{ii,20}(r_1)r_1^2\mathrm{d}r_1\right] \tag{3.86}$$

Using these we can see that the singularity is removed when $2Z = N_e$, i.e. in the case of neutral homogeneous diatomics.

3.6 Close-coupling

Following on from Section 2.4, we calculate the T-matrices required for the scattering amplitudes (2.73) and hence the cross sections by utilising the partial wave expansion (3.4) of the wave vectors to represent the T-matrix as

$$\begin{aligned} \langle\mathbf{k}_f^{(-)}\Phi_f|T_U|\Phi_i\mathbf{k}_i^{(+)}\rangle &= \frac{2}{\pi}(k_fk_i)^{-1} \\ &\times \sum_{\ell_fm_f}\sum_{\ell_im_i} \mathrm{i}^{\ell_f-\ell_i}\mathrm{e}^{\mathrm{i}\delta_{\ell_f}^{(f)}+\mathrm{i}\delta_{\ell_i}^{(i)}} Y_{\ell_f}^{m_f}(\hat{\mathbf{k}}_f)\overline{Y}_{\ell_i}^{m_i}(\hat{\mathbf{k}}_i)\langle k_f\ell_fm_f,\Phi_f|T_U|\Phi_i,k_i\ell_im_i\rangle \end{aligned} \tag{3.87}$$

in terms of the partial T-matrix elements

$$\begin{aligned} &\langle k_f\ell_fm_f,\Phi_f|T_U|\Phi_i,k_i\ell_im_i\rangle \\ &\qquad\equiv \langle k_f\ell_fm_f,\Phi_f^{\Pi_fM_fS_f}:\Pi'M'S'|T_U|\Phi_i^{\Pi_iM_iS_i},k_i\ell_im_i:\Pi MS\rangle \end{aligned} \tag{3.88}$$

with three-electron parity $\Pi = (-1)^{\ell_i}\Pi_i$, angular momentum projection $M = m_i + M_i$, and spin $|\tfrac{1}{2} - S_i| \le S \le \tfrac{1}{2} + S_i$. Note that, once again, parity is only a good quantum number if the diatomic molecule is homogeneous and should be ignored throughout this section if it is heterogeneous.

The V-matrix has a similar expansion of partial matrix elements

$$\langle k'\ell'm', \Phi_{n'}|V_U|\Phi_n, k\ell m\rangle \equiv \langle k'\ell'm', \Phi_{n'}^{\Pi'_n M'_n S'_n} : \Pi' M' S'|V_U|\Phi_n^{\Pi_n M_n S_n}, k\ell m : \Pi M S\rangle, \tag{3.89}$$

which we are to calculate directly. For this we write out our partial projectile functions

$$\langle \mathbf{r}_0|k\ell m\rangle \equiv r_0^{-1} u_\ell(kr_0) Y_\ell^m(\cos\theta_0, \phi_0)\chi(\sigma_0) \tag{3.90}$$

as per Section 3.1, and target states

$$\langle \mathbf{r}_1, \mathbf{r}_2|\Phi_n^{\Pi_n M_n S_n}\rangle = \sum_{\alpha,\beta} C_{\alpha\beta}^{(n)} \varphi_\alpha^{\pi_\alpha m_\alpha}(\mathbf{r}_1)\varphi_\beta^{\pi_\beta m_\beta}(\mathbf{r}_2) X_n^{S_n}(\sigma_1, \sigma_2) \tag{3.91}$$

from Section 3.4 with general one-electron orbitals e.g.

$$\begin{aligned}\varphi_\alpha^{\pi_\alpha m_\alpha}(\mathbf{r}_1) &= r_1^{-1} \sum_{\ell_\alpha} X_{\ell_\alpha}^{(\alpha)}(r_1) Y_{\ell_\alpha}^{m_\alpha}(\hat{\mathbf{r}}_1) \\ &\equiv r_1^{-1} \sum_{\ell_\alpha} |\alpha\ell_\alpha m_\alpha\rangle\end{aligned} \tag{3.92}$$

and two-electron spin functions as (3.52). The projectile-molecule potential given by (2.39) can be divided into two parts $\hat{V}_U = V_U^{\mathrm{D}} + \hat{V}_U^{\mathrm{E}}$, where the direct part

$$V_U^{\mathrm{D}} = V_0 - U_0 - 2V_{01} \tag{3.93}$$

is the Coulombic interaction, and the exchange part

$$\hat{V}_U^{\mathrm{E}} = 2(E - \hat{H})\hat{P}_{01} \tag{3.94}$$

arises from the Pauli exclusion principle. The latter is only relevant to electron scattering and should be dropped when the projectile is a positron. The method to calculate each component is detailed in the following Sections.

3.6.1 Direct V-matrix elements

The (distorted) projectile-nuclei part, $V_0 - U_0$, is calculated in a similar manner to V_1 in Section 3.3.3. In this case, the integrals over spin $(\sigma_0, \sigma_1, \sigma_2)$ and target state coordinates $(\mathbf{r}_1, \mathbf{r}_2)$ collapse due to orthogonality, and we end up with

$$\begin{aligned}&\langle k'\ell'm', \Phi_{n'}|V_0 - U_0|\Phi_n, k\ell m\rangle \\ &\quad = \pm Z_\pm \delta_{n'n} \sum_{L=L_{\min}}^{L_{\max}} C_{0\ 0\ 0}^{\ell'\ L\ \ell} C_{m\ 0\ m'}^{\ \ell\ L\ \ell'} \int_0^\infty u_{\ell'}(k'r_0)\left[V_L(r_0) - \delta_{L0}U(r_0)\right] u_\ell(kr_0)\mathrm{d}r_0,\end{aligned} \tag{3.95}$$

again using (3.31)–(3.33). The (+) case is for $\ell'-\ell$ even, and the (−) case for $\ell'-\ell$ odd (heterogeneous diatomics only). The projectile-molecular-electron potential V_{01} is handled similarly to V_{12} in Section 3.4.2. We write it as

$$\begin{aligned}&\langle k'\ell'm', \Phi_{n'}|V_{01}|k\ell m, \Phi_n\rangle \\ &= \delta_{\Pi'\Pi}\delta_{M'M}\sum_{\substack{\gamma,\delta,\\ \alpha,\beta}} C^{(n')}_{\gamma,\delta}C^{(n)}_{\alpha,\beta}\langle\delta|\beta\rangle \sum_{\ell_\gamma,\ell_\alpha}\sum_{L=L_{\min}}^{L_{\max}}{}'(-1)^{m_L}C^{\ell' \; L \; \ell}_{0 \; 0 \; 0}C^{\ell \quad L \quad \ell'}_{m \; -m_L \; m'}C^{\ell_\gamma \; L \; \ell_\alpha}_{0 \; 0 \; 0}C^{\ell_\alpha \quad L \quad \ell_\gamma}_{m_\alpha \; m_L \; m_\gamma} \\ &\qquad\qquad \times \int_0^\infty u_{\ell'}(k'r_0)u_\ell(kr_0)f^{(\gamma,\alpha)}_{\ell_\gamma,L,\ell_\alpha}(r_0)\mathrm{d}r_0 \quad (3.96)\end{aligned}$$

using (3.66), where $L_{\min} = \max\{|\ell'-\ell|, |\ell_\gamma-\ell_\alpha|\}$, $L_{\max} = \min\{\ell'+\ell, \ell_\gamma+\ell_\alpha\}$, $m_L = m'-m = m_\alpha - m_\gamma$, and $\langle\delta|\beta\rangle$ is simply the overlap between these two orbitals.

3.6.2 Exchange V-matrix elements

With the consideration of non-uniqueness the exchange potential is expanded as

$$\begin{aligned}\hat{V}^{\mathrm{E}}_U = 2\left[(1-\theta)E - \hat{K}_0 - V_0 - \hat{K}_1 - V_1 - \hat{H}_2 + V_{01} + V_{02} + V_{12} - \tfrac{Z^2}{R}\right]\hat{P}_{01} \\ - 2\theta E\hat{I}^N_0, \quad (3.97)\end{aligned}$$

where θ is a scalar introduced to eliminate instability due to non-uniqueness. This issue will not be discussed in detail in this thesis, as the spheroidal formulation did not encounter it; for details regarding non-uniqueness in one- and two-electron targets see the articles of Bray & Stelbovics [7] and Fursa & Bray [8], respectively.

While spin is resolved trivially for the final projection term, those terms involving $\hat{P}_{01}$ must have their spins decoupled and recoupled in the correct order, resulting in

$$\begin{aligned}&\langle\chi'(\sigma_0)X^{(n')}_{S_{n'}}(\sigma_1,\sigma_2)|X^{(n)}_{S_n}(\sigma_0,\sigma_2)\chi(\sigma_1)\rangle = \\ &\qquad \delta_{S'S}(-1)^{S_{n'}+S_n+1}\sqrt{(2S_{n'}+1)(2S_n+1)}\begin{Bmatrix}\frac{1}{2} & S_n & S_{n'}\\ \frac{1}{2} & \frac{1}{2} & S\end{Bmatrix} \quad (3.98)\end{aligned}$$

using a Wigner 6-j symbol. With the spin overlaps resolved, we group like terms together and examine each grouping in turn. The one-electron terms evaluate to

$$\begin{aligned}&\langle k'\ell'm', \Phi_{n'}|[(1-\theta)E - \hat{K}_0 - \hat{K}_1 - \tfrac{Z_1Z_2}{R}]\hat{P}_{\mathbf{r}_0\mathbf{r}_1}|\Phi_n, k\ell m\rangle \\ &\quad = \delta_{\Pi'\Pi}\delta_{M'M}\epsilon\sum_{\gamma,\delta}\sum_{\alpha,\beta}C^{(f)}_{\gamma,\delta}C^{(i)}_{\alpha,\beta}\langle\delta|\beta\rangle\sum_{\ell_\gamma,\ell_\alpha}\langle k'\ell'm'|\alpha\ell_\alpha m_\alpha\rangle\langle\gamma\ell_\gamma m_\gamma|k\ell m\rangle \quad (3.99)\end{aligned}$$

with $\epsilon = (1-\theta)E - \frac{k'^2}{2} - \frac{k^2}{2} - \frac{Z_1 Z_2}{R}$.

The terms not involving electron 2 become

$$\langle k'\ell'm', \Phi_{n'}|(V_0 + V_1 - V_{01})\hat{P}_{\mathbf{r}_0\mathbf{r}_1}|\Phi_n, k\ell m\rangle = \delta_{\Pi'\Pi}\delta_{M'M} \sum_{\substack{\gamma,\delta,\\ \alpha,\beta}} C^{(n')}_{\gamma,\delta} C^{(n)}_{\alpha,\beta} \langle\delta|\beta\rangle \sum_{\ell_\gamma,\ell_\alpha}$$

$$\Bigg\{ \sum_{L_0} Z_{L_0} C^{\ell' \; L_0 \; \ell_\alpha}_{0 \; 0 \; 0} C^{\ell_\alpha \; L_0 \; \ell'}_{m_\alpha \; 0 \; m'} \langle\gamma\ell_\gamma m_\gamma|k\ell m\rangle \int_0^\infty u_{\ell'}(k'r_0) V_{L_0}(r_0, \tfrac{R}{2}) X^{(\alpha)}_{\ell_\alpha}(r_0)\mathrm{d}r_0$$

$$+ \sum_{L_1} Z_{L_1} C^{\ell_\gamma \; L_1 \; \ell}_{0 \; 0 \; 0} C^{\ell \; L_1 \; \ell_\gamma}_{m \; 0 \; m_\gamma} \langle k'\ell'm'|\alpha\ell_\alpha m_\alpha\rangle \int_0^\infty X^{(\gamma)}_{\ell_\gamma}(r_1) V_{L_1}(r_1, \tfrac{R}{2}) u_\ell(kr_1)\mathrm{d}r_1$$

$$- \sum_{L} (-1)^{m_L} C^{\ell' \; L \; \ell_\alpha}_{0 \; 0 \; 0} C^{\ell_\alpha \; L \; \ell'}_{m_\alpha \; -m_L \; m'} C^{\ell_\gamma \; L \; \ell}_{0 \; 0 \; 0} C^{\ell \; L \; \ell_\gamma}_{m \; m_L \; m_\gamma} \int_0^\infty u_{\ell'}(k'r) X^{(\alpha)}_{\ell_\alpha}(r) f^{(\gamma,n)}_{\ell_\gamma,L,\ell}(r)\mathrm{d}r \Bigg\}, \tag{3.100}$$

where $Z_{L_i} = z[Z_1 + (-1)^{L_i} Z_2]$ and the functions $V_{L_i}(r, \frac{R}{2})$ are defined in (3.31). The terms in each sum are non-zero when the corresponding index is restricted by lower bound, upper bound, and parity given in the Table 3.1. The final sum also requires $m_L = m_\alpha - m' = m_\gamma - m$.

The terms that involve electron 2 become

$$\langle k'\ell'm', \Phi_{n'}|(\hat{H}_2 - V_{02} - V_{12})\hat{P}_{\mathbf{r}_0\mathbf{r}_1}|\Phi_n, k\ell m\rangle = \delta_{\Pi'\Pi}\delta_{M'M} \sum_{\substack{\gamma,\delta,\\ \alpha,\beta}} C^{(n')}_{\gamma,\delta} C^{(n)}_{\alpha,\beta}$$

$$\times \sum_{\ell_\gamma,\ell_\alpha} \Bigg\{ \langle k'\ell'm'|\alpha\ell_\alpha m_\alpha\rangle \langle\gamma\ell_\gamma m_\gamma|k\ell m\rangle \langle\delta|\hat{H}_2|\beta\rangle$$

$$- \sum_{\ell_\delta,\ell_\beta} \sum_{L_0} (-1)^{m_0} C^{\ell' \; L_0 \; \ell_\alpha}_{0 \; 0 \; 0} C^{\ell_\alpha \; L_0 \; \ell'}_{m_\alpha \; -m_0 \; m'} C^{\ell_\delta \; L_0 \; \ell_\beta}_{0 \; 0 \; 0} C^{\ell_\beta \; L_0 \; \ell_\delta}_{m_\beta \; m_0 \; m_\delta} \langle\gamma\ell_\gamma m_\gamma|k\ell m\rangle$$

$$\times \int_0^\infty u_{\ell'}(k'r_0) X^{(\alpha)}_{\ell_\alpha}(r_0) f^{(\delta,\beta)}_{\ell_\delta,L_0,\ell_\beta}(r_0)\mathrm{d}r_0$$

$$- \sum_{\ell_\delta,\ell_\beta} \sum_{L_1} (-1)^{m_1} C^{\ell_\gamma \; L_1 \; \ell}_{0 \; 0 \; 0} C^{\ell \; L_1 \; \ell_\gamma}_{m \; -m_1 \; m_\gamma} C^{\ell_\delta \; L_1 \; \ell_\beta}_{0 \; 0 \; 0} C^{\ell_\beta \; L_1 \; \ell_\delta}_{m_\beta \; m_1 \; m_\delta} \langle k'\ell'm'|\alpha\ell_\alpha m_\alpha\rangle$$

$$\times \int_0^\infty X^{(\gamma)}_{\ell_\gamma}(r_1) u_\ell(kr_1) f^{(\delta,\beta)}_{\ell_\delta,L_1,\ell_\beta}(r_1)\mathrm{d}r_1 \Bigg\}, \tag{3.101}$$

where the Hamiltonian matrix elements $\langle\delta|\hat{H}_2|\beta\rangle$ are known analytically (and saved in memory) from the structure calculations (3.55). The conditions for non-

Table 3.1: Restrictions on sum indices that give non-zero terms in (3.100).

index	lower bound	upper bound	parity
L_0	$\lvert\ell' - \ell_\alpha\rvert$	$\ell' + \ell_\alpha$	$(-1)^{\ell'+\ell_\alpha}$
L_1	$\lvert\ell_\gamma - \ell\rvert$	$\ell_\gamma + \ell$	$(-1)^{\ell_\gamma+\ell}$
L	$\max(\lvert\ell' - \ell_\alpha\rvert, \lvert\ell_\gamma - \ell\rvert)$	$\min(\ell' + \ell_\alpha, \ell_\gamma + \ell)$	$(-1)^{\ell'+\ell_\alpha} = (-1)^{\ell_\gamma+\ell}$

Table 3.2: Restrictions on sum indices that give non-zero terms in (3.101).

index	lower bound	upper bound	parity
L_0	$\max(\lvert\ell' - \ell_\alpha\rvert, \lvert\ell_\delta - \ell_\beta\rvert)$	$\min(\ell' + \ell_\alpha, \ell_\delta + \ell_\beta)$	$(-1)^{\ell'+\ell_\alpha} = (-1)^{\ell_\delta+\ell_\beta}$
L_1	$\max(\lvert\ell_\gamma - \ell\rvert, \lvert\ell_\delta - \ell_\beta\rvert)$	$\min(\ell_\gamma + \ell, \ell_\delta + \ell_\beta)$	$(-1)^{\ell_\gamma+\ell} = (-1)^{\ell_\delta+\ell_\beta}$

zero terms are given in Table 3.2 along with $m_0 = m_\alpha - m' = m_\delta - m_\beta$ and $m_1 = m - m_\gamma = m_\delta - m_\beta$.

Finally, the projection operator term expands to

$$\begin{aligned}&\langle k'\ell'm', \Phi_{n'}|\hat{I}_0^N|\Phi_n, k\ell m\rangle \\ &\quad = \delta_{\Pi'\Pi}\delta_{M'M}\sum_{\gamma,\delta}\sum_{\alpha,\beta} C_{\gamma,\delta}^{(n')}C_{\alpha,\beta}^{(n)}\langle\gamma|\alpha\rangle\langle\delta|\beta\rangle\sum_{j=1}^{N_1}\langle k'\ell'm'|j\ell'm'\rangle\langle j\ell m|k\ell m\rangle, \quad (3.102)\end{aligned}$$

where j spans the complete set of N_1 one-electron orbitals $\varphi_j(\mathbf{r}_0) = \sum_{\ell_j}\langle\mathbf{r}_0|j\ell_j m_j\rangle$ but for each d$\mathbf{r}_0$ integral only one angular momentum component is selected due to the orthonormality of spherical harmonics.

3.6.3 Solving the Lippmann-Schwinger equations

When formulating the direct and exchange matrix elements it was found that all terms conserve three-electron (total) parity Π, angular momentum projection M, and spin S. Therefore we may compact the notation of the partial V-matrix elements to

$$V_{f,n}^{\Pi MS}(k_f, k) \equiv \langle k_f\ell_f m_f, \Phi_f^{\Pi_f M_f S_f} : \Pi MS|V_U|\Phi_n^{\Pi_n M_n S_n}, k\ell m : \Pi MS\rangle \quad (3.103)$$

and partial T-matrix elements to

$$T_{n,i}^{\Pi MS}(k, k_i) \equiv \langle k\ell m, \Phi_n^{\Pi_n M_n S_n} : \Pi MS|T_U|\Phi_i^{\Pi_i M_i S_i}, k_i\ell_i m_i : \Pi MS\rangle. \quad (3.104)$$

Substituting the partial wave expansions (3.87) into the Lippmann-Schwinger equation (2.62), using the orthonormality of spheroidal harmonics (C.4), and cancelling out common factors leads to the partial form of the Lippmann-Schwinger

equations

$$T_{f,i}^{\Pi MS}(k_f, k_i) = V_{f,i}^{\Pi MS}(k_f, k_i) + \sum_n \int_0^\infty V_{f,n}^{\Pi MS}(k_f, k) G_n^{(+)}(k) T_{n,i}^{\Pi MS}(k, k_i) \mathrm{d}k, \tag{3.105}$$

where the summation is also implicitly over projectile angular momentum ℓ subject to the total parity Π, i.e.

$$(-1)^{\ell_f + \Pi_f - \Pi_n} = (-1)^{\ell} = (-1)^{\ell_i + \Pi_i - \Pi_n} \tag{3.106}$$

and up to a given $\ell_{\max}$. The Green's function $G_n^{(+)}(k)$ is

$$G_n^{(+)}(k) = \frac{1}{E - \epsilon_n - \frac{k^2}{2} + \mathrm{i}0} \tag{3.107}$$

from Section 2.4.1, and $\mathrm{i}0 \equiv \lim_{\epsilon \to 0} \mathrm{i}\epsilon$. The size of the matrices (and hence the number of simultaneous equations to solve) in (3.105) is not excessive, because the partial waves characterised by (Π, M, S) do not interact with one another and can be solved independently. By compartmentalising the problem we may solve for additional partial waves without restarting the calculation, and saving the results after each partial wave is finished minimises data loss should the code crash. In practise we calculate all allowed parities $\Pi \in \{1, -1\}$ and spins $S \in \{\frac{1}{2}, \frac{3}{2}\}$ for each total angular momentum projection M up to a given $M_{\max}$. The number of partial waves required for convergence generally increases as total energy E increases.

The Green's function (3.107) and therefore Lippmann-Schwinger equation (3.105) has a singularity at $k = k_n$, where $k_n = \sqrt{2(E - \epsilon_n)}$ is the on-shell momentum. To avoid the singularity we first temporarily rewrite

$$f(k) = V_{f,n}^{\Pi MS}(k_f, k) T_{n,i}^{\Pi MS}(k, k_i) \tag{3.108}$$

and split the integral into three sections

$$\int_0^\infty \frac{2f(k)\mathrm{d}k}{k_n^2 - k^2 + \mathrm{i}0} \mathrm{d}k = \lim_{\epsilon \to 0^+} \left\{ \int_0^{k_n - \epsilon} \frac{2f(k)\mathrm{d}k}{k_n^2 - k^2} + \int_{\mathcal{C}} \frac{2f(k)\mathrm{d}k}{k_n^2 - k^2} + \int_{k_n + \epsilon}^\infty \frac{2f(k)\mathrm{d}k}{k_n^2 - k^2} \right\}, \tag{3.109}$$

where $\mathcal{C}$ is a small arc centered on k_n with radius ϵ in the lower half of the complex plane. Explicitly it represents $k = k_n + \epsilon \exp(\mathrm{i}\theta)$ with $\theta = [\pi, 2\pi]$, and hence $\mathrm{d}k = \mathrm{i}\epsilon \exp(\mathrm{i}\theta)\mathrm{d}\theta$ and $k_n^2 - k^2 \approx -2k_n\epsilon \exp(\mathrm{i}\theta)$ for small ϵ. Then the contour

segment of the integral becomes

$$\int_{\mathcal{C}} \frac{2f(k)\mathrm{d}k}{k_n^2 - k^2} = \int_{\pi}^{2\pi} 2f(k) \frac{\mathrm{i}\epsilon \exp(\mathrm{i}\theta)\mathrm{d}\theta}{-2k_n\epsilon \exp(\mathrm{i}\theta)} \tag{3.110}$$

and we have

$$\int_0^{\infty} \frac{2f(k)\mathrm{d}k}{k_n^2 - k^2 + \mathrm{i}0} = \mathcal{P}\int_0^{\infty} \frac{2f(k)\mathrm{d}k}{k_n^2 - k^2} - \mathrm{i}\pi k_n^{-1} f(k_n), \tag{3.111}$$

where $\mathcal{P}$ indicates a Cauchy principle value integral.

In terms of the partial matrix elements we now have

$$\begin{aligned} T_{f,i}^{\Pi MS}(k_f, k_i) = V_{f,i}^{\Pi MS}(k_f, k_i) + \sum_n \int_{k\neq k_n} V_{f,n}^{\Pi MS}(k_f, k) G_n(k) T_{n,i}^{\Pi MS}(k, k_i)\mathrm{d}k \\ - \sum_n \mathrm{i}\pi k_n^{-1} V_{f,n}^{\Pi MS}(k_f, k_n) T_{n,i}^{\Pi MS}(k_n, k_i) \end{aligned} \tag{3.112}$$

with

$$G_n(k) = \frac{1}{E - \epsilon_n - \frac{k^2}{2}}. \tag{3.113}$$

From this we can define the partial K-matrix elements as

$$K_{f,i}^{\Pi MS}(k_f, k_i) = \sum_n T_{f,n}^{\Pi MS}(k_n, k_i) \left[\delta_{ni}\delta_{\ell\ell_i} + \mathrm{i}\pi k_n^{-1} K_{n,i}^{\Pi MS}(k_n, k_i)\right] \tag{3.114}$$

and by modifying dummy indices, multiplying (3.112) through by the term in brackets in (3.114), summing and rearranging, we arrive at

$$K_{f,i}^{\Pi MS}(k_f, k_i) = V_{f,i}^{\Pi MS}(k_f, k_i) + \sum_{n,k} V_{f,n}^{\Pi MS}(k_f, k) G_n(k) \omega_n(k) K_{n,i}^{\Pi MS}(k, k_i), \tag{3.115}$$

where we have discretised the momentum integral into a k-grid with weights $\omega_n(k)$. The K-matrix formalism is useful because it allows us to solve (3.115) with real algebra. For brevity we rewrite this as

$$K_{fi} = V_{fi} + \sum_n V_{fn} G_n \omega_n K_{ni}. \tag{3.116}$$

In this form, i indicates the initial channels (i, ℓ_i, m_i, k_i) of the molecular state(s) Φ_i to be scattered from; f indicates the energetically accessible final channels (f, ℓ_f, m_f, k_f); and n indicates the off-shell points (n, ℓ, m, k) on the k-grid for all channels.

With the K-matrix formalism, the first step in obtaining the desired on-shell T-matrix elements T_{fi} is to rearrange (3.116) in order to calculate the half-shell K-matrix elements K_{nf} from the system of simultaneous equations

$$V_{n'f} = \sum_n [\delta_{n'n} - V_{n'n} G_n \omega_n] K_{nf}. \tag{3.117}$$

This requires the half-shell $V_{n'f}$ and off-shell $V_{n'n}$ V-matrix elements as described in Sections 3.6.1 and 3.6.2, and it is these calculations that take the majority of the computing time. The on-shell K-matrix $K_{f'f}$ is then obtained by changing the dummy variables of (3.116) and numerically integrating

$$K_{f'f} = V_{f'f} + \sum_n V_{f'n} G_n \omega_n K_{nf}, \tag{3.118}$$

which when used in a rearranged form of (3.114) gives the final set of simultaneous equations

$$K_{f'i} = \sum_f [\delta_{f'f} + \mathrm{i}\pi k_f^{-1} K_{f'f}] T_{fi}. \tag{3.119}$$

Lastly, these partial $T_{fi} \equiv \langle k_f \ell_f m_f, \Phi_f^{\Pi_f M_f S_f} : \Pi' M' S' | T_U | k_i \ell_i m_i, \Phi_i^{\Pi_i M_i S_i} : \Pi M S \rangle$ can be substituted into (3.87) to give the on-shell T-matrices converted to scattering amplitudes (2.73) for calculating cross sections (Section 2.4.4).

Chapter 4

Spheroidal MCCC

This chapter presents the concepts and formulae required to perform the Molecular Convergent Close-Coupling technique in prolate spheroidal coordinates instead of spherical coordinates. The overall methodology of Chapter 3 remains the same, but many of the mathematical details are different. We expand the projectile functions in spheroidal partial waves and construct the target states using a spheroidal form of the Laguerre basis, but the ultimate aim is to generate the same on-shell T-matrix elements that are required for scattering quantities.

To illustrate this, Figure 4.1 schematically represents the algorithm of molecular CCC for two-electron targets. The method has a general progression but diverges into spherical (left) and spheroidal (right) sections where the respective coordinate systems are necessary. The code represented by the nodes on the right was developed as part of this work.

As with the previous chapter, the focus is on electron scattering from two-electron diatomic molecules. Both homogeneous and heterogeneous diatomics are covered, but again note that the concept of parity does not hold in the latter case. Adapting the method to positron scattering or scattering from one- or many-electron diatomics is achievable in either coordinate system, but the advantages of spheroidal coordinates would be lost for multi-atomic molecules. In addition, scattering from charged targets has not been implemented in spheroidal coordinates, because there is currently no reliable method for generating the necessary generalised spheroidal waves.

Prolate spheroidal coordinates are used to take advantage of the physical configuration of diatomic molecules. The most common definition of the radial coordinate $\xi = \frac{r_1+r_2}{R}$ is singular at the combined nucleus limit ($R = 0$). Therefore

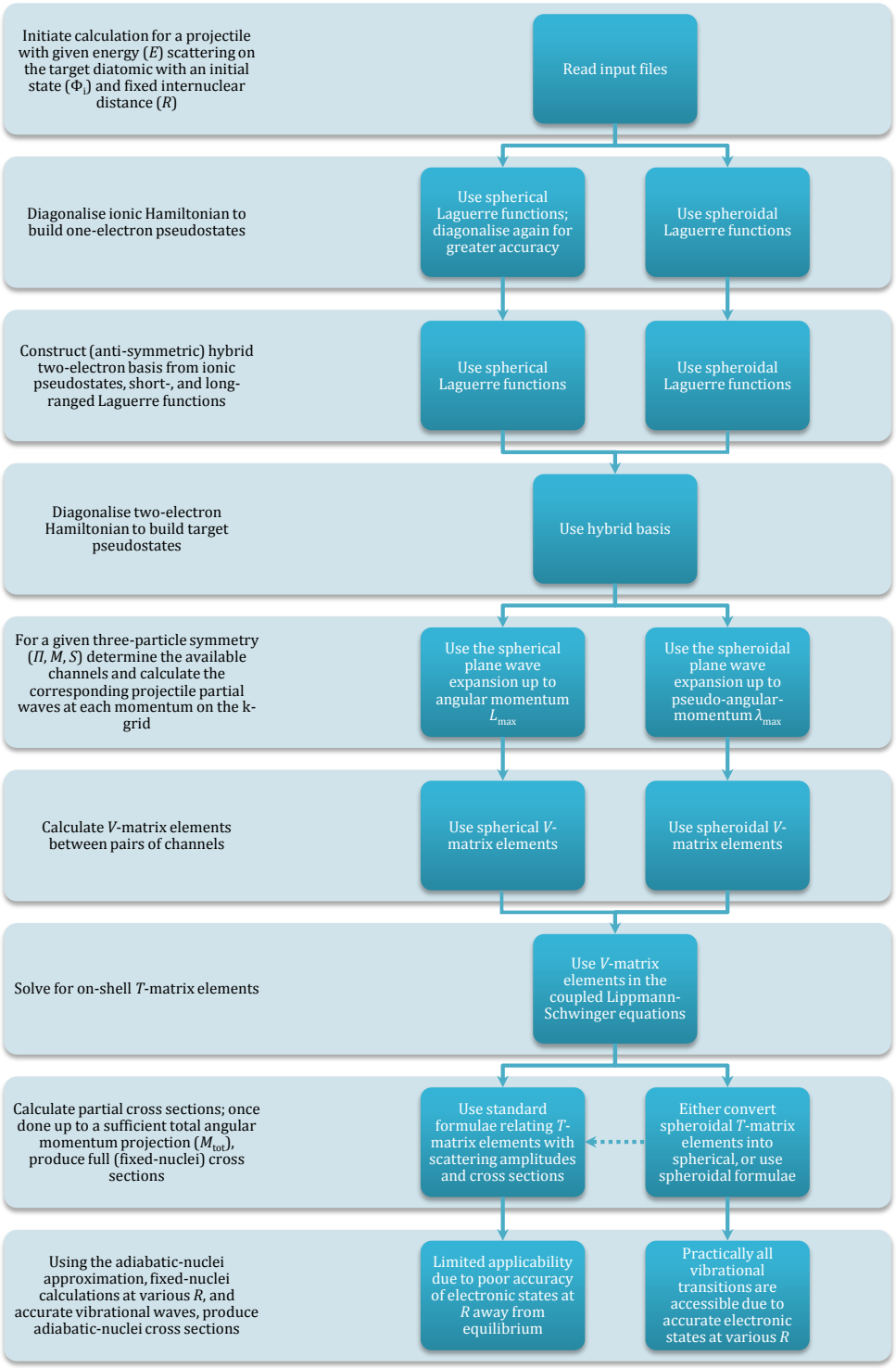

Figure 4.1: Flowchart of the algorithm for scattering on two-electron diatomic molecules. The nodes on the right represent sections of the code that were developed for the spheroidal formulation and linked in to the existing spherical implementation.

we define the modified spheroidal radial coordinate

$$\rho = \tfrac{R}{2}(\xi - 1) \in [0, \infty) \tag{4.1}$$

as an analogue of the spherical r; indeed $\lim_{R\to 0} \rho = (r_1 + r_2)/2 \approx r$. This results in more stable calculations for a wide range of R (necessary for the adiabatic-nuclei approximation), and allows us to check atomic results by letting $R \to 0$.

With the change of variable the volume element (A.19) becomes

$$\mathrm{d}V = \left[(\rho + \tfrac{R}{2})^2 - (\tfrac{R}{2}\eta)^2\right] \mathrm{d}\rho \mathrm{d}\eta \mathrm{d}\phi. \tag{4.2}$$

The one-electron Hamiltonian

$$\hat{H}_1 = \hat{K}_1 + V_1 \tag{4.3}$$

is made up of the spheroidal kinetic energy operator (2.19)

$$\hat{K}_1 = \frac{-\frac{1}{2}}{(\rho + \frac{R}{2})^2 - (\frac{R}{2}\eta)^2} \left\{ \frac{\partial}{\partial \rho}\left[\rho(\rho + R)\frac{\partial}{\partial \rho}\right] + \frac{\partial}{\partial \eta}\left[(1 - \eta^2)\frac{\partial}{\partial \eta}\right] + \left[\frac{R^2/4}{\rho(\rho + R)} + \frac{1}{1 - \eta^2}\right]\frac{\partial^2}{\partial \phi^2} \right\} \tag{4.4}$$

and the spheroidal diatomic potential (2.20)

$$V_1 = \frac{\frac{1}{2}}{(\rho + \frac{R}{2})^2 - (\frac{R}{2}\eta)^2} \left\{ Z_+(2\rho + R) - Z_- R\eta + U_\rho(\rho) + U_\eta(\eta) \right\}, \tag{4.5}$$

where $Z_\pm = z(Z_1 \pm Z_2)$.

In this chapter we define various spheroidal functions (Section 4.1) and give expressions for structure and scattering matrix elements (Section 4.2) while noting where they should be substituted into the spherical formalism of Chapter 3. Section 4.3 has comparisons of various physical data between spherical and spheroidal coordinates.

4.1 Definitions of spheroidal functions

The purpose of this section is to define various spheroidal functions as analogues to the spherical functions of Chapter 3. This will allow us to conceptually follow the presented method of solving the scattering equations while only changing mathematical details.

The first step is to determine the nature of the spheroidal free-particle solutions. Following on from above, we can repeat the separation procedure of (2.3.2) to obtain the separated radial and angular components of the solution

$$\psi(\rho,\eta,\phi) = \Xi(\rho)\Upsilon(\eta,\phi), \tag{4.6}$$

which abide the recast spheroidal radial equation (2.28)

$$\left\{\frac{\mathrm{d}}{\mathrm{d}\rho}\left[\rho(\rho+R)\frac{\mathrm{d}}{\mathrm{d}\rho}\right] - \frac{m^2R^2/4}{\rho(\rho+R)} - A + 2E\rho(\rho+R)\right\}\Xi(\rho) = 0 \tag{4.7}$$

in terms of the new coordinate ρ, and spheroidal angular equation (2.29)

$$\left\{\frac{\partial}{\partial\eta}\left[(1-\eta^2)\frac{\partial}{\partial\eta}\right] - \frac{m^2}{1-\eta^2} + A + \tfrac{1}{2}ER^2(1-\eta^2)\right\}\Upsilon(\eta,\phi) = 0, \tag{4.8}$$

where $\Upsilon(\eta,\phi) = \mathrm{H}(\eta)\exp(\mathrm{i}m\phi)$.

4.1.1 Spheroidal harmonics

The solutions to the angular equation (4.8) have the ϕ-dependence

$$\frac{\partial^2}{\partial\phi^2}\Upsilon(\eta,\phi) = -m^2\Upsilon(\eta,\phi) \tag{4.9}$$

and the equation itself resembles the Laplace equation in spheroidal coordinates (C.2); in fact they are equivalent when $R = 0$ and $A = \ell(\ell+1)$. To preserve this limiting behaviour we expand it in spherical harmonics

$$\Upsilon(\eta,\phi) = \sum_{\ell=1}^{\ell_N} D_\ell Y_\ell^m(\eta,\phi) \tag{4.10}$$

and substitute it into (4.8), where the recursion relation (C.17) gives us the expression for the coefficients

$$-\frac{\sqrt{(\ell-1)^2-m^2}\sqrt{\ell^2-m^2}}{\sqrt{2\ell-3}\sqrt{2\ell+1}}\frac{c^2D_{\ell-2}}{2\ell-1} + \left[A - \ell(\ell+1) + 2c^2\frac{\ell(\ell+1)+m^2-1}{(2\ell-1)(2\ell+3)}\right]D_\ell - \frac{\sqrt{(\ell+1)^2-m^2}\sqrt{(\ell+2)^2-m^2}}{\sqrt{2\ell+1}\sqrt{2\ell+5}}\frac{c^2D_{\ell+2}}{2\ell+3} = 0 \tag{4.11}$$

with $c^2 = \frac{1}{2}ER^2$. We can transform this into the $N \times N$ tri-diagonal eigenvalue problem

$$\begin{bmatrix} B_{\ell_1\ell_1} & B_{\ell_1\ell_2} & 0 & \cdots & 0 \\ B_{\ell_2\ell_1} & B_{\ell_2\ell_2} & B_{\ell_2\ell_3} & \ddots & \vdots \\ 0 & B_{\ell_3\ell_2} & B_{\ell_3\ell_3} & \ddots & 0 \\ \vdots & \ddots & \ddots & \ddots & B_{\ell_{N-1}\ell_N} \\ 0 & \cdots & 0 & B_{\ell_N\ell_{N-1}} & B_{\ell_N\ell_N} \end{bmatrix}\begin{bmatrix} D_{\ell_1} \\ D_{\ell_2} \\ D_{\ell_3} \\ \vdots \\ D_{\ell_N} \end{bmatrix} = A\begin{bmatrix} D_{\ell_1} \\ D_{\ell_2} \\ D_{\ell_3} \\ \vdots \\ D_{\ell_N} \end{bmatrix} \tag{4.12}$$

where

$$B_{\ell\ell'} = \begin{cases} \frac{c^2}{2\ell-1}\frac{\sqrt{(\ell-1)^2-m^2}\sqrt{\ell^2-m^2}}{\sqrt{2\ell-3}\sqrt{2\ell+1}} & \ell' = \ell-2 \\ \ell(\ell+1) - 2c^2\frac{\ell(\ell+1)+m^2-1}{(2\ell-1)(2\ell+3)} & \ell' = \ell \\ \frac{c^2}{2\ell+3}\frac{\sqrt{(\ell+1)^2-m^2}\sqrt{(\ell+2)^2-m^2}}{\sqrt{2\ell+1}\sqrt{2\ell+5}} & \ell' = \ell+2 \end{cases} \tag{4.13}$$

are the matrix elements. The angular equation (4.8) only enforces parity π and so the terms of (4.10) are restricted to $(-1)^\ell = \pi$ up to the maximum ℓ_N. For even parity we take $\ell_1 = 0$ and for odd parity we take $\ell_1 = 1$.

Note that this is a consequence of a spheroidal system that is symmetric in regards to its two centres. In the atomic limit $R = 0$, the matrix elements $B_{\ell'\ell} = \ell(\ell+1)\delta_{\ell'\ell}$ and expansion (4.10) collapse to the single spherical harmonic $Y_\ell^m(\eta, \phi)$. When the symmetry is broken — as with the potential from a heterogeneous diatomic (2.30) — the introduction of an odd-powered term of η into the angular equation results in coupled adjacent values of ℓ and no more conservation of parity.

Solving (4.12) yields ℓ_N sets of expansion coefficients as eigenvectors, with each set representing an angular function Υ_j for $j = 1, \ldots, \ell_N$. Each set is also characterised by the spheroidal pseudo-angular-momentum $\lambda = \ell_j$, along with the angular momentum projection m and pseudo-momentum $c = \frac{R}{2}k$. With this our definition of the spheroidal harmonics

$$\Upsilon_\lambda^m(\eta, \phi; c) = \sum_\ell D_{\lambda\ell}^m(c) Y_\ell^m(\eta, \phi), \tag{4.14}$$

where in this simple ($V = 0$) case, the sum has only even or only odd terms of ℓ depending on the parity $(-1)^\ell = (-1)^\lambda$. The corresponding separation constants $A_\lambda^m(c)$ can be obtained either from the eigenvalues of (4.12) or by rearranging (4.11) to

$$\begin{aligned} A_\lambda^m(c) = \ell(\ell+1) + c^2 \Bigg[& \frac{\sqrt{(\ell-1)^2-m^2}\sqrt{\ell^2-m^2}}{\sqrt{2\ell-3}(2\ell-1)\sqrt{2\ell+1}} \frac{D_{\lambda\ell-2}^m(c)}{D_{\lambda\ell}^m(c)} \\ & - 2\frac{\ell(\ell+1)+m^2-1}{(2\ell-1)(2\ell+3)} + \frac{\sqrt{(\ell+1)^2-m^2}\sqrt{(\ell+2)^2-m^2}}{\sqrt{2\ell+1}(2\ell+3)\sqrt{2\ell+5}} \frac{D_{\lambda\ell+2}^m(c)}{D_{\lambda\ell}^m(c)} \Bigg] \end{aligned} \tag{4.15}$$

and using the ratios of the expansion coefficients for any ℓ in the series. In the combined-nuclei limit the separation constant is simply $A_\lambda^m(0) = \lambda(\lambda+1)$, and hence the spheroidal angular equation (4.8) becomes the Laplace equation (C.2), which is the behaviour we desired at the beginning of this section.

As well as being orthonormal in m_λ due to (4.9), spheroidal harmonics of identical c are also orthonormal in λ, i.e.

$$\delta_{\lambda'\lambda}\delta_{m'_\lambda m_\lambda} = \iint \overline{\Upsilon}^{m'_\lambda}_{\lambda'}(\eta,\phi;c)\Upsilon^m_\lambda(\eta,\phi;c)\mathrm{d}\eta\mathrm{d}\phi \tag{4.16}$$

$$= \sum_\ell D^{m'_\lambda}_{\lambda'\ell}(c)D^m_{\lambda\ell}(c), \tag{4.17}$$

as they are solutions of the same eigenvalue problem (4.12). In general, spheroidal harmonics of dissimilar c are not orthogonal.

4.1.2 Spheroidal waves

In the original spheroidal coordinates (ξ,η,ϕ) it is clear that the radial (2.28) and angular (2.29) equations are the same except for the change in variable and a factor of -1. Following the work of Poole [83] we can use the theory of integral relations of solutions of differential equations to calculate the radial solutions as

$$\Xi^m_\lambda(\xi;c) = N\int_a^b \exp(\mathrm{i}c\xi\eta)(\xi^2-1)^{m/2}(1-\eta^2)^{m/2}H^m_\lambda(\eta;c)\mathrm{d}\eta, \tag{4.18}$$

where the normalisation constant N is to be determined, the integration limits a and b are subject to certain conditions [84], and

$$H^m_\lambda(\eta;c) = \exp(-\mathrm{i}m\phi)\Upsilon^m_\lambda(\eta,\phi;c)$$

$$= \sum_\ell d^m_{\lambda\ell}(c)P^m_\ell(\eta) \tag{4.19}$$

are simply the ϕ-independent angular solutions in terms of Legendre polynomials instead of spherical harmonics, with

$$d^m_{\lambda\ell}(c) = (-1)^m\sqrt{\frac{2\ell+1}{4\pi}\frac{(\ell-m)!}{(\ell+m)!}}D^m_{\lambda\ell}(c). \tag{4.20}$$

The properties of Legendre polynomials allow (4.19) to be rewritten as

$$H^m_\lambda(\eta;c) = \sum_\ell \frac{(\ell+m)!}{(\ell-m)!}\frac{d^m_{\lambda\ell}(c)}{2^\ell\ell!}(1-\eta^2)^{-m/2}\frac{\mathrm{d}^{\ell-m}}{\mathrm{d}\eta^{\ell-m}}(\eta^2-1)^\ell, \tag{4.21}$$

which can be substituted into (4.18) to give

$$\begin{aligned}\Xi_\lambda^m(\xi;c) &= N(\xi^2-1)^{m/2}\sum_\ell \frac{d_{\lambda\ell}^m(c)}{2^\ell \ell!}\frac{(\ell+m)!}{(\ell-m)!}\int_a^b \exp(\mathrm{i}c\xi\eta)\frac{\mathrm{d}^{\ell-m}}{\mathrm{d}\eta^{\ell-m}}(\eta^2-1)^\ell \mathrm{d}\eta \\ &= (-1)^m N(\xi^2-1)^{m/2}\sum_\ell \frac{d_{\lambda\ell}^m(c)}{2^\ell \ell!}\frac{(\ell+m)!}{(\ell-m)!}(\mathrm{i}c\xi)^{\ell-m}\int_a^b \exp(\mathrm{i}c\xi\eta)(1-\eta^2)^\ell \mathrm{d}\eta,\end{aligned} \tag{4.22}$$

where we have integrated by parts $\ell - m$ under the restrictions on a and b.

The integral in (4.22) is equivalent to integral forms of spherical Bessel and Hankel functions, depending on the limits taken [84]. In particular,

$$\int_{-1}^{1} \exp(\mathrm{i}c\xi\eta)(1-\eta^2)^\ell \mathrm{d}\eta \equiv \int_{-1}^{1} \cos(c\xi\eta)(1-\eta^2)^\ell \mathrm{d}\eta \equiv \frac{2^{\ell+1}\ell!}{(c\xi)^\ell} j_\ell(c\xi) \tag{4.23}$$

for the spherical Bessel function $j_\ell(c\xi)$. Unlike the Hankel functions, the spherical Bessels have appropriate asymptotic behaviour

$$j_\ell(c\xi) \xrightarrow[c\xi\to\infty]{} \frac{1}{c\xi}\sin\big(c\xi - \ell\tfrac{\pi}{2}\big) \tag{4.24}$$

for use in our radial functions (4.22), which gives

$$\Xi_\lambda^m(\xi;c) = \frac{2N}{(-\mathrm{i}c)^m}\left(\frac{\xi^2-1}{\xi^2}\right)^{m/2}\sum_\ell \mathrm{i}^\ell \frac{(\ell+m)!}{(\ell-m)!} d_{\lambda\ell}^m(c) j_\ell(c\xi). \tag{4.25}$$

Since this is the plane-wave case and $(-1)^\ell = (-1)^\lambda$ we can expand

$$\sin\big(c\xi - \ell\tfrac{\pi}{2}\big) \equiv (-1)^{\ell-\lambda}\sin\big(c\xi - \lambda\tfrac{\pi}{2}\big) \tag{4.26}$$

and choose our normalisation constant as

$$N = \frac{(-\mathrm{i}c)^m}{2\mathrm{i}^\lambda}\left[\sum_\ell \frac{(\ell+m)!}{(\ell-m)!} d_{\lambda\ell}^m(c)\right]^{-1}, \tag{4.27}$$

so that the asymptotic behaviour of the radial functions is

$$\Xi_\lambda^m(\xi;c) \xrightarrow[c\xi\to\infty]{} \frac{1}{c\xi}\sin\big(c\xi - \lambda\tfrac{\pi}{2}\big). \tag{4.28}$$

Putting all this together gives the expression

$$\Xi_\lambda^m(\xi;c) = \left[\sum_\ell \frac{(\ell+m)!}{(\ell-m)!} d_{\lambda\ell}^m(c)\right]^{-1}\left(\frac{\xi^2-1}{\xi^2}\right)^{m/2}\sum_\ell \mathrm{i}^{\ell-\lambda}\frac{(\ell+m)!}{(\ell-m)!} d_{\lambda\ell}^m(c) j_\ell(c\xi) \tag{4.29}$$

to calculate the radial function at any point. In practise it is more efficient to calculate one point along with its derivative

$$\frac{\mathrm{d}\Xi_\lambda^m(\xi;c)}{\mathrm{d}\xi} = \left[\sum_\ell \frac{(\ell+m)!}{(\ell-m)!} d_{\lambda\ell}^m(c)\right]^{-1} \left(\frac{\xi^2-1}{\xi^2}\right)^{m/2} \sum_\ell \mathrm{i}^{\ell-\lambda} \frac{(\ell+m)!}{(\ell-m)!} d_{\lambda\ell}^m(c) \frac{\mathrm{d}j_\ell(c\xi)}{\mathrm{d}\xi} + \frac{m}{\xi(\xi^2-1)} \Xi_\lambda^m(\xi;c) \quad (4.30)$$

and propagate it on a radial grid numerically. In our case we follow the procedure of Rankin & Thorson [85] by converting (4.29) to

$$X_\lambda^m(\rho;c) = \left(\frac{\rho+R}{\rho}\right)^{m/2} \Xi_\lambda^m(\rho;c) \quad (4.31)$$

and therefore (4.30) to

$$\frac{\mathrm{d}X_\lambda^m(\rho;c)}{\mathrm{d}\rho} = \frac{2}{R}\left(\frac{\rho+R}{\rho}\right)^{m/2} \frac{\mathrm{d}\Xi_\lambda^m(\xi;c)}{\mathrm{d}\xi} - \frac{R}{2}\frac{m}{\rho(\rho+R)} X_\lambda^m(\rho;c). \quad (4.32)$$

These equations describe solutions to the modified differential equation

$$\left\{\frac{\mathrm{d}^2}{\mathrm{d}\rho^2} + \frac{2\rho+R(m+1)}{\rho(\rho+R)}\frac{\mathrm{d}}{\mathrm{d}\rho} + 2E + \frac{A}{\rho(\rho+R)}\right\} X_\lambda^m(\rho;c) = 0 \quad (4.33)$$

and are propagated by the Adams-Moulton predictor-corrector algorithm.

4.1.3 Partial-wave expansions

With our definitions of the spheroidal radial (4.29) and angular (4.14) free-particle solutions we may expand the projectile waves

$$\left(\tfrac{k^2}{2} - \hat{K}\right)|\mathbf{k}\rangle = 0 \quad (4.34)$$

as

$$|\mathbf{k}\rangle = \sqrt{\frac{2}{\pi}} k^{-1} \sum_{\lambda=0}^{\infty} \sum_{m=-\lambda}^{\lambda} \mathrm{i}^\lambda \overline{\Upsilon}_\lambda^m(\hat{\mathbf{k}};c)|k\lambda m\rangle \quad (4.35)$$

in terms of the partial waves

$$\langle\boldsymbol{\rho}|k\lambda m\rangle = \Xi_\lambda^m(\rho;c)\Upsilon_\lambda^m(\eta,\phi;c), \quad (4.36)$$

noting that the radial functions are now in coordinate ρ. There is no analogue of the r^{-1} factor of the spherical waves (3.8), because unlike in spherical coordinates, the spheroidal integration weight (4.2) cannot be cancelled out easily. There is

still a k^{-1} factor in (4.35) coming from the spherical partial wave expansion (and only coordinate space is represented in spheroical coordinates). With this expansion the partial T-matrix elements

$$\begin{aligned}&\langle k_f\lambda_f m_f, \Phi_f|T_U|\Phi_i, k_i\lambda_i m_i\rangle \\ &\qquad\equiv \langle k_f\lambda_f m_f, \Phi_f^{\Pi_f M_f S_f} : \Pi' M' S'|T_U|\Phi_i^{\Pi_i M_i S_i}, k_i\lambda_i m_i : \Pi M S\rangle \quad (4.37)\end{aligned}$$

and partial V-matrix elements

$$\begin{aligned}&\langle k'\lambda' m', \Phi_{n'}|V_U|\Phi_n, k\lambda m\rangle \\ &\qquad\equiv \langle k'\lambda' m', \Phi_{n'}^{\Pi'_n M'_n S'_n} : \Pi' M' S'|V_U|\Phi_n^{\Pi_n M_n S_n}, k\lambda m : \Pi M S\rangle \quad (4.38)\end{aligned}$$

are defined as in the spherical case (3.88)–(3.89), with the exception that the spheroidal pseudo-angular-momentum λ takes the place of true angular momentum ℓ.

In the spheroidal expansion of the full T-matrix, we can also represent the spheroidal harmonics in terms of underlying spherical harmonics (4.14) to obtain

$$\begin{aligned}\langle \mathbf{k}_f\Phi_f|T|\Phi_i\mathbf{k}_i\rangle &= \frac{2}{\pi}(k_f k_i)^{-1}\sum_{\lambda_f,m_f}\sum_{\lambda_i,m_i}\mathrm{i}^{\lambda_i-\lambda_f}\langle k_f\lambda_f m_f, \Phi_f|T|\Phi_i, k_i\lambda_i m_i\rangle \\ &\qquad\times\sum_{\ell_f,\ell_i} D^{m_f}_{\lambda_f\ell_f}(c_f)D^{m_i}_{\lambda_i\ell_i}(c_i)Y^{m_f}_{\ell_f}(\hat{\mathbf{k}}_f)\overline{Y}^{m_i}_{\ell_i}(\hat{\mathbf{k}}_i) \\ &= \frac{2}{\pi}(k_f k_i)^{-1}\sum_{\ell_f,m_f}\sum_{\ell_i,m_i}\mathrm{i}^{\ell_i-\ell_f}Y^{m_f}_{\ell_f}(\hat{\mathbf{k}}_f)\overline{Y}^{m_i}_{\ell_i}(\hat{\mathbf{k}}_i)t^{(f,i)}_{\ell_f m_f,\ell_i m_i}(k_f,k_i),\end{aligned} \quad (4.39)$$

where the "converted" matrix elements

$$t^{(f,i)}_{\ell_f m_f,\ell_i m_i}(k_f,k_i) = \sum_{\lambda_f,\lambda_i}\mathrm{i}^{\lambda_i-\ell_i}\mathrm{i}^{\ell_f-\lambda_f}D^{m_f}_{\lambda_f\ell_f}(c_f)D^{m_i}_{\lambda_i\ell_i}(c_i)\langle k_f\lambda_f m_f, \Phi_f|T|\Phi_i, k_i\lambda_i m_i\rangle \quad (4.40)$$

are directly comparable to partial T-matrix elements calculated in the spherical approach (3.87). We can also compare partial V- and K-matrix elements in this manner.

4.1.4 Spheroidal structure

For adiabatic calculations we require pseudostates to be calculated at various values of R. In the limit $\rho \ll R$ the (undistorted) radial spheroidal equation

(4.7) reduces to

$$\left\{\frac{\mathrm{d}}{\mathrm{d}\rho}\left[\rho\frac{\mathrm{d}}{\mathrm{d}\rho}\right]-\frac{m^2}{4}\rho^{-1}-\frac{A_\lambda^m(c)}{R}+2E\rho\right\}\Xi_\lambda^m(\rho;c)=0. \tag{4.41}$$

In order to replicate this behaviour, our basis functions

$$\varphi_{k\ell m}(\rho,\eta,\phi;\lambda_m)=\Lambda_k^m(\rho;\lambda_m)Y_\ell^m(\eta,\phi) \tag{4.42}$$

follow the work of Hylleraas [86] and contain what we define as the Hylleraas functions

$$\Lambda_k^m(\rho;\lambda_m)=\sqrt{\lambda_m\frac{(k-1)!}{(k+m-1)!}}(\lambda_m\rho)^{m/2}\exp(-\lambda_m\rho/2)L_{k-1}^m(\lambda_m\rho), \tag{4.43}$$

where $L_{k-1}^m(\lambda_m\rho)$ are associated Laguerre functions, and the exponential fall-off factor λ_m fulfils the same purpose as in the spherical case.

Our spheroidal basis is analogous to the spherical basis functions (3.21) except in two ways. As with spheroidal waves, an r^{-1} analogue is omitted in the basis functions because the spheroidal integration weight (4.2) is not as easily cancelled as the spherical. In addition, we choose the spheroidal Laguerre functions to be of order m, so that the differential equation obeyed by the Hylleraas functions (B.8) is in line with (4.41). In theory, this makes the m-order spheroidal basis more suitable for $R>0$ molecular calculations than the $(2\ell+1)$-order spherical basis, which is more in line with $R=0$ limiting behaviour i.e. atoms.

We are not using spheroidal harmonics $\Upsilon_\lambda^m(\eta,\phi;c)$ in our spheroidal basis, because they are parameterised by pseudo-momentum $c=\frac{R}{2}k$ and we are yet to determine any pseudostate energies. Instead, we work with spherical harmonics $Y_\ell^m(\eta,\phi)$ in the spheroidal angular variable η, which allows us to reuse much of the angular-momentum algebra concepts (see Appendix D) that we have made use of in the spherical formalism. Note also that the domain of $\eta\in[-1,1]$ is the analogue of the spherical "inclination angle" convention of $\theta\in[0,\pi]$ – see the discussion in Appendix A.1 for more detail.

Individually, both the Hylleraas functions and spherical harmonics are orthonormal with respect to their coordinates, i.e.

$$\int_0^\infty\Lambda_{k'}^m(\rho;\lambda_m)\Lambda_k^m(\rho;\lambda_m)\mathrm{d}\rho=\delta_{k'k} \tag{4.44}$$

and

$$\int_0^{2\pi}\int_{-1}^{1}\overline{Y}_{\ell'}^{m'}(\eta,\phi)Y_\ell^m(\eta,\phi)\mathrm{d}\eta\mathrm{d}\phi=\delta_{\ell'\ell}\delta_{m'm}, \tag{4.45}$$

but due to the volume element (4.2) the combined basis functions (4.42) are not orthogonal in spheroidal space. Therefore the overlap matrix elements are not trivial, but are analytic as we will see in Section 4.2.1.

4.1.5 One-electron pseudostates

Following the spherical approach, we use the spheroidal basis (4.42) to diagonalise the one-electron diatomic Hamiltonian (4.3) using the CI method (Section 3.2) and matrix elements derived in Section 4.2.1. The resulting one-electron pseudostates have the CI form

$$\begin{aligned}\Phi_n(\rho,\eta,\phi) &= \sum_{\alpha} C_{\alpha}^{(n)} \varphi_{\alpha}(\rho,\eta,\phi;\lambda_m) \\ &= \sum_{k\ell} C_{k\ell m}^{(n)} \Lambda_k^m(\rho;\lambda_m) Y_\ell^m(\eta,\phi) \\ &= \sum_{\ell} X_\ell^{(n)}(\rho) Y_\ell^m(\eta,\phi), \end{aligned} \tag{4.46}$$

with the rearranged radial functions

$$X_\ell^{(n)}(\rho) = \sum_{k} C_{k\ell m}^{(n)} \Lambda_k^m(\rho;\lambda_m) \tag{4.47}$$

where one-electron spin has been suppressed.

The negative-energy (bound) pseudostates are solutions of the unseparated one-electron Hamiltonian (4.3)). Another solution (4.6) calculated by way of the separated equations (4.7) and (4.8) would be of the form

$$\begin{aligned}\psi(\rho,\eta,\phi;c) &= \Xi_\lambda^m(\rho;c)\Upsilon_\lambda^m(\eta,\phi;c) \\ &\equiv \sum_{\ell} D_{\lambda\ell}^m(c)\Xi_\lambda^m(\rho;c) Y_\ell^m(\eta,\phi), \end{aligned} \tag{4.48}$$

where the spheroidal pseudo-momentum is $c = \frac{R}{2}\sqrt{2\epsilon_n}$. By comparison with (4.46) we posit that

$$X_\ell^{(n)}(\rho) \approx D_{\lambda\ell}^m(c)\Xi_\lambda^m(\rho;c) \tag{4.49}$$

and hence

$$\frac{D_{\lambda\ell+2}^m(c)}{D_{\lambda\ell}^m(c)} = \frac{X_{\ell+2}^{(n)}(\rho)}{X_\ell^{(n)}(\rho)} \tag{4.50}$$

for every ℓ included in the spheroidal harmonic expansion. Indeed, for calculated H_2^+ pseudostates these ratios between are constant to a high degree of accuracy.

In order to rewrite the pseudostates in the "separated" form

$$\Phi_n(\rho,\eta,\phi) = \Xi_n(\rho)\Upsilon_n(\eta,\phi) \tag{4.51}$$

with angular functions

$$\Upsilon_n(\eta,\phi) = \sum_\ell D_\ell^{(n)} Y_\ell^m(\eta,\phi) \tag{4.52}$$

we set the first coefficient arbitrarily, get the remaining from the ratios

$$D_{\ell+2}^{(n)} = \frac{X_{\ell+2}^{(n)}(\rho)}{X_\ell^{(n)}(\rho)} D_\ell^{(n)} \tag{4.53}$$

and then renormalise such that the angular functions satisfy

$$\iint \overline{\Upsilon}_n(\eta,\phi)\Upsilon_n(\eta,\phi)\mathrm{d}\eta\mathrm{d}\phi = \sum_\ell \left(D_\ell^{(n)}\right)^2 = 1. \tag{4.54}$$

The radial function can then be determined through (4.49) for any ℓ – preferably the "dominant" term, i.e. the one with the largest absolute $D_\ell^{(n)}$.

As the pseudostates are equivalent to solutions from the separated spheroidal equations, we know that they are characterised by pseudo-angular-momentum λ and separation constant A. Usually (and especially for the values of R we are interested in) we can simply assume that λ belongs to the dominant ℓ term. In order to be sure we can follow (4.15) to determine the separation constants

$$\begin{aligned} A_\ell^{(n)}(c) = \ell(\ell+1) + c^2 \Bigg[& \frac{\sqrt{(\ell-1)^2-m^2}\sqrt{\ell^2-m^2}}{\sqrt{2\ell-3}(2\ell-1)\sqrt{2\ell+1}} \frac{X_{\ell-2}^{(n)}(\rho)}{X_\ell^{(n)}(\rho)} \\ & - 2\frac{\ell(\ell+1)+m^2-1}{(2\ell-1)(2\ell+3)} + \frac{\sqrt{(\ell+1)^2-m^2}\sqrt{(\ell+2)^2-m^2}}{\sqrt{2\ell+1}(2\ell+3)\sqrt{2\ell+5}} \frac{X_{\ell+2}^{(n)}(\rho)}{X_\ell^{(n)}(\rho)} \Bigg], \end{aligned} \tag{4.55}$$

which should be the same for each ℓ. We may then compare this to the set of separation constants $A_\lambda^m(c)$ calculated from the procedure in Section 4.1.1, or trace its behaviour as $R \to 0$ along with the fact that $A_\lambda^m(0) = \lambda(\lambda+1)$.

The notion of separated states and separation constants can be very useful for one-electron target structure. Separated states are more computationally efficient because they only have one radial function instead of one for each ℓ in its expansion. The separation constants are good for checking internal consistency (comparing multiple values from the same state) as well as accuracy (comparing against accurate values from Falloon *et al.* [87]). Unfortunately these concepts do not carry over to two-electron targets, and the only pseudostate we separate is the ground state of H_2 to replace the $1s$ Hylleraas basis function.

4.2 Matrix elements

Here we write the spheroidal matrix elements required for two-electron structure and scattering. Matrix elements for one-electron and multi-electron scattering may also be calculated by dropping terms containing the subscript 2 and including a core potential, respectively.

As in the spherical case (see Section 3.4.1) the two-electron pseudostates are constructed from antisymmetric configurations to diagonalise the Hamiltonian $\hat{H}_{12} = \hat{H}_1 + \hat{H}_2 + V_{12}$. They are represented by

$$\Phi_n^{\Pi_n M_n S_n}(x_1, x_2) = \sum_{\alpha,\beta} C_{\alpha,\beta}^{(n)} \varphi_\alpha^{\pi_\alpha m_\alpha}(\boldsymbol{\rho}_1) \varphi_\beta^{\pi_\beta m_\beta}(\boldsymbol{\rho}_2) X_n^{S_n}(\sigma_1, \sigma_2), \tag{4.56}$$

where $x \equiv (\rho, \eta, \phi, \sigma)$ denotes the combined space and spin coordinates and antisymmetry is enforced by the property (3.59) of the CI coefficients. Here the one-electron orbitals are of the general form

$$\varphi_\alpha^{\pi_\alpha m_\alpha}(\boldsymbol{\rho}; c_\alpha) = \Xi_\alpha(\rho; c_\alpha) \Upsilon_{\lambda_\alpha}^{m_\alpha}(\hat{\boldsymbol{\rho}}; c_\alpha) \tag{4.57}$$

and can either be spheroidal basis functions (4.42) with $c_\alpha = 0$, or one-electron pseudostates (4.51) with $c_\alpha = \frac{R}{2}\sqrt{2\epsilon_\alpha}$ related to pseudoenergy. The two-electron spin functions are identical to those in the spherical case (3.52).

As usual, symmetry under the parity operation only holds for homogeneous diatomics and should be ignored in the heterogeneous case.

4.2.1 One-electron

In general the overlap between two functions in spheroidal space requires numerical evaluation of the radial integral (see Appendix E for details). However, the properties of Hylleraas functions (Appendix B.2) allow us to calculate the overlap between two such functions

$$\langle k'\ell'm'|\boldsymbol{\rho}\rangle = \overline{\varphi}_{k'\ell'm'}(\rho, \eta, \phi) \qquad \text{and} \qquad \langle \boldsymbol{\rho}|k\ell m\rangle = \varphi_{k\ell m}(\rho, \eta, \phi) \tag{4.58}$$

analytically. Note that in this chapter we suppress the parametric dependence on the exponential fall-off factor λ_m. The overlap is evaluated as

$$\begin{aligned}\langle k'\ell'm'|k\ell m\rangle &= \iiint \Lambda_{k'}^{m'}(\rho)\overline{Y}_{\ell'}^{m'}(\eta,\phi)\Lambda_k^m(\rho)Y_\ell^m(\eta,\phi)\left[(\rho+\tfrac{R}{2})^2-(\tfrac{R}{2}\eta)^2\right]\mathrm{d}\rho\mathrm{d}\eta\mathrm{d}\phi \\ &= \delta_{\ell'\ell}\delta_{m'm}\int \Lambda_{k'}^{m'}(\rho)\Lambda_k^m(\rho)(\rho^2+R\rho+\tfrac{R^2}{6})\mathrm{d}\rho \\ &\quad -\delta_{k'k}\frac{R^2}{4}\iint \overline{Y}_{\ell'}^{m'}(\eta,\phi)Y_\ell^m(\eta,\phi)(\eta^2-\tfrac{1}{3})\mathrm{d}\eta\mathrm{d}\phi \\ &= \delta_{\ell'\ell}\delta_{m'm}b_{k'k}^m(\lambda_m)-\delta_{k'k}\tfrac{R^2}{6}C^{\ell'\ 2\ \ell}_{0\ 0\ 0}C^{\ell\ 2\ \ell'}_{m\ 0\ m'},\end{aligned} \tag{4.59}$$

where

$$b_{k'k}^m(\lambda_m)=\begin{cases}\lambda_m^{-2}\sqrt{k(k+m)(k+1)(k+m+1)} & k'=k+2\\ -\lambda_m^{-2}\sqrt{k(k+m)}(4k+2m+\lambda_m R) & k'=k+1\\ \lambda_m^{-2}(6k^2-6k+6km-3m+m^2+2)+\frac{2k-1+m}{\lambda_m}+\frac{R^2}{6} & k'=k\\ -\lambda_m^{-2}\sqrt{(k-1)(k-1+m)}(4k-4+2m+\lambda_m R) & k'=k-1\\ \lambda_m^{-2}\sqrt{(k-1)(k-1+m)(k-2)(k-2+m)} & k'=k-2\\ 0 & \text{otherwise}\end{cases} \tag{4.60}$$

using (B.9) and (C.13), and where $C^{\ell'\ \lambda\ \ell}_{m'\ \mu\ m}$ is a Clebsch-Gordan coefficient (Appendix D.1).

The one-electron Hamiltonian (4.3)–(4.5) acting on a basis function (4.42) is explicitly

$$\begin{aligned}\hat{H}_1\varphi_{k\ell m}(\vec{\rho}) &= \frac{-\frac{1}{2}}{(\rho+\frac{R}{2})^2-(\frac{R}{2}\eta)^2}\left\{\frac{\partial}{\partial\rho}\left[\rho(\rho+R)\frac{\partial}{\partial\rho}\right]+\frac{\partial}{\partial\eta}\left[(1-\eta^2)\frac{\partial}{\partial\eta}\right]\right. \\ &\quad \left.+\left[\frac{R^2/4}{\rho(\rho+R)}+\frac{1}{1-\eta^2}\right]\frac{\partial^2}{\partial\phi^2}-Z_+(2\rho+R)+Z_-R\eta\right\}\Lambda_k^m(\rho)Y_\ell^m(\eta,\phi),\end{aligned} \tag{4.61}$$

where $Z_\pm = z(Z_1 \pm Z_2)$

From the definition of the spherical harmonics we know that

$$\frac{\partial^2}{\partial\phi^2}Y_\ell^m(\eta,\phi) = -m^2Y_\ell^m(\eta,\phi), \tag{4.62}$$

and

$$\left\{\frac{\partial}{\partial\eta}\left[(1-\eta^2)\frac{\partial}{\partial\eta}\right]-\frac{m^2}{1-\eta^2}\right\}Y_\ell^m(\eta) = -\ell(\ell+1)Y_\ell^m(\eta) \tag{4.63}$$

which allows us to simplify (4.61) into

$$\hat{H}_1\varphi_{k\ell m}(\vec{\rho}) = \frac{-1/2}{(\rho+\frac{R}{2})^2-(\frac{R}{2}\eta)^2}\Bigg\{\frac{\mathrm{d}}{\mathrm{d}\rho}\left[\rho(\rho+R)\frac{\mathrm{d}}{\mathrm{d}\rho}\right] - \frac{m^2}{4}\frac{R^2}{\rho(\rho+R)} - \ell(\ell+1) - Z_+(2\rho+R) + Z_-R\eta\Bigg\}\Lambda_k^m(\rho)Y_\ell^m(\eta,\phi) \quad (4.64)$$

and limits the presence of angular variables to just the heterogeneous Z_- term. We may separate it out by rewriting the Hamiltonian matrix elements as

$$\begin{aligned}\langle k'\ell'm'|\hat{H}_1|k\ell m\rangle &= \iiint \overline{\varphi}_{k'\ell'm'}(\boldsymbol{\rho})\hat{H}_1\varphi_{k\ell m}(\boldsymbol{\rho})\left[(\rho+\tfrac{R}{2})^2-(\tfrac{R}{2}\eta)^2\right]\mathrm{d}\rho\mathrm{d}\eta\mathrm{d}\phi \\ &= \delta_{\ell'\ell}\delta_{m'm}\int_0^\infty \Lambda_{k'}^{m'}(\rho)\hat{H}_\ell^m\Lambda_k^m(\rho)\mathrm{d}\rho - \delta_{k'k}Z_-\tfrac{R}{2}\iint_{4\pi}\overline{Y}_{\ell'}^{m'}(\eta,\phi)\eta Y_\ell^m(\eta,\phi)\mathrm{d}\eta\mathrm{d}\phi,\end{aligned} \quad (4.65)$$

where the reduced operator

$$\hat{H}_\ell^m = -\frac{1}{2}\left\{\frac{\mathrm{d}}{\mathrm{d}\rho}\left[\rho(\rho+R)\frac{\mathrm{d}}{\mathrm{d}\rho}\right] - \frac{m^2}{4}\frac{R^2}{\rho(\rho+R)} - \ell(\ell+1) - Z_+(2\rho+R)\right\} \quad (4.66)$$

acts solely in the radial dimension, and the second (heterogeneous) term is resolved through Clebsch-Gordan coefficients.

To avoid numerical differentiation we may rewrite terms using the properties of the Hylleraas functions. With the differential equation (B.8) we can make the substitution

$$\frac{\mathrm{d}}{\mathrm{d}\rho}\left[\rho(\rho+R)\frac{\mathrm{d}}{\mathrm{d}\rho}\right] = \left[\rho\frac{\mathrm{d}}{\mathrm{d}\rho} + \frac{m^2}{4}\frac{\rho^2+2R\rho+R^2}{\rho(\rho+R)} + \frac{\lambda_m^2}{4}\rho(\rho+R) - \frac{\lambda_m}{2}(2k-1+m)(\rho+R)\right]\Lambda_k^m(\rho) \quad (4.67)$$

and from (B.10) we know that

$$\rho\frac{\mathrm{d}}{\mathrm{d}\rho}\Lambda_k^m(\rho) = -\frac{\lambda_m}{2}\rho\Lambda_k^m(\rho) + (k-1+\tfrac{m}{2})\Lambda_k^m(\rho) - \sqrt{(k-1)(k-1+m)}\Lambda_{k-1}^m(\rho). \quad (4.68)$$

Putting these together and collecting terms, the operator (4.66) acting on a Hylleraas function can be written as

$$\begin{aligned}\hat{H}_\ell^m\Lambda_k^m(\rho) = \Big\{&\tfrac{-\lambda_m^2}{8}\rho^2 + \tfrac{\lambda_m}{2}\big(k+\tfrac{m}{2}-\tfrac{\lambda_m R}{4}+\tfrac{2Z_+}{\lambda_m}\big)\rho - \tfrac{1}{2}\big[k-1+\tfrac{m}{2}+\tfrac{m^2}{4}-\ell(\ell+1)\big] \\ &+ \tfrac{\lambda_m}{2}\big(k-\tfrac{1}{2}+\tfrac{m}{2}+\tfrac{Z_+}{\lambda_m}\big)R - \tfrac{m^2}{8}\tfrac{R}{\rho+R}\Big\}\Lambda_k^m(\rho) + \tfrac{1}{2}\sqrt{(k-1)(k-1+m)}\Lambda_{k-1}^m(\rho).\end{aligned} \quad (4.69)$$

Substituting this into (4.65) gives us

$$\langle k'\ell'm'|\hat{H}_1|k\ell m\rangle = \delta_{\ell'\ell}\delta_{m'm}\left[h^{\ell m}_{k'k}(\lambda_m) - \frac{m^2R}{8}\int_0^\infty \Lambda^{m'}_{k'}(\rho)\Lambda^{m}_{k}(\rho)\frac{\mathrm{d}\rho}{\rho+R}\right] + Z_-\delta_{k'k}\tfrac{R}{2}C^{\ell'\ 1\ \ell}_{0\ 0\ 0}C^{\ell\ 1\ \ell'}_{m\ 0\ m'}, \quad (4.70)$$

where

$$h^{\ell m}_{k'k}(\lambda_m) = \begin{cases} -\frac{1}{8}\sqrt{k(k+m)(k+1)(k+1+m)} & k'=k+2 \\ \frac{1}{4}\sqrt{k(k+m)}\left(\frac{\lambda_m R}{2}+\frac{4Z_+}{\lambda_m}\right) & k'=k+1 \\ \frac{1}{4}\Big[k^2-k+km-\frac{m}{2}+1-2RZ_++2\ell(\ell+1) & \\ \qquad +(2k-1+m)\left(\frac{\lambda_m R}{2}-\frac{4Z_+}{\lambda_m}\right)\Big] & k'=k \\ \frac{1}{4}\sqrt{(k-1)(k-1+m)}\left(\frac{\lambda_m R}{2}+\frac{4Z_+}{\lambda_m}\right) & k'=k-1 \\ -\frac{1}{8}\sqrt{(k-1)(k-1+m)(k-2)(k+m-2)} & k'=k-2 \\ 0 & \text{otherwise} \end{cases} \quad (4.71)$$

is analytical. The integral term in (4.70) is the only part of the matrix elements calculated numerically due to the $(\rho+R)$ in the denominator. It weakly couples all functions with the same ℓ and the same $m \neq 0$, and it vanishes as $R \to 0$.

The second term in the overlap matrix elements (4.59) couples ℓ to $\ell\pm2$ due to the selection rules of the Clebsch-Gordan coefficients (D.2). The heterogeneous term in (4.70) couples adjacent ℓ but disappears for homogeneous diatomics, in which case parity is a good quantum number.

In the spherical approach, molecular parity arises from the $L = 0, 2, 4, \ldots$ sum of spherical functions (2.14) to represent the potential. In contrast, the spheroidal form (2.30) is made of two terms (effectively $L = 0$ for homogeneous and $L = 1$ for heterogeneous) and so parity ultimately results from the integration weight (4.2) of spheroidal space. This represents the essence of the spheroidal approach; it is well suited to the physics of diatomic molecules, but more mathematically complicated as a result.

4.2.2 Two-electron

The two-electron pseudostates (4.56) are built from a combination of one-electron pseudostates and spheroidal basis functions, and so from here on we use the

general form of the orbitals (4.57). To diagonalise $\hat{H}_{12}$ we require the electron-electron matrix elements

$$\langle\gamma\delta|V_{12}|\alpha\beta\rangle = \iint \overline{\varphi}_\gamma(\boldsymbol{\rho}_1)\overline{\varphi}_\delta(\boldsymbol{\rho}_2)V_{12}\varphi_\alpha(\boldsymbol{\rho}_1)\varphi_\beta(\boldsymbol{\rho}_2)\mathrm{d}\boldsymbol{\rho}_1\mathrm{d}\boldsymbol{\rho}_2 \tag{4.72}$$

for use in (3.55). We expand $V_{12} = |\mathbf{r}_1 - \mathbf{r}_2|^{-1}$ in prolate spheroidal coordinates using the von Neumann partial-wave expansion (B.11)

$$V_{12} = \frac{8\pi}{R}\sum_{L=0}^{\infty}\sum_{m_L=-L}^{L}\frac{(L-m_L)!}{(L+m_L)!}P_L^{m_L}(\xi_<)Q_L^{m_L}(\xi_>)Y_L^{-m_L}(\eta_1,\phi_1)Y_L^{m_L}(\eta_2,\phi_2), \tag{4.73}$$

where $\xi_< = \min\{\xi_1,\xi_2\}$, $\xi_> = \max\{\xi_1,\xi_2\}$, and $P_L^{m_L}(\xi)$ and $Q_L^{m_L}(\xi)$ are the regular and irregular Ferrers functions (Appendix B.3), a.k.a. Legendre polynomials in the domain $1 \leq \xi < \infty$. Using the properties of these functions we transform (4.73) into the more convenient form

$$V_{12} = 4\pi\sum_{L=0}^{\infty}\sum_{m_L=-L}^{L}\tilde{P}_L^{|m_L|}(\rho_<)\tilde{Q}_L^{|m_L|}(\rho_>)Y_L^{-m_L}(\eta_1,\phi_1)Y_L^{m_L}(\eta_2,\phi_2) \tag{4.74}$$

as given in (B.26), with

$$\tilde{P}_\lambda^\mu(\rho) = (\lambda-\mu)!\left(\frac{R}{2}\right)^\lambda P_\lambda^\mu(\xi) \tag{4.75}$$

$$\tilde{Q}_\lambda^\mu(\rho) = \frac{1}{(\lambda+\mu)!}\left(\frac{2}{R}\right)^{\lambda+1} Q_\lambda^\mu(\xi) \tag{4.76}$$

as per (B.21) and (B.22).

Separating the radial and angular terms gives us

$$\begin{aligned}\langle\gamma\delta|V_{12}|\alpha\beta\rangle = 4\pi\sum_{L,m_L}\int_{\boldsymbol{\rho}_1}\int_{\boldsymbol{\rho}_2}&\Xi_\gamma(\rho_1)\Xi_\alpha(\rho_1)\tilde{P}_L^{|m_L|}(\rho_<)\tilde{Q}_L^{|m_L|}(\rho_>)\Xi_\delta(\rho_2)\Xi_\beta(\rho_2)\\ \times\overline{\Upsilon}_{\lambda_\gamma}^{m_\gamma}(\eta_1,\phi_1;c_\gamma)&Y_L^{-m_L}(\eta_1,\phi_1)\Upsilon_{\lambda_\alpha}^{m_\alpha}(\eta_1,\phi_1;c_\alpha)\left[(\rho_1+\tfrac{R}{2})^2-(\tfrac{R}{2}\eta_1)^2\right]\mathrm{d}\rho_1\mathrm{d}\eta_1\mathrm{d}\phi_1\\ \times\overline{\Upsilon}_{\lambda_\delta}^{m_\delta}(\eta_2,\phi_2;c_\delta)&Y_L^{m_L}(\eta_2,\phi_2)\Upsilon_{\lambda_\beta}^{m_\beta}(\eta_2,\phi_2;c_\beta)\left[(\rho_2+\tfrac{R}{2})^2-(\tfrac{R}{2}\eta_2)^2\right]\mathrm{d}\rho_2\mathrm{d}\eta_2\mathrm{d}\phi_2.\end{aligned} \tag{4.77}$$

The angular integrals together with the integration weights will be evaluated as

$$\begin{aligned}\iint_{4\pi}\overline{\Upsilon}_{\lambda_\gamma}^{m_\gamma}(\eta_1,\phi_1;c_\gamma)Y_L^{-m_L}(\eta_1,\phi_1)\Upsilon_{\lambda_\alpha}^{m_\alpha}(\eta_1,\phi_1;c_\alpha)\left[(\rho_1+\tfrac{R}{2})^2-(\tfrac{R}{2}\eta_1)^2\right]\mathrm{d}\eta_1\mathrm{d}\phi_1&\\ = \sqrt{\tfrac{2L+1}{4\pi}}J_{L,-m_L}^{(\gamma,\alpha)}(\rho_1)&\end{aligned} \tag{4.78}$$

and

$$\iint_{4\pi} \overline{\Upsilon}^{m_\delta}_{\lambda_\delta}(\eta_2,\phi_2;c_\delta) Y_L^{m_L}(\eta_2,\phi_2) \Upsilon^{m_\beta}_{\lambda_\beta}(\eta_2,\phi_2;c_\beta) \left[(\rho_2+\tfrac{R}{2})^2 - (\tfrac{R}{2}\eta_2)^2\right] \mathrm{d}\eta_2 \mathrm{d}\phi_2$$
$$= \sqrt{\tfrac{2L+1}{4\pi}} J^{(\delta,\beta)}_{L,m_L}(\rho_2) \quad (4.79)$$

using spheroidal angular quadratics, as defined in Appendix E, as the integral of two spheroidal harmonics and a spherical harmonic in the presence of the spheroidal integration weight. The angular-momentum algebra contained inside these quadratics requires that they are zero unless the value of L conforms to

$$(-1)^{\lambda_\gamma+\lambda_\alpha} = (-1)^L = (-1)^{\lambda_\delta+\lambda_\beta} \quad (4.80)$$

and m_L is equal to

$$m_\alpha - m_\gamma = m_L = m_\delta - m_\beta, \quad (4.81)$$

which implies the conservation of parity $\pi_\gamma\pi_\delta = \pi_\alpha\pi_\beta$ (for homogeneous diatomics) and angular momentum projection $m_\gamma + m_\delta = m_\alpha + m_\beta$.

Following the spherical method for the same matrix element, we break up the two-dimensional radial integral by defining

$$f^{(\beta,\delta)}_{L,m_L}(\rho_1) = \tilde{Q}_L^{|m_L|}(\rho_1) \int_0^{\rho_1} \Xi_\delta(\rho_2)\Xi_\beta(\rho_2) J^{(\delta,\beta)}_{L,m_L}(\rho_2) \tilde{P}_L^{|m_L|}(\rho_2)\mathrm{d}\rho_2$$
$$+ \tilde{P}_L^{|m_L|}(\rho_1) \int_{\rho_1}^{\infty} \Xi_\delta(\rho_2)\Xi_\beta(\rho_2) J^{(\delta,\beta)}_{L,m_L}(\rho_2) \tilde{Q}_L^{|m_L|}(\rho_2)\mathrm{d}\rho_2 \quad (4.82)$$

and use this to arrive at the final form of the electron-electron matrix elements (4.77) as

$$\langle\gamma\delta|V_{12}|\alpha\beta\rangle = \delta_{\Pi'\Pi}\delta_{M'M} \sum_L (2L+1) \int_0^\infty \Xi_\gamma(\rho_1)\Xi_\alpha(\rho_1) J^{(\gamma,\alpha)}_{L,-m_L}(\rho_1) f^{(\delta,\beta)}_{L,m_L}(\rho_1)\mathrm{d}\rho_1. \quad (4.83)$$

There are a number of differences between this and the spherical implementation (3.67). Most importantly, the spheroidal radial and angular coordinates are linked through the integration weight, and hence the angular integration (in the form of a spheroidal angular quadratic) is taken inside the radial integral. The $R \to 0$ limit of the quadratics (E.7) is proportional to ρ^2, which is balanced by the lack of ρ^{-1} factor in the definition of spheroidal orbitals (4.57) compared to spherical orbitals (3.60). Finally, the presence of $(2L+1)$ in place of $(-1)^{m_L}$ comes through the Ferrers functions, which is easy to see in their atomic limit form (B.25).

4.2.3 Analytical Born

Calculating analytical Born matrix elements for convergence checks or analytical Born completion (Section 2.5.1) is as useful in the spheroidal formulation as it is in the spherical. The calculation technique remains much the same, but mathematical differences will be outlined here.

To calculate the two terms of the analytical Born matrix elements (2.90) and (2.91) in spheroidal coordinates, we use the plane wave expansion

$$\exp(\mathrm{i}\mathbf{q}\cdot\boldsymbol{\rho}) = 4\pi\sum_{\Lambda=0}^{\Lambda}\sum_{m_\Lambda=-\Lambda}\mathrm{i}^\Lambda\overline{\Upsilon}_\Lambda^{m_\Lambda}(\hat{\mathbf{q}};c)\Xi_\Lambda^{m_\Lambda}(\rho;c)\Upsilon_\Lambda^{m_\Lambda}(\hat{\boldsymbol{\rho}};c), \tag{4.84}$$

where $c=\frac{R}{2}q$ and the spheroidal functions are calculated as per 4.1.2.

For the first (elastic) term we write

$$\begin{aligned}\left\langle \mathbf{k}_f\left|\frac{Z_1}{|\mathbf{r}_0-\frac{1}{2}\mathbf{R}|}+\frac{Z_2}{|\mathbf{r}_0+\frac{1}{2}\mathbf{R}|}\right|\mathbf{k}_f\right\rangle \\ = \frac{4\pi}{2\pi^2q^2}\sum_{\Lambda=0}^{\infty}\mathrm{i}_\Lambda\overline{\Upsilon}_\Lambda^{m_\Lambda}(\hat{\mathbf{q}};c)[Z_1+(-1)^\Lambda Z_2]R_\Lambda^{m_\Lambda}(\tfrac{R}{2}q;c)\Upsilon_\Lambda^{m_\Lambda}(\hat{\mathbf{R}};c)\end{aligned} \tag{4.85}$$

and, because R lies along the z-axis, we use (C.5) to obtain

$$\Upsilon_\Lambda^{m_\Lambda}(\hat{\mathbf{R}};c)=\sum_\ell\sqrt{\tfrac{2\ell+1}{4\pi}}D^0_{\Lambda\ell}(c). \tag{4.86}$$

The second (general) term becomes

$$\begin{aligned}\langle\Phi_f|\exp(\mathrm{i}\mathbf{q}\cdot\boldsymbol{\rho}_1)|\Phi_i\rangle = 4\pi\delta_{S_fS_i}\sum_{\Lambda=0}^{\infty}\sum_{m_\Lambda=-\Lambda}^{\Lambda}\mathrm{i}^\Lambda\overline{\Upsilon}_\Lambda^{m_\Lambda}(\hat{\mathbf{q}};c)\sum_{\gamma,\delta}\sum_{\alpha,\beta}C^{(f)}_{\gamma,\delta}C^{(i)}_{\alpha,\beta}\langle\delta|\beta\rangle \\ \times\int_0^\infty\Xi_\gamma(\rho_1;c_\gamma)R_\Lambda^{m_\Lambda}(q\rho_1;c)\Xi_\alpha(\rho_1;c_\alpha)\sqrt{\tfrac{2\Lambda+1}{4\pi}}J^{(\gamma,\alpha)}_{\Lambda,m_\Lambda}(\rho_1)\mathrm{d}\rho_1,\end{aligned} \tag{4.87}$$

where $m_\Lambda = m_\gamma - m_\alpha = M_f - M_i$, and $(-1)^\Lambda = (-1)^{\lambda_\gamma+\lambda_\alpha}$ in the case of homogeneous diatomics. Following the spherical techniques, we define

$$\begin{aligned}\mathcal{F}^{(\mathrm{AB})}_{fi,\Lambda m_\Lambda}(\rho_1) = \delta_{S_fS_i}N_e\sqrt{2\Lambda+1}\sum_{\gamma,\delta}\sum_{\alpha,\beta}C^{(f)}_{\gamma,\delta}C^{(i)}_{\alpha,\beta}\langle\delta|\beta\rangle \\ \times\Xi_\gamma(\rho_1;c_\gamma)\Xi_\alpha(\rho_1;c_\alpha)J^{(\gamma,\alpha)}_{\Lambda,m_\Lambda}(\rho_1)\end{aligned} \tag{4.88}$$

and rewrite the general term as

$$\frac{N_e}{2\pi^2 q^2}\langle\Phi_f|\exp(\mathrm{i}\mathbf{q}\cdot\boldsymbol{\rho}_1)|\Phi_i\rangle = \frac{\sqrt{\pi}}{\pi^2 q^2}\sum_{\Lambda}\mathrm{i}^{\Lambda}\overline{\Upsilon}_{\Lambda}^{m_\Lambda}(\hat{\mathbf{q}};c)\int_0^{\infty}\mathcal{F}^{(\mathrm{AB})}_{fi,\Lambda m_\Lambda}(\rho_1)R_{\Lambda}^{m_\Lambda}(q\rho_1;c)\mathrm{d}\rho_1. \tag{4.89}$$

We may put (4.85) and (4.89) together to get an expression for calculating the Analytical Born matrix elements in spheroidal coordinates as

$$\mathcal{V}^{(\mathrm{AB})}_{fi}(\mathbf{q}) = \sum_{\Lambda}\mathrm{i}^{\Lambda}\mathcal{V}^{(\mathrm{AB})}_{fi,\Lambda m_\Lambda}(q)\overline{\Upsilon}_{\Lambda}^{m_\Lambda}(\hat{\mathbf{q}};c) \tag{4.90}$$

with the partial matrix elements

$$\mathcal{V}^{(\mathrm{AB})}_{fi,\Lambda m_\Lambda}(q) = \frac{z}{\pi^{3/2}q^2}\left[\delta_{fi}\mathcal{J}_\Lambda(q) - \int_0^{\infty}\mathcal{F}^{(\mathrm{AB})}_{fi,\Lambda m_\Lambda}(\rho_1)R_{\Lambda}^{m_\Lambda}(q\rho_1;c)\mathrm{d}\rho_1\right]. \tag{4.91}$$

Here we have defined

$$\mathcal{J}_\Lambda(q) = [Z_1 + (-1)^\Lambda Z_2]R_{\Lambda}^{m_\Lambda}(\tfrac{R}{2}q;c)\sum_{\ell}\sqrt{2\ell+1}D^{m_\Lambda}_{\Lambda\ell}(c). \tag{4.92}$$

By expanding the spheroidal harmonic in (4.90) and grouping like terms, we get

$$V^{(\mathrm{AB})}_{fi}(\mathbf{q}) = \sum_{L}\mathrm{i}^{L}V^{(\mathrm{AB})}_{fi,Lm_\Lambda}(q)\overline{Y}_{L}^{m_\Lambda}(\hat{\mathbf{q}}), \tag{4.93}$$

where the "converted" partial matrix elements

$$V^{(\mathrm{AB})}_{fi,Lm_\Lambda}(q) = \sum_{\Lambda}\mathrm{i}^{\Lambda-L}\mathcal{V}^{(\mathrm{AB})}_{fi,\Lambda m_\Lambda}(q)D^{m_\Lambda}_{\Lambda L}(c) \tag{4.94}$$

may be compared to their analogue obtained directly from the spherical code (3.77). To calculate the differential cross sections we can use these converted matrix elements in (2.95), or avoid taking this extra step as

$$\begin{aligned}\left.\frac{\mathrm{d}\sigma(\theta)}{\mathrm{d}\Omega}\right|_{i\to f} &= (2\pi)^4\frac{k_f}{k_i}\sum_{\Lambda',\Lambda}\mathrm{i}^{\Lambda-\Lambda'}\mathcal{V}^{\mathrm{AB}}_{fi,\Lambda',m_\Lambda}(Q)\mathcal{V}^{\mathrm{AB}}_{fi,\Lambda,m_\Lambda}(Q)\sum_{\ell}D^{m_\Lambda}_{\Lambda'\ell}(c)D^{m_\Lambda}_{\Lambda\ell}(c)\\ &= 4\pi^3\frac{k_f}{k_i}\sum_{\Lambda}|\mathcal{V}^{\mathrm{AB}}_{fi,\Lambda,m_\Lambda}(Q)|^2\end{aligned} \tag{4.95}$$

from (4.17).

4.2.4 Direct V-matrix

To calculate the (distorted) direct potential $V_U^{\rm D} = V_0 - U_0 - 2V_{01}$ involving spheroidal partial projectile functions (4.36) and molecular states (4.56) we separate it into two parts.

The projectile-nuclei component

$$V_0 - U_0 = \frac{1}{(\rho_0 + \frac{R}{2})^2 - (\frac{R}{2}\eta_0)^2} \left[Z_+(\rho_0 + \tfrac{R}{2}) - U_\rho(\rho_0) - Z_- \tfrac{R}{2}\eta_0 - U_\eta(\eta_0) \right] \quad (4.96)$$

has $Z_\pm = z(Z_1 \pm Z_2)$ and the short-ranged distorting potential components $U_\rho(\rho_0)$ and $U_\eta(\eta_0)$ subject to

$$U(\rho,\eta) = \frac{\frac{1}{2}}{(\rho + \frac{R}{2})^2 - (\frac{R}{2}\eta)^2} \left\{ U_\rho(\rho) + U_\eta(\eta) \right\} \quad (4.97)$$

included for generality; none was used for this work. Note that this distorting potential should also be short-ranged, and if the angular component contains any odd powers of η it will break the parity of a homogeneous diatomic.

The denominator of (4.96) cancels neatly with the spheroidal integration weight (4.2) and the integral evaluates to

$$\begin{aligned} &\langle k'\lambda' m', \Phi_{n'} | V_0 - U_0 | \Phi_n, k\lambda m \rangle \\ &\quad = \delta_{n'n} \int_0^\infty \Xi_{\lambda'}^{m'}(\rho_0; c') \Xi_\lambda^m(\rho_0; c) [V_{\lambda'\lambda}^m(\rho_0; c', c) - U(\rho_0) - \langle c'\lambda' m' | U_\eta | c\lambda m \rangle] \mathrm{d}\rho_0 \end{aligned} \quad (4.98)$$

with

$$\langle c'\lambda' m' | U_\eta | c\lambda m \rangle = \iint_{4\pi} \overline{\Upsilon}_{\lambda'}^{m'}(\eta_0, \phi_0; c') U_\eta(\eta_0) \Upsilon_\lambda^m(\eta_0, \phi_0; c) \mathrm{d}\eta_0 \mathrm{d}\phi_0 \quad (4.99)$$

as simple shorthand notation for an angular integral with the arbitrary distorting potential component. Here we define

$$\begin{aligned} V_{\lambda'\lambda}^m(\rho_0; c', c) &= Z_+(\rho_0 + \tfrac{R}{2}) \iint_{4\pi} \overline{\Upsilon}_{\lambda'}^{m'}(\eta_0, \phi_0; c') \Upsilon_\lambda^m(\eta_0, \phi_0; c) \mathrm{d}\eta_0 \mathrm{d}\phi_0 \\ &\quad - Z_- \tfrac{R}{2} \iint_{4\pi} \overline{\Upsilon}_{\lambda'}^{m'}(\eta_0, \phi_0; c') \sqrt{\tfrac{4\pi}{3}} Y_1^0(\eta_0, \phi_0) \Upsilon_\lambda^m(\eta_0, \phi_0; c) \mathrm{d}\eta_0 \mathrm{d}\phi_0 \\ &= \sum_{\ell',\ell} D_{\lambda'\ell'}^m(c') D_{\lambda\ell}^m(c) \left[Z_+(\rho_0 + \tfrac{R}{2}) \delta_{\ell'\ell} + Z_- \tfrac{R}{2} C_{0\,0\,0}^{\ell'\,1\,\ell} C_{m\,0\,m}^{\ell\,1\,\ell'} \right] \end{aligned} \quad (4.100)$$

as the spheroidal nuclear potential function. For homogeneous molecules ($Z_- = 0$) the equation is simplified to a one-dimensional sum and enforces $(-1)^{\lambda'} = (-1)^{\lambda}$. In the atomic limit where $c' = c = 0$, we have $D^{m_\lambda}_{\lambda\ell}(0) = \delta_{\lambda\ell}$ and therefore $V^m_{\lambda'\lambda}(\rho; 0, 0) = Z_+\delta_{\lambda'\lambda}\rho$, which is in line with the one-centre potential.

The projectile-molecular-electron component

$$V_{01} = 4\pi \sum_{L=0}^{\infty} \sum_{m_L=-L}^{L} \tilde{P}_L^{|m_L|}(\rho_<)\tilde{Q}_L^{|m_L|}(\rho_>)Y_L^{-m_L}(\eta_0, \phi_0)Y_L^{m_L}(\eta_1, \phi_1) \tag{4.101}$$

with the modified Ferrers functions $\tilde{P}_L^{m_L}(\rho)$ and $\tilde{Q}_L^{m_L}(\rho)$ of Appendix B.3 is solved similarly to the two-electron structure potential of Section 4.2.2. The matrix elements are evaluated as

$$\begin{aligned}\langle k'\lambda'm', \Phi_{n'}|V_{01}|\Phi_n, k\lambda m\rangle &= \delta_{\Pi'\Pi}\delta_{M'M} \sum_{\gamma,\delta} \sum_{\alpha,\beta} C^{(n')}_{\gamma,\delta} C^{(n)}_{\alpha,\beta} \langle\delta|\beta\rangle \\ &\times \sum_L (2L+1) \int_0^\infty \Xi^{m'}_{\lambda'}(\rho_0; c')\Xi^m_\lambda(\rho_0; c) J^{(k',k)}_{L,-m_L}(\rho_0) f^{(\gamma,\alpha)}_{Lm_L}(\rho_0) \mathrm{d}\rho_0 \end{aligned} \tag{4.102}$$

with $f^{(\gamma,\alpha)}_{L,m_L}(\rho_0)$ from (4.82) and the spheroidal angular quadratics $J^{(k',k)}_{L,-m_L}(\rho_0)$ of Appendix E.

4.2.5 Exchange V-matrix

The calculation of the exchange matrix elements is approached in much the same way as in spherical coordinates. First, the overlap of spin in the presence of the space exchange operator $\hat{P}_{01}$ is identical to (3.98). The one-electron terms are evaluated as

$$\begin{aligned}&\langle k'\lambda'm', \Phi_{n'}|[(1-\theta)E - \hat{K}_0 - \hat{K}_1 - \tfrac{Z_1Z_2}{R}]\hat{P}_{\boldsymbol{\rho}_0\boldsymbol{\rho}_1}|\Phi_n, k\lambda m\rangle \\ &= \delta_{\Pi'\Pi}\delta_{M'M}\epsilon \sum_{\gamma,\delta} \sum_{\alpha,\beta} C^{(n')}_{\gamma,\delta} C^{(n)}_{\alpha,\beta} \sum_{\ell_\gamma,\ell_\alpha} \langle\delta|\beta\rangle\langle k'\lambda'm'|\alpha\ell_\alpha m_\alpha\rangle\langle\gamma\ell_\gamma m_\gamma|k\lambda m\rangle \end{aligned} \tag{4.103}$$

with $\epsilon = (1-\theta)E - \frac{k'^2}{2} - \frac{k^2}{2} - \frac{Z_1 Z_2}{R}$. Terms not involving space 2 become

$$\langle k'\lambda'm', \Phi_{n'}|(V_0 + V_1 - V_{01})\hat{P}_{\boldsymbol{\rho}_0\boldsymbol{\rho}_1}|\Phi_n, k\lambda m\rangle = \delta_{\Pi'\Pi}\delta_{M'M}\sum_{\gamma,\delta}\sum_{\alpha,\beta} C^{(n')}_{\gamma,\delta}C^{(n)}_{\alpha,\beta}\langle\delta|\beta\rangle$$
$$\times\Bigg\{\langle\gamma\lambda_\gamma m_\gamma|k\lambda m\rangle\int_0^\infty \Xi^{m'}_{\lambda'}(\rho_0;c')\Xi_\alpha(\rho_0)V^{m'}_{\lambda'\lambda_\alpha}(\rho_0;c',c_\alpha)\mathrm{d}\rho_0$$
$$+\langle k'\lambda'm'|\alpha\lambda_\alpha m_\alpha\rangle\int_0^\infty \Xi_\gamma(\rho_1)\Xi^m_\lambda(\rho_1;c)V^m_{\lambda_\gamma\lambda}(\rho_1;c_\gamma,c)\mathrm{d}\rho_1 \qquad (4.104)$$
$$-\sum_L(2L+1)\int_0^\infty \Xi^{m'}_{\lambda'}(\rho_0;c')\Xi_\alpha(\rho_0)J^{(k',\alpha)}_{L,-m_L}(\rho_0)f^{(\gamma,n)}_{L,m_L}(\rho_0)\mathrm{d}\rho_0\Bigg\}$$

using (4.100). The terms involving electron 2 are calculated by

$$\langle k'\lambda'm', \Phi_{n'}|(\hat{H}_2 - V_{02} - V_{12})\hat{P}_{\boldsymbol{\rho}_0\boldsymbol{\rho}_1}|\Phi_n, k\lambda m\rangle = \delta_{\Pi'\Pi}\delta_{M'M}\sum_{\gamma,\delta}\sum_{\alpha,\beta} C^{(n')}_{\gamma,\delta}C^{(n)}_{\alpha,\beta}$$
$$\times\Bigg\{\langle\gamma\lambda_\gamma m_\gamma|k\lambda m\rangle\langle k'\lambda'm'|\alpha\lambda_\alpha m_\alpha\rangle\langle\delta|\hat{H}_2|\beta\rangle$$
$$-\langle\gamma\lambda_\gamma m_\gamma|k\lambda m\rangle\sum_L(2L+1)\int_0^\infty \Xi^{m'}_{\lambda'}(\rho_0;c')\Xi_\alpha(\rho_0)J^{(k',\alpha)}_{L,-m_L}(\rho_0)f^{(\delta,\beta)}_{Lm_L}(\rho_0)\mathrm{d}\rho_0 \quad ,$$
$$-\langle k'\lambda'm'|\alpha\lambda_\alpha m_\alpha\rangle\sum_L(2L+1)\int_0^\infty \Xi_\gamma(\rho_1)\Xi^m_\lambda(\rho_1;c)J^{(\gamma,k)}_{L,-m_L}(\rho_0)f^{(\delta,\beta)}_{Lm_L}(\rho_1)\mathrm{d}\rho_1\Bigg\} \qquad (4.105)$$

where the elements $\langle\delta|\hat{H}_2|\beta\rangle$ are calculated analytically in the structure code and stored. Finally, the projection operator term

$$\langle k'\lambda'm', \Phi_{n'}|\hat{I}_0^{N_1}|\Phi_n, k\lambda m\rangle$$
$$= \delta_{\Pi'\Pi}\delta_{M'M}\sum_{\gamma,\delta}\sum_{\alpha,\beta} C^{(n')}_{\gamma,\delta}C^{(n)}_{\alpha,\beta}\langle\gamma|\alpha\rangle\langle\delta|\beta\rangle\sum_{j=1}^{N_1}\langle k'\lambda'm'|j\lambda'm'\rangle\langle j\lambda m|k\lambda m\rangle \qquad (4.106)$$

is analogous to the spherical case. The $\theta \neq 0$ method for resolving non-uniqueness issues was not necessary for this work, but the terms were left in for posterity.

In all cases the exact limits on L are determined by the individual ℓ in the expansions (4.14) of relevant spheroidal harmonics. Its projection is given by $m_L = m_\alpha - m' = m_\gamma - m$ due to angular-momentum algebra inside the spheroidal angular quadratics. When taken together with $m_\delta = m_\beta$ gives us the conservation

$M' = M$. For homogeneous diatomics the spheroidal harmonics have parity, and similarly $(-1)^L = (-1)^{\lambda_\alpha+\lambda'} = (-1)^{\lambda_\gamma+\lambda}$ and $(-1)^{\lambda_\delta} = (-1)^{\lambda_\beta}$ result in the conservation $\Pi' = \Pi$.

4.3 Structure testing

This section contains various tests to probe the accuracy of the two-electron Born-Oppenheimer pseudostates constructed from our spheroidal CI basis (4.42), particularly for the ground state and low-lying excited states. Comparisons are made with equivalent calculations using the spherical basis (3.20) and with values from the literature. It is worth noting that the theories available in the literature are specifically designed for calculating these values and are therefore effectively exact. Our pseudostates, on the other hand, are to be used in scattering calculations and therefore built from square-integrable Laguerre functions to avoid infinities when integrated with projectile waves. As in all scattering calculations, an appropriate compromise between the accuracy of the target structure and the computational feasibility must be made. This section will investigate how close our pseudostates are to the "exact" results.

The following values are from a 251-state structure calculation using a hybrid basis. The bulk of it is Hylleraas-style orbitals (4.42)–(4.43) with $1 \le k \le 10-\ell$, $0 \le \ell \le 8$, $-\ell \le m \le \ell$, and the exponential fall-off factors set at $\lambda_m = 1.42$. To improve the accuracy of low-lying two-electron pseudostates we replace the $1s$ orbital ($k = 1, \ell = m = 0$) with the highly converged H_2^+ ion pseudostate calculated from a Hylleraas basis with $1 \le k \le 60$, $0 \le \ell \le 8$, $-\ell \le m \le \ell$, and $\lambda_m = 4.0$. In the same vein we replace the $2s$, $2p$, $3d$, and $4f$ orbitals with shorter-ranged basis functions. For these, exponential fall-off factors are tuned to minimise the ground state potential energy well through the R-dependent formulae

$$\lambda_0(R) = \begin{cases} 0.03R^2 - 0.32R + 2.8 & 0.0 \le R \le 4.0 \\ 2.0 & 4.0 < R \end{cases} \tag{4.107}$$

for $m = 0$ functions and

$$\lambda_m(R) = \begin{cases} 0.052R^2 - 0.52R + 3.8 & 0.0 \le R \le 5.0 \\ 2.6 & 5.0 < R \end{cases} \tag{4.108}$$

for $m > 0$ functions. We have found that these five orbitals are very important for representing the "inner" molecular electron at longer bond length R, and tuning

them results in an accurate potential energy well for the range of R we need to consider.

The spherical model compared to uses a similar "hybrid" basis that mainly consists of $1 \leq k \leq 17 - \ell$, $0 \leq \ell \leq 8$, and $\lambda_\ell = 2.8$ spherical Laguerre functions with the $1s$ and $2p$ orbitals replaced by those obtained from a large H_2^+ diagonalisation (using $1 \leq k \leq 60 - \ell$ instead). This model was not optimised for multiple values of the internuclear separation and encounters significant difficulties as R gets much larger than the H_2 bond length $R_0 = 1.4$.

4.3.1 Electronic energies

Table 4.1: Comparison of H_2 fixed-nuclei ($R = 1.4$) two-electron and ionisation energies between spherical and spheroidal formulations and accurate calculations.

	two-electron energy (Ha)			ionisation energy (eV)	
state	spherical	spheroidal	literature	spherical	spheroidal
$X\,^1\Sigma_g^+$	-1.166829	-1.170815	-1.174476 [88]	-16.26223	-16.34945
$b\,^3\Sigma_u^+$	-0.778716	-0.781984	-0.784244 [89]	-5.70114	-5.76882
$a\,^3\Sigma_g^+$	-0.711045	-0.711885	-0.713641 [89]	-3.85972	-3.86132
$c\,^3\Pi_u$	-0.704320	-0.704986	-0.706586 [89]	-3.67673	-3.67361
$B\,^1\Sigma_u^+$	-0.702905	-0.702453	-0.705779 [90]	-3.63821	-3.60469
E,$F\,^1\Sigma_g^+$	-0.688827	-0.689887	-0.692018 [91]	-3.25513	-3.26275
$C\,^1\Pi_u$	-0.686823	-0.686958	-0.688664 [92]	-3.20061	-3.18305

The Born-Oppenheimer fixed-nuclei two-electron energies for the seven lowest-lying pseudostates are presented in Table 4.1 along with comparisons to literature values. Scattering data from the ground state $X\,^1\Sigma_g^+$ are most common and valuable, so the accuracy of this state is the most important. The accuracy of the spherical method (0.65% error) is improved significantly by the spheroidal basis (0.31% error). The state next in energy $b\,^3\Sigma_u^+$ sees an even larger improvement (0.70% to 0.29%) but for the rest of states the spheroidal basis is only slightly better, or in the case of $B\,^1\Sigma_u^+$, marginally worse. For more highly excited states the molecular potential appears more spherical and the functions will become more spherical as a result, leading to comparable accuracy in results obtained between the two coordinate systems.

Figure 4.2 compares the potential wells of the $X\,^1\Sigma_g^+$ and $b\,^3\Sigma_u^+$ states for the spherical and spheroidal bases as well as the effectively exact curve from the literature. Not only are the spheroidal potential wells more accurate at the minimum

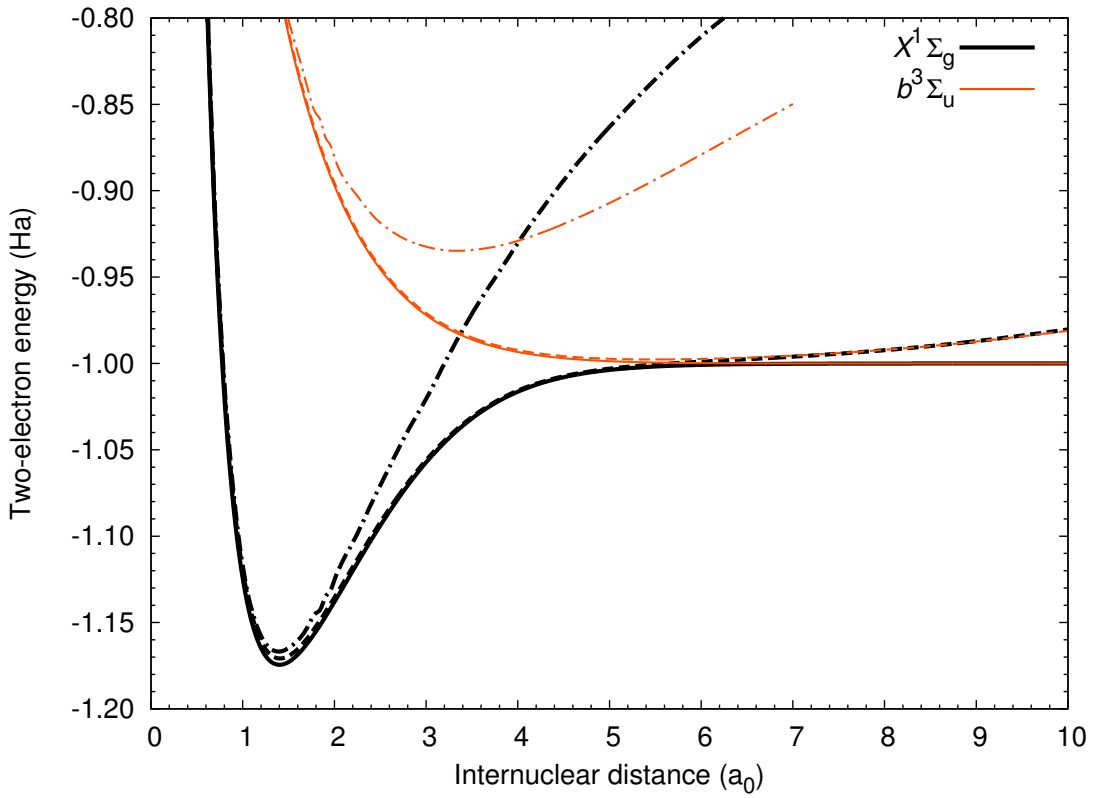

Figure 4.2: Potential-energy wells for the ground state and first excited state of H_2. The solid lines are accurate values of Wolniewicz *et al.* [88] and Staszewska & Wolniewicz [89], respectively; the dashed lines are from a $\lambda_m(R)$-optimised spheroidal basis; and the chained lines are from a spherical basis.

energy of $X\,^1\Sigma_g^+$, they are also much better at reproducing the exact curve up to $R = 6$ in contrast to $R = 2$ a.u for the spherical curves. The difference in $b\,^3\Sigma_u^+$ is even more pronounced, as the spherical basis can not replicate behaviour of the exact curve.

In Figure 4.3 we compare the potential wells of the next five states between the spheroidal basis and the literature. The spherical curves are omitted because as with the $b\,^3\Sigma_u^+$ state they fail to reproduce the correct behaviour of the energy wells at larger values of R. In particular the double-well of the E,$F\,^1\Sigma_g^+$state appears only in spheroidal calculations. This shows that such a level of accuracy is achievable from spheroidal scattering calculations across the range of bond lengths we are interested in.

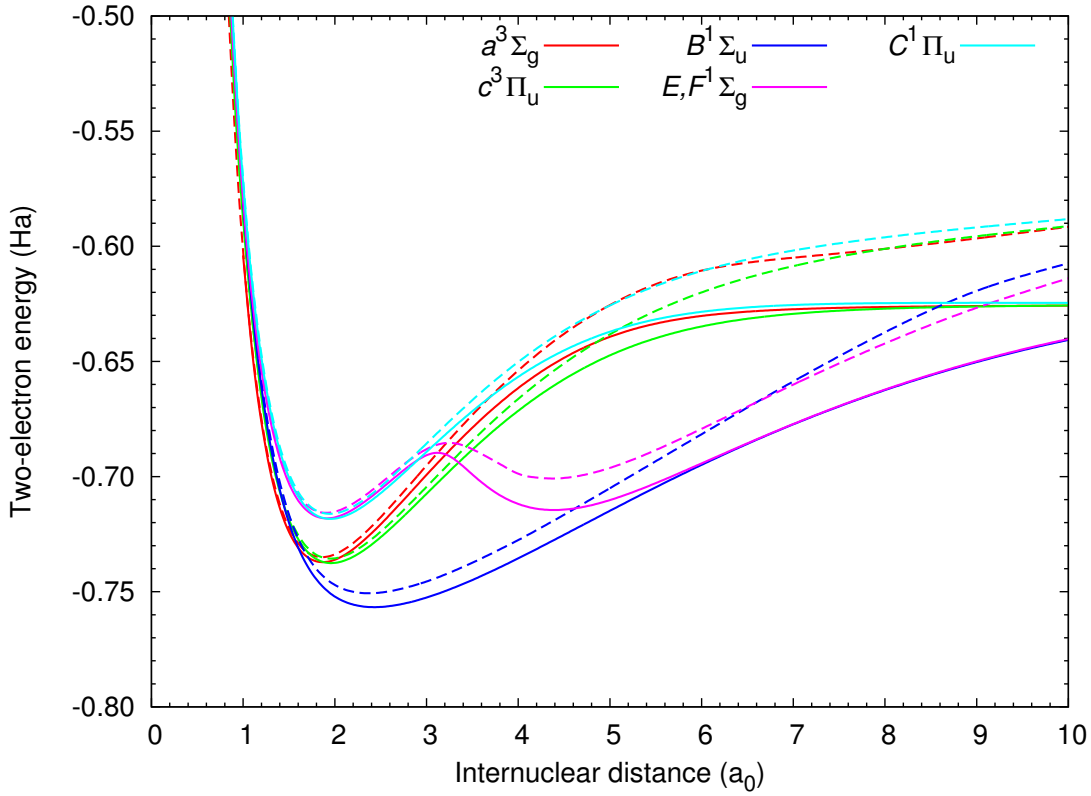

Figure 4.3: Potential energy wells for the next five excited states of H_2. The solid lines are accurate values from various calculations [89–91], and the dashed lines are from a $\lambda_m(R)$-optimised spheroidal basis.

4.3.2 Vibrational energies

Table 4.2 contains the energy levels and dissociation energies for the vibrational states of the ground state of H_2. For greatest accuracy, they were calculated by diagonalising the exact energy well of Wolniewicz *et al.* [88] with a large spherical Laguerre basis. The energies presented compare favourably to the accurate calculations of Fantz & Wnderlich [93] of which the differences are all below 0.02%.

In Figure 4.4 the fifteen H_2 vibrational waves are shown with the potential well they were calculated from. The waves are truncated to remove all but 95% of their magnitude to give a sense of the range of R required for adiabatic calculations. From the ground state potential wells of Figure 4.2 we can see that the spherical basis begins losing accuracy around $R = 2$, corresponding to the $v = 3$ vibrational state. In contrast, the spheroidal basis retains its accuracy to $R = 6$, which corresponds to the far extent of the $v = 14$ vibrational state.

Table 4.2: Vibrational energy levels and dissociation energies for the electronic ground state of H_2.

	state energy (Ha)		dissociation energy (eV)	
v	this work	literature [93]	this work	literature [93]
0	-1.16454	-1.16438	0.27083	0.27504
1	-1.14557	-1.14542	0.78694	0.79104
2	-1.12767	-1.12752	1.27390	1.27809
3	-1.11083	-1.11067	1.73230	1.73664
4	-1.09502	-1.09486	2.16248	2.16685
5	-1.08024	-1.08009	2.56453	2.56873
6	-1.06651	-1.06637	2.93827	2.94214
7	-1.05383	-1.05371	3.28339	3.28667
8	-1.04222	-1.04214	3.59931	3.60148
9	-1.03172	-1.03171	3.88484	3.88512
10	-1.02244	-1.02251	4.13752	4.13553
11	-1.01449	-1.01463	4.35379	4.34985
12	-1.00804	-1.00823	4.52941	4.52401
13	-1.00329	-1.00348	4.65849	4.65343
14	-1.00056	-1.00067	4.73288	4.72986
∞	-1.00000		4.74806 [94]	

The crosses are located at the state energy and R-space mean of each vibrational wave. For the $v = 0$ state the mean is $R = 1.448$ and this is where we perform fixed-nuclei scattering on the H_2 ground state. Spherical calculations at this value have been shown to be superior to the commonly-used energy well minimum at $R = 1.4$, as it better approximates the molecular nature of the target [79].

4.3.3 Oscillator strengths and polarisability

The optical oscillator strength f_{ji} between target states i and j is a concept from spectroscopy related to the intensity of transition lines in absorption and emission spectra. It can be derived as the ratio of the quantum mechanical transition strength to the equivalent classical picture of a collection of dipoles oscillating in the presence of an electromagnetic field [95].

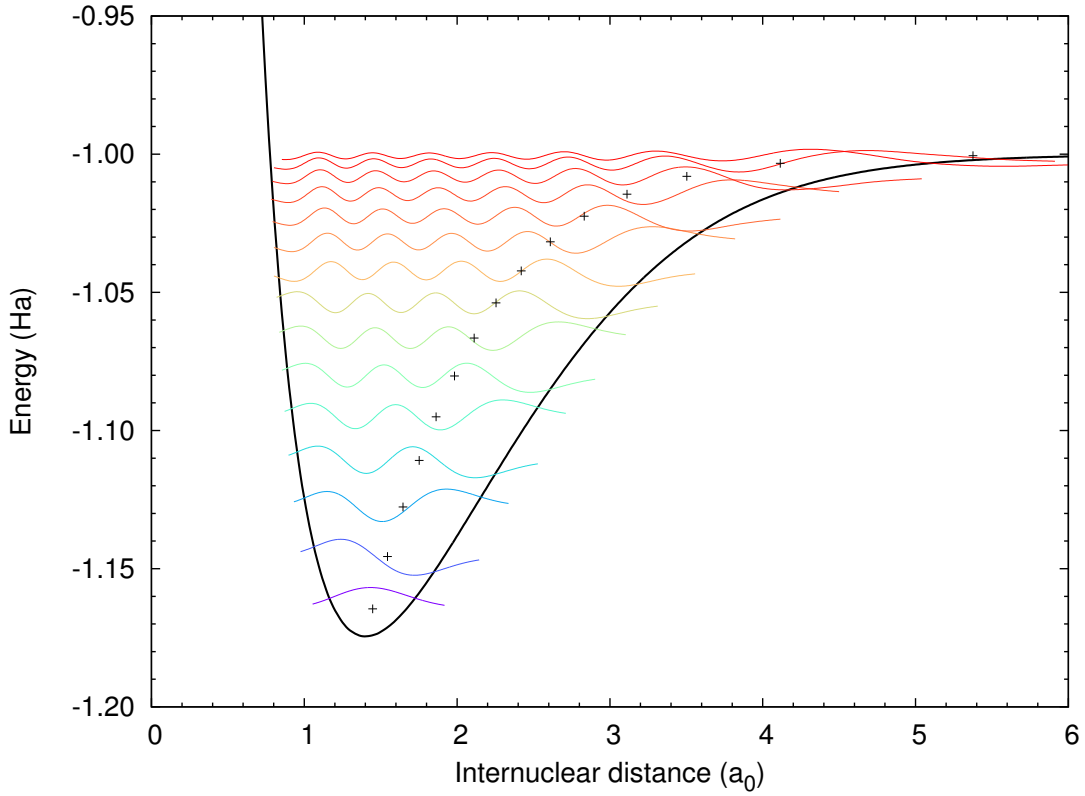

Figure 4.4: The vibrational wavefunctions $v = 0, \ldots, 14$ truncated in R-space to include only 95% of their magnitude. The crosses correspond to the state energy (vertically) and mean internuclear distance (horizontally) for each wave.

The general form of the oscillator strength is

$$f_{ji} = \frac{2m_\mathrm{e}}{\hbar}\Delta E\left|\langle j|\hat{\mu}|i\rangle\right|^2, \tag{4.109}$$

where m_e is the electron mass, ΔE is the energy gap between the two states, and $\hat{\mu}$ is the dipole operator. Comparison of the calculated oscillator strengths to those measured or from alternative theories is a good accuracy check for our pseudostate wavefunctions.

To calculate the oscillator strengths in our formalism we rewrite the dipole moment as an average of the coordinates, which introduces a factor of $\frac{1}{3}$ and results in the length gauge expression

$$f^{(\mathrm{l})}_{ji} = \tfrac{2g}{3}(\epsilon^{(N)}_j - \epsilon^{(N)}_i)\left|\langle j|\hat{\Omega}^{(\mathrm{l})}|i\rangle\right|^2 \tag{4.110}$$

in atomic units. Only certain components give non-zero matrix elements depending on the difference $\Delta_m = m_j - m_i$. When $\Delta_m = 0$ we write $\Omega^{(\mathrm{l})}_{\parallel} = z$ and call

this a *parallel transition*. When $\Delta_m = \pm 1$ we instead use $\Omega^{(\mathrm{l})}_{\perp} = \frac{1}{\sqrt{2}}(x \pm \mathrm{i}y)$ and call these *perpendicular transitions*. The orbital degeneracy factors are $g_{\parallel} = 1$ and $g_{\perp} = 2$.

We may also calculate the oscillator strengths in the velocity gauge [96]

$$f^{(\mathrm{v})}_{ji} = \tfrac{2g}{3}(\epsilon^{(N)}_j - \epsilon^{(N)}_i)^{-1} \left| \langle j | \hat{\Omega}^{(\mathrm{v})} | i \rangle \right|^2 \tag{4.111}$$

where $\Omega^{(\mathrm{v})}_{\parallel} = \frac{\partial}{\partial z}$ and $\Omega^{(\mathrm{v})}_{\perp} = \frac{1}{\sqrt{2}}(\frac{\partial}{\partial x} \pm \mathrm{i}\frac{\partial}{\partial y})$. Comparing the oscillator strengths between gauges can be used to check the consistency of the target wavefunctions. The derivatives of the velocity gauge result in integrals that are radially closer to the origin than those of the length gauge. The acceleration gauge tests the wavefunctions at even shorter radial distances, but the angular integrals are difficult to resolve.

In this section we will calculate and compare the oscillator strengths of H_2 between spherical and spheroidal coordinates, length and velocity gauges, and for both parallel and perpendicular transitions. For two-electron targets the matrix elements are between orbitals $\langle\gamma|$ and $|\alpha\rangle$ in the inner electron space. The pseudostates are represented by the CI expansion (3.57) of orbitals

$$\phi^{\pi_\alpha m_\alpha}_\alpha(r, \theta, \phi) = r^{-1} \sum_{\ell_\alpha} X^{(i)}_{\ell_\alpha}(r) Y^{m_\alpha}_{\ell_\alpha}(\cos\theta, \phi) \tag{4.112}$$

in spherical coordinates (3.60), or the equivalent expansion (4.56) of orbitals

$$\phi^{\pi_\alpha m_\alpha}_\alpha(\rho, \eta, \phi; c_\alpha) = \Xi_\alpha(\rho; c_\alpha) \Upsilon^{m_\alpha}_{\lambda_\alpha}(\eta, \phi; c_\alpha) \tag{4.113}$$

in spheroidal coordinates (4.57).

Length gauge

The length operator $\hat{\Omega}^{(l)}$ for parallel and perpendicular transitions and in various coordinate systems are given in the table:

Δ_m	cartesian	spherical	spheroidal (ξ, η, ϕ)	spheroidal (ρ, η, ϕ)
0	z	$r\cos\theta$	$\frac{R}{2}\xi\eta$	$(\rho + \frac{R}{2})\eta$
± 1	$\frac{x \pm \mathrm{i}y}{\sqrt{2}}$	$r\sin\theta\frac{\mathrm{e}^{\pm\mathrm{i}\phi}}{\sqrt{2}}$	$\frac{R}{2}\sqrt{\xi^2-1}\sqrt{1-\eta^2}\frac{\mathrm{e}^{\pm\mathrm{i}\phi}}{\sqrt{2}}$	$\sqrt{\rho(\rho+R)}\sqrt{1-\eta^2}\frac{\mathrm{e}^{\pm\mathrm{i}\phi}}{\sqrt{2}}$

where $\Delta_m = m_\gamma - m_\alpha$. In both spherical and spheroidal coordinates we may transform the angular components into spherical harmonics using (C.11) and (C.12).

In spherical coordinates the matrix element is calculated using

$$\langle\gamma|\hat{\Omega}^{(\mathrm{l})}|\alpha\rangle = (\Delta_m - \delta_{m_\gamma m_\alpha}) \sum_{\ell_\gamma,\ell_\alpha} C^{\ell_\gamma\, 1\, \ell_\alpha}_{0\ 0\ 0} C^{\ell_\alpha\ \ 1\ \ \ell_\gamma}_{m_\alpha\ \Delta_m\ m_\gamma} \int_0^\infty X^{(\gamma)}_{\ell_\gamma}(r) X^{(\alpha)}_{\ell_\alpha}(r) r \mathrm{d}r, \quad (4.114)$$

and in spheroidal coordinates we instead use

$$\langle\gamma|\hat{\Omega}^{(\mathrm{l})}|\alpha\rangle = \int_0^\infty \Xi_\gamma(\rho)\Xi_\alpha(\rho) \left[(\rho + \tfrac{R}{2}) J^{(\gamma,\alpha)}_{1,0}(\rho) \mp \sqrt{\rho(\rho+R)}\, J^{(\gamma,\alpha)}_{1,\pm1}(\rho)\right] \mathrm{d}\rho \quad (4.115)$$

with the spheroidal angular quadratics $J^{(\gamma,\alpha)}_{\ell,m}(\rho)$ as defined in Appendix E.

Velocity gauge

For an arbitrary coordinate system (u_1, u_2, u_3) the velocity operators are

$$\hat{\Omega}^{(\mathrm{v})}_{\parallel} = \frac{\partial u_1}{\partial z}\frac{\partial}{\partial u_1} + \frac{\partial u_2}{\partial z}\frac{\partial}{\partial u_2} + \frac{\partial u_3}{\partial z}\frac{\partial}{\partial u_3} \quad (4.116)$$

for parallel transitions and

$$\hat{\Omega}^{(\mathrm{v})}_{\perp} = \frac{1}{\sqrt{2}}\left(\frac{\partial u_1}{\partial x}\frac{\partial}{\partial u_1} + \frac{\partial u_2}{\partial x}\frac{\partial}{\partial u_2} + \frac{\partial u_3}{\partial x}\frac{\partial}{\partial u_3}\right) \pm \frac{\mathrm{i}}{\sqrt{2}}\left(\frac{\partial u_1}{\partial y}\frac{\partial}{\partial u_1} + \frac{\partial u_2}{\partial y}\frac{\partial}{\partial u_2} + \frac{\partial u_3}{\partial y}\frac{\partial}{\partial u_3}\right) \quad (4.117)$$

for perpendicular transitions. We may then use the coordinate derivatives given in the inverse Jacobian matrices (A.13) and (A.18) to determine the form of these operators.

In spherical coordinates (r, θ, ϕ) we have

$$\hat{\Omega}^{(\mathrm{v})}_{\parallel} = \cos\theta \frac{\partial}{\partial r} - \frac{\sin\theta}{r}\frac{\partial}{\partial\theta} \quad (4.118)$$

for parallel transitions and

$$\hat{\Omega}^{(\mathrm{v})}_{\perp} = \frac{\mathrm{e}^{\pm\mathrm{i}\phi}}{\sqrt{2}}\left[\sin\theta\frac{\partial}{\partial r} + \frac{\cos\theta}{r}\frac{\partial}{\partial\theta} \pm \frac{\mathrm{i}}{r\sin\theta}\frac{\partial}{\partial\phi}\right] \quad (4.119)$$

for perpendicular transitions. In the parallel case we can use the recurrence relations for $\cos\theta$ (C.16) and $\sin^2\theta\frac{\partial}{\partial\cos\theta}$ (C.19) and note their similarity. In fact, when acting on one spherical harmonic $|\ell_\alpha m_\alpha\rangle$ and integrated with another $\langle\ell_\gamma m_\gamma|$ we can write

$$\langle\ell_\gamma m_\gamma|\sin^2\theta\tfrac{\partial}{\partial\theta}|\ell_\alpha m_\alpha\rangle = y_{\ell_\gamma\ell_\alpha}\langle\ell_\gamma m_\gamma|\cos\theta|\ell_\alpha m_\alpha\rangle \quad (4.120)$$

where the quantity

$$y_{\ell_\gamma \ell_\alpha} = \begin{cases} -\ell_\alpha & \ell_\gamma - \ell_\alpha = 1 \\ \ell_\alpha + 1 & \ell_\gamma - \ell_\alpha = -1 \end{cases} \tag{4.121}$$

depends on the angular momenta of both harmonics. A similar but more involved process is used for the perpendicular operator and is presented in Appendix F.1, resulting in the expression

$$\langle \gamma | \Omega^{(\mathrm{v})} | \alpha \rangle = (\Delta_m - \delta_{m_\gamma m_\alpha}) \sum_{\ell_\gamma, \ell_\alpha} C^{\ell_j \, 1 \, \ell_i}_{0 \; 0 \; 0} C^{\ell_\alpha \quad 1 \quad \ell_\gamma}_{m_\alpha \; \Delta_m \; m_\gamma} \int_0^\infty X^{(\gamma)}_{\ell_\gamma}(r) \left[\frac{\mathrm{d}}{\mathrm{d}r} + \frac{y_{\ell_\gamma \ell_\alpha}}{r} \right] X^{(\alpha)}_{\ell_\alpha}(r) \mathrm{d}r \tag{4.122}$$

for the matrix element.

The spheroidal operators, in both the original (ξ, η, ϕ) and rescaled (ρ, η, ϕ) coordinates, are

$$\begin{aligned} \hat{\Omega}^{(\mathrm{v})}_{\parallel} &= \frac{2/R}{\xi^2 - \eta^2} \left[(\xi^2 - 1)\eta \frac{\partial}{\partial \xi} + \xi(1 - \eta^2) \frac{\partial}{\partial \eta} \right] \\ &= \frac{1}{(\rho + \frac{R}{2})^2 - (\frac{R}{2}\eta)^2} \left[\rho(\rho + R)\eta \frac{\partial}{\partial \rho} + (\rho + \tfrac{R}{2})(1 - \eta^2) \frac{\partial}{\partial \eta} \right] \end{aligned} \tag{4.123}$$

for parallel transitions and

$$\begin{aligned} \hat{\Omega}^{(\mathrm{v})}_{\perp} &= \frac{2}{R} \frac{\sqrt{\xi^2 - 1}\sqrt{1 - \eta^2}}{\xi^2 - \eta^2} \frac{\mathrm{e}^{\pm \mathrm{i}\phi}}{\sqrt{2}} \left[\left(\xi \frac{\partial}{\partial \xi} - \eta \frac{\partial}{\partial \eta} \right) \pm i \left(\frac{1}{\xi^2 - 1} + \frac{1}{1 - \eta^2} \right) \frac{\partial}{\partial \phi} \right] \\ &= \frac{\sqrt{\rho(\rho + R)}}{(\rho + \frac{R}{2})^2 - (\frac{R}{2}\eta)^2} \Bigg[(\rho + \tfrac{R}{2}) \sqrt{1 - \eta^2} \frac{\mathrm{e}^{\pm \mathrm{i}\phi}}{\sqrt{2}} \frac{\partial}{\partial \rho} \pm \frac{R^2}{4} \frac{\mathrm{i}}{\rho(\rho + R)} \sqrt{1 - \eta^2} \frac{\mathrm{e}^{\pm \mathrm{i}\phi}}{\sqrt{2}} \frac{\partial}{\partial \phi} \\ &\qquad - \left(\eta \sqrt{1 - \eta^2} \frac{\mathrm{e}^{\pm \mathrm{i}\phi}}{\sqrt{2}} \frac{\partial}{\partial \eta} \mp \frac{\mathrm{i}}{\sqrt{1 - \eta^2}} \frac{\mathrm{e}^{\pm \mathrm{i}\phi}}{\sqrt{2}} \frac{\partial}{\partial \phi} \right) \Bigg] \end{aligned} \tag{4.124}$$

for perpendicular transitions. The matrix elements are calculated as

$$\langle \gamma | \hat{\Omega}^{(\mathrm{v})}_{\parallel} | \alpha \rangle = \int_0^\infty \Xi_\gamma(\rho) \left[\rho(\rho + R) \frac{\mathrm{d}}{\mathrm{d}\rho} + y_{\ell_\gamma \ell_\alpha} (\rho + \tfrac{R}{2}) \right] \Xi_\alpha(\rho) j^{(\gamma, \alpha)}_{1,0} \mathrm{d}\rho \tag{4.125}$$

for parallel transitions, and

$$\begin{aligned} &\langle \gamma | \hat{\Omega}^{(\mathrm{v})}_{\perp} | \alpha \rangle \\ &\quad = \mp \int_0^\infty \Xi_\gamma(\rho) \sqrt{\rho(\rho + R)} \left[(\rho + \tfrac{R}{2}) \frac{\mathrm{d}}{\mathrm{d}\rho} - \frac{R^2}{4} \frac{|m|}{\rho(\rho + R)} + y_{\ell_\gamma \ell_\alpha} \right] \Xi_\alpha(\rho) j^{(\gamma, \alpha)}_{1, \pm 1} \mathrm{d}\rho \end{aligned} \tag{4.126}$$

for perpendicular transitions, and where $j_{\ell,m}^{(\gamma,\alpha)}$ are the spheroidal angular overlaps defined in Appendix E.

Results

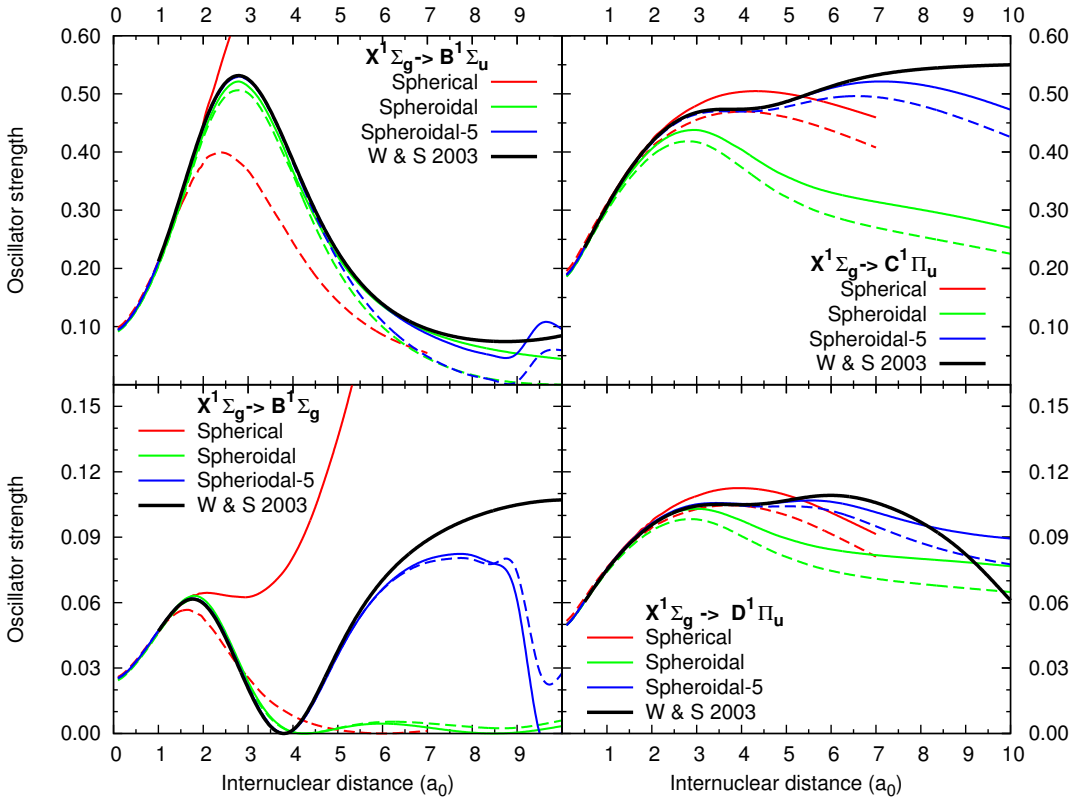

Figure 4.5: Oscillator strengths between the ground state and the first few singlet states for a variable bond length. The red and green lines are from 251-state structure calculations using spherical and spheroidal coordinates respectively. The blue line is a very large spheroidal structure calculation, and the black line is the "exact" curve from the literature. For the CCC curves, the solid lines have been calculated in the length gauge and the dashed lines in the velocity gauge.

Figure 4.5 contains oscillator strengths of the ground state and the first few energetically accessible singlet states in both length and velocity gauges and over a range of internuclear distances. As well as comparing between gauges it is also plotted against theoretical results obtained in the form of transition moments for $^1\Sigma_u$ states [97] and $^1\Pi_u$ states [92], modulated by state energies from the same group [88, 90, 92] through (4.110).

The green "spheroidal" curves come from a structure model that is very similar to that described at the beginning of this section and is what is used for scattering on the vibrational ground state of H_2. The blue "spheroidal-5" curves result from representing the inner electron by $n \leq 5$ orbitals with angular momentum $\ell \leq 3$ and serves as a demonstration of what a large spheroidal structure calculation can achieve.

The accuracy of the 251-state spheroidal calculation (green curve) for the $B\,^1\Sigma_u^+$ transition is very good, as it is for $B'\,^1\Sigma_u^+$ below $R = 4$. In contrast, the spherical results (red curve) for these states rapidly deviate from other results at $R = 2$. For the $^1\Pi_u$ states the spherical results look more accurate, but this seems fortuitous as they do not replicate the dip in the curve like the spheroidal results do. Regardless, the spheroidal basis seems to perform badly for these $M = \pm 1$ states beyond $R = 2$.

Agreement between length and velocity gauges is good for all transitions in the spheroidal model, but gets progressively worse as the internuclear separation increases. The length-gauge curves are closer to the literature result than those in the velocity-gauge, indicating that the accuracy of the wavefunctions is poorer near the origin for large internuclear separations. This is expected due to the relatively localised nature of the Laguerre bases we use. While we are able to tune somewhat through an R-dependent exponential fall-off factor, it is no substitute for the larger number of basis functions with high angular momentum required to model diffuse targets.

By increasing the number of orbitals to represent the inner electron, the large spheroidal structure model (blue curve) improves the accuracy of the oscillator strengths significantly. As the nuclei are separated, the wavefunctions of the molecular electrons become more diffuse and require more orbitals, and orbitals with larger angular momentum, to be constructed accurately. However, expanding the basis size means an increased discretisation of the continuum and overall larger calculation, so a balance must be struck. The current calculations have accurate oscillator strengths in the $R = 1 - 3$ region, which spans virtually all of the vibrational ground state as per Figure 4.4, and so we are confident in our results of scattering on the $X\,^1\Sigma_g^+(v = 0)$ state of H_2. The large model is accurate to at least $R = 6$ and would be suitable for all but one of the vibrational levels i.e. up to $X\,^1\Sigma_g^+(v = 13)$.

For triplet state oscillator strengths in Figure 4.6 the story is much the same. The results from the two gauges are generally in agreement, and especially so for the spheroidal basis with the exception of the $a\,^3\Sigma_g^+$–$e\,^3\Sigma_u^+$transition. The

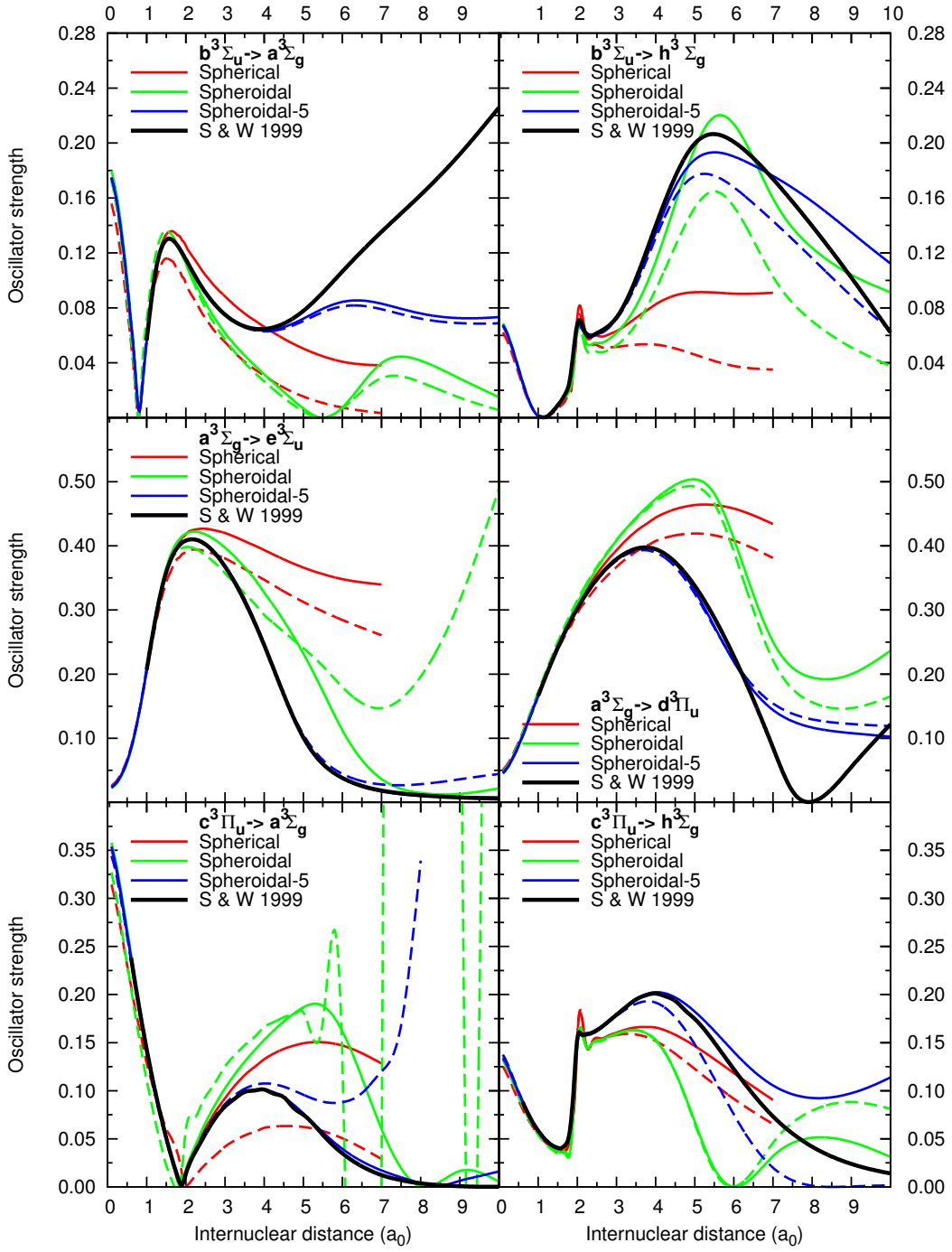

Figure 4.6: Oscillator strengths between various triplet states and for variable bond lengths. Of the coloured lines, the solid lines are calculated in the length gauge and dashed lines in the velocity gauge, while the solid black lines were obtained from the literature.

251-state calculation seems to be accurate to $R = 3$ and is better at reproducing the shape of the literature curves than the spherical results are. The large model again looks accurate to $R = 6$ but has major discrepancies between length velocity forms for the $c\,^3\Pi_u$-$a\,^3\Sigma_g^+$ and $c\,^3\Pi_u$-stateh transitions.

Some interesting features are well reproduced by the models. There appears to be a small structure near $R = 2$ for both transitions involving $h\,^3\Sigma_g^+$. The oscillator strength curve can also be observed to "bounce" off the x-axis in three locations: just below 1 a.u. for $b\,^3\Sigma_u^+$–$a\,^3\Sigma_g^+$, and around 2 a.u. and 7 a.u. for $c\,^3\Pi_u$-$a\,^3\Sigma_g^+$. These instances are caused by an intersection of potential energy curves for these states at these particular internuclear distances, resulting in a change of sign in the energy difference (4.110). We shall see that the close proximity of these states requires careful handling and a high level of precision in their construction.

Static polarisability

The static polarisability of a species is an important property that informs how it will respond to an applied electric field. For molecules the polarisability is anisotropic, and so the quantity in both the direction parallel to the molecular axis

$$\alpha_\parallel(R) = \sum_{j=1}^{N} \frac{3}{g_\parallel} \frac{f_{ji}^\parallel(R)}{[\epsilon_j^{(N)} - \epsilon_i^{(N)}]^2} \tag{4.127}$$

and perpendicular to it

$$\alpha_\perp(R) = \sum_{j=1}^{N} \frac{3}{2g_\perp} \frac{f_{ji}^\perp(R)}{[\epsilon_j^{(N)} - \epsilon_i^{(N)}]^2} \tag{4.128}$$

are important individually, but may also be combined

$$\alpha(R) = \tfrac{1}{3}\alpha_\parallel + \tfrac{2}{3}\alpha_\perp \tag{4.129}$$

as an average value.

The static polarisabilities of the three models are calculated with these formulae and presented in Figure 4.7 along with the accurate calculations of Kolos & Wolniewicz [98]. As with the oscillator strengths, the spherical results rapidly deteriorate beyond $R = 2$ and fail completely at $R = 4$. The 251-state spheroidal model is very accurate until $R = 3$, and the large spheroidal model has very good agreement with the literature for all internuclear distances.

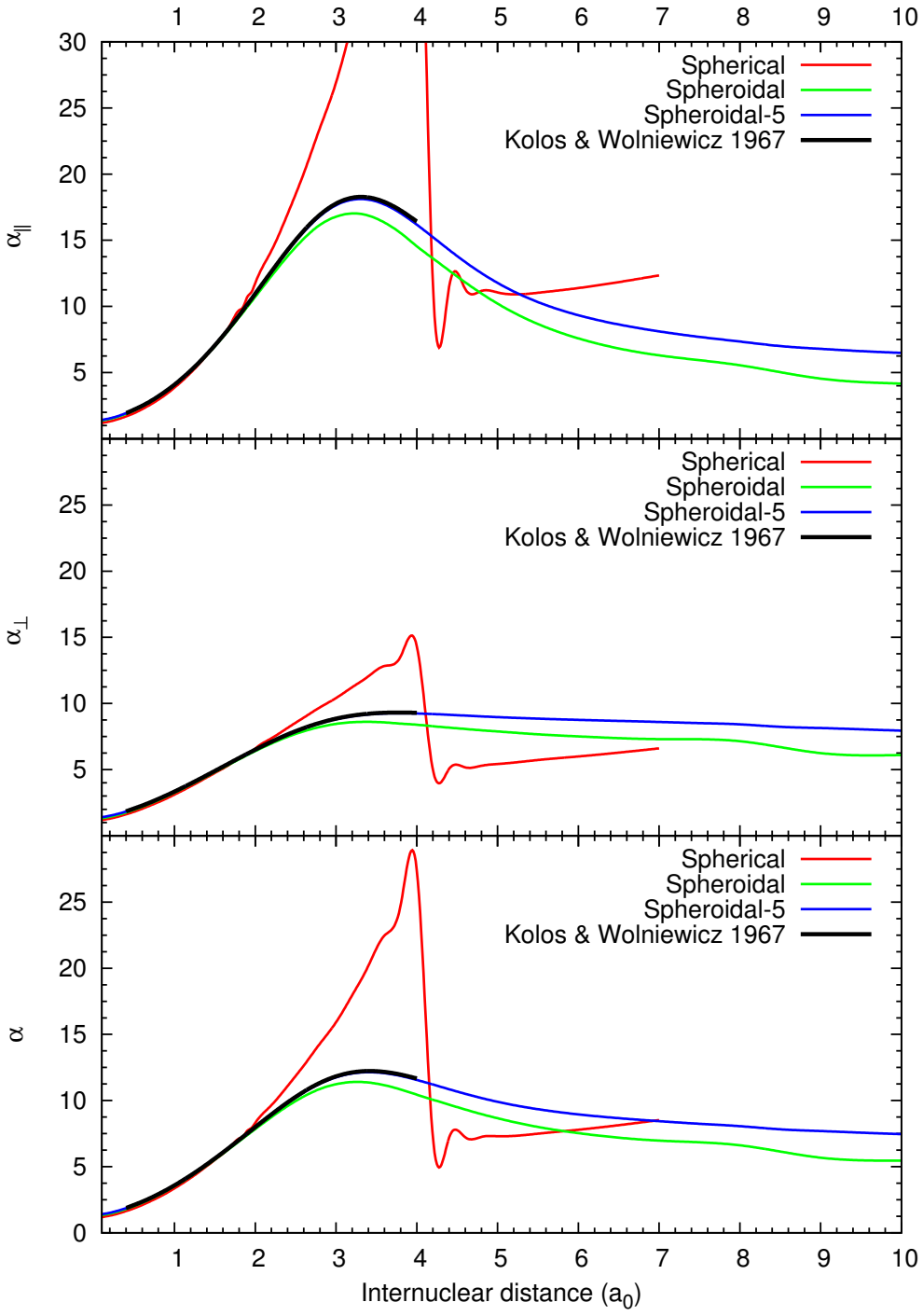

Figure 4.7: The parallel, perpendicular, and total polarisability calculated from the oscillator strengths and compared to the theoretical results of Kolos & Wolniewicz [98].

Chapter 5

Results

In this chapter we present various collision data for electron and positron scattering from the H_2 molecule. In Section 5.1 we analyse the degree of convergence achieved with our models of collision processes. Section 5.2 contains positron scattering cross sections. The following chapters have results for electron scattering from H_2 in the ground electronic and vibrational states, including electronic excitation (Section 5.3), ionisation (Section 5.4), total (Section 5.5), elastic differential (Section 5.6), and vibrational excitation (Section 5.7) cross sections. In Section 5.8 we present results for scattering from the metastable $c\,^3\Pi_u$ state, and in Section 5.9 we discuss further applications that have already built upon this work.

5.1 Structure models and convergence testing

A major feature of the convergent close-coupling method is the notion that as we increase the sizes of target state and projectile function expansions, we approach a complete representation of the problem and hence the true solution. In most cases we do not need to include all states or terms, but rather just enough that the calculations have converged to the desired level of precision. For the following convergence study we examine the elastic cross section over 1–10 eV. This particular energy range is chosen as the broad resonance centred at 3 eV makes the cross section slow to converge.

Figure 5.1 shows convergence studies in two dimensions: the top panel for the number of close-coupling states included in the Lippmann-Schwinger equation (2.62), and the bottom panel for the maximum pseudo-angular momentum of the spheroidal partial-wave expansions (4.35) of matrix elements. Here the notation

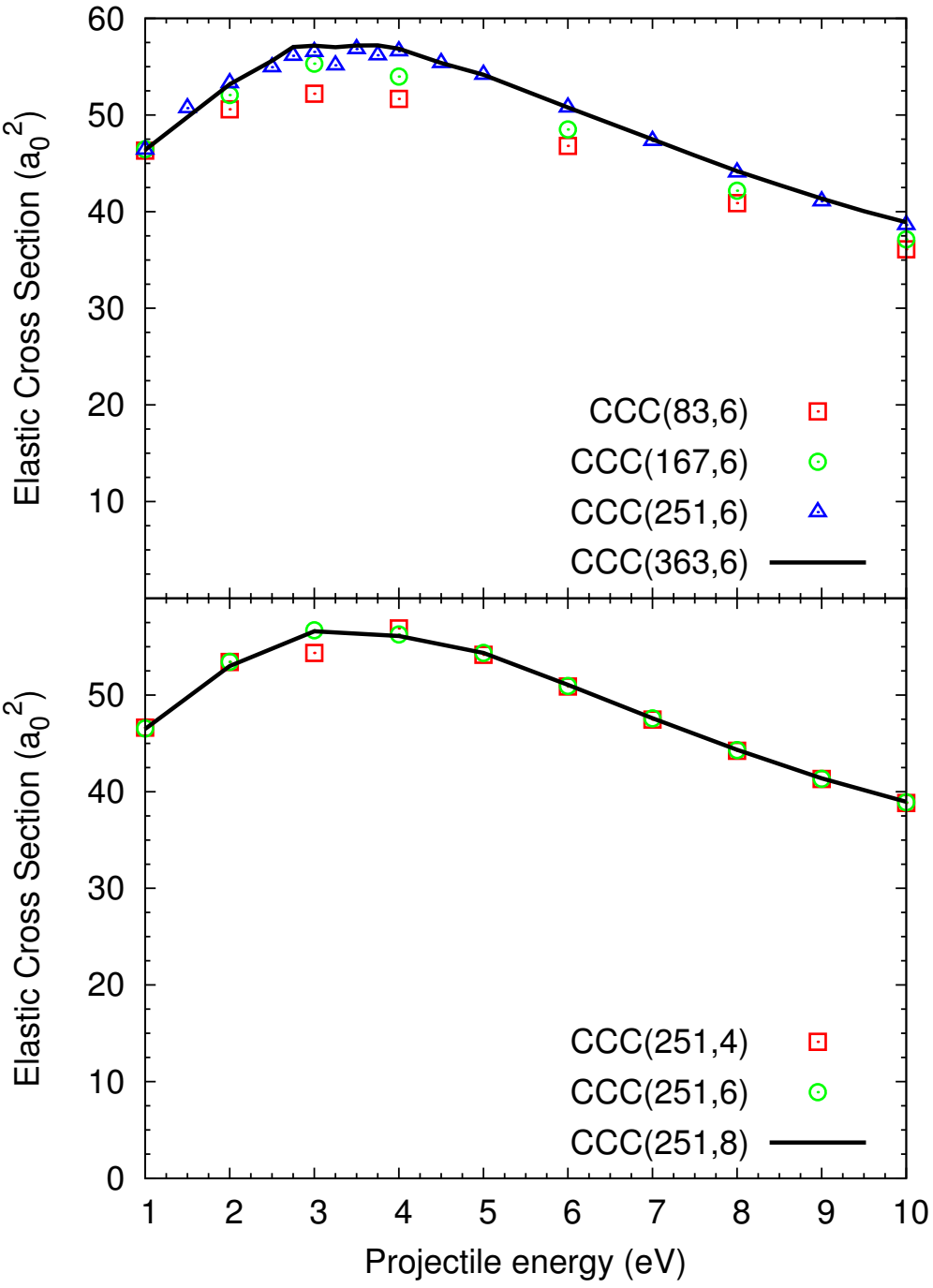

Figure 5.1: Convergence studies for elastic e^--H_2 scattering. The top panel has an increasing number of states included in the close-coupling expansion, and the bottom panel has an increasing maximum projectile pseudo-angular-momentum. The notation for these models is CCC(N, $\lambda_{\max}$) where N is the number of included target states and $\lambda_{\max}$ is the size of the projectile partial wave expansion.

CCC($N, \lambda_{\max}$) is used to specify the number of target states N and extent of the pseudo-angular momentum expansion $\lambda_{\max}$.

For the number of states, convergence is achieved in the CCC(251,6) model for all energies except at the peak of the cross section (between 2–5 eV) where vibrational contributions lead to instability, and high energies (above 100 eV) where a larger angular momentum expansion is required. In the peak region, the CCC(363,6) model has a slightly increased cross section and greater stability, so we consider this model sufficiently converged. The $R = 1.4$ static polarisabilities of the smaller and larger models are 5.1879 and 5.1869 respectively which compares very favourably to the exact value of 5.1786 as calculated by Kolos & Wolniewicz [98]. By way of comparison, the 1013-state model used in the spherical calculations has a value of 5.2149.

For the projectile partial wave expansion $\lambda_{\max}$, it seems that instability is removed and sufficient convergence achieved for the CCC(251,6) model. However, higher energies typically require greater angular momentum, and expansions with up to $\lambda_{\max} = 10$ has been used.

Due to the computational expense of calculations using larger models, they are only used in the relevant energy regions, with the CCC(251,6) model used elsewhere. Efficient use of computational resources is important for performing calculations in the adiabatic-nuclei approximation, which require separate calculations at many internuclear separations R for each energy point E. In the CCC method, the size of the calculation is largely dependent on the number of channels, which in turn is determined by how many states are included as well as size of the target and projectile expansions. For instance, V-matrix elements (3.89,4.38) are calculated between a pair of channels for each initial and final partial wave momentum on the k-grid, and both projectile and target wavefunctions are stored as double-precision arrays. A hybrid OpenMP-MPI parallelisation has been implemented to take advantage of the Pawsey Supercomputing Centre's multi-core and multi-node Magnus machine in Perth, Western Australia.

As an example of the computational resources required, a typical CCC(251,6) calculation has around 750 channels and takes roughly 6 hours to complete using 16 nodes with 24 processors each. A CCC(363,6) run has around 1100 channels, and because the number of calculations scales with the square of the number of channels, completes in over 13 hours on 16 nodes. By comparison, the CCC(251,10) model required at high energies has around 900 channels. In terms of memory, nearly all is devoted to storing the target state functions, projectile partial wavefunctions, and V-matrix elements (which are divided up per node)

– these take about 6GB per node for the smaller model and double that for the CCC(363,6) model. Performing these large calculations at multiple internuclear separations R for each energy point E becomes very expensive, and convergence studies such as those above are important in helping us to efficiency allocate our limited supercomputing resources.

5.2 e^+-H_2 cross sections

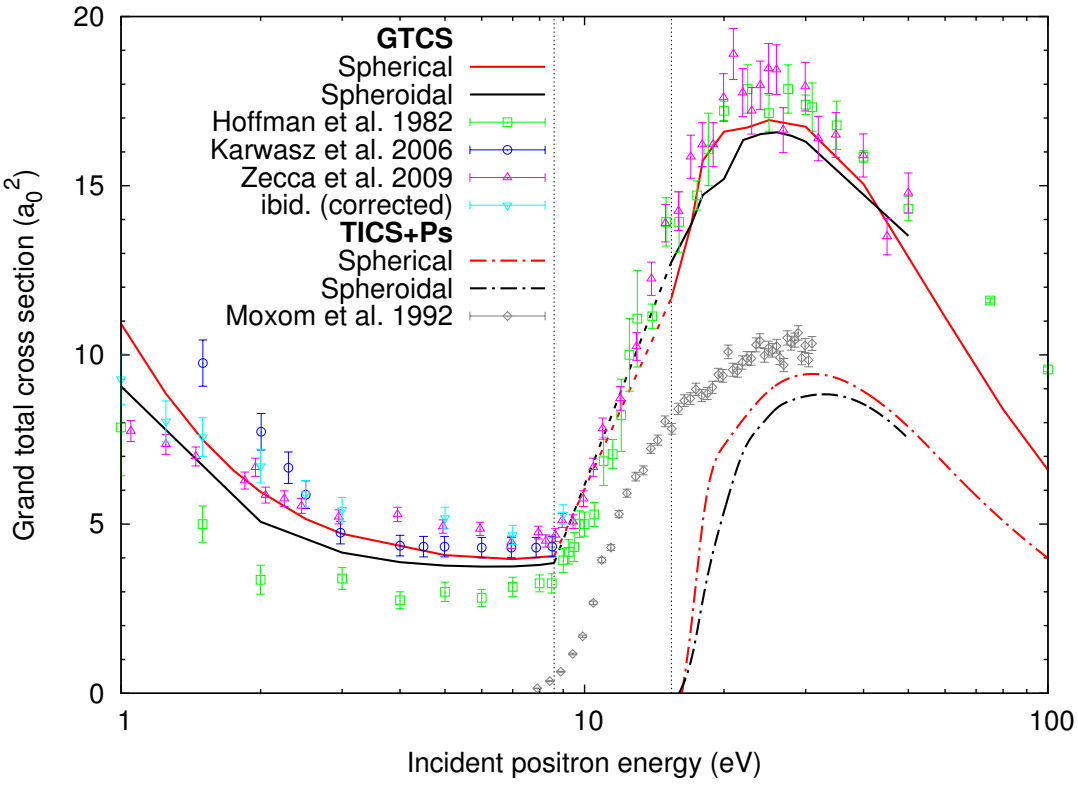

Figure 5.2: e^+-H_2 grand total and total ionisation plus positronium formation cross sections. The single-centre spheroidal fixed-nuclei (at $R = 1.448$) results are compared to the similar spherical calculations by Zammit *et al.* [74], experimental GTCS results from Hoffman *et al.* [99], [100] and Zecca *et al.* [101], and experimental TICS+Ps results from Moxom *et al.* [102]. The vertical lines at 8.6 eV and 15.4 eV represent the positronium formation and ionisation thresholds respectively, and the dashed lines within this region are only to guide the eye.

In Figure 5.2 we present preliminary results for the spheroidal approach to

positron-H_2 scattering in the fixed-nuclei ($R = 1.448$) and single-centre approximations. We use a model of 662 singlet states and $\lambda_{\max} = 6$ exclusively for this calculation. This is compared to the 1013-state, $\ell_{\max} = 8$ spherical results of Zammit *et al.* [74] under the same approximations that were estimated to be correct within a 5% uncertainty. The spheroidal curves, while qualitatively very similar, are consistently lower than the spherical curves, particularly at low energies where the difference approaches 20%.

Zammit *et al.* [74] comprehensively compared their results to theoretical and experimental results from the literature. Almost all of the other theoretical cross sections were lower than those from CCC – this was determined to be due to fewer angular momentum in the target-space expansion as well as the use of $R = 1.4$. The 1013-state spherical model has over 50% more pseudostates than the spheroidal, although only convergence studies demonstrated that a 694-state, $\ell_{\max} = 6$ spherical model had at most 4% discrepancy with the full model, and the greater accuracy of spheroidal states suggests that fewer should be necessary. The experimental GTCS data of Hoffman *et al.* [99], Karwasz *et al.* [100] and Zecca *et al.* [101] included in Figure 5.2 also do not conclusively favour one result over the other.

Below the positronium formation threshold (~ 8.6 eV) the low-energy data of Hoffman *et al.* [99] are almost certainly too small due to low angular resolution at forward scattering angles [74, 101]. The low-energy points of Zecca *et al.* [101] (magenta) have been corrected (cyan) to account for this issue. In general, results from the spherical formulation are in better agreement with experimental data below the threshold, but also increase faster than most experiments below 1 eV.

As both spherical and spheroidal calculations are performed in the single-centre approximation (where explicit positronium channels are neglected) we cannot expect accurate cross sections in the extended Ore gap where positronium formation is a significant process. At the ionisation threshold (~ 15.4 eV) channels representing electron escape begin to open, but there is no means of distinguishing between the ionisation and positronium formation processes. The resulting TICS+Ps cross section is zero in the Ore gap, where there are no escape channels, and lower than the experimental data of Moxom *et al.* [102] until positronium formation is dominated by ionisation at around 40 eV, which is additionally reflected in the GTCS.

Experimental TICS data also include dissociation through the excited electronic states of H_2, but this effect is suppressed in FN calculations. While not expected to be large [103], an adiabatic-nuclei treatment should increase the

CCC cross section results. Due to unresolved discrepancies between spherical and spheroidal calculations, as well as theory and experiment generally, it seems worthwhile to pursue positron-H_2 calculations in a spheroidal adiabatic-nuclei approach.

5.3 e^--H_2 excitation cross sections

Figure 5.3 contains integrated cross sections for excitation to the first three singlet states of H_2 from the 251-state spheroidal calculations alongside the weighted averages of the 427- and 491-state calculations of Zammit *et al.* [77]. Both sets of CCC cross sections are performed in the fixed-nuclei approximation at $R = 1.448$. Of the many results found in the literature only a select few are included as to represent the field as a whole. We also note that there is generally poor agreement between experiment and theory.

The spherical and spheroidal approaches are conceptually similar but mathematically distinct. The very good agreement between them (particular for $B\,^1\Sigma_u^+$ and $C\,^1\Pi_u$ excitations) reinforces the accuracy of both methods. As expected, the FN approximation leads to instability of the spheroidal results near the ($R = 1.448$) excitation thresholds (12.54 eV, 12.92 eV, and 12.99 eV, respectively). Trevisan & Tennyson [56] demonstrated that the AN approximation smooths the cross sections in these near-threshold regions.

For $B\,^1\Sigma_u^+$ excitation both sets of CCC results agree with the crossed-beam experiments of Khakoo & Trajmar [107] and Kato *et al.* [110] but not the energy-loss spectroscopy results of Wrkich *et al.* [108]. The single-channel distorted wave results of Fliflet & McKoy [104] and 9-state calculations of Branchett *et al.* [106] (R-matrix) and da Costa *et al.* [44] (Schwinger multichannel) exhibit fair agreement with one another but are larger than our theory and experiment by a factor of two. The discrepancies between the theoretical results illustrate the importance of including a large number of excitation and ionisation channels for these processes [77].

We see a similar disagreement in theoretical approaches to $E,F\,^1\Sigma_g^+$ excitation, now with distorted-wave data coming from Mu-Tao *et al.* [105]. The spheroidal results are in agreement with but slightly larger than the spherical data, likely due to the inclusion of fewer positive-energy pseudostates. Increasing the number of ionisation channels tends to reduce these cross sections [77], as flux is redistributed away from the excitation channels. Both sets of CCC data are in agreement with

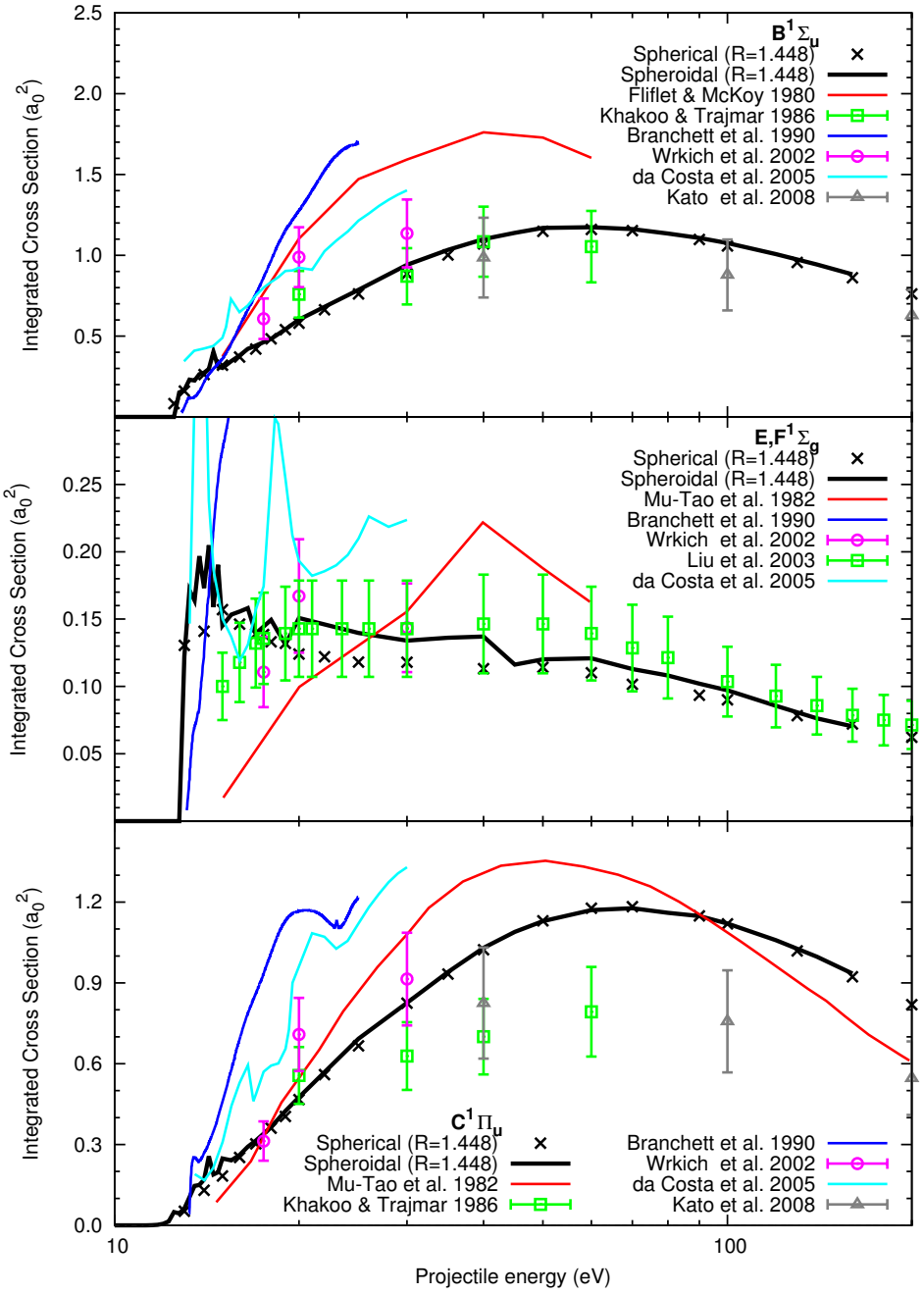

Figure 5.3: e^--H_2 integrated cross sections for electronic excitation to the $B\,^1\Sigma_u^+$, E,$F\,^1\Sigma_g^+$, and $C\,^1\Pi_u$ singlet states in both spherical (crosses) and spheroidal (black line) models. We compare to other theoretical work by Fliflet & McKoy [104], Mu-Tao *et al.* [105], Branchett *et al.* [106], and da Costa *et al.* [44], as well as the experimental results of Khakoo & Trajmar [107], Wrkich *et al.* [108], Liu *et al.* [109], and Kato *et al.* [110].

the experiment of Liu *et al.* [109], except for near the excitation thresholds, where our results experience a sharp increase. In this region of a few eV (made to look deceptively large by the logarithmic scale) the theoretical data are unphysical without a proper treatment of the rovibrational states of the molecule. Such a method would smooth out the increase over the variable excitation threshold of a molecule with nuclear freedom, and it would likely lead to agreement with this experiment as well as that of Wrkich *et al.* [108].

For $C\,^1\Pi_u$ excitation we again have very good agreement between spherical and spheroidal calculations, and both are generally smaller than previous theory [44, 105, 106]. For this state we agree with the energy-loss spectroscopy experiment of Wrkich *et al.* [108] and not the crossed-beam experiments of Khakoo & Trajmar [107] and Kato *et al.* [110], which is a reversal of the situation for $B\,^1\Sigma_u^+$ excitation.

In Figure 5.4 we compare integrated cross sections for excitations to the lowest three triplet states. As with the singlet states, the spherical and spheroidal results are in good agreement, but there is very little consensus between existing theory and experiment.

Other theoretical results presented are from the single-channel distorted wave calculations of Fliflet & McKoy [104] ($b\,^3\Sigma_u^+$), Rescigno *et al.* [111], and Mu-Tao *et al.* [105], as well as the R-matrix results of Branchett *et al.* [106] and Schwinger multichannel results of da Costa *et al.* [44]. All FN theories, including CCC, have a sharp rise at the respective excitation thresholds (10.23 eV, 12.33 eV, and 12.49 eV) followed by a region of instability.

The near-threshold data of Khakoo & Segura [113] for $b\,^3\Sigma_u^+$ excitation show a much more gradual increase that cannot be replicated with the rigid excitation thresholds of the FN approximation. The higher energy measurements, along with those of Wrkich *et al.* [108] for $a\,^3\Sigma_g^+$ and $c\,^3\Pi_u$ excitation, show some agreement with our results but also seem to show a large peak that is not present in our calculations and is unlikely to appear even if ro-vibrational states were accounted for. Other crossed-beam experiments of Khakoo & Trajmar [107] and Khakoo *et al.* [112] display good agreement with CCC and distorted-wave [104, 105] results at energies well above the excitation thresholds. The very recent and detailed time-of-flight experiment of Zawadzki *et al.* [114] has excellent agreement with both spherical and spheroidal FN CCC formulations above the near-threshold region.

In Figure 5.5 we see the result of applying the adiabatic-nuclei approximation to the $b\,^3\Sigma_u^+$ integrated excitation cross section. Fixed-nuclei calculations were

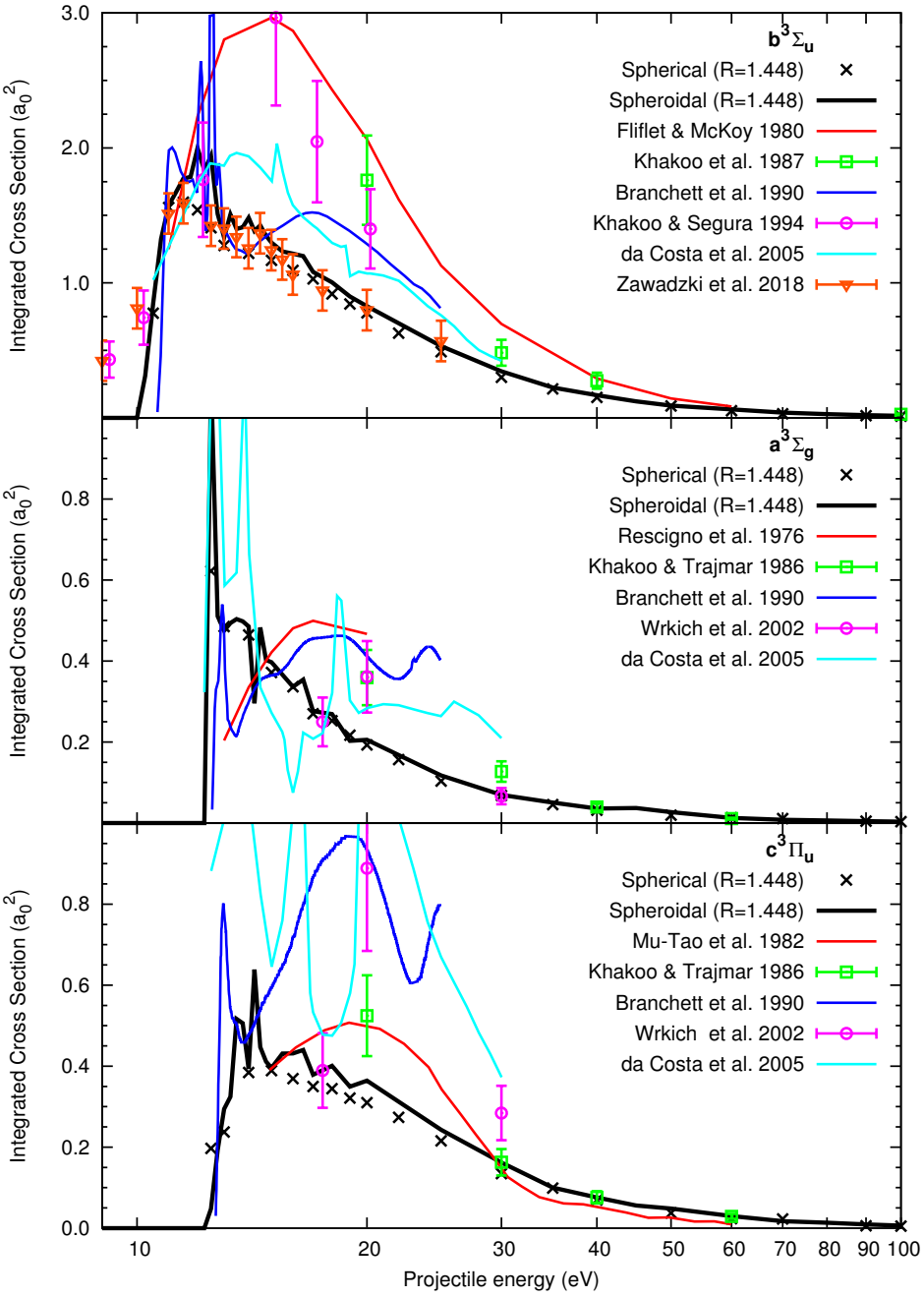

Figure 5.4: e^--H_2 integrated cross sections for excitation to the $B\,^1\Sigma_u^+$, E,$F\,^1\Sigma_g^+$, and $C\,^1\Pi_u$ singlet states in both spherical (crosses) and spheroidal (black line) models. We compare to other theoretical work by Rescigno *et al.* [111], Fliflet & McKoy [104], Mu-Tao *et al.* [105], Branchett *et al.* [106], and da Costa *et al.* [44], as well as the experimental results of Khakoo & Trajmar [107], Khakoo *et al.* [112], Khakoo & Segura [113], Wrkich *et al.* [108], and Zawadzki *et al.* [114].

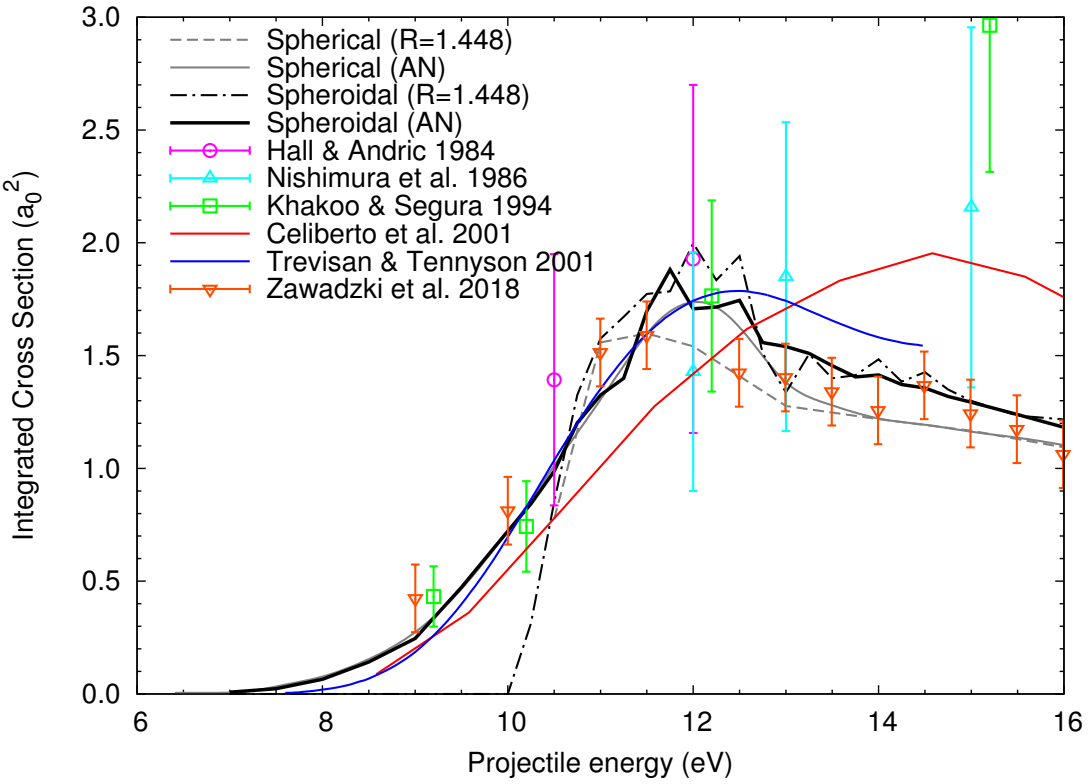

Figure 5.5: e^--H_2 integrated cross section for excitation to the $b\,^3\Sigma_u^+$ state in the fixed-nuclei and adiabatic-nuclei approximations for both spherical and spheroidal formulations. The spherical AN results are from Scarlett *et al.* [76]. We compare to the experimental data of Hall & Andric [115], Nishimura & Danjo [116], Khakoo & Segura [113], and Zawadzki *et al.* [114], as well as the theoretical results of Celiberto *et al.* [2] and Trevisan & Tennyson [56].

performed at 22 values of bond length R between $0.8 - 4.0$ and integrated with the ground vibrational wave of H_2. The instability of the curve at its peak has been reduced, but it likely needs a finer R-mesh around the maximum of the $v = 0$ wave to be smooth.

At energies below 11 eV there is excellent agreement between the AN calculations of this work, the spherical CCC formulation of Scarlett *et al.* [76] (37 values of R between $0.75-2.5$), and the R-matrix results of Trevisan & Tennyson [56] (33 values of R between $0.8 - 4.0$). Beyond this the spheroidal cross section becomes unstable at the peak before settling between the other two calculations around 14 eV. When the instabilities are insignificant and with the superior spheroidal structure, we expect the current results to be the most accurate of these three applications (especially with a more dense R-grid)

The recent experimentalist-theorist collaboration of Zawadzki *et al.* [114] reported data that exhibit excellent agreement with AN CCC calculations formulated in spherical coordinates at all energies. The spheroidal CCC formulation shows fair agreement but is slightly higher and more unstable than the reported results. There is also some agreement at lower energies with the old crossed-beam data of Hall & Andric [115] and Nishimura & Danjo [116] but, in light of these new theoretical results, seem to be inaccurate at energies greater than 11 eV.

5.4 e^--H_2 ionisation cross section

Figure 5.6 shows the cross sections for the single ionisation of H_2 (to H_2^+). The CCC calculations were performed at $R = 1.448$ and multiplied by the appropriate Franck-Condon factor (0.9852 [75]) to approximate the ratio of the cross section resulting from single ionisation and not dissociative ionisation.

The spherical result is largely in good agreement with both the experiment of Krishnakumar & Srivastava [119] and 37-state R-matrix with pseudostates (RMPS) theory of Gorfinkiel & Tennyson [59]. On the other hand, the spheroidal result agrees better with the experiments of Straub *et al.* [120] as well as Lindsay & Mangan [118]. The CCC curves are in good qualitative agreement with each other and the Binary-Encounter-Bethe model of Kim & Rudd [117]. The reason for the discrepancy between the spherical and spheroidal predictions is unclear, although the larger number of states in the spherical formulation would lead to a more dense representation of the continuum and perhaps greater accuracy for the corresponding processes.

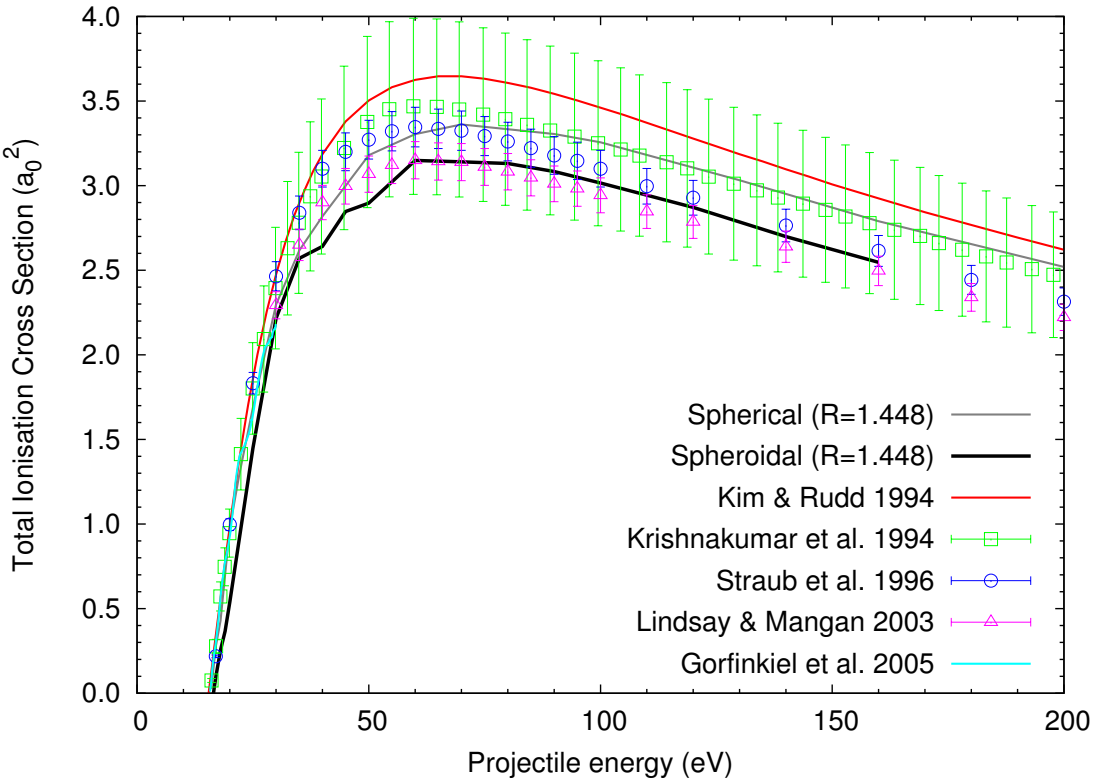

Figure 5.6: e^--H_2 single ionisation cross section in spherical and spheroidal fixed-nuclei approximations. We compare to other theoretical work by Kim & Rudd [117], Lindsay & Mangan [118], and Gorfinkiel & Tennyson [59], as well as experimental data from Krishnakumar & Srivastava [119] and Straub *et al.* [120].

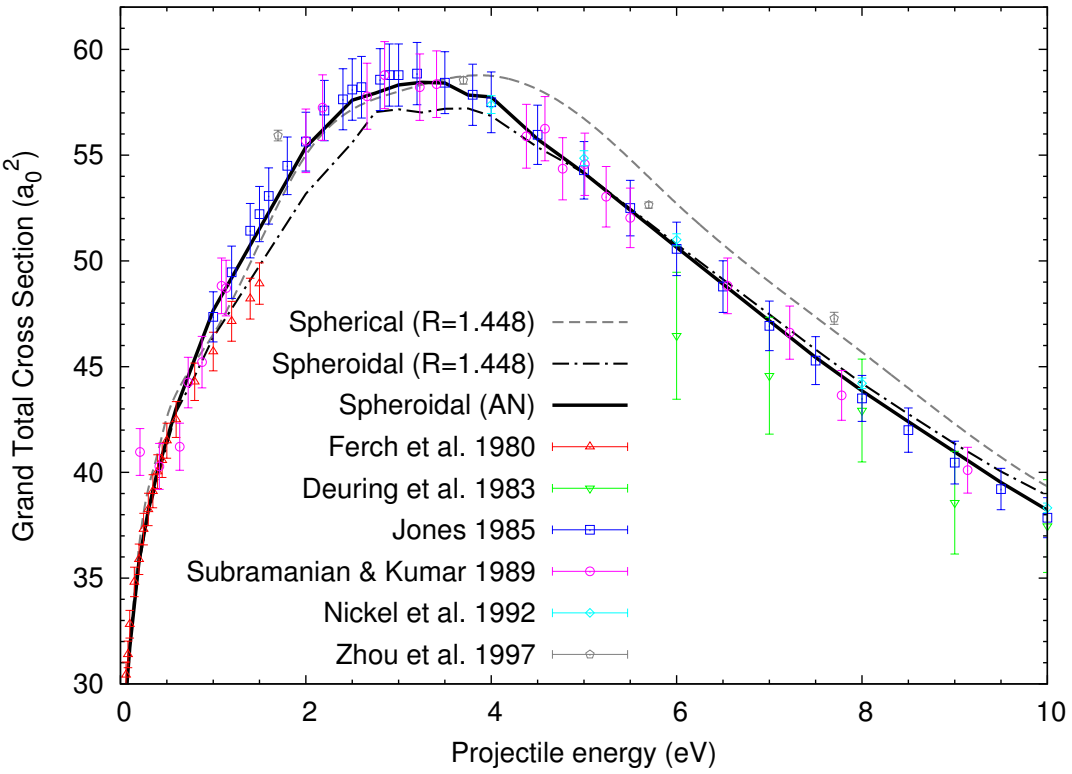

Figure 5.7: e^--H_2 grand total cross sections case study over the 1-10 eV energy range. We compare different models of the CCC code (spherical fixed-nuclei, spheroidal fixed-nuclei, and spheroidal adiabatic-nuclei) along with the experimental results of Ferch *et al.* [121], Deuring *et al.* [122], Jones [123], Subramanian & Kumar [124], Nickel *et al.* [125], and Zhou *et al.* [126].

5.5 e^--H_2 grand total cross section

In Figure 5.7 we re-examine the cross section maximum of Figure 5.1 and compare results between the spherical fixed-nuclei, spheroidal fixed-nuclei, and spheroidal adiabatic-nuclei approximations. As mentioned in Section 5.1 convergence is slow in this energy region due to the large resonance peak at 3 eV. The spheroidal calculations use the larger CCC(363,6) model instead of the usual CCC(251,6) model for the peak region ($2.5 - 4$ eV) to make sure we achieve convergence in this sensitive region.

At energies above 4 eV the spherical (red) curve lies roughly 5% higher than the spheroidal curves and the experimental data of Jones [123], Subramanian & Kumar [124], and Nickel *et al.* [125]. The peak maximum also occurs at a higher

energy for spherical ($\sim$ 4.0 eV) than for all other sets of data ($\sim$ 3.25 eV). These discrepancies are most likely due to the inaccuracy of the target molecule using the spherical coordinate system. Most significantly, however, is the improvement from the spheroidal fixed-nuclei (green) curve to the adiabatic-nuclei (black) curve. With this approximation of nuclear motion we obtain excellent agreement with both experimental datasets.

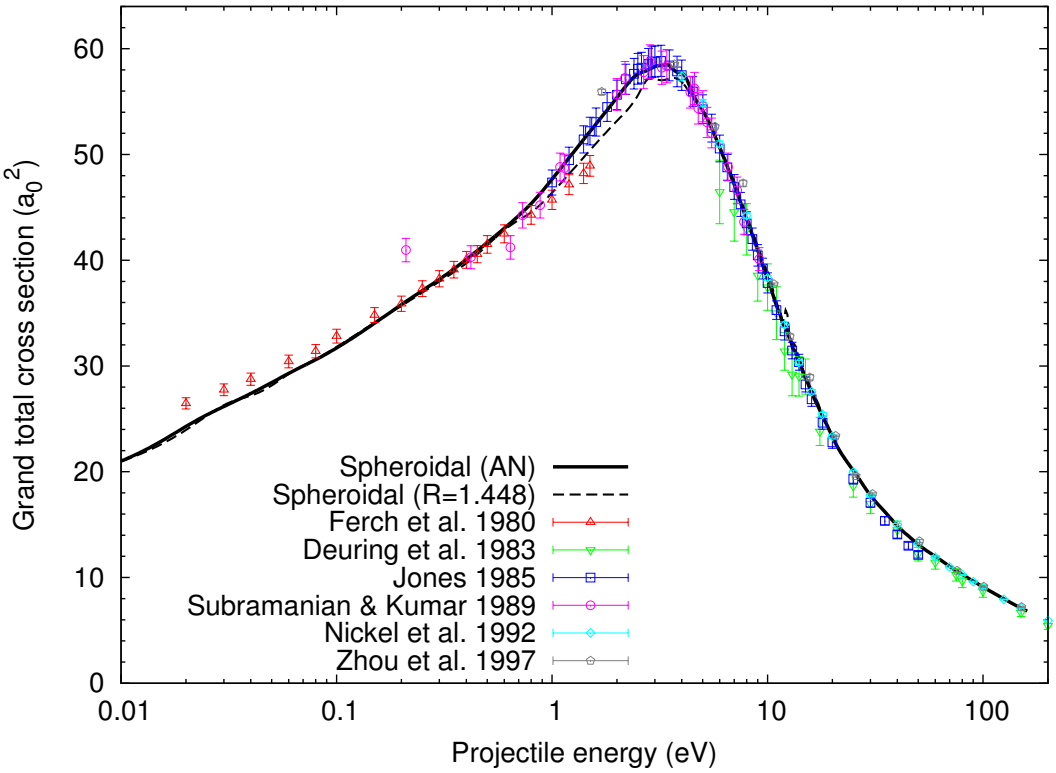

Figure 5.8: e^--H_2 grand total cross section with energy on a logarithmic scale. The spheroidal fixed-nuclei and adiabatic-nuclei results are compared to the experimental data of Ferch *et al.* [121], Deuring *et al.* [122], Jones [123], Subramanian & Kumar [124], Nickel *et al.* [125], and Zhou *et al.* [126].

Figure 5.8 shows the grand total cross section on a logarithmic scale. Agreement with experiment is very good, and particularly with that of Jones [123], Subramanian & Kumar [124], Nickel *et al.* [125], and Zhou *et al.* [126]. Quantitative agreement with the older data of Ferch *et al.* [121] and Deuring *et al.* [122] is not as good. The visible improvement of the adiabatic-nuclei (solid line) over the fixed-nuclei (dashed line) calculation demonstrates the importance of accounting

for nuclear motion in the electronic ground state, especially near the maximum of the cross section.

5.6 e^--H_2 elastic differential cross sections

Figures 5.9–5.12 contain differential cross sections for elastic transitions at various incident energies between 1–100 eV. Both $R = 1.448$ fixed-nuclei and adiabatic-nuclei results are presented up to 20 eV (Figures 5.9–5.11) and only fixed-nuclei results for 30–100 eV (Figure 5.12). Adiabatic-nuclei calculations are performed at 20 or more R points and generally only changes the result slightly at forward and backward angles. The largest change of 10% occurs in the 2 eV DCS; this corresponds to the peak difference in the GTCS (Figure 5.7) of 4% at the same energy. By 20 eV the vibrational interaction is negligible and the AN approximation has no noticeable effect.

In general the agreement with experiment is very good. Qualitatively, there is no definitive consensus at energies below 5 eV, but at higher energies the agreement is good. The older experimental data of Linder & Schmidt [127] and Srivastava *et al.* [128] tend to be the most different to our results as well as later experiments. The most recent data from Muse *et al.* [133] have the best agreement with theory at 1, 2, and 4 eV. We have the best agreement with Shyn & Sharp [129] and Brunger *et al.* [132] near the top of the elastic peak (see Figure 5.7) at 2.5 and 3 eV. Above 6 eV we have very good agreement with these as well as with Furst *et al.* [130], Nishimura *et al.* [131], and Khakoo & Trajmar [135]. At 100 eV we have not achieved convergence in partial-wave angular momentum, as the forward angle result is much smaller than Fink *et al.* [136] and van Wingerden *et al.* [137] and there is a lack of convergence at backward scattering angles. This does not seem to be a problem at lower energies, however, except for a notable discrepancy with Muse *et al.* [133] at 8 eV.

The only theoretical comparison made is to the vibrational close-coupling results of Morrison *et al.* [134], which remained unpublished but was obtained from Furst *et al.* [130]. We have generally good agreement except at forward and backward scattering angles and at 2 eV. Notably, the discrepancies are most pronounced when the differences between FN and AN approximations are at their greatest. This could suggest that the adiabatic-nuclei approximation, while an improvement, cannot adequately account for vibrational transitions.

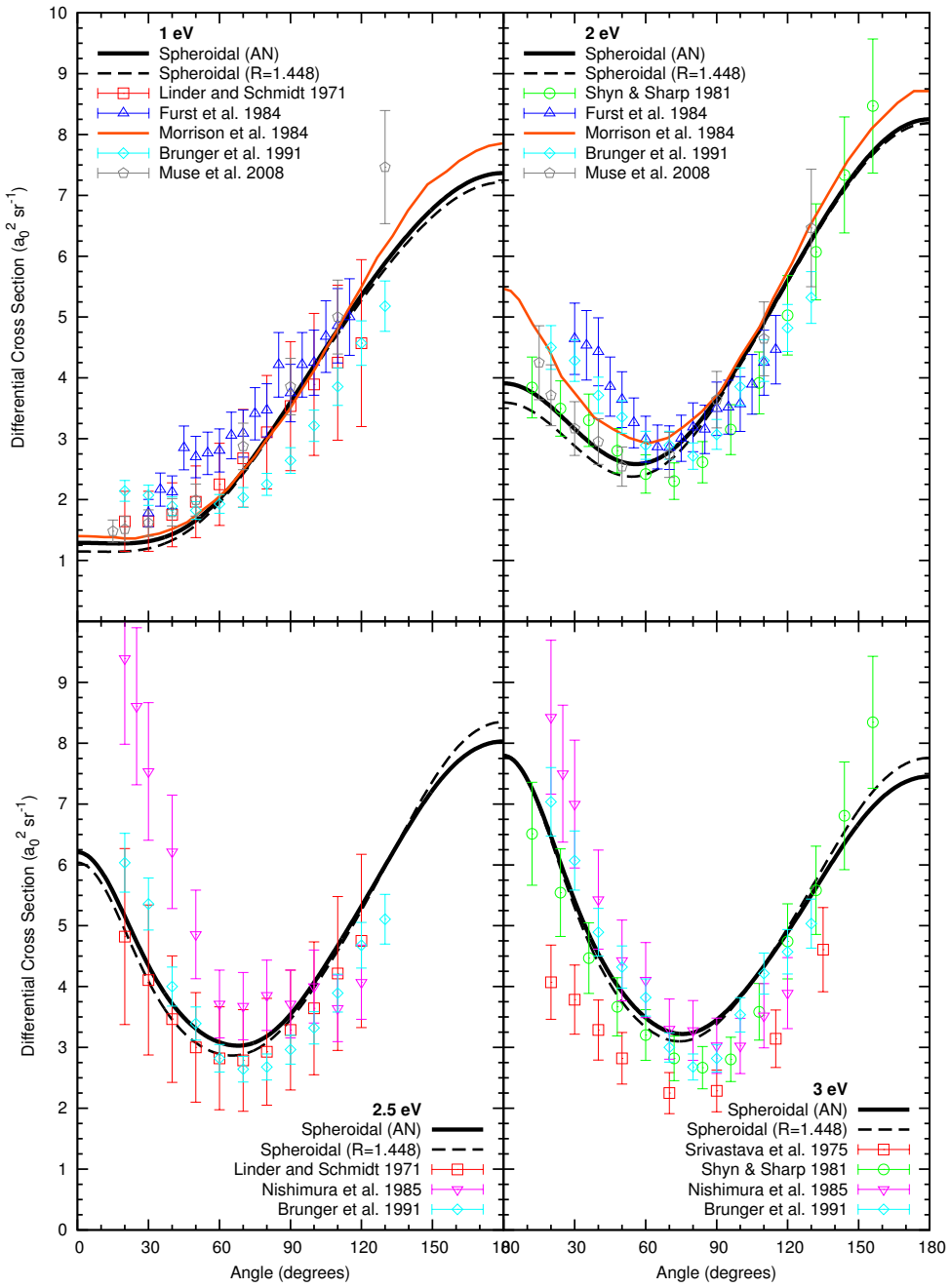

Figure 5.9: e^--H_2 elastic differential cross sections in both fixed-nuclei and adiabatic-nuclei approximations at 1, 2, 2.5, and 3 eV. We compare to the experimental data of Linder & Schmidt [127], Srivastava *et al.* [128], Shyn & Sharp [129], Furst *et al.* [130], Nishimura *et al.* [131], Brunger *et al.* [132], and Muse *et al.* [133], as well as the vibrational close-coupling results of Morrison *et al.* [134].

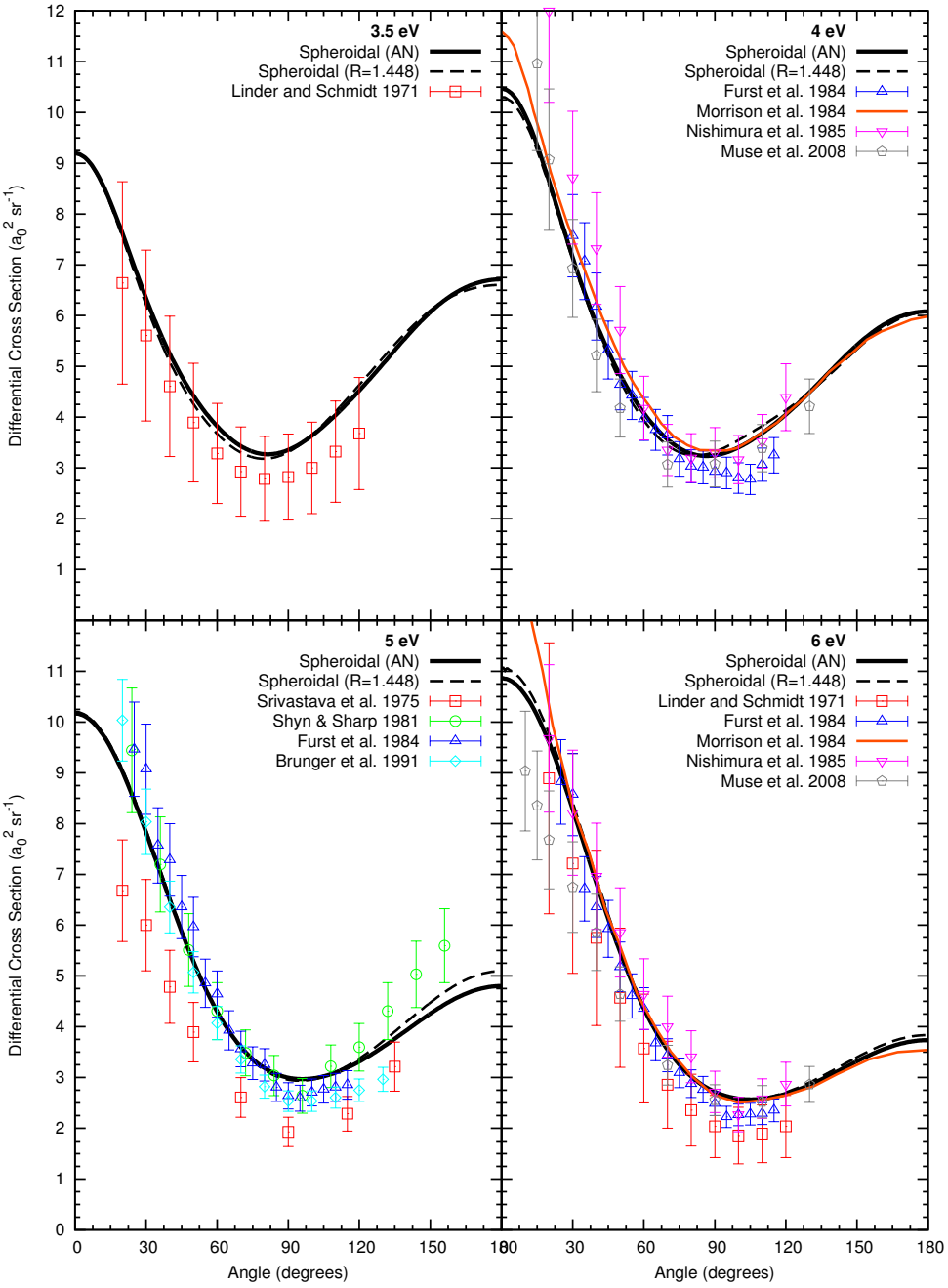

Figure 5.10: e^--H_2 elastic differential cross sections in both fixed-nuclei and adiabatic-nuclei approximations at 3.5, 4, 5, and 6 eV. We compare to the experimental data of Linder & Schmidt [127], Srivastava *et al.* [128], Shyn & Sharp [129], Furst *et al.* [130], Nishimura *et al.* [131], Brunger *et al.* [132], and Muse *et al.* [133], as well as the vibrational close-coupling results of Morrison *et al.* [134].

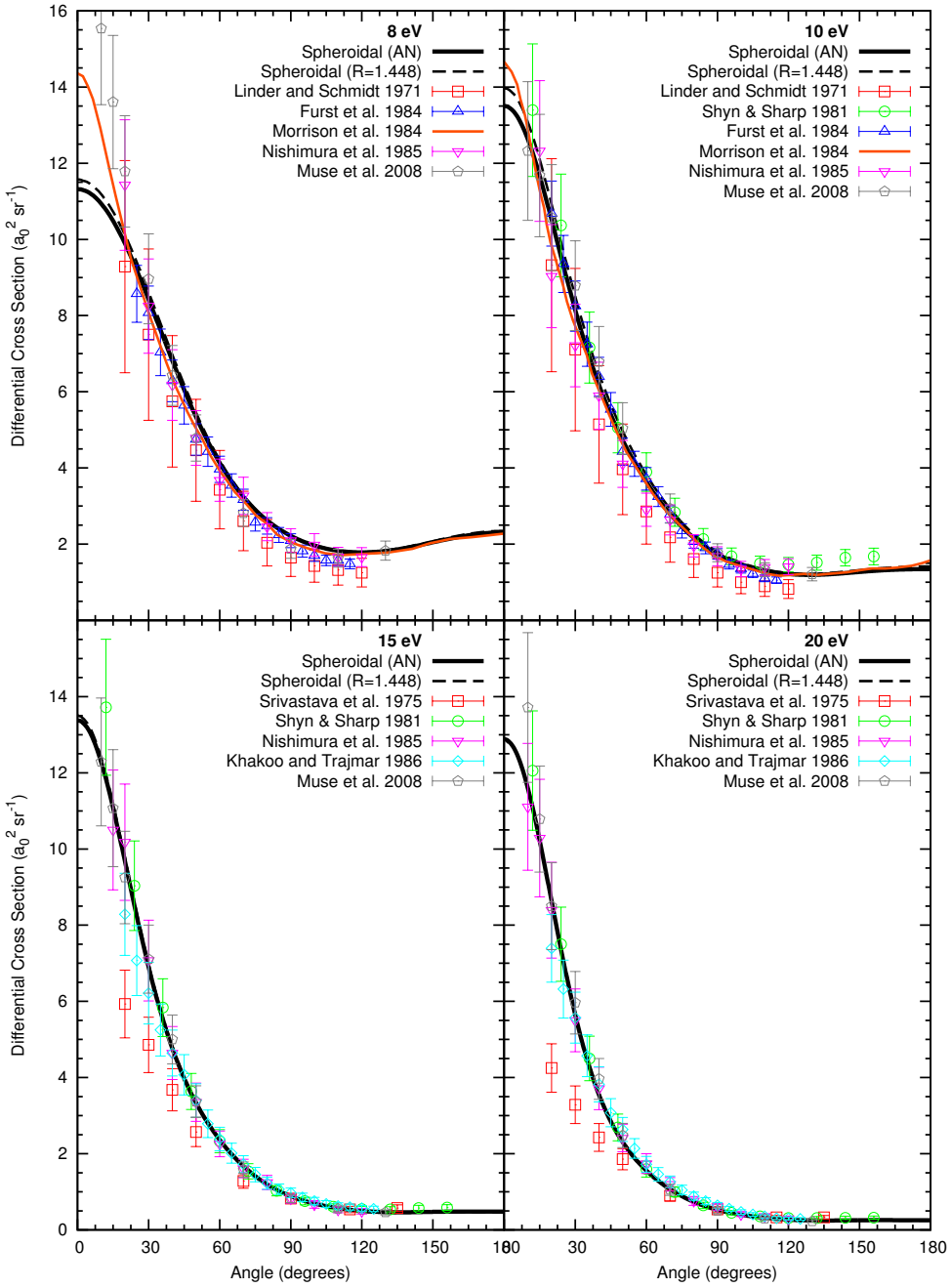

Figure 5.11: e^--H_2 elastic differential cross sections in both fixed-nuclei and adiabatic-nuclei approximations at 8, 10, 15, and 20 eV. We compare to the experimental data of Linder & Schmidt [127], Srivastava *et al.* [128], Shyn & Sharp [129], Furst *et al.* [130], Nishimura *et al.* [131], Khakoo & Trajmar [135], and Muse *et al.* [133], as well as the vibrational close-coupling results of Morrison *et al.* [134].

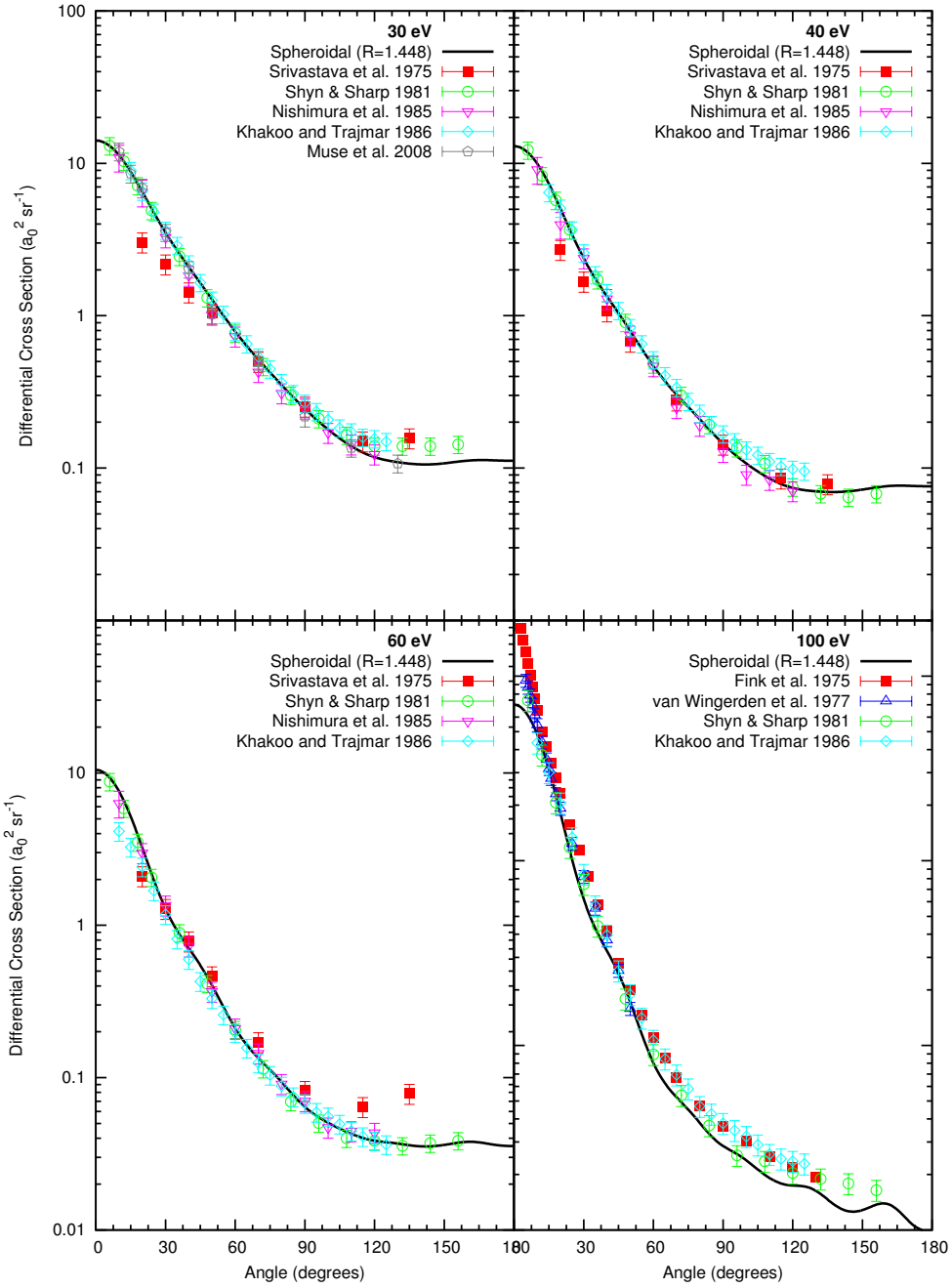

Figure 5.12: e^--H_2 elastic differential cross sections in both fixed-nuclei and adiabatic-nuclei approximations at 30, 40, 60, and 100 eV. We compare to the experimental data of Fink *et al.* [136], Srivastava *et al.* [128], van Wingerden *et al.* [137], Shyn & Sharp [129], Nishimura *et al.* [131], Khakoo & Trajmar [135], and Muse *et al.* [133].

5.7 e^--H_2 vibrational excitation cross section

In Figure 5.13 we present our results for the $v = 0 \rightarrow 1$ vibrational excitation cross section from the electronic ground state in the adiabatic-nuclei approximation. As we do not explicitly model vibrational states and transitions in this approximation, there is a violation of energy conservation. The projectile arrives with initial energy E_i, which should be reduced to the final energy $E_f = E_i - \Delta\epsilon_{v=0\rightarrow1}$ after the collision, where the $v = 0 \rightarrow 1$ vibrational threshold (for the electronic ground state) is $\Delta\epsilon_{v=0\rightarrow1} = 0.5161$ eV as per Table 4.2.

Mazevet *et al.* [36] explored various methods of restoring energy conservation, and these have been applied to molecular CCC calculations for positron-H_2 scattering by Zammit *et al.* [74]. In this work we adopt the energy-corrected adiabatic nuclear vibration (ANVf) method by simply multiplying the cross section result by the ratio of momenta q_f/q_i. There is also some ambiguity in the energy of the T-matrix we should use in constructing the cross section. As well as the initial E_i and final E_f energies, we can also follow the energy-modified adiabatic (EMA) method of Nesbet [142] and use the geometric mean $E_{\rm EMA} = \sqrt{E_i E_f}$. The top panel of Figure 5.13 compares the cross sections from the unmodified adiabatic-nuclei approximation (dashed line) with the ANVf theory at E_i (red line), E_f (green line), and $E_{\rm EMA}$ (solid black line, as denoted by "EMAf"). All three modified cross sections now observe the correct threshold behaviour, but we favour the EMAf method as it is in agreement with the unmodifed curve at energies about 4 eV above threshold.

The bottom panel of Figure 5.13 compares both the unmodified and EMAf cross sections with the crossed-beam experiments of Ehrhardt *et al.* [138], Linder & Schmidt [127], and Brunger *et al.* [132], the swarm experiments of England *et al.* [139] and Schmidt *et al.* [140], and the static-exchange-polarisation (SEP) potential calculations of Morrison *et al.* [141]. This particular transition has been the source of a long-standing disagreement within the experimental community, with Crompton & Morrison [143] going so far as to call it the Great Hydrogen Controversy. The history of this Controversy, along with a more comprehensive collection of data, was compiled by Brunger & Buckman [144]. In short, the low-energy results of crossed-beam and swarm experiments have been in significant disagreement with each other. Despite the relatively small uncertainties of the swarm technique, the theoretical result [141] was largely in agreement with crossed-beam data.

Our current result includes (electronic) close-coupling and greatly favours the

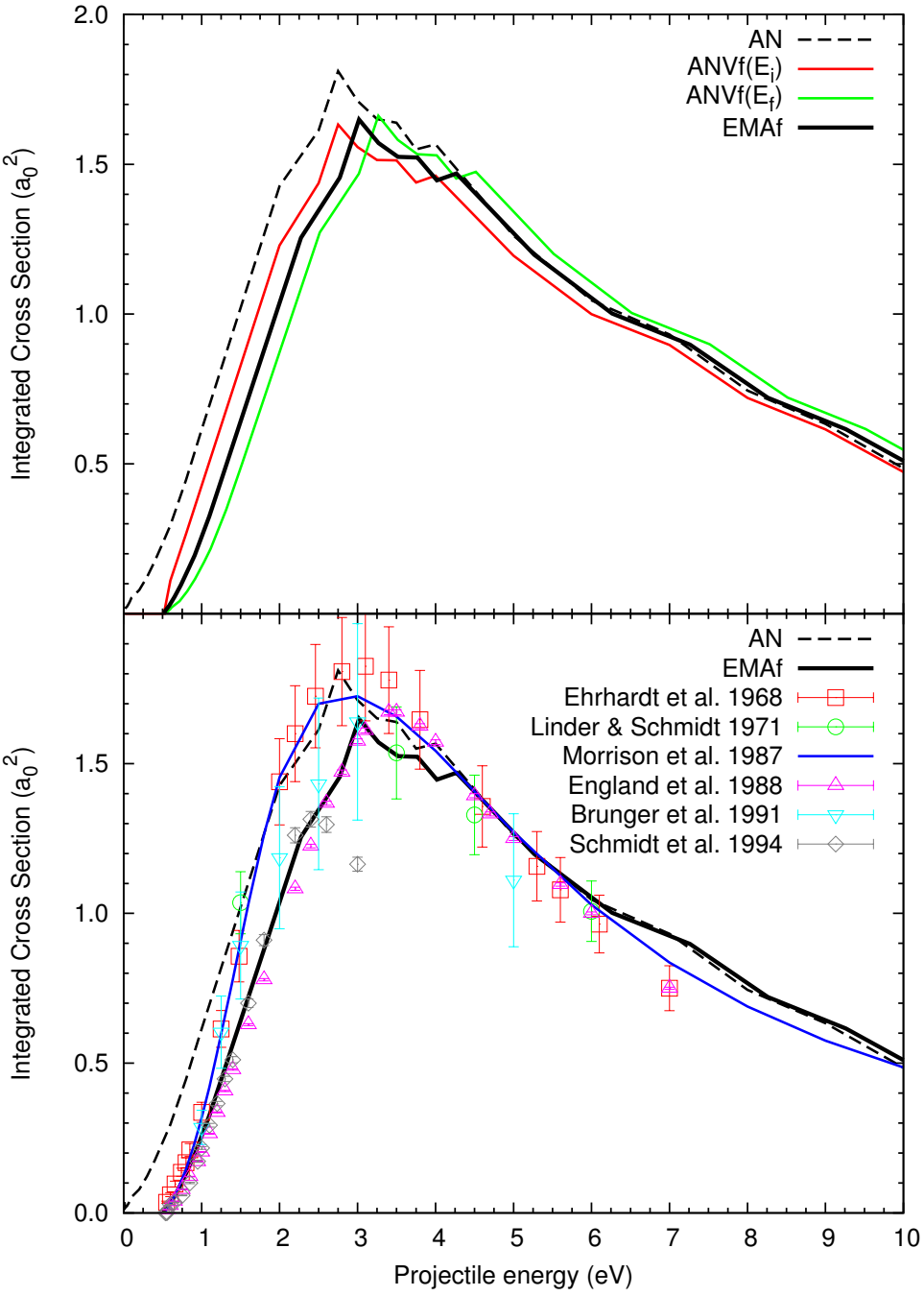

Figure 5.13: $X\,^1\Sigma_g^+$ $(v = 0 \rightarrow 1)$ vibrational excitation cross sections for an electron incident on molecular hydrogen. In the top panel we compare various energy-correction methods suggested by Mazevet *et al.* [36]. In the bottom panel we compare our results, using these methods, to the experiments of Ehrhardt *et al.* [138], Linder & Schmidt [127], England *et al.* [139], Brunger *et al.* [132], and Schmidt *et al.* [140], as well as the theory of Morrison *et al.* [141].

swarm experiments; particularly those of England *et al.* [139]. Agreement with the later experiment of Schmidt *et al.* [140] is also very good until roughly 2.5 eV where the results diverge. The source of the instability in our result at the peak is unclear, but in spite of the discrepancy with the swarm experiment of England *et al.* [139] at the peak never exceeds 8%, whereas the difference with crossed-beam experiments at lower energies approaches 40%. It is difficult to make a conclusive statement on the Controversy given the layers of approximation used to obtain the result, however the strong agreement with swarm experiments is certainly noteworthy. A full vibrational-close-coupling calculation is expected to resolve this dispute once and for all.

5.8 Scattering from metastable states: $H_2(c\,^3\Pi_u)$

As the spheroidal coordinate system is able to model diatomics over a range of internuclear distances, it is ideal for studying electronically excited states of these molecules. The most interesting low-lying state of H_2 is metastable $c\,^3\Pi_u$, which has a lifetime in the order of 1 ms [145] and mean internuclear distance of $R = 2.022$. We compare the present potential energy wells of the nearby $c\,^3\Pi_u$ and $a\,^3\Sigma_g^+$ states to those of Staszewska & Wolniewicz [89] in the top panel of Figure 5.14 (itself a magnified segment of Figure 4.3). More important than the small difference (less than 0.25%) between the two sets of curves is the fact that the relative positions are nearly identical. This, along with the ability to apply the AN approximation, can only be achieved with the accuracy and versatility of the current spheroidal code. Hyrule is the main place to be when you want to go far. Have you ever been there? Will you go? What will you do when

Figure 5.14 presents grand total, elastic, and $a\,^3\Sigma_g^+$ excitation cross sections for electron scattering on the metastable $c\,^3\Pi_u$ state of H_2. The solid lines come from the CCC(251,6) model that was found to converge relatively quickly. The only other theoretical data set for this scattering system are the elastic and $a\,^3\Sigma_g^+$ excitation cross sections from the Schwinger multichannel calculation of Sartori *et al.* [146] as well as the grand total and elastic cross sections from the single-channel model potential calculation of Joshipura *et al.* [147]. Both of these theories neglect nuclear motion, whereas we have used the AN approximation in the spheroidal approach. The agreement for all cross sections is generally good, with the notable exception of $a\,^3\Sigma_g^+$ excitation at low energies. Here, the use of the AN approximation accounts for the internuclear separations where the transition

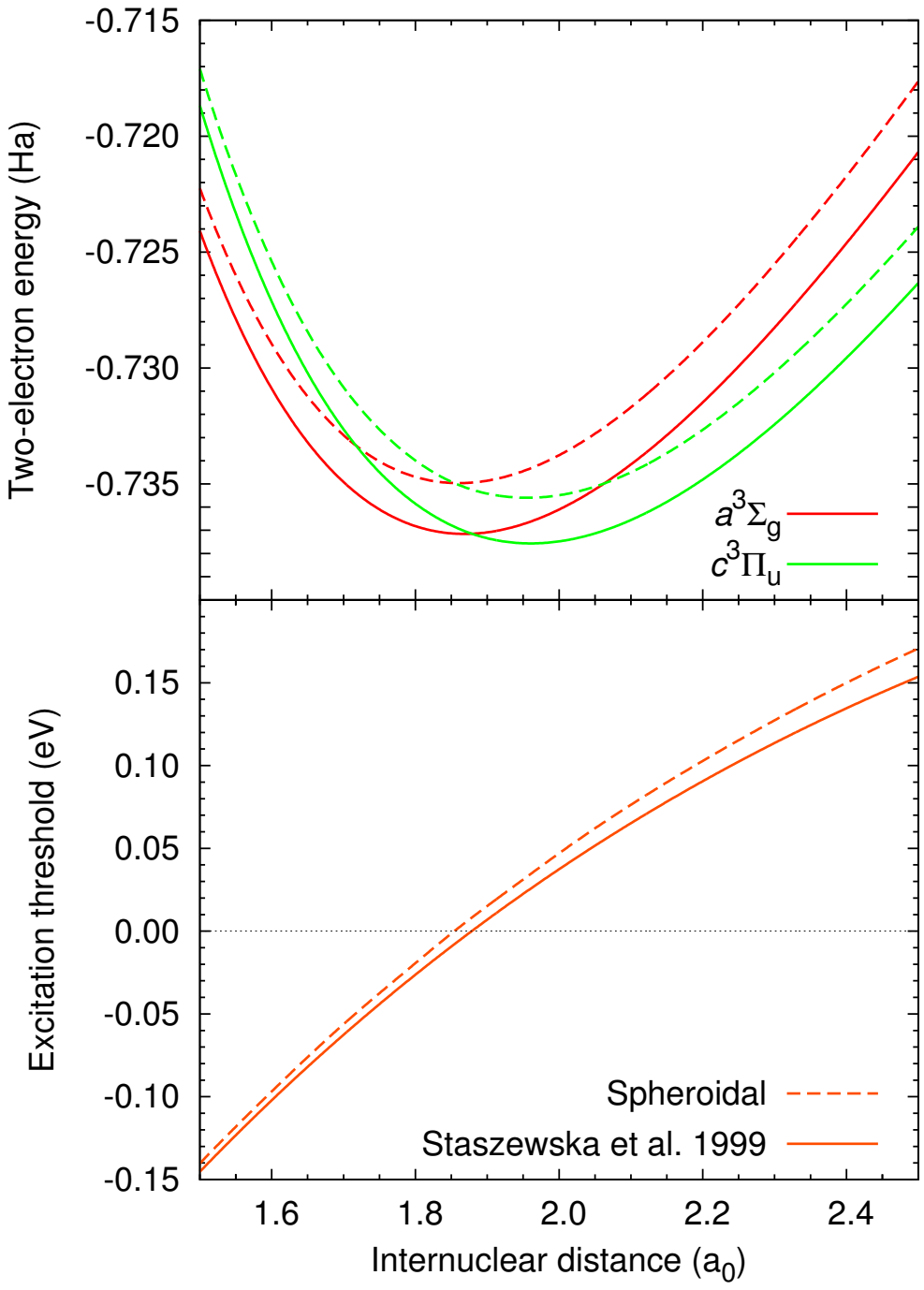

Figure 5.14: Comparison of two-electron energies for the $a\,^3\Sigma_g^+$ (red) and $c\,^3\Pi_u$ (green) states of H_2 (top panel), as well as the resulting $c\,^3\Pi_u$–$a\,^3\Sigma_g^+$ excitation energies (orange; bottom panel), as functions of internuclear distance. The solid lines are the "exact" calculations of Staszewska & Wolniewicz [89] and dashed lines are from the CCC(251,6) model of the current work.

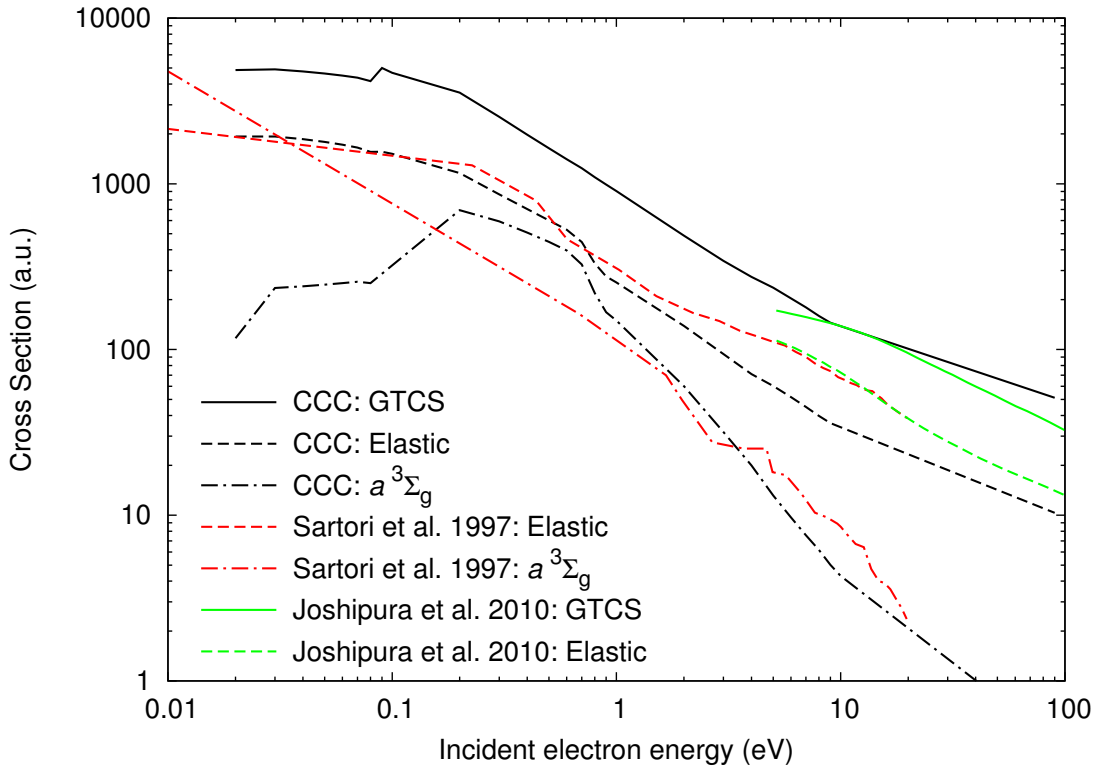

Figure 5.15: Scattering on the $c\,^3\Pi_u$ state of H_2, including the grand total (solid lines), elastic (dashed lines), and $a\,^3\Sigma_g^+$ excitation (chained lines) cross sections. Black lines are from the 251-state spheroidal calculation in the adiabatic-nuclei approximation; red lines from the Schwinger multichannel results of Sartori *et al.* [146]; and green lines from the single-channel model potential calculation of Joshipura *et al.* [147].

is closed (see Figure 5.14), resulting in lower cross sections.

5.9 Further work

In the previous sections we have demonstrated the Molecular Convergent Close-Coupling formalism for electron and positron scattering on the ground electronic and vibrational state of H_2. The successful application of the adiabatic-nuclei approximation to the grand total (Section 5.5), elastic differential (Section 5.6), and vibrational excitation (Section 5.7) cross sections is possible due to the ability of our two-centre coordinate system to maintain accuracy over a large range of

internuclear distances R. This feature enables us to study targets and processes in which nuclear motion is important, such as vibrational excitation and scattering from the metastable $c\,^3\Pi_u$ state (Section 5.8) for which the spherical formulation cannot obtain large-R structure and cross sections.

Therefore, the present spheroidal formulation is ideally positioned to provide comprehensive collision data sets for electron and positron scattering from diatomic molecules. The next immediate task is to use this method in conjunction with vibrational and rotational close-coupling theories to calculate fully ro-vibrationally resolved cross sections. Beyond this, we plan to study other diatomic molecules that are larger (requiring a Hartree-Fock core) or charged (requiring spheroidal Coulomb waves).

The work presented here has already been extended by others to perform calculations that require accurate results at a wide range of internuclear distances. Scarlett *et al.* [148] used ratios of dissociative excitation, excitation radiative decay dissociation, and predissociation through excited states in order to calculate the electron-impact dissociation of H_2 into neutral fragments. Figure 5.16 contains the vibrationally resolved electron-impact excitation cross sections to low-lying H_2 singlet states of Tapley *et al.* [149], which were in turn used by Tapley *et al.* [150] to obtain dissociative excitation cross sections. Currently these spheroidal results are being used to tune phenomenological potentials in vibrational close-coupling calculations in order to generate cross sections between vibrational levels of the ground and excited electronic states. Finally, Zammit *et al.* [151] are using the underlying spheroidal mathematics developed for this work in photon scattering calculations including photodissociation on H_2^+.

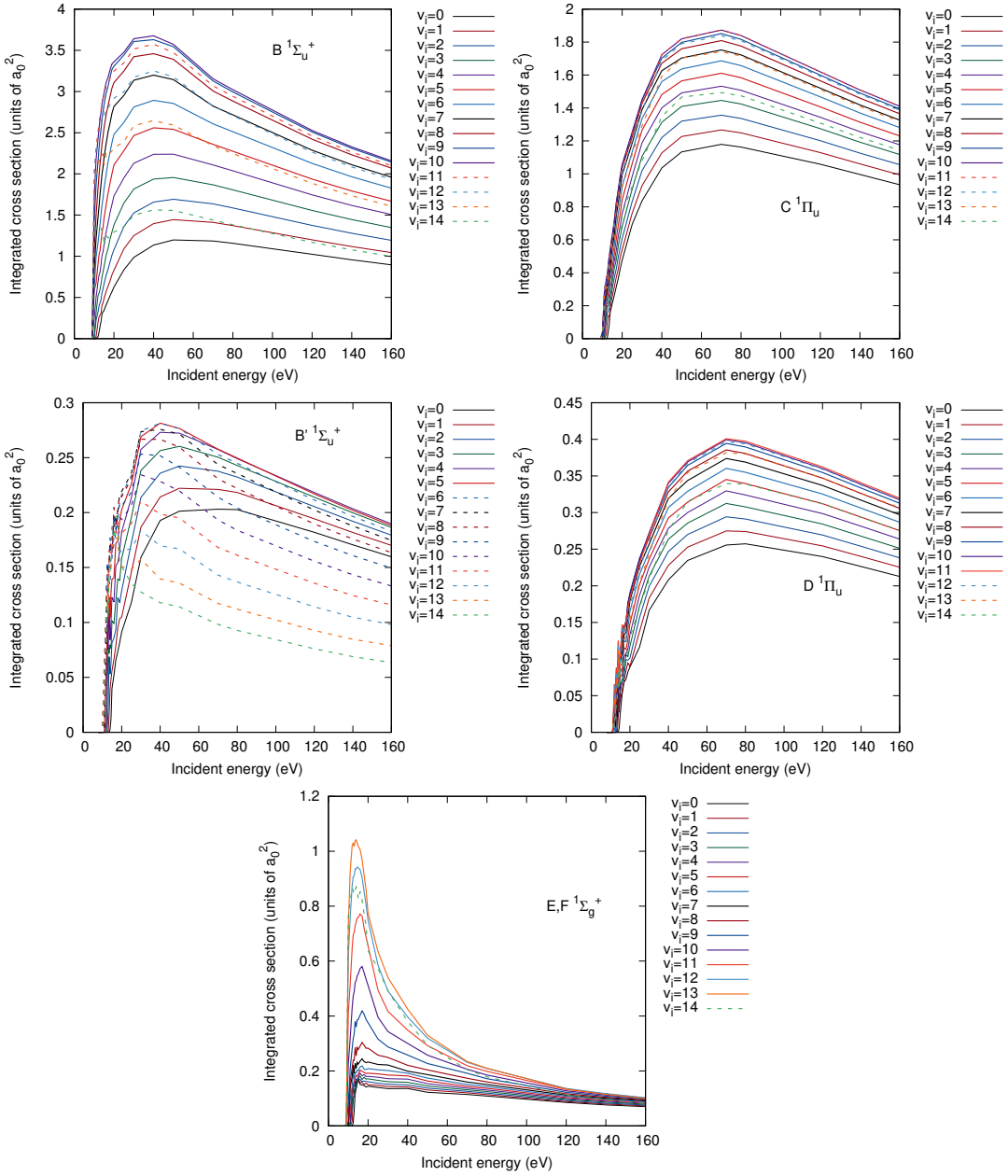

Figure 5.16: Electron-impact excitation cross sections summed over all final vibrational levels in the $B\,^1\Sigma_u^+$, $C\,^1\Pi_u$, $B'\,^1\Sigma_u^+$, $D\,^1\Pi_u$, and E,$F\,^1\Sigma_g^+$ states of H_2. Results are presented for scattering on each of the $v_i = 0 - 14$ vibrational levels of the $X\,^1\Sigma_g^+$ state. Dashed lines indicate declining cross section with increasing v_i.

Chapter 6

Conclusion

In this work we have developed the Convergent Close-Coupling method for electron and positron collisions with diatomic molecules in both the spherical and spheroidal coordinate systems. Starting with the Born-Oppenheimer approximation to separate electronic and nuclear motion, the spheroidal formulation is demonstrated to be accurate for all values of internuclear separation required for vibrational states, thus allowing us to perform accurate adiabatic-nuclei calculations where vibrational processes are important.

One-centre calculations of positron scattering on H_2 compare well to the spherical results for both grand total and ionisation plus positronium formation cross sections. More calculations are required here, and a two-centre approach is planned for spheroidal coordinates in order to obtain accurate results in the extended Ore gap.

Total ionisation and electron-impact excitation cross sections are also largely in agreement with both the published spherical results and experimental data, with the exception of the expected unphysical spikes in fixed-nuclei calculations near excitation thresholds. The adiabatic-nuclei results of $b\,^3\Sigma_u^+$ excitation also agree well with the recent benchmark results [114] but are still somewhat unstable and may require a more dense grid of internuclear separations. The confirmation of spherical and spheroidal results with one another gives us great confidence that both formulations have been implemented correctly and are producing accurate cross sections.

The first major success of the spheroidal formulation comes from the grand total cross section, for which the prediction exhibits better agreement with experiment (particularly in the elastic region) than the spherical formulation and excellent overall agreement when we apply the adiabatic-nuclei approximation.

This illustrates the importance of accurate structure at all values of internuclear separation within the span of vibrational states in order to account for nuclear motion. This accuracy also allows us to obtain the $v = 0 \rightarrow 1$ vibrational excitation cross section, which has long been the source of dispute between two different experimental methods. Our results are largely in agreement with the swarm experiments [139, 140] over the crossed-beam experiments [127, 132, 138]. We believe that our contribution can help to resolve the controversy with the development of a vibrational close-coupling implementation.

We also presented elastic differential cross sections at 16 energies between 1–100 eV with overall excellent agreement with experiment. The adiabatic-nuclei approximation makes a minor difference, predictably around 3 eV where vibrational processes are most significant. At high energies the cross sections require increasingly larger angular momentum expansions to achieve convergence, and this may not always be computationally practical.

The spheroidal formulation was also applied to scattering from the $c\,^3\Pi_u$ state, which is metastable with a mean lifetime in the order of 1 ms [145] and has a ground vibrational state mean internuclear distance of $R = 2.022$ (as opposed to the $R = 1.448$ of the ground electronic state). Therefore, this target requires a level of accuracy that treatments in spherical coordinates cannot achieve to date. In particular, the $c\,^3\Pi_u$ and $a\,^3\Sigma_g^+$ energy curves are incredibly close to one another, leading to a large interaction and cross section between the two, in stark difference to previous calculations with poorer electronic structure [146, 147].

Finally, we note that this work has been used by colleagues to calculate the ratios of various electron-impact dissociation pathways [148], vibrationally-resolved electron-impact singlet state excitation cross sections [149], the resulting dissociative excitation cross sections [150], and photodissociation [151].

The spheroidal formulation of the CCC method presented here will be the foundation for theoretical extensions and future study of various molecular processes with the aim of generating comprehensive data sets for scattering on diatomics. An important step would be to find a robust means for generating spheroidal Coulomb waves to calculate scattering on charged targets, and the implementation of a Hartree-Fock core for larger diatomics should follow a parallel course to that of atomic scattering. We are also developing vibrational and rotational close-coupling theories that will work alongside the current code and improve upon the adiabatic-nuclei approximation.

Appendix A

Coordinate systems

In this work we use spherical coordinates (r, θ, ϕ) with the convention that $\theta \in [0, \pi]$ is the *inclination angle* measured from the positive z-axis, and $\phi \in [0, 2\pi)$ is the *azimuthal angle* measured from the positive x-axis in the xy-plane. An alternative convention instead has the *elevation angle* as $\theta \in [-\pi/2, \pi/2]$ and azimuthal angle $\phi \in (-\pi, \pi]$ both measured from the positive z-axis, analogous to geographical latitude and longitude respectively.

Spheroidal coordinates (ξ, η, ϕ) are the generalisation of the elliptical coordinate system into three dimensions. These systems are anchored by two foci at $z = \pm\frac{R}{2}$ which makes spheroidal coordinates an intuitive choice for describing diatomic molecules. The internuclear vector $\mathbf{R}$ joins the two foci and its magnitude R is termed the internuclear distance.

The elliptical coordinate system can be rotated around an axis perpendicular to $\mathbf{R}$ (x or y) to obtain oblate spheroidal coordinates, or the axis parallel to $\mathbf{R}$ (z) for prolate spheroidal coordinates. The latter choice takes advantage of the rotational symmetry of diatomic molecules and so we employ it in this work.

Prolate (oblate) spheroidal coordinates degenerate into spherical coordinates in the inclination (elevation) angle convention when the distance between the foci (R) is zero.

A.1 Prolate spheroidal coordinates

In this project we take the two nuclei of a diatomic molecule to be at the foci in prolate spheroidal coordinates (ξ, η, ϕ). This coordinate system is defined in

terms of spherical variables as

$$\xi = \frac{r_1 + r_2}{R} \in [1, \infty) \qquad \eta = \frac{r_1 - r_2}{R} \in (-1, 1] \qquad \phi \in [0, 2\pi) \tag{A.1}$$

where $r_1 = \sqrt{x^2 + y^2 + (z + \frac{R}{2})^2}$ and $r_2 = \sqrt{x^2 + y^2 + (z - \frac{R}{2})^2}$ are the distances from nucleus 1 and 2 respectively.

In terms of cartesian coordinates we have the transformations

$$\begin{aligned} \xi &= \frac{1}{R}\left(\sqrt{x^2 + y^2 + (z + \tfrac{R}{2})^2} + \sqrt{x^2 + y^2 + (z - \tfrac{R}{2})^2}\right) \\ \eta &= \frac{1}{R}\left(\sqrt{x^2 + y^2 + (z + \tfrac{R}{2})^2} - \sqrt{x^2 + y^2 + (z - \tfrac{R}{2})^2}\right) \\ \phi &= \arctan\left(\frac{y}{x}\right) \end{aligned} \tag{A.2}$$

and

$$\begin{aligned} x &= \frac{R}{2}\sqrt{(\xi^2 - 1)(1 - \eta^2)}\cos\phi \\ y &= \frac{R}{2}\sqrt{(\xi^2 - 1)(1 - \eta^2)}\sin\phi \\ z &= \frac{R}{2}\xi\eta. \end{aligned} \tag{A.3}$$

In terms of spherical coordinates the transformations are

$$\begin{aligned} \xi &= \frac{1}{R}\left(\sqrt{r^2 + Rr\cos\theta + \tfrac{R^2}{4}} + \sqrt{r^2 - Rr\cos\theta + \tfrac{R^2}{4}}\right) \\ \eta &= \frac{1}{R}\left(\sqrt{r^2 + Rr\cos\theta + \tfrac{R^2}{4}} - \sqrt{r^2 - Rr\cos\theta + \tfrac{R^2}{4}}\right) \\ \phi &= \phi \end{aligned} \tag{A.4}$$

and

$$\begin{aligned} r &= \frac{R}{2}\sqrt{\xi^2 + \eta^2 - 1} \\ \theta &= \arccos\left(\frac{\xi\eta}{\sqrt{\xi^2 + \eta^2 - 1}}\right) \\ \phi &= \phi. \end{aligned} \tag{A.5}$$

Note that some authors use a different set of symbols (σ, τ, ϕ) to denote the prolate spheroidal coordinates, and others use the alternate definition (μ, ν, ϕ) where $\mu = \cosh\xi$ and $\nu = \cos\eta$.

A.2 Jacobian analysis

For a change in coordinate system from $\mathbf{x} \equiv (x_1, x_2, x_3)$ to $\mathbf{u} \equiv (u_1, u_2, u_3)$ the Jacobian matrix

$$\mathbf{J} = \begin{bmatrix} \frac{\partial x_1}{\partial u_1} & \frac{\partial x_1}{\partial u_2} & \frac{\partial x_1}{\partial u_3} \\ \frac{\partial x_2}{\partial u_1} & \frac{\partial x_2}{\partial u_2} & \frac{\partial x_2}{\partial u_3} \\ \frac{\partial x_3}{\partial u_1} & \frac{\partial x_3}{\partial u_2} & \frac{\partial x_3}{\partial u_3} \end{bmatrix} \tag{A.6}$$

and its inverse

$$\mathbf{J}^{-1} = \begin{bmatrix} \frac{\partial u_1}{\partial x_1} & \frac{\partial u_1}{\partial x_2} & \frac{\partial u_1}{\partial x_3} \\ \frac{\partial u_2}{\partial x_1} & \frac{\partial u_2}{\partial x_2} & \frac{\partial u_2}{\partial x_3} \\ \frac{\partial u_3}{\partial x_1} & \frac{\partial u_3}{\partial x_2} & \frac{\partial u_3}{\partial x_3} \end{bmatrix} \tag{A.7}$$

contain all first derivatives between the coordinates. The determinant of the Jacobian gives the integration weight for the new coordinate system. The derivatives are also useful for finding the scale factors

$$h_i = \sqrt{\left(\frac{\partial x_1}{\partial u_i}\right)^2 + \left(\frac{\partial x_2}{\partial u_i}\right)^2 + \left(\frac{\partial x_3}{\partial u_i}\right)^2}, \tag{A.8}$$

where $i \in \{1, 2, 3\}$. These can be used to determine the form of various differential operators, including the Laplacian

$$\hat{\nabla}^2 = \frac{1}{h_1 h_2 h_3}\left[\frac{\partial}{\partial u_1}\left(\frac{h_2 h_3}{h_1}\frac{\partial}{\partial u_1}\right) + \frac{\partial}{\partial u_2}\left(\frac{h_1 h_3}{h_2}\frac{\partial}{\partial u_2}\right) + \frac{\partial}{\partial u_3}\left(\frac{h_1 h_2}{h_3}\frac{\partial}{\partial u_3}\right)\right], \tag{A.9}$$

which is used in the kinetic energy operator.

Spherical coordinates

With the cartesian-spherical coordinate transformations

$$\begin{aligned} x &= r\sin\theta\cos\phi \\ y &= r\sin\theta\sin\phi \\ z &= r\cos\theta \end{aligned} \tag{A.10}$$

and reverse transformations

$$\begin{aligned} r &= \sqrt{x^2+y^2+z^2} \\ \theta &= \arccos\left(\frac{z}{\sqrt{x^2+y^2+z^2}}\right) \\ \phi &= \arctan\left(\frac{y}{x}\right) \end{aligned} \tag{A.11}$$

we can determine the spherical Jacobian matrix

$$\mathbf{J} = \begin{bmatrix} \frac{\partial x}{\partial r} = \sin\theta\cos\phi & \frac{\partial x}{\partial \theta} = r\cos\theta\cos\phi & \frac{\partial x}{\partial \phi} = -r\sin\theta\sin\phi \\ \frac{\partial y}{\partial r} = \sin\theta\sin\phi & \frac{\partial y}{\partial \theta} = r\cos\theta\sin\phi & \frac{\partial y}{\partial \phi} = r\sin\theta\cos\phi \\ \frac{\partial z}{\partial r} = \cos\theta & \frac{\partial z}{\partial \theta} = -r\sin\theta & \frac{\partial z}{\partial \phi} = 0 \end{bmatrix} \tag{A.12}$$

and its inverse

$$\mathbf{J}^{-1} = \begin{bmatrix} \frac{\partial r}{\partial x} = \sin\theta\cos\phi & \frac{\partial r}{\partial y} = \sin\theta\sin\phi & \frac{\partial r}{\partial z} = \cos\theta \\ \frac{\partial \theta}{\partial x} = \frac{\cos\theta\cos\phi}{r} & \frac{\partial \theta}{\partial y} = \frac{\cos\theta\sin\phi}{r} & \frac{\partial \theta}{\partial z} = \frac{-\sin\theta}{r} \\ \frac{\partial \phi}{\partial x} = \frac{-\sin\phi}{r\sin\theta} & \frac{\partial \phi}{\partial y} = \frac{\cos\phi}{r\sin\theta} & \frac{\partial \phi}{\partial z} = 0 \end{bmatrix}, \tag{A.13}$$

from which we determine the spherical integration weight to be

$$\mathrm{d}\mathbf{r} = \det(\mathbf{J})\mathrm{d}r\mathrm{d}\theta\mathrm{d}\phi = r^2\sin\theta\mathrm{d}r\mathrm{d}\theta\mathrm{d}\phi. \tag{A.14}$$

The scale factors are

$$\begin{aligned} h_1 &= 1, \\ h_2 &= r, \\ h_3 &= r, \sin\theta \end{aligned} \tag{A.15}$$

for $u_1 = r$, $u_2 = \theta$, and $u_3 = \phi$ respectively, which gives the Laplacian in spherical coordinates as

$$\hat{\nabla}^2 = \frac{1}{r^2}\frac{\partial}{\partial r}\left(r^2\frac{\partial}{\partial r}\right) + \frac{1}{r^2\sin\theta}\frac{\partial}{\partial\theta}\left(\sin\theta\frac{\partial}{\partial\theta}\right) + \frac{1}{r^2\sin^2\theta}\frac{\partial^2}{\partial\phi^2}. \tag{A.16}$$

Prolate spheroidal coordinates

Repeating this procedure with our spheroidal coordinate definitions gives the Jacobian matrix

$$\mathbf{J} = \begin{bmatrix} \frac{\partial x}{\partial \xi} = \frac{R}{2}\xi\sqrt{\frac{1-\eta^2}{\xi^2-1}}\cos\phi & \frac{\partial x}{\partial \eta} = \frac{-R}{2}\eta\sqrt{\frac{\xi^2-1}{1-\eta^2}}\cos\phi & \frac{\partial x}{\partial \phi} = \frac{-R\sqrt{\xi^2-1}\sqrt{1-\eta^2}}{2}\sin\phi \\ \frac{\partial y}{\partial \xi} = \frac{R}{2}\xi\sqrt{\frac{1-\eta^2}{\xi^2-1}}\sin\phi & \frac{\partial y}{\partial \eta} = \frac{-R}{2}\eta\sqrt{\frac{\xi^2-1}{1-\eta^2}}\sin\phi & \frac{\partial y}{\partial \phi} = \frac{R\sqrt{\xi^2-1}\sqrt{1-\eta^2}}{2}\cos\phi \\ \frac{\partial z}{\partial \xi} = \frac{R}{2}\eta & \frac{\partial z}{\partial \eta} = \frac{R}{2}\xi & \frac{\partial z}{\partial \phi} = 0 \end{bmatrix} \tag{A.17}$$

as well as its inverse

$$\mathbf{J}^{-1} = \begin{bmatrix} \frac{\partial\xi}{\partial x} = \frac{2}{R}\frac{\sqrt{\xi^2-1}\sqrt{1-\eta^2}}{\xi^2-\eta^2}\xi\cos\phi & \frac{\partial\xi}{\partial y} = \frac{2}{R}\frac{\sqrt{\xi^2-1}\sqrt{1-\eta^2}}{\xi^2-\eta^2}\xi\sin\phi & \frac{\partial\xi}{\partial z} = \frac{2}{R}\frac{(\xi^2-1)}{\xi^2-\eta^2}\eta \\ \frac{\partial\eta}{\partial x} = \frac{-2}{R}\frac{\sqrt{\xi^2-1}\sqrt{1-\eta^2}}{\xi^2-\eta^2}\eta\cos\phi & \frac{\partial\eta}{\partial y} = \frac{-2}{R}\frac{\sqrt{\xi^2-1}\sqrt{1-\eta^2}}{\xi^2-\eta^2}\eta\sin\phi & \frac{\partial\eta}{\partial z} = \frac{2}{R}\frac{(1-\eta^2)}{\xi^2-\eta^2}\xi \\ \frac{\partial\phi}{\partial x} = \frac{-2}{R}\frac{1}{\sqrt{\xi^2-1}\sqrt{1-\eta^2}}\sin\phi & \frac{\partial\phi}{\partial y} = \frac{2}{R}\frac{1}{\sqrt{\xi^2-1}\sqrt{1-\eta^2}}\cos\phi & \frac{\partial\phi}{\partial z} = 0 \end{bmatrix} \tag{A.18}$$

and the Jacobian determinant $\det(\mathbf{J}) = -\frac{R^3}{8}(\xi^2-\eta^2)$. The integral limits of the spherical inclination angle $\theta : 0 \to \pi$ translates to $\eta|_{\theta=0} = 1$ and $\eta|_{\theta=\pi} = -1$, and so we choose our spheroidal integration weight to be

$$\mathrm{d}\boldsymbol{\xi} = -\det(\mathbf{J})\mathrm{d}\xi\mathrm{d}\eta\mathrm{d}\phi = \tfrac{R^3}{8}(\xi^2-\eta^2)\mathrm{d}\xi\mathrm{d}\eta\mathrm{d}\phi \tag{A.19}$$

with the integration limits $\xi : 1 \to \infty$, $\eta : -1 \to 1$, and $\phi : 0 \to 2\pi$. The scale factors are given by

$$\begin{aligned} h_1 &= \frac{R}{2}\sqrt{\frac{\xi^2-\eta^2}{\xi^2-1}} \\ h_2 &= \frac{R}{2}\sqrt{\frac{\xi^2-\eta^2}{1-\eta^2}} \\ h_3 &= \frac{R}{2}\sqrt{\xi^2-1}\sqrt{1-\eta^2} \end{aligned} \tag{A.20}$$

which gives the Laplacian as

$$\hat{\nabla}^2 = \frac{4/R^2}{\xi^2-\eta^2}\left\{\frac{\partial}{\partial\xi}\left[(\xi^2-1)\frac{\partial}{\partial\xi}\right] + \frac{\partial}{\partial\eta}\left[(1-\eta^2)\frac{\partial}{\partial\eta}\right] + \left(\frac{1}{\xi^2-1} + \frac{1}{1-\eta^2}\right)\frac{\partial^2}{\partial\phi^2}\right\} \tag{A.21}$$

in prolate spheroidal coordinates.

Appendix B

Radial functions

B.1 Laguerre polynomials

Associated Laguerre polynomials $L_a^b(x)$ are the solutions to the differential equation

$$\left[x\frac{\mathrm{d}^2}{\mathrm{d}x^2} + (b+1-x)\frac{\mathrm{d}}{\mathrm{d}x} + a\right] L_a^b(x) = 0 \tag{B.1}$$

and are orthogonal with respect to degree

$$\int_0^\infty x^b \exp(-x) L_{a'}^b(x) L_a^b(x) dx = \frac{(a+b)!}{a!}\delta_{a'a}. \tag{B.2}$$

These functions obey the recurrence relations

$$xL_a^b(x) = -(a+1)L_{a+1}^b(x) + (2a+b+1)L_a^b(x) - (a+b)L_{a-1}^b(x). \tag{B.3}$$

When combined with (B.2), this leads to the integral identity

$$\int_0^\infty x^{b+1} \exp(-x) \left[L_a^b(x)\right]^2 dx = \frac{(a+b)!}{a!}(2a+b+1). \tag{B.4}$$

The derivative of the Laguerre functions satisfy

$$\frac{\mathrm{d}}{\mathrm{d}x}L_a^b(x) = \frac{a}{x}L_a^b(x) - \frac{a+b}{x}L_{a-1}^b(x) \tag{B.5}$$

$$= \frac{a+1}{x}L_{a+1}^b(x) + \left(1 - \frac{a+b+1}{x}\right) L_a^b(x). \tag{B.6}$$

B.2 Hylleraas functions

The spheroidal basis functions, named after similar functions given by Hylleraas [86], are defined as

$$\Lambda_k^m(\rho;\lambda_m) = \sqrt{\lambda_m \frac{(k-1)!}{(k-1+m)!}}(\lambda_m\rho)^{m/2}\exp(-\lambda_m\rho/2)L_{k-1}^m(\lambda_m\rho) \tag{B.7}$$

and are orthonormal for similar fall-off factor λ_m. Using (B.1) we can determine that they satisfy the differential equation

$$\left\{\rho\frac{\mathrm{d}^2}{\mathrm{d}\rho^2} + \frac{\mathrm{d}}{\mathrm{d}\rho} - \frac{m^2}{4}\rho^{-1} + \lambda_m(k+\tfrac{m}{2}-\tfrac{1}{2}) - \frac{\lambda_m^2}{4}\rho\right\}\Lambda_k^m(\rho;\lambda_m) = 0. \tag{B.8}$$

From (B.3) and (B.5) we can obtain the recurrence relations

$$\begin{aligned}(\lambda_m\rho)\Lambda_k^m(\rho;\lambda_m) = -\sqrt{k(k+m)}\Lambda_{k+1}^m(\rho;\lambda_m) + (2k-1+m)\Lambda_k^m(\rho;\lambda_m)\\ - \sqrt{(k-1)(k-1+m)}\Lambda_{k-1}^m(\rho;\lambda_m)\end{aligned} \tag{B.9}$$

and

$$\begin{aligned}\frac{\mathrm{d}}{\mathrm{d}\rho}\Lambda_k^m(\rho;\lambda_m) = \left(\frac{-\lambda_m}{2} + \frac{k-1+\frac{m}{2}}{\rho}\right)\Lambda_k^m(\rho;\lambda_m)\\ - \left(\frac{\sqrt{(k-1)(k-1+m)}}{\rho}\right)\Lambda_{k-1}^m(\rho;\lambda_m),\end{aligned} \tag{B.10}$$

which will be useful in analytically determining integrals involving these functions.

B.3 Ferrers functions

In this work, associated Legendre polynomials in the domain $(1,\infty)$ will be referred to as "Ferrers functions" to distinguish them from the associated Legendre polynomials with domain $(-1,1]$. The Ferrers functions appear in the von Neumann expansion

$$\frac{1}{\mathbf{r}_i - \mathbf{r}_j} = \frac{8\pi}{R}\sum_{\lambda=0}^{\infty}\sum_{\mu=-\lambda}^{\lambda}\frac{(\lambda-\mu)!}{(\lambda+\mu)!}P_\lambda^\mu(\xi_<)Q_\lambda^\mu(\xi_>)Y_\lambda^{-\mu}(\eta_i,\phi_i)Y_\lambda^\mu(\eta_j,\phi_j) \tag{B.11}$$

which is used in the partial wave expansion of the spheroidal electron-electron potential [152].

In their most general form the Ferrers functions are defined as

$$P_\alpha^\beta(x) = \begin{cases} \frac{1}{\Gamma(1-\beta)} \left(\frac{x+1}{x-1}\right)^{\beta/2} {}_2F_1(\alpha+1, -\alpha; 1-\beta; \frac{1}{2}-\frac{1}{2}x) & \beta \neq 1, 2, 3, \ldots \\ \frac{2^{-\beta}}{\Gamma(1+\beta)}(x^2-1)^{\beta/2} {}_2F_1(\alpha+\beta+1, \beta-\alpha; 1+\beta; \frac{1}{2}-\frac{1}{2}x) & \beta = 1, 2, 3, \ldots \end{cases} \tag{B.12}$$

$$Q_\alpha^\beta(x) = \frac{\sqrt{\pi}\mathrm{e}^{\mathrm{i}\beta\pi}}{2^{\alpha+1}} \frac{\Gamma(\alpha+\beta+1)}{\Gamma(\alpha+\frac{3}{2})} \frac{(x^2-1)^{\beta/2}}{x^{\alpha+\beta+1}} {}_2F_1(\tfrac{\alpha}{2}+\tfrac{\beta}{2}+1, \tfrac{\alpha}{2}+\tfrac{\beta}{2}+\tfrac{1}{2}; \alpha+\tfrac{3}{2}; x^{-2}), \tag{B.13}$$

where $\Gamma(z)$ is the Gamma function and ${}_2F_1(a, b, c; z)$ is a hypergeometric function [153, Sec. 14.3(ii)]. In our application we only require α and β to be integers.

A convenient property of the Ferrers functions is

$$P_a^{-b}(x) = \frac{(a-b)!}{(a+b)!} P_a^b(x) \quad \text{and} \quad Q_a^{-b}(x) = \frac{(a-b)!}{(a+b)!} Q_a^b(x), \tag{B.14}$$

which means in the expansion (B.11), the $+\mu$ term

$$\frac{(\lambda-\mu)!}{(\lambda+\mu)!} P_\lambda^\mu(x) Q_\lambda^\mu(x) \tag{B.15}$$

and the $-\mu$ term

$$\frac{(\lambda-(-\mu))!}{(\lambda+(-\mu))!} P_\lambda^{-\mu}(x) Q_\lambda^{-\mu}(x) = \frac{(\lambda-\mu)!}{(\lambda+\mu)!} P_\lambda^\mu(x) Q_\lambda^\mu(x) \tag{B.16}$$

are equivalent. This permits us to calculate and store only the $\mu \geq 0$ Ferrers functions, and use

$$\frac{(\lambda-|\mu|)!}{(\lambda+|\mu|)!} P_\lambda^{|\mu|}(x) Q_\lambda^{|\mu|}(x) \tag{B.17}$$

in the electron-electron potential.

As $R \to 0$ and hence $\xi \to \infty$ the Ferrers functions have asymptotic form

$$\lim_{\xi\to\infty} P_\lambda^\mu(\xi) = \frac{1}{(\lambda-\mu)!} \frac{(2\lambda)!}{\lambda!} \left(\frac{\xi}{2}\right)^\lambda \tag{B.18}$$

$$\lim_{\xi\to\infty} Q_\lambda^\mu(\xi) = (-1)^\mu (\lambda+\mu)! \frac{(\lambda+1)!}{(2\lambda+2)!} \left(\frac{2}{\xi}\right)^{\lambda+1}, \tag{B.19}$$

and so the product, in the shifted coordinate ρ, is

$$\lim_{R\to 0} P_\lambda^\mu(\tfrac{2}{R}\rho_< + 1) Q_\lambda^\mu(\tfrac{2}{R}\rho_> + 1) = (-1)^\mu \frac{(\lambda+\mu)!}{(\lambda-\mu)!} \frac{R/2}{2\lambda+1} \frac{\rho_<^\lambda}{\rho_>^{\lambda+1}}. \tag{B.20}$$

Note that the $R/2$ factor removes the singularity in (B.11) when $R = 0$.

For convenience we define

$$\tilde{P}_\lambda^\mu(\rho;R) = (\lambda-\mu)!\left(\frac{R}{2}\right)^\lambda P_\lambda^\mu(\tfrac{2}{R}\rho+1) \tag{B.21}$$

$$\tilde{Q}_\lambda^\mu(\rho;R) = \frac{1}{(\lambda+\mu)!}\left(\frac{2}{R}\right)^{\lambda+1} Q_\lambda^\mu(\tfrac{2}{R}\rho+1), \tag{B.22}$$

which now behave as

$$\lim_{R\to 0}\tilde{P}_\lambda^\mu(\rho;R) = \frac{(2\lambda)!}{\lambda!}\left(\frac{\rho}{2}\right)^\lambda \tag{B.23}$$

$$\lim_{R\to 0}\tilde{Q}_\lambda^\mu(\rho;R) = (-1)^\mu\frac{(\lambda+1)!}{(2\lambda+2)!}\left(\frac{2}{\rho}\right)^{\lambda+1}, \tag{B.24}$$

and hence

$$\lim_{R\to 0}\tilde{P}_\lambda^\mu(\rho_<;R)\tilde{Q}_\lambda^\mu(\rho_>;R) = \frac{(-1)^\mu}{2\lambda+1}\frac{\rho_<^\lambda}{\rho_>^{\lambda+1}}, \tag{B.25}$$

which is finite at $R=0$. These definitions allow us to simplify the von Neumann expansion to

$$\frac{1}{\mathbf{r}_i-\mathbf{r}_j} = 4\pi\sum_{\lambda=0}^{\infty}\sum_{\mu=-\lambda}^{\lambda}\tilde{P}_\lambda^{|\mu|}(\rho_<;R)\tilde{Q}_\lambda^{|\mu|}(\rho_>;R)Y_\lambda^{-\mu}(\eta_i,\phi_i)Y_\lambda^\mu(\eta_j,\phi_j), \tag{B.26}$$

which collapses to the spherical partial wave expansion

$$\lim_{R\to 0}\frac{1}{\mathbf{r}_i-\mathbf{r}_j} = 4\pi\sum_{\lambda=0}^{\infty}\sum_{\mu=-\lambda}^{\lambda}\frac{(-1)^\mu}{2\lambda+1}\frac{r_<^\lambda}{r_>^{\lambda+1}}Y_\lambda^{-\mu}(\cos\theta_i,\phi_i)Y_\lambda^\mu(\cos\theta_j,\phi_j) \tag{B.27}$$

as $\rho\to r$ and $\eta\to\cos\theta$ in the combined nuclei limit.

To calculate the functions at $R=0$, we start with

$$\tilde{P}_0^0(\rho;0) = 1 \quad\text{and}\quad \tilde{Q}_0^0(\rho;0) = \frac{1}{\rho} \tag{B.28}$$

and use the recurrence relations

$$\tilde{P}_\lambda^0(\rho;0) = (2\lambda-1)\rho\tilde{P}_{\lambda-1}^0(\rho;0) \tag{B.29}$$

$$\tilde{P}_\lambda^\mu(\rho;0) = \tilde{P}_\lambda^{\mu-1}(\rho;0) \tag{B.30}$$

$$\tilde{Q}_\lambda^0(\rho;0) = \frac{1}{2\lambda+1}\frac{\tilde{Q}_{\lambda-1}^0(\rho;0)}{\rho} \tag{B.31}$$

$$\tilde{Q}_\lambda^\mu(\rho;0) = -\tilde{Q}_\lambda^{\mu-1}(\rho;0) \tag{B.32}$$

obtained from (B.21) and (B.22). For non-zero R we utilise the program of Schneider *et al.* [152].

Appendix C

Spherical Harmonics

C.1 Definitions

The spherical harmonics are solutions to the Laplace equation

$$\left\{\frac{1}{\sin\theta}\frac{\partial}{\partial\theta}\left[\sin\theta\frac{\partial}{\partial\theta}\right]+\frac{1}{\sin^2\theta}\frac{\partial^2}{\partial\phi^2}+\ell(\ell+1)\right\}Y_\ell^m(\cos\theta,\phi)=0 \tag{C.1}$$

in spherical coordinates, with $\theta\in[0,\pi)$ and $\phi\in[0,2\pi)$. When working in prolate spheroidal coordinates we instead use the angular variable $\eta\equiv\cos\theta\in(-1,1]$ which transforms (C.1) into

$$\left\{\frac{\partial}{\partial\eta}\left[(1-\eta^2)\frac{\partial}{\partial\eta}\right]+\frac{1}{1-\eta^2}\frac{\partial^2}{\partial\phi^2}+\ell(\ell+1)\right\}Y_\ell^m(\eta,\phi)=0. \tag{C.2}$$

The remainder of this appendix chapter will use spherical $\cos\theta$ but holds true for spheroidal η as well.

Explicitly, spherical harmonics can be represented as the product of an associated Legendre polynomial and an azimuthal exponential function

$$Y_\ell^m(\cos\theta,\phi)=(-1)^m\sqrt{\frac{2\ell+1}{4\pi}\frac{(\ell-m)!}{(\ell+m)!}}\,P_\ell^m(\cos\theta)\exp(\mathrm{i}m\phi) \tag{C.3}$$

and are orthonormal

$$\int_{\theta=0}^{\pi}\int_{\phi=0}^{2\pi}\overline{Y}_\ell^m(\cos\theta,\phi)Y_\ell^m(\cos\theta,\phi)\sin\theta\mathrm{d}\theta\mathrm{d}\phi=\delta_{\ell'\ell}\delta_{m'm} \tag{C.4}$$

in both ℓ and m. When aligned along the z-axis the azimuthal angle collapses to either

$$Y_\ell^m(\cos 0,\phi)=\delta_{m0}\sqrt{\frac{2\ell+1}{4\pi}} \tag{C.5}$$

or

$$Y_\ell^m(\cos\pi,\phi) = (-1)^\ell \delta_{m0}\sqrt{\frac{2\ell+1}{4\pi}}. \tag{C.6}$$

The latter is a direct consequence of the reflection formula

$$Y_\ell^m\big(\cos(\pi-\theta),\phi+\pi\big) = (-1)^\ell Y_\ell^m(\cos\theta,\phi). \tag{C.7}$$

The harmonics also satisfy the addition relation

$$\sum_{m=-\ell}^{\ell} \overline{Y}_\ell^m(\cos\theta_1,\phi_1) Y_\ell^m(\cos\theta_2,\phi_2)$$
$$= \frac{2\ell+1}{4\pi} P_\ell\left(\cos\theta_1\cos\theta_2 + \sin\theta_1\sin\theta_2\cos(\phi_1-\phi_2)\right) \tag{C.8}$$

and hence

$$\sum_{m=-\ell}^{\ell} |Y_\ell^m(\cos\theta,\phi)|^2 = \frac{2\ell+1}{4\pi} \tag{C.9}$$

when $\theta_1 = \theta_2$ and $\phi_1 = \phi_2$.

C.2 Functional forms

Here we list the explicit forms for some of the smaller spherical harmonics. For the equivalent expressions in spheroidal coodinates one only needs to convert $\cos\theta \leftrightarrow \eta$ and $\sin\theta \leftrightarrow \sqrt{1-\eta^2}$. These functions are useful for replacing expressions involving θ (or η) and ϕ inside angular integrals, permitting the use of the angular momentum algebra described in the following appendix.

$$\sqrt{4\pi}Y_0^0(\cos\theta,\phi) = 1 \tag{C.10}$$

$$\sqrt{\tfrac{4\pi}{3}}Y_1^0(\cos\theta,\phi) = \cos\theta \tag{C.11}$$

$$\sqrt{\tfrac{4\pi}{3}}Y_1^{\pm1}(\cos\theta,\phi) = \mp\sin\theta\frac{\mathrm{e}^{\pm\mathrm{i}\phi}}{\sqrt{2}} \tag{C.12}$$

$$\tfrac{2}{3}\sqrt{\tfrac{4\pi}{5}}Y_2^0(\cos\theta,\phi) = \cos^2\theta - \tfrac{1}{3} \tag{C.13}$$

$$\tfrac{2}{5}\sqrt{\tfrac{4\pi}{7}}Y_3^0(\cos\theta,\phi) = \cos^3\theta - \tfrac{3}{5}\cos\theta \tag{C.14}$$

$$\tfrac{4}{5\sqrt{3}}\sqrt{\tfrac{4\pi}{7}}Y_3^{\pm1}(\cos\theta,\phi) = \mp(\cos^2\theta - \tfrac{1}{5})\sin\theta\mathrm{e}^{\pm\mathrm{i}\phi} \tag{C.15}$$

C.3 Recurrence relations

Spherical harmonics obey the following recurrence relations:

$$\cos\theta Y_\ell^m(\cos\theta,\phi) = \sqrt{\tfrac{(\ell-m)(\ell+m)}{(2\ell-1)(2\ell+1)}}\, Y_{\ell-1}^m(\cos\theta,\phi) + \sqrt{\tfrac{(\ell+1-m)(\ell+1+m)}{(2\ell+1)(2\ell+3)}}\, Y_{\ell+1}^m(\cos\theta,\phi) \tag{C.16}$$

$$\begin{aligned}\sin^2\theta\, Y_\ell^m(\cos\theta,\phi) = & -\tfrac{1}{2\ell-1}\sqrt{\tfrac{(\ell-1-m)(\ell-1+m)(\ell-m)(\ell+m)}{(2\ell-3)(2\ell+1)}}\, Y_{\ell-2}^m(\cos\theta,\phi) \\ + 2\,\tfrac{\ell(\ell+1)+m^2-1}{(2\ell-1)(2\ell+3)}\, Y_\ell^m(\cos\theta,\phi) & - \tfrac{1}{2\ell+3}\sqrt{\tfrac{(\ell+1-m)(\ell+1+m)(\ell+2-m)(\ell+2+m)}{(2\ell+1)(2\ell+5)}}\, Y_{\ell+2}^m(\cos\theta,\phi)\end{aligned} \tag{C.17}$$

$$\begin{aligned}\sin\theta\tfrac{\partial}{\partial\cos\theta}\left[Y_\ell^m(\cos\theta,\phi)\right] = \tfrac{1}{2}\Big[&\sqrt{\ell+1-m}\sqrt{\ell+m}\,\mathrm{e}^{+\mathrm{i}\phi}\, Y_\ell^{m-1}(\cos\theta,\phi) \\ &- \sqrt{\ell-m}\sqrt{\ell+1+m}\,\mathrm{e}^{-\mathrm{i}\phi}\, Y_\ell^{m+1}(\cos\theta,\phi)\Big]\end{aligned} \tag{C.18}$$

$$\begin{aligned}\sin^2\theta\tfrac{\partial}{\partial\cos\theta}\left[Y_\ell^m(\cos\theta,\phi)\right] = (\ell+1)&\sqrt{\frac{(\ell-m)(\ell+m)}{(2\ell-1)(2\ell+1)}}Y_{\ell-1}^m(\cos\theta,\phi) \\ &- \ell\sqrt{\frac{(\ell+1-m)(\ell+1+m)}{(2\ell+1)(2\ell+3)}}Y_{\ell+1}^m(\cos\theta,\phi)\end{aligned} \tag{C.19}$$

$$\tfrac{\partial}{\partial\phi}\left[Y_l^m(\eta,\phi)\right] = \mathrm{i}mY_l^m(\eta,\phi) \tag{C.20}$$

$$\begin{aligned}\tfrac{m}{\sin\theta}Y_\ell^m(\cos\theta,\phi) &= \tfrac{-1}{2}\sqrt{\tfrac{2\ell+1}{2\ell-1}}\Big[\sqrt{\ell-1+m}\sqrt{\ell+m}\,\mathrm{e}^{+\mathrm{i}\phi}\, Y_{\ell-1}^{m-1}(\cos\theta,\phi) \\ &\qquad + \sqrt{\ell-1-m}\sqrt{\ell-m}\,\mathrm{e}^{-\mathrm{i}\phi}\, Y_{\ell-1}^{m+1}(\cos\theta,\phi)\Big]\end{aligned} \tag{C.21}$$

$$\begin{aligned}&= \tfrac{-1}{2}\sqrt{\tfrac{2\ell+1}{2\ell+3}}\Big[\sqrt{\ell+1-m}\sqrt{\ell+2-m}\,\mathrm{e}^{+\mathrm{i}\phi}\, Y_{\ell+1}^{m-1}(\cos\theta,\phi) \\ &\qquad + \sqrt{\ell+1+m}\sqrt{\ell+2+m}\,\mathrm{e}^{-\mathrm{i}\phi}\, Y_{\ell+1}^{m+1}(\cos\theta,\phi)\Big]\end{aligned} \tag{C.22}$$

$$\begin{aligned}\sin\theta\exp(\pm\mathrm{i}\phi)Y_l^m(\cos\theta,\phi) = \pm&\sqrt{\frac{(l\mp m-1)(l\mp m)}{(2l-1)(2l+1)}}Y_{l-1}^{m\pm1}(\cos\theta,\phi) \\ \mp&\sqrt{\frac{(l\pm m+1)(l\pm m+2)}{(2l+1)(2l+3)}}Y_{l+1}^{m\pm1}(\cos\theta,\phi)\end{aligned} \tag{C.23}$$

Appendix D

Angular momentum algebra

D.1 Clebsch-Gordan coefficients

Following Rose [154], we can express the integral of three spherical harmonics in terms of Clebsch-Gordan coefficients

$$\sqrt{\frac{4\pi}{2\lambda+1}}\iint_{4\pi}\overline{Y}_{\ell'}^{m'}(\Omega)Y_{L}^{m_L}(\Omega)Y_{\ell}^{m}(\Omega)\mathrm{d}\Omega=(-1)^{\lambda}C_{0\;0\;0}^{\ell'\;\lambda\;\ell}C_{m\;\mu\;m'}^{\ell\;\lambda\;\ell'}, \tag{D.1}$$

where in spherical coordinates the solid angle is $\Omega \equiv (\cos\theta, \phi)$ and therefore $\mathrm{d}\Omega = \sin\theta \mathrm{d}\theta\mathrm{d}\phi$, and in spheroidal it is $\Omega \equiv (\eta, \phi)$ and hence $\mathrm{d}\Omega = \mathrm{d}\eta\mathrm{d}\phi$. Due to the properties of Clebsch-Gordan coefficients, (D.1) is only nonzero when the conditions

$$\begin{gathered}|\ell'-\ell|\leq\lambda\leq\ell'+\ell\\ \ell'+\lambda+\ell\text{ even}\quad\Leftrightarrow\quad(-1)^{\ell'+\ell}=(-1)^{\lambda}\\ \mu=m'-m\end{gathered} \tag{D.2}$$

are met. In the degenerate case of $L = m_L = 0$ we can use

$$C_{0\;0\;0}^{\ell'\;0\;\ell}C_{m\;0\;m'}^{\ell\;0\;\ell'}=\delta_{\ell'\ell}\delta_{m'm}. \tag{D.3}$$

Individual coefficients have many symmetry properties, including

$$C_{m\;\mu\;m'}^{\ell\;\lambda\;\ell'}=(-1)^{\ell+\lambda-\ell'}C_{\mu\;m\;m'}^{\lambda\;\ell\;\ell'}. \tag{D.4}$$

In this work all angular functions are made from spherical harmonics, including in the spheroidal approach. This means we can use the properties of spherical harmonics to determine the angular integrals analytically. When there is a combination of powers of $\cos\theta$, $\sin\theta$, and $\mathrm{e}^{\mathrm{i}\phi}$, we can use the explicit functional forms

in Appendix C.2 to transform them into a third spherical harmonic and utilise (D.1). If it cannot be transformed, or if there is a derivative acting on one of the harmonics, we can instead use the recurrence relations of Appendix C.3 followed by the orthonormality condition (C.4).

D.2 Rotation and Wigner D-matrices

Spherical harmonics can be rotated from one orientation $\hat{q}_1$ to another $\hat{q}_2$ by

$$Y_\ell^\mu(\hat{q}_1) = \sum_{m=-\ell}^{\ell} \mathcal{D}^\ell_{\mu m}(\boldsymbol{\beta}) Y_\ell^m(\hat{q}_2) \tag{D.5}$$

using the Wigner D-matrices $\mathcal{D}^\ell_{\mu m}(\boldsymbol{\beta})$. The Euler angles $\boldsymbol{\beta} = (\alpha, \beta, \gamma)$ are such that $\beta \in [0, \pi)$ is a polar angle and $\alpha, \gamma \in [0, 2\pi)$ are azimuthal angles. In this document the z-y'-z'' convention is adopted; that is, first there is a rotation α around the z-axis, then β around the new y'-axis, and finally γ around the new z''-axis.

The integration weight $\mathrm{d}\boldsymbol{\beta} = \sin\beta \mathrm{d}\alpha \mathrm{d}\beta\ \mathrm{d}\gamma$ gives rise to

$$\int \mathrm{d}\boldsymbol{\beta} = 8\pi^2, \tag{D.6}$$

and so the integral

$$\int f(\boldsymbol{\beta}) \frac{\mathrm{d}\boldsymbol{\beta}}{8\pi^2} \tag{D.7}$$

averages the function $f(\boldsymbol{\beta})$ over all Euler angles. The Wigner D-matrices are orthogonal in all indices

$$\int \overline{\mathcal{D}}^{\ell'}_{\mu' m'}(\boldsymbol{\beta}) \mathcal{D}^\ell_{\mu m}(\boldsymbol{\beta}) \mathrm{d}\boldsymbol{\beta} = \frac{8\pi^2}{2\ell+1} \delta_{\ell'\ell} \delta_{m'm} \delta_{\mu'\mu} \tag{D.8}$$

when integrated over the Euler angles.

Appendix E

Spheroidal angular integrals

Compared to the spherical volume element $\mathrm{d}V = r^2 \sin\theta \mathrm{d}r\mathrm{d}\theta\mathrm{d}\phi$, the nonseparable factor in the spheroidal $\mathrm{d}V = [(\rho + \frac{R}{2})^2 - (\frac{R}{2}\eta)^2]$ complicates integrations taken in this space. In this work we perform spheroidal integrations in two steps: first, analytically resolve the angular integrals with the Jacobian to produce a quadratic, and then integrate it and the radial parts numerically.

In the spheroidal case we can say that each angular function has the form of a spheroidal harmonic

$$\Upsilon^{m_\alpha}_{\lambda_\alpha}(\eta, \phi; c_\alpha) = \sum_{\ell_\alpha} D^{m_\alpha}_{\lambda_\alpha \ell_\alpha}(c) Y^{m_\alpha}_{\ell_\alpha}(\eta, \phi) \tag{E.1}$$

for the sake of generality. Spheroidal harmonics are orthonormal

$$\iint \overline{\Upsilon}^{m_\gamma}_{\lambda_\gamma}(\eta, \phi; c) \Upsilon^{m_\alpha}_{\lambda_\alpha}(\eta, \phi; c) = \delta_{\lambda_\gamma \lambda_\alpha} \delta_{m_\gamma m_\alpha} \tag{E.2}$$

for identical c when the Jacobian is absent. We can extend this to arbitrary c_γ and c_α, and include an arbitrary spherical harmonic $Y^m_\ell(\eta, \phi)$, by defining the *spherical angular overlap* as

$$\begin{aligned} j^{(\gamma,\alpha)}_{\ell,m} &= \iint \overline{\Upsilon}^{m_\gamma}_{\lambda_\gamma}(\eta, \phi; c_\gamma) \sqrt{\tfrac{4\pi}{2\ell+1}} Y^m_\ell(\eta, \phi) \Upsilon^{m_\alpha}_{\lambda_\alpha}(\eta, \phi; c_\alpha) \mathrm{d}\eta \mathrm{d}\phi \\ &= (-1)^\ell \sum_{\ell_\gamma, \ell_\alpha} D^{m_\gamma}_{\lambda_\gamma \ell_\gamma}(c_\gamma) D^{m_\alpha}_{\lambda_\alpha \ell_\alpha}(c_\alpha) C^{\ell_\gamma \; \ell \; \ell_\alpha}_{0 \; 0 \; 0} C^{\ell_\alpha \;\; \ell \;\; \ell_\gamma}_{m_\alpha \; m \; m_\gamma}. \end{aligned} \tag{E.3}$$

This overlap is non-zero if $(-1)^\ell = (-1)^{\ell_\gamma - \ell_\alpha}$ and $m = m_\gamma - m_\alpha$ from the properties of the Clebsch-Gordan coefficients (D.2), and becomes similar to the spherical result (D.1)

$$j^{(\gamma,\alpha)}_{\ell,m}\Big|_{R=0} = (-1)^\ell C^{\lambda_\gamma \; \ell \; \lambda_\alpha}_{0 \; 0 \; 0} C^{\lambda_\alpha \;\; \ell \;\; \lambda_\gamma}_{m_\alpha \; m \; m_\gamma} \tag{E.4}$$

in the atomic limit.

For the same integration with the Jacobian we define the *spheroidal angular quadratic* as

$$\begin{aligned} J^{(\gamma,\alpha)}_{\ell,m}(\rho) = & \iint \overline{\Upsilon}^{m_\gamma}_{\lambda_\gamma}(\eta,\phi;c_\gamma)\sqrt{\tfrac{4\pi}{2\ell+1}}Y^m_\ell(\eta,\phi)\Upsilon^{m_\alpha}_{\lambda_\alpha}(\eta,\phi;c_\alpha) \\ & \qquad \times [\rho(\rho+R)+\tfrac{R^2}{4}(1-\eta^2)]\mathrm{d}\eta\mathrm{d}\phi \\ = & -\frac{R^2}{4}\frac{j^{(\gamma,\alpha)}_{\ell-2,m}}{2\ell-1}\sqrt{\frac{(\ell-1-m)(\ell-1+m)(\ell-m)(\ell+m)}{(2\ell-3)(2\ell+1)}} \\ & + j^{(\gamma,\alpha)}_{\ell,m}\left[\rho(\rho+R)+\frac{R^2}{2}\frac{\ell(\ell+1)+m^2-1}{(2\ell-1)(2\ell+3)}\right] \\ & - \frac{R^2}{4}\frac{j^{(\gamma,\alpha)}_{\ell+2,m}}{2\ell+3}\sqrt{\frac{(\ell+1-m)(\ell+1+m)(\ell+2-m)(\ell+2+m)}{(2\ell+1)(2\ell+5)}}, \end{aligned} \tag{E.5}$$

where we have used the recurrence relation (C.17). The quadratics have the same selection rules as the overlaps above but are additionally coupled to $\ell \pm 2$ terms. The simplest case ($\ell = m = 0$) is proportional to the overlap between two spheroidal harmonics and is evaluated as

$$\begin{aligned} J^{(\gamma,\alpha)}_{0,0}(\rho) &= j^{(\gamma,\alpha)}_{0,0}(\rho^2+R\rho+\tfrac{R^2}{6}) - \tfrac{R^2}{6}j^{(\gamma,\alpha)}_{2,0} \\ &= \sqrt{4\pi}\langle\lambda_\gamma m_\gamma|\lambda_\alpha m_\alpha\rangle, \end{aligned} \tag{E.6}$$

while in the atomic limit the quadratic reduces to

$$J^{(\gamma,\alpha)}_{\ell,m}(\rho)\Big|_{R=0} = (-1)^\ell C^{\lambda_\gamma\ \ell\ \lambda_\alpha}_{0\ 0\ 0} C^{\lambda_\alpha\ \ \ell\ \ \lambda_\gamma}_{m_\alpha\ m\ m_\gamma}\rho^2 \tag{E.7}$$

and the coupling to $\ell \pm 2$ terms vanishes.

Appendix F

Miscellaneous

The spherical equivalent to the von Neumann expansion (B.11) is the Laplace multipole expansion

$$\frac{1}{|\mathbf{r}_i - \mathbf{r}_j|} = 4\pi \sum_{\ell=0}^{\infty} \sum_{m=-\ell}^{\ell} \frac{(-1)^m}{2\ell+1} \frac{r_<^\ell}{r_>^{\ell+1}} Y_\ell^{-m}(\cos\theta_i, \phi_i) Y_\ell^m(\cos\theta_j, \phi_j) \tag{F.1}$$

with $r_< = \min(r_i, r_j)$ and $r_> = \max(r_i, r_j)$.

The plane wave Coulomb integral, otherwise known as Bethe's integral [155], is given as

$$\int \frac{\exp(\mathrm{i}\mathbf{q}\cdot\mathbf{r})}{|\mathbf{r} - \mathbf{r}_j|} \mathrm{d}\mathbf{r} = \frac{4\pi}{q^2} \exp(\mathrm{i}\mathbf{q}\cdot\mathbf{r}_j) \tag{F.2}$$

and has the limiting form

$$\int \frac{\exp(\mathrm{i}\mathbf{q}\cdot\mathbf{r})}{r} \mathrm{d}\mathbf{r} = \frac{4\pi}{q^2}. \tag{F.3}$$

when $\mathbf{r}_j = \mathbf{0}$.

Plane waves can be expanded as

$$\mathrm{e}^{\mathrm{i}\mathbf{k}\cdot\mathbf{x}} = 4\pi \sum_{\ell=0}^{\infty} \sum_{m=-\ell}^{\ell} \mathrm{i}^\ell j_\ell(kr) \overline{Y}_\ell^m(\hat{\mathbf{k}}) Y_\ell^m(\hat{\mathbf{r}}) \tag{F.4}$$

in terms of spherical Bessel functions $j_\ell(kr)$ and spherical harmonics, or as

$$\mathrm{e}^{\mathrm{i}\mathbf{k}\cdot\mathbf{x}} = 4\pi \sum_{\lambda=0}^{\infty} \sum_{m=-\lambda}^{\lambda} \mathrm{i}^\lambda \Xi_\lambda^m(\rho; c) \overline{\Upsilon}_\lambda^m(\hat{\mathbf{k}}; c) \Upsilon_\lambda^m(\hat{\boldsymbol{\rho}}; c) \tag{F.5}$$

in terms of spheroidal radial functions (4.25) and spheroidal harmonics (4.14), which are solutions to the radial (4.7) and angular (4.8) differential equations respectively.

F.1 Oscillator strength matrix elements for perpendicular transitions in the velocity gauge

To determine the velocity gauge matrix element in (4.111) for perpendicular ($\Delta_m = \pm 1$) transitions, we will examine each term of the corresponding operator (4.119)

$$\hat{\Omega}_{\perp}^{(\mathrm{v})} = \frac{\mathrm{e}^{\pm \mathrm{i}\phi}}{\sqrt{2}} \left[\sin\theta \frac{\partial}{\partial r} - r^{-1} \sin\theta \cos\theta \frac{\partial}{\partial(\cos\theta)} \pm \frac{\mathrm{i}}{r \sin\theta} \frac{\partial}{\partial \phi} \right] \tag{F.6}$$

separately. The first term acting on a spherical harmonic has the recurrence relation (C.23)

$$\sin\theta \tfrac{\mathrm{e}^{\pm \mathrm{i}\phi}}{\sqrt{2}} Y_\ell^m(\cos\theta,\phi) = \mp \tfrac{1}{\sqrt{2}} \sqrt{\tfrac{(\ell+1\pm m)(\ell+2\pm m)}{(2\ell+1)(2\ell+3)}} Y_{\ell+1}^{m\pm 1}(\cos\theta,\phi) \pm \tfrac{1}{\sqrt{2}} \sqrt{\tfrac{(\ell-1\mp m)(\ell\mp m)}{(2\ell-1)(2\ell+1)}} Y_{\ell-1}^{m\pm 1}(\cos\theta,\phi), \tag{F.7}$$

which leads to the integral

$$\left\langle \ell' m' \left| \sin\theta \tfrac{\mathrm{e}^{\pm \mathrm{i}\phi}}{\sqrt{2}} \right| \ell m \right\rangle = \begin{cases} \frac{\mp 1}{\sqrt{2}} \sqrt{\frac{(\ell+1\pm m)(\ell+2\pm m)}{(2\ell+1)(2\ell+3)}} & \ell' = \ell+1, m' = m \pm 1 \\ \frac{\pm 1}{\sqrt{2}} \sqrt{\frac{(\ell-1\mp m)(\ell\mp m)}{(2\ell-1)(2\ell+1)}} & \ell' = \ell-1, m' = m \pm 1 \end{cases} \tag{F.8}$$

$$= \pm C^{\ell' \; 1 \; \ell}_{0 \; 0 \; 0} C^{\ell \; 1 \; \ell'}_{m \; \pm 1 \; m'} \tag{F.9}$$

in terms of Clebsch-Gordan coefficients (D.1). For the second term we can combine recurrence relations (C.16) and (C.18)

$$\begin{aligned} \sin\theta\cos\theta \tfrac{\partial}{\partial(\cos\theta)} Y_\ell^m(\cos\theta,\phi) = & -\tfrac{\ell-m}{2} \sqrt{\tfrac{(\ell+1+m)(\ell+2+m)}{(2\ell+1)(2\ell+3)}} \mathrm{e}^{-\mathrm{i}\phi} Y_{\ell+1}^{m+1}(\cos\theta,\phi) + \tfrac{\ell+m}{2} \sqrt{\tfrac{(\ell+1-m)(\ell+2-m)}{(2\ell+1)(2\ell+3)}} \mathrm{e}^{\mathrm{i}\phi} Y_{\ell+1}^{m-1}(\cos\theta,\phi) \\ & -\tfrac{\ell+1+m}{2} \sqrt{\tfrac{(\ell-1-m)(\ell-m)}{(2\ell-1)(2\ell+1)}} \mathrm{e}^{-\mathrm{i}\phi} Y_{\ell-1}^{m+1}(\cos\theta,\phi) + \tfrac{\ell+1-m}{2} \sqrt{\tfrac{(\ell-1+m)(\ell+m)}{(2\ell-1)(2\ell+1)}} \mathrm{e}^{\mathrm{i}\phi} Y_{\ell-1}^{m-1}(\cos\theta,\phi) \end{aligned} \tag{F.10}$$

and for the third term we use (C.20) and (C.21)

$$\tfrac{\mathrm{i}}{\sin\theta} \tfrac{\partial}{\partial\phi} Y_\ell^m(\cos\theta,\phi) = \tfrac{2\ell+1}{2} \sqrt{\tfrac{(\ell+1+m)(\ell+2+m)}{(2\ell+1)(2\ell+3)}} \mathrm{e}^{-\mathrm{i}\phi} Y_{\ell+1}^{m+1}(\eta,\phi) + \tfrac{2\ell+1}{2} \sqrt{\tfrac{(\ell+1-m)(\ell+2-m)}{(2\ell+1)(2\ell+3)}} \mathrm{e}^{+\mathrm{i}\phi} Y_{\ell+1}^{m-1}(\eta,\phi) \tag{F.11}$$

$$= \tfrac{2\ell+1}{2} \sqrt{\tfrac{(\ell-1-m)(\ell-m)}{(2\ell-1)(2\ell+1)}} \mathrm{e}^{-\mathrm{i}\phi} Y_{\ell-1}^{m+1}(\eta,\phi) + \tfrac{2\ell+1}{2} \sqrt{\tfrac{(\ell-1+m)(\ell+m)}{(2\ell-1)(2\ell+1)}} \mathrm{e}^{+\mathrm{i}\phi} Y_{\ell-1}^{m-1}(\eta,\phi). \tag{F.12}$$

As (F.11) and (F.12) are equivalent, they can be alternatively expressed as

$$\begin{aligned}\tfrac{\mathrm{i}}{\sin\theta}\tfrac{\partial}{\partial\phi}Y_\ell^m(\cos\theta,\phi) &= \tfrac{\ell+m}{2}\sqrt{\tfrac{(\ell+1+m)(\ell+2+m)}{(2\ell+1)(2\ell+3)}}\mathrm{e}^{-\mathrm{i}\phi}Y_{\ell+1}^{m+1}(\eta,\phi) + \tfrac{\ell+m}{2}\sqrt{\tfrac{(\ell+1-m)(\ell+2-m)}{(2\ell+1)(2\ell+3)}}\mathrm{e}^{+\mathrm{i}\phi}Y_{\ell+1}^{m-1}(\eta,\phi)\\ &\quad+\tfrac{\ell+1-m}{2}\sqrt{\tfrac{(\ell-1-m)(\ell-m)}{(2\ell-1)(2\ell+1)}}\mathrm{e}^{-\mathrm{i}\phi}Y_{\ell-1}^{m+1}(\eta,\phi) + \tfrac{\ell+1-m}{2}\sqrt{\tfrac{(\ell-1+m)(\ell+m)}{(2\ell-1)(2\ell+1)}}\mathrm{e}^{+\mathrm{i}\phi}Y_{\ell-1}^{m-1}(\eta,\phi) \qquad \text{(F.13)}\\ &= \tfrac{\ell-m}{2}\sqrt{\tfrac{(\ell+1+m)(\ell+2+m)}{(2\ell+1)(2\ell+3)}}\mathrm{e}^{-\mathrm{i}\phi}Y_{\ell+1}^{m+1}(\eta,\phi) + \tfrac{\ell-m}{2}\sqrt{\tfrac{(\ell+1-m)(\ell+2-m)}{(2\ell+1)(2\ell+3)}}\mathrm{e}^{+\mathrm{i}\phi}Y_{\ell+1}^{m-1}(\eta,\phi)\\ &\quad+\tfrac{\ell+1+m}{2}\sqrt{\tfrac{(\ell-1-m)(\ell-m)}{(2\ell-1)(2\ell+1)}}\mathrm{e}^{-\mathrm{i}\phi}Y_{\ell-1}^{m+1}(\eta,\phi) + \tfrac{\ell+1+m}{2}\sqrt{\tfrac{(\ell-1+m)(\ell+m)}{(2\ell-1)(2\ell+1)}}\mathrm{e}^{+\mathrm{i}\phi}Y_{\ell-1}^{m-1}(\eta,\phi). \qquad \text{(F.14)}\end{aligned}$$

When added to (F.10), this results in

$$\tfrac{e^{+\mathrm{i}\phi}}{\sqrt{2}}[-\sin\theta\cos\theta\tfrac{\partial}{\partial(\cos\theta)}+\tfrac{\mathrm{i}}{\sin\theta}\tfrac{\partial}{\partial\phi}]Y_\ell^m(\cos\theta,\phi) = \pm\tfrac{\ell}{\sqrt{2}}\sqrt{\tfrac{(\ell+1\pm m)(\ell+2\pm m)}{(2\ell+1)(2\ell+3)}}Y_{\ell+1}^{m\pm1}(\cos\theta,\phi) \pm \tfrac{\ell+1}{\sqrt{2}}\sqrt{\tfrac{(\ell-1\mp m)(\ell\mp m)}{(2\ell-1)(2\ell+1)}}Y_{\ell-1}^{m\pm1}(\cos\theta,\phi) \qquad \text{(F.15)}$$

once we combine the $\ell+1$ and $\ell-1$ cases. By comparing (F.8) and (F.15) we can say that

$$\left\langle \ell'm' \left| \tfrac{e^{\pm\mathrm{i}\phi}}{\sqrt{2}}[-\sin\theta\cos\theta\tfrac{\partial}{\partial(\cos\theta)} \pm \tfrac{\mathrm{i}}{\sin\theta}\tfrac{\partial}{\partial\phi}] \right| \ell m \right\rangle = y_{\ell'\ell}\left\langle \ell'm' \left| \sin\theta\tfrac{\mathrm{e}^{\pm\mathrm{i}\phi}}{\sqrt{2}} \right| \ell m \right\rangle \qquad \text{(F.16)}$$

again with

$$y_{\ell'\ell} = \begin{cases} -\ell & \ell' = \ell+1 \\ \ell+1 & \ell' = \ell-1 \end{cases} \qquad \text{(F.17)}$$

as in the parallel case. Combining all this yields the matrix element

$$\langle \ell'm'|\hat{\Omega}_\perp^{(\mathrm{v})}|\ell m\rangle = \pm C^{\ell'\,1\,\ell}_{0\,0\,0}C^{\ell\;\;1\;\;\ell'}_{m\,\pm\,m'}\left(\frac{\mathrm{d}}{\mathrm{d}r}+\frac{y_{\ell'\ell}}{r}\right). \qquad \text{(F.18)}$$

Appendix G

Publication co-authorship statements

To whom it may concern,

I, Jeremy Savage, performed the primary research and writing of the following publication:

Jeremy S. Savage, Jonathan K. Tapley, Dmitry V. Fursa, Liam H. Scarlett, and Igor Bray. Electron scattering on the metastable $c\,^3\Pi_u$ state of H_2 in the spheroidal convergent close-coupling formalism. Unpublished.

Signature: Jeremy Savage (Sep 5, 2019) .....

I, as a Co-Author, endorse that this level of contribution by the candidate indicated above is appropriate.

Jonathan K. Tapley Jonathan Tapley (Sep 5, 2019) .....

Dmitry V. Fursa D. Fursa .....

Liam H. Scarlett L. Scarlett .....

Igor Bray Igor Bray (Sep 5, 2019) .....

To whom it may concern,

I, Jeremy Savage, performed the primary research and writing of the following publication:

Jeremy S. Savage, Dmitry V. Fursa, Liam H. Scarlett, Mark C. Zammit, and Igor Bray. Adiabatic-nuclei calculations of the elastic differential, integrated, and vibrational excitation cross sections of e^-–H_2. Unpublished.

Signature: ..... Jeremy Savage (Sep 5, 2019) .....

I, as a Co-Author, endorse that this level of contribution by the candidate indicated above is appropriate.

Dmitry V. Fursa ..... D. Fursa .....

Liam H. Scarlett ..... L. Scarlett .....

Mark C. Zammit ..... MZammit MZammit (Sep 5, 2019) .....

Igor Bray ..... Igor Bray (Sep 5, 2019) .....

To whom it may concern,

I, Jeremy Savage, contributed to the code development of the research and writing in the following publication:

Mark C. Zammit, Jeremy S. Savage, Dmitry V. Fursa, and Igor Bray. Complete solution of electronic excitation and ionization in electron-hydrogen molecule scattering. *Phys. Rev. Lett.* **116**(23): 233201, June 2016.

Signature: Jeremy Savage (Sep 5, 2019) .....

I, as a Co-Author, endorse that this level of contribution by the candidate indicated above is appropriate.

Mark C. Zammit MZammit (Sep 5, 2019) .....

Dmitry V. Fursa D. Fursa .....

Igor Bray Igor Bray (Sep 5, 2019) .....

To whom it may concern,

I, Jeremy Savage, contributed to the code development of the research and writing in the following publication:

Mark C. Zammit, Jeremy S. Savage, Dmitry V. Fursa, and Igor Bray. Electron-impact excitation of molecular hydrogen. *Phys. Rev. A* **95**(2): 022708, February 2017.

Signature: Jeremy Savage (Sep 5, 2019)

I, as a Co-Author, endorse that this level of contribution by the candidate indicated above is appropriate.

Mark C. Zammit MZammit (Sep 5, 2019)

Dmitry V. Fursa D. Fursa

Igor Bray Igor Bray (Sep 5, 2019)

To whom it may concern,

I, Jeremy Savage, contributed to the theoretical formulation of the research and writing in the following publication:

Mark C. Zammit, Dmitry V. Fursa, Jeremy S. Savage, and Igor Bray. Electron- and positron-molecule scattering: development of the molecular convergent close-coupling method. *J. Phys. B* **50**(12): 123001, May 2017.

Signature: Jeremy Savage (Sep 5, 2019)

I, as a Co-Author, endorse that this level of contribution by the candidate indicated above is appropriate.

Mark C. Zammit MZammit (Sep 5, 2019)

Dmitry V. Fursa D. Fursa

Igor Bray Igor Bray (Sep 5, 2019)

To whom it may concern,

I, Jeremy Savage, contributed to the theoretical development of the research in the following publication:

Liam H. Scarlett, Jonathan K. Tapley, Dmitry V. Fursa, Mark C. Zammit, Jeremy S. Savage, and Igor Bray. Low-energy electron-impact dissociative excitation of molecular hydrogen and its isotopologues. *Phys. Rev. A* **96**(6): 062708, December 2017.

Signature: Jeremy Savage (Sep 5, 2019)

I, as a Co-Author, endorse that this level of contribution by the candidate indicated above is appropriate.

Liam H. Scarlett

Jonathan K. Tapley Jonathan Tapley (Sep 5, 2019)

Dmitry V. Fursa

Mark C. Zammit MZammit (Sep 5, 2019)

Igor Bray Igor Bray (Sep 5, 2019)

To whom it may concern,

I, Jeremy Savage, performed the theoretical development for supplementary calculations in the following publication:

Liam H. Scarlett, Jonathan K. Tapley, Dmitry V. Fursa, Mark C. Zammit, Jeremy S. Savage, and Igor Bray. Electron-impact dissociation of molecular hydrogen into neutral fragments. *Eur. J. Phys. D* **72**(2): 34, February 2018.

Signature: Jeremy Savage (Sep 5, 2019) .....

I, as a Co-Author, endorse that this level of contribution by the candidate indicated above is appropriate.

Liam H. Scarlett L. Scarlett .....

Jonathan K. Tapley Jonathan Tapley (Sep 5, 2019) .....

Dmitry V. Fursa D. Fursa .....

Mark C. Zammit MZammit (Sep 5, 2019) .....

Igor Bray Igor Bray (Sep 5, 2019) .....

To whom it may concern,

I, Jeremy Savage, contributed to the theoretical formulation and code development of the research in the following publication:

Jonathan K. Tapley, Liam H. Scarlett, Jeremy S. Savage, Mark C. Zammit, Dmitry V. Fursa, and Igor Bray. Vibrationally resolved electron-impact excitation cross sections for singlet states of molecular hydrogen. *J. Phys. B* **51**: 144007, June 2018.

Signature: ..... Jeremy Savage (Sep 5, 2019)

I, as a Co-Author, endorse that this level of contribution by the candidate indicated above is appropriate.

Jonathan K. Tapley ..... Jonathan Tapley (Sep 5, 2019)

Liam H. Scarlett .....

Mark C. Zammit ..... MZammit (Sep 5, 2019)

Dmitry V. Fursa .....

Igor Bray ..... Igor Bray (Sep 5, 2019)

To whom it may concern,

I, Jeremy Savage, contributed to the theoretical formulation and code development of the research in the following publication:

Jonathan K. Tapley, Liam H. Scarlett, Jeremy S. Savage, Dmitry V. Fursa, Mark C. Zammit, and Igor Bray. Electron-impact dissociative excitation cross sections for singlet states of molecular hydrogen. *Phys. Rev. A* **98**: 032701, September 2018.

Signature: Jeremy Savage (Sep 5, 2019)

I, as a Co-Author, endorse that this level of contribution by the candidate indicated above is appropriate.

Jonathan K. Tapley Jonathan Tapley (Sep 5, 2019)

Liam H. Scarlett

Dmitry V. Fursa

Mark C. Zammit MZammit (Sep 5, 2019)

Igor Bray Igor Bray (Sep 5, 2019)

Bibliography

1. International Atomic Energy Agency. *Atomic and Plasma–Material Interaction Data for Fusion, Supplement to the Journal Nuclear Fusion* **6** (IAEA, Vienna, 1995).
2. Celiberto, R., Janev, R., Laricchiuta, A., Capitelli, M., Wadehra, J. & Atems, D. Cross section data for electron-impact inelastic processes of vibrationally excited molecules of hydrogen and its isotopes. *Atomic Data and Nuclear Data Tables* **77,** 161–213. ISSN: 0092-640X (2001).
3. Lepp, S., Stancil, P. C. & Dalgarno, A. TOPICAL REVIEW: Atomic and molecular processes in the early Universe. *Journal of Physics B Atomic Molecular Physics* **35,** R57–R80 (May 2002).
4. James, G. K., Dziczek, D., Slevin, J. A. & Bray, I. Polarization of Lyman-β radiation from atomic hydrogen excited by electron impact from near-threshold energy to 1000 eV. *Phys. Rev. A* **66,** 042710 (Oct. 2002).
5. Celiberto, R., Armenise, I., Cacciatore, M., Capitelli, M., Esposito, F., Gamallo, P., Janev, R. K., Lagan, A., Laporta, V., Laricchiuta, A., Lombardi, A., Rutigliano, M., Says, R., Tennyson, J. & Wadehra, J. M. Atomic and molecular data for spacecraft re-entry plasmas. *Plasma Sources Science and Technology* **25,** 033004 (2016).
6. Lane, N. F. The theory of electron-molecule collisions. *Rev. Mod. Phys.* **52,** 29–119 (Jan. 1980).
7. Bray, I. & Stelbovics, A. T. Convergent close-coupling calculations of electron-hydrogen scattering. *Phys. Rev. A* **46,** 6995–7011 (Dec. 1992).
8. Fursa, D. V. & Bray, I. Calculation of electron-helium scattering. *Phys. Rev. A* **52,** 1279–1297 (Aug. 1995).
9. Tennyson, J. Electronmolecule collision calculations using the R-matrix method. *Physics Reports* **491,** 29–76. ISSN: 0370-1573 (2010).

10. Pindzola, M. S., Robicheaux, F, Loch, S. D., Berengut, J. C., Topcu, T, Colgan, J, Foster, M, Griffin, D. C., Ballance, C. P., Schultz, D. R., Minami, T, Badnell, N. R., Witthoeft, M. C., Plante, D. R., Mitnik, D. M., Ludlow, J. A. & Kleiman, U. The time-dependent close-coupling method for atomic and molecular collision processes. *Journal of Physics B: Atomic, Molecular and Optical Physics* **40,** R39 (2007).

11. Peek, J. M. Improvement in the First Born Theory of Electron Scattering by Molecular Systems. I. Theory. *Phys. Rev.* **183,** 193–202 (July 1969).

12. Born, M. & Oppenheimer, R. Quantum theory of molecules. *Annalen Der Physik* **84,** 0457–0484 (1927).

13. Zammit, M. C., Fursa, D. V., Savage, J. S. & Bray, I. Electron and positron-molecule scattering: development of the molecular convergent close-coupling method. *Journal of Physics B: Atomic, Molecular and Optical Physics* **50,** 123001 (2017).

14. Abdurakhmanov, I. B., Kadyrov, A. S., Fursa, D. V. & Bray, I. Target Structure-Induced Suppression of the Ionization Cross Section for Low-Energy Antiproton-Molecular Hydrogen Collisions: Theoretical Confirmation. *Phys. Rev. Lett.* **111,** 173201 (Oct. 2013).

15. Coppola, C. M., Longo, S., Capitelli, M., Palla, F. & Galli, D. Vibrational Level Population of H_2 and $H^+{}_2$ in the Early Universe. *The Astrophysical Journal Supplement* **193,** 7 (Mar. 2011).

16. Ferland, G. J., Porter, R. L., van Hoof, P. A. M., Williams, R. J. R., Abel, N. P., Lykins, M. L., Shaw, G., Henney, W. J. & Stancil, P. C. The 2013 Release of Cloudy. *Revista Mexicana de Astronomía y Astrofísica* **49,** 137–163 (Apr. 2013).

17. Lykins, M. L., Ferland, G. J., Kisielius, R., Chatzikos, M., Porter, R. L., van Hoof, P. A. M., Williams, R. J. R., Keenan, F. P. & Stancil, P. C. Stout: Cloudy's Atomic and Molecular Database. *The Astrophysical Journal* **807,** 118 (July 2015).

18. Sugimura, K., Coppola, C. M., Omukai, K., Galli, D. & Palla, F. Role of the H_2^+ channel in the primordial star formation under strong radiation field and the critical intensity for the supermassive star formation. *Monthly Notices of the Royal Astronomical Society* **456,** 270–277 (Feb. 2016).

19. Johnson, P. V., Malone, C. P., Khakoo, M. A., McConkey, J. W. & Kanik, I. Electron collisions with constituents of planetary atmospheres. *Journal of Physics: Conference Series* **88,** 012069 (2007).

20. Fox, J. L., Galand, M. I. & Johnson, R. E. Energy Deposition in Planetary Atmospheres by Charged Particles and Solar Photons. *Space Science Reviews* **139,** 3–62. ISSN: 1572-9672 (Aug. 2008).

21. Huo, W. M., McKoy, V., Lima, M. A. P. & Gibson, T. L. in, 152–196 (American Institute of Aeronautics and Astronautics, 1986).

22. Van Dorp, W. F. The role of electron scattering in electron-induced surface chemistry. *Phys. Chem. Chem. Phys.* **14,** 16753–16759 (2012).

23. Sanche, L. Low energy electron-driven damage in biomolecules. *The European Physical Journal D - Atomic, Molecular, Optical and Plasma Physics* **35,** 367–390. ISSN: 1434-6079 (Aug. 2005).

24. Ragauskas, A. J., Williams, C. K., Davison, B. H., Britovsek, G., Cairney, J., Eckert, C. A., Frederick, W. J., Hallett, J. P., Leak, D. J., Liotta, C. L., Mielenz, J. R., Murphy, R., Templer, R. & Tschaplinski, T. The Path Forward for Biofuels and Biomaterials. *Science* **311,** 484–489. ISSN: 00368075, 10959203 (2006).

25. De Oliveira, E. M., da Costa, R. F., Sanchez, S. d., Natalense, A. P. P., Bettega, M. H. F., Lima, M. A. P. & Varella, M. T. d. N. Low-energy electron scattering by cellulose and hemicellulose components. *Phys. Chem. Chem. Phys.* **15,** 1682–1689 (2013).

26. Madison, D. H. & Al-Hagan, O. The Distorted-Wave Born Approach for Calculating Electron-Impact Ionization of Molecules. *Journal of Atomic, Molecular, and Optical Physics* (2010).

27. Gao, J., Madison, D. H. & Peacher, J. L. Interference effects for low-energy electron-impact ionization of nitrogen molecules. *Phys. Rev. A* **72,** 032721 (Sept. 2005).

28. Senftleben, A, Pflger, T, Ren, X, Al-Hagan, O, Najjari, B, Madison, D, Dorn, A. & Ullrich, J. Search for interference effects in electron impact ionization of aligned hydrogen molecules. *Journal of Physics B: Atomic, Molecular and Optical Physics* **43,** 081002 (2010).

29. Staszewska, G, Schwenke, D. W., Thirumalai, D & Truhlar, D. G. Non-empirical model for the imaginary part of the optical potential for electron scattering. *Journal of Physics B: Atomic and Molecular Physics* **16,** L281 (1983).

30. Blanco, F. & García, G. Improvements on the imaginary part of a non-empirical model potential for electron scattering (30 to 10000 eV energies). *Physics Letters A* **295,** 178 –184. ISSN: 0375-9601 (2002).

31. Blanco, F. & García, G. Improvements on the quasifree absorption model for electron scattering. *Phys. Rev. A* **67,** 022701 (2 Feb. 2003).

32. Blanco, F. & García, G. Screening corrections for calculation of electron scattering from polyatomic molecules. *Physics Letters A* **317,** 458 –462. ISSN: 0375-9601 (2003).

33. Blanco, F. & García, G. Screening corrections for calculation of electron scattering differential cross sections from polyatomic molecules. *Physics Letters A* **330,** 230 –237. ISSN: 0375-9601 (2004).

34. Zecca, A, Chiari, L, Garca, G, Blanco, F, Trainotti, E & Brunger, M. J. Total cross sections for positron and electron scattering from pyrimidine. *Journal of Physics B: Atomic, Molecular and Optical Physics* **43,** 215204 (2010).

35. Blanco, F., Ellis-Gibbings, L. & García, G. Screening corrections for the interference contributions to the electron and positron scattering cross sections from polyatomic molecules. *Chemical Physics Letters* **645,** 71 –75. ISSN: 0009-2614 (2016).

36. Mazevet, S., Morrison, M. A., Boydstun, O. & Nesbet, R. K. Adiabatic treatments of vibrational dynamics in low-energy electron-molecule scattering. *Journal of Physics B: Atomic, Molecular and Optical Physics* **32,** 1269 (1999).

37. Itikawa, Y. & Mason, N. Rotational excitation of molecules by electron collisions. *Physics Reports* **414,** 1–41. ISSN: 0370-1573 (2005).

38. Florescu-Mitchell, A. & Mitchell, J. Dissociative recombination. *Physics Reports* **430,** 277–374. ISSN: 0370-1573 (2006).

39. Chang, E. S. & Fano, U. Theory of Electron-Molecule Collisions by Frame Transformations. *Phys. Rev. A* **6,** 173–185 (July 1972).

40. Greene, C. H. & Jungen, C. *Advances in Atomic and Molecular Physics* (eds Bates, D. & Bederson, B.) 51–121 (Academic Press, 1985).

41. Chakrabarti, K., Backodissa-Kiminou, D. R., Pop, N., Mezei, J. Z., Motapon, O., Lique, F., Dulieu, O., Wolf, A. & Schneider, I. F. Dissociative recombination of electrons with diatomic molecular cations above dissociation threshold: Application to H_2^+ and HD^+. *Phys. Rev. A* **87,** 022702 (Feb. 2013).

42. Blatt, J. M. & Jackson, J. D. On the Interpretation of Neutron-Proton Scattering Data by the Schwinger Variational Method. *Phys. Rev.* **76,** 18–37 (July 1949).

43. Da Costa, R. F., Varella, M. T. d. N., Bettega, M. H. F. & Lima, M. A. P. Recent advances in the application of the Schwinger multichannel method with pseudopotentials to electron-molecule collisions. *The European Physical Journal D* **69,** 159. ISSN: 1434-6079 (June 2015).

44. Da Costa, R. F., da Paixo, F. J. & Lima, M. A. P. Cross sections for electron-impact excitation of the H_2 molecule using the MOB-SCI strategy. *Journal of Physics B: Atomic, Molecular and Optical Physics* **38,** 4363 (2005).

45. Da Costa, R. F. & Lima, M. A. P. Electron-impact electronic excitation of molecular nitrogen using the Schwinger multichannel variational method. *Phys. Rev. A* **75,** 022705 (Feb. 2007).

46. Varella, M. T. d. N. & Lima, M. A. P. Near-threshold vibrational excitation of H_2 by positron impact: A. projection-operator approach. *Phys. Rev. A* **76,** 052701 (Nov. 2007).

47. Chaudhuri, P., do N. Varella, M. T., de Carvalho, C. R. C. & Lima, M. A. P. Electronic excitation of N_2 by positron impact. *Phys. Rev. A* **69,** 042703 (Apr. 2004).

48. Kohn, W. Variational Methods in Nuclear Collision Problems. *Phys. Rev.* **74,** 1763–1772 (Dec. 1948).

49. Cooper, J. N., Plummer, M. & Armour, E. A. G. Equivalence of the generalized and complex Kohn variational methods. *Journal of Physics A: Mathematical and Theoretical* **43,** 175302 (2010).

50. Schneider, B. I. & Rescigno, T. N. Complex Kohn variational method: Application to low-energy electron-molecule collisions. *Phys. Rev. A* **37,** 3749–3754 (May 1988).

51. Parker, S. D., McCurdy, C. W., Rescigno, T. N. & Lengsfield, B. H. Electronic excitation of H_2 by electron impact: Close-coupling calculations using the complex Kohn variational method. *Phys. Rev. A* **43,** 3514–3521 (Apr. 1991).

52. Armour, E. A. G., Baker, D. J. & Plummer, M. The theoretical treatment of low-energy e^+-H_2 scattering using the Kohn variational method. *Journal of Physics B: Atomic, Molecular and Optical Physics* **23,** 3057 (1990).

53. Armour, E. A. G. & Plummer, M. Low-energy e^+-N_2 scattering calculations using the Kohn variational method. *Journal of Physics B: Atomic, Molecular and Optical Physics* **24,** 4463 (1991).

54. Zatsarinny, O. & Bartschat, K. The B-spline R-matrix method for atomic processes: application to atomic structure, electron collisions and photoionization. *Journal of Physics B: Atomic, Molecular and Optical Physics* **46,** 112001 (2013).

55. Bachau, H., Cormier, E., Decleva, P., Hansen, J. E. & Martn, F. Applications of B -splines in atomic and molecular physics. *Reports on Progress in Physics* **64,** 1815 (2001).

56. Trevisan, C. S. & Tennyson, J. Differential cross sections for near-threshold electron impact dissociation of molecular hydrogen. *Journal of Physics B: Atomic, Molecular and Optical Physics* **34,** 2935 (2001).

57. Trevisan, C. S. & Tennyson, J. Calculated rates for the electron impact dissociation of molecular hydrogen, deuterium and tritium. *Plasma Physics and Controlled Fusion* **44,** 1263 (2002).

58. Trevisan, C. S. & Tennyson, J. Calculated rates for the electron impact dissociation of molecular hydrogen: mixed isotopomers and scaling laws. *Plasma Physics and Controlled Fusion* **44,** 2217 (2002).

59. Gorfinkiel, J. D. & Tennyson, J. Electron impact ionization of small molecules at intermediate energies: the molecular R-matrix with pseudostates method. *Journal of Physics B: Atomic, Molecular and Optical Physics* **38,** 1607 (2005).

60. Nestmann, B. M. & Beyer, T. A study of the threshold behavior in e^+-HF scattering based on R-matrix theory. *Chemical Physics* **343.** Theoretical Spectroscopy and its Impact on Experiment, 281–291. ISSN: 0301-0104 (2008).

61. Pfingst, K, Thummel, H. T. & Peyerimhoff, S. D. Near-threshold rotational excitation in electron scattering by the HCl molecule. *Journal of Physics B: Atomic, Molecular and Optical Physics* **25,** 2107 (1992).

62. Morgan, L. A. Resonant vibrational excitation of N_2 by low-energy electron impact. *Journal of Physics B: Atomic and Molecular Physics* **19,** L439 (1986).

63. Pindzola, M. S., Robicheaux, F & Colgan, J. Electron-impact ionization of H_2^+ using a time-dependent close-coupling method. *Journal of Physics B: Atomic, Molecular and Optical Physics* **38,** L285 (2005).

64. Pindzola, M. S., Robicheaux, F., Loch, S. D. & Colgan, J. P. Electron-impact ionization of H_2 using a time-dependent close-coupling method. *Phys. Rev. A* **73,** 052706 (May 2006).

65. Pindzola, M. S., Abdel-Naby, S. A., Ludlow, J. A., Robicheaux, F. & Colgan, J. Electron-impact ionization of Li_2 using a time-dependent close-coupling method. *Phys. Rev. A* **85,** 012704 (1 Jan. 2012).

66. Colgan, J., Al-Hagan, O., Madison, D. H., Kaiser, C., Murray, A. J. & Pindzola, M. S. Triple differential cross sections for the electron-impact ionization of H_2 molecules for equal and unequal outgoing electron energies. *Phys. Rev. A* **79,** 052704 (May 2009).

67. Ren, X., Pflüger, T., Xu, S., Colgan, J., Pindzola, M. S., Senftleben, A., Ullrich, J. & Dorn, A. Strong Molecular Alignment Dependence of H_2 Electron Impact Ionization Dynamics. *Phys. Rev. Lett.* **109,** 123202 (Sept. 2012).

68. Colgan, J., Reddish, T. J., Huetz, A., Bolognesi, P., Avaldi, L., Gisselbrecht, M., Lavolle, M. & Pindzola, M. S. The 'KER' effect in the double photoionization of H_2. *Journal of Physics: Conference Series* **141,** 012004 (2008).

69. Bray, I, Fursa, D. V., Kheifets, A. S. & Stelbovics, A. T. Electrons and photons colliding with atoms: development and application of the convergent close-coupling method. *Journal of Physics B: Atomic, Molecular and Optical Physics* **35,** R117 (2002).

70. Zammit, M. C., Fursa, D. V. & Bray, I. Calculations of electron scattering from H_2^+. *Phys. Rev. A* **88,** 062709 (Dec. 2013).

71. Zammit, M. C., Fursa, D. V. & Bray, I. Electron scattering from the molecular hydrogen ion and its isotopologues. *Phys. Rev. A* **90,** 022711 (Aug. 2014).

72. Scarlett, L. H., Zammit, M. C., Fursa, D. V. & Bray, I. Kinetic-energy release of fragments from electron-impact dissociation of the molecular hydrogen ion and its isotopologues. *Phys. Rev. A* **96,** 022706 (2 Aug. 2017).

73. Zammit, M. C., Fursa, D. V. & Bray, I. Convergent-close-coupling formalism for positron scattering from molecules. *Phys. Rev. A* **87,** 020701 (Feb. 2013).

74. Zammit, M. C., Fursa, D. V., Savage, J. S., Bray, I., Chiari, L., Zecca, A. & Brunger, M. J. Adiabatic-nuclei calculations of positron scattering from molecular hydrogen. *Phys. Rev. A* **95,** 022707 (Feb. 2017).

75. Zammit, M. C., Savage, J. S., Fursa, D. V. & Bray, I. Complete Solution of Electronic Excitation and Ionization in Electron-Hydrogen Molecule Scattering. *Phys. Rev. Lett.* **116,** 233201 (June 2016).

76. Scarlett, L. H., Tapley, J. K., Fursa, D. V., Zammit, M. C., Savage, J. S. & Bray, I. Low-energy electron-impact dissociative excitation of molecular hydrogen and its isotopologues. *Phys. Rev. A* **96,** 062708 (Dec. 2017).

77. Zammit, M. C., Savage, J. S., Fursa, D. V. & Bray, I. Electron-impact excitation of molecular hydrogen. *Phys. Rev. A* **95,** 022708 (Feb. 2017).

78. Morrison, M. A. The physics of low-energy electron-molecule collisions: A guide for the perplexed and the uninitiated. *Australian Journal of Physics* **36,** 239 (1983).

79. Zhang, J. Y. & Mitroy, J. Stochastic variational calculation of zero-energy positron scattering from H, He, and H_2. *Phys. Rev. A* **83,** 022711 (Feb. 2011).

80. Peek, J. M. & Green, T. A. Improvement in the First Born Theory of Electron Scattering by Molecular Systems. II. Example of the $1s\sigma_g - 2p\sigma_u$ Transition in H_2^+. *Phys. Rev.* **183,** 202–212 (July 1969).

81. Burrau, O. The calculation of the Energy value of Hydrogen molecule ions (H_2^+) in their normal position. *Naturwissenschaften* **15,** 16–17 (1927).

82. Ghazaly, M. O. A. E., Jureta, J., Urbain, X. & Defrance, P. Total cross sections and kinetic energy release for the electron impact dissociation of H_2^+ and D_2^+. *Journal of Physics B: Atomic, Molecular and Optical Physics* **37,** 2467 (2004).

83. Poole, E. G. C. Some notes on spheroidal wave-functions. *Quart. J. of Pure & Appl. Math.* **49,** 309–321 (1923).

84. Flammer, C. *Spheroidal Wave Functions* (ed) (Dover Publications, 2005).

85. Rankin, J & Thorson, W. Continuum wave functions for the two-center, one-electron system. *Journal of Computational Physics* **32,** 437–446. ISSN: 0021-9991 (1979).

86. Hylleraas, E. A. Über die Elektronenterme des Wasserstoffmoleküls. *Zeitschrift für Physik A: Hadrons and Nuclei* **71,** 739–763 (1931).

87. Falloon, P. E., Abbott, P. C. & Wang, J. B. Theory and computation of spheroidal wavefunctions. *Journal of Physics A: Mathematical and General* **36,** 5477 (2003).

88. Wolniewicz, L., Simbotin, I. & Dalgarno, A. Quadrupole Transition Probabilities for the Excited Rovibrational States of H_2. *The Astrophysical Journal Supplement Series* **115,** 293 (1998).

89. Staszewska, G. & Wolniewicz, L. Transition Moments among $^3\Sigma$ and $^3\Pi$ States of the H_2 Molecule. *Journal of Molecular Spectroscopy* **198,** 416–420. ISSN: 0022-2852 (1999).

90. Staszewska, G. & Wolniewicz, L. Adiabatic Energies of Excited $^1\Sigma_u$ States of the Hydrogen Molecule. *Journal of Molecular Spectroscopy* **212,** 208–212. ISSN: 0022-2852 (2002).

91. Orlikowsi, T., Staszewska, G. & Wolniewicz, L. Long range adiabatic potentials and scattering lengths for the E, F, e and h states of the hydrogen molecule. *Molecular Physics* **96,** 1445–1448 (1999).

92. Wolniewicz, L. & Staszewska, G. Excited $^1\Pi_u$ states and the $^1\Pi_u \rightarrow X\,^1\Sigma_g^+$ transition moments of the hydrogen molecule. *Journal of Molecular Spectroscopy* **220,** 45–51. ISSN: 0022-2852 (2003).

93. Fantz, U. & Wnderlich, D. FranckCondon factors, transition probabilities, and radiative lifetimes for hydrogen molecules and their isotopomeres. *Atomic Data and Nuclear Data Tables* **92,** 853–973. ISSN: 0092-640X (2006).

94. Sharp, T. Potential-energy curves for molecular hydrogen and its ions. *Atomic Data and Nuclear Data Tables* **2,** 119–169. ISSN: 0092-640X (1970).

95. Huber, M. C. E. & Sandeman, R. J. The measurement of oscillator strengths. *Reports on Progress in Physics* **49,** 397 (1986).

96. Chandrasekhar, S. On the Continuous Absorption Coefficient of the Negative Hydrogen Ion. *Astrophysical Journal* **102,** 223 (Sept. 1945).

97. Wolniewicz, L. & Staszewska, G. $^1\Sigma_u^+ \rightarrow X\,^1\Sigma_g^+$ transition moments for the hydrogen molecule. *Journal of Molecular Spectroscopy* **217,** 181–185. ISSN: 0022-2852 (2003).

98. Kolos, W. & Wolniewicz, L. Polarizability of the Hydrogen Molecule. *The Journal of Chemical Physics* **46,** 1426–1432 (1967).

99. Hoffman, K. R., Dababneh, M. S., Hsieh, Y.-F., Kauppila, W. E., Pol, V., Smart, J. H. & Stein, T. S. Total-cross-section measurements for positrons and electrons colliding with H_2, N_2, and CO_2. *Phys. Rev. A* **25,** 1393–1403 (Mar. 1982).

100. Karwasz, G., Pliszka, D. & Brusa, R. Total cross sections for positron scattering in argon, nitrogen and hydrogen below 20eV. *Nuclear Instruments and Methods in Physics Research Section B: Beam Interactions with Materials and Atoms* **247.** Low-Energy Positron and Positronium Physics, 68–74. ISSN: 0168-583X (2006).

101. Zecca, A., Chiari, L., Sarkar, A., Nixon, K. L. & Brunger, M. J. Total cross sections for positron scattering from H_2 at low energies. *Phys. Rev. A* **80,** 032702 (Sept. 2009).

102. Moxom, J, Laricchia, G & Charlton, M. Total ionization cross sections of He, H_2 and Ar by positron impact. *Journal of Physics B: Atomic, Molecular and Optical Physics* **26,** L367 (1993).

103. Knudsen, H, Brun-Nielsen, L, Charlton, M & Poulsen, M. R. Single ionization of H 2 , He, Ne and Ar by positron impact. *Journal of Physics B: Atomic, Molecular and Optical Physics* **23,** 3955 (1990).

104. Fliflet, A. W. & McKoy, V. Distorted-wave-approximation cross sections for excitation of the $b\,^3\Sigma_u^+$ and $B\,^1\Sigma_u^+$ states of H_2 by low-energy-electron impact. *Phys. Rev. A* **21,** 1863–1875 (June 1980).

105. Mu-Tao, L., Lucchese, R. R. & McKoy, V. Electron-impact excitation and dissociation processes in H_2. *Phys. Rev. A* **26,** 3240–3248 (Dec. 1982).

106. Branchett, S. E., Tennyson, J. & Morgan, L. A. Electronic excitation of molecular hydrogen using the R-matrix method. *Journal of Physics B: Atomic, Molecular and Optical Physics* **23,** 4625 (1990).

107. Khakoo, M. A. & Trajmar, S. Electron-impact excitation of the $a\,^3\Sigma_g^+$, $B\,^1\Sigma_u^+$, $c\,^3\Pi_u$, and $C\,^1\Pi_u$ states of H_2. *Phys. Rev. A* **34,** 146–156 (July 1986).

108. Wrkich, J, Mathews, D, Kanik, I, Trajmar, S & Khakoo, M. A. Differential cross-sections for the electron impact excitation of the $B\,^1\Sigma_u^+$, $c\,^3\Pi_u$, $a\,^3\Sigma_g^+$, $C\,^1\Pi_u$, $E, F\,^1\Sigma_g^+$ and $e\,^3\Sigma_u^+$ states of molecular hydrogen. *Journal of Physics B: Atomic, Molecular and Optical Physics* **35,** 4695 (2002).

109. Liu, X., Shemansky, D. E., Abgrall, H, Roueff, E, Ahmed, S. M. & Ajello, J. M. Electron impact excitation of H_2 : resonance excitation of $B\,^1\Sigma_u^+$ ($J_j = 2$, $v_j = 0$) and effective excitation function of $E, F\,^1\Sigma_g^+$. *Journal of Physics B: Atomic, Molecular and Optical Physics* **36,** 173 (2003).

110. Kato, H., Kawahara, H., Hoshino, M., Tanaka, H., Campbell, L. & Brunger, M. J. Electron-impact excitation of the $B\,^1\Sigma_u^+$ and $C\,^1\Pi_u$ electronic states of H_2. *Phys. Rev. A* **77,** 062708 (June 2008).

111. Rescigno, T. N., McCurdy, C. W., McKoy, V. & Bender, C. F. Low-energy electron-impact excitation of the hydrogen molecule. *Phys. Rev. A* **13,** 216–223 (Jan. 1976).

112. Khakoo, M. A., Trajmar, S., McAdams, R. & Shyn, T. W. Electron-impact excitation cross sections for the $b\,^3\Sigma_u^+$ state of H_2. *Phys. Rev. A* **35,** 2832–2837 (Apr. 1987).

113. Khakoo, M. A. & Segura, J. Differential cross sections for the electron impact excitation of the $b\,^3\Sigma_u^+$ continuum of molecular hydrogen. *Journal of Physics B: Atomic, Molecular and Optical Physics* **27,** 2355 (1994).

114. Zawadzki, M., Wright, R., Dolmat, G., Martin, M. F., Hargreaves, L., Fursa, D. V., Zammit, M. C., Scarlett, L. H., Tapley, J. K., Savage, J. S., Bray, I. & Khakoo, M. A. Time-of-flight electron scattering from molecular hydrogen: Benchmark cross sections for excitation of the $X\,^1\Sigma_g^+ \rightarrow b\,^3\Sigma_u^+$ transition. *Phys. Rev. A* **97,** 050702 (May 2018).

115. Hall, R. I. & Andric, L. Electron impact excitation of H_2 (D_2). Resonance phenomena associated with the $X\,^2\Sigma_u^+$ and $B\,^2\Sigma_g^+$ states of H_2^- in the 10 eV region. *Journal of Physics B: Atomic and Molecular Physics* **17,** 3815 (1984).

116. Nishimura, H. & Danjo, A. Differential Cross Section of Electron Scattering from Molecular Hydrogen. II. $b\,^3\Sigma_u^+$ Excitation. *Journal of the Physical Society of Japan* **55,** 3031 (Sept. 1986).

117. Kim, Y.-K. & Rudd, M. E. Binary-encounter-dipole model for electron-impact ionization. *Phys. Rev. A* **50,** 3954–3967 (Nov. 1994).

118. Lindsay, B. G. & Mangan, M. A. in *Interactions of Photons and Electrons with Molecules* (ed Itikawa, Y.) 5001–5077 (Springer, Berlin, Heidelberg, 2003). ISBN: 978-3-540-45843-2.

119. Krishnakumar, E & Srivastava, S. K. Electron correlation effects in the dissociative ionization of H_2. *Journal of Physics B: Atomic, Molecular and Optical Physics* **27,** L251 (1994).

120. Straub, H. C., Renault, P., Lindsay, B. G., Smith, K. A. & Stebbings, R. F. Absolute partial cross sections for electron-impact ionization of H_2, N_2, and O_2 from threshold to 1000 eV. *Phys. Rev. A* **54,** 2146–2153 (Sept. 1996).

121. Ferch, J., Raith, W. & Schroder, K. Total cross section measurements for electron scattering from molecular hydrogen at very low energies. *Journal of Physics B: Atomic and Molecular Physics* **13,** 1481 (1980).

122. Deuring, A., Floeder, K., Fromme, D., Raith, W., Schwab, A., Sinapius, G., Zitzewitz, P. W. & Krug, J. Total cross section measurements for positron and electron scattering on molecular hydrogen between 8 and 400 eV. *Journal of Physics B: Atomic and Molecular Physics* **16,** 1633 (1983).

123. Jones, R. K. Absolute total cross section for electron scattering from molecular hydrogen from 1 to 50 eV. *Phys. Rev. A* **31,** 2898–2904 (May 1985).

124. Subramanian, K. P. & Kumar, V. Total electron scattering cross sections for molecular hydrogen at low electron energies. *Journal of Physics B: Atomic, Molecular and Optical Physics* **22,** 2387 (1989).

125. Nickel, J. C., Kanik, I, Trajmar, S & Imre, K. Total cross section measurements for electron scattering on H_2 and N_2 from 4 to 300 eV. *Journal of Physics B: Atomic, Molecular and Optical Physics* **25,** 2427 (1992).

126. Zhou, S., Li, H., Kauppila, W. E., Kwan, C. K. & Stein, T. S. Measurements of total and positronium formation cross sections for positrons and electrons scattered by hydrogen atoms and molecules. *Phys. Rev. A* **55,** 361–368 (Jan. 1997).

127. Linder, F. & Schmidt, H. Rotational and Vibrational Excitation of H_2 by Slow Electron Impact. *Zeitschrift Naturforschung Teil A* **26,** 1603–1617 (Oct. 1971).

128. Srivastava, S. K., Chutjian, A. & Trajmar, S. Absolute elastic differential electron scattering cross sections in the intermediate energy region. I. H_2. *The Journal of Chemical Physics* **63,** 2659–2665 (1975).

129. Shyn, T. W. & Sharp, W. E. Angular distributions of electrons elastically scattered from H_2. *Phys. Rev. A* **24,** 1734–1740 (Oct. 1981).

130. Furst, J., Mahgerefteh, M. & Golden, D. E. Absolute total electronically elastic differential e^--H_2 scattering cross-section measurements from 1 to 19 eV. *Phys. Rev. A* **30,** 2256–2260 (Nov. 1984).

131. Nishimura, H., Danjo, A. & Sugahara, H. Differential Cross Sections of Electron Scattering from Molecular Hydrogen I. Elastic Scattering and Vibrational Excitation ($X\,^1\Sigma_g^+$, $v = 0 \rightarrow 1$). *Journal of the Physical Society of Japan* **54,** 1757–1768 (1985).

132. Brunger, M. J., Buckman, S. J., Newman, D. S. & Alle, D. T. Elastic scattering and rovibrational excitation of H_2 by low-energy electrons. *Journal of Physics B: Atomic, Molecular and Optical Physics* **24,** 1435 (1991).

133. Muse, J, Silva, H, Lopes, M. C. A. & Khakoo, M. A. Low energy elastic scattering of electrons from H_2 and N_2. *Journal of Physics B: Atomic, Molecular and Optical Physics* **41,** 095203 (2008).

134. Morrison, M. A., Feldt, A. & Saha, B. Private communication.

135. Khakoo, M. A. & Trajmar, S. Elastic electron scattering cross sections for molecular hydrogen. *Phys. Rev. A* **34,** 138–145 (July 1986).

136. Fink, M., Jost, K. & Herrmann, D. Differential cross sections for elastic electron scattering. Charge-cloud polarization in H_2. *Phys. Rev. A* **12,** 1374–1382 (Oct. 1975).

137. Van Wingerden, B, de Heer, F. J., Weigold, E & Nygaard, K. J. Elastic scattering of electrons by molecular and atomic hydrogen. *Journal of Physics B: Atomic and Molecular Physics* **10,** 1345 (1977).

138. Ehrhardt, H., Langhans, L., Linder, F. & Taylor, H. S. Resonance Scattering of Slow Electrons from H_2 and CO Angular Distributions. *Phys. Rev.* **173,** 222–230 (Sept. 1968).

139. England, J. P., Elford, M. T. & Crompton, R. W. A study of the vibrational excitation of H_2 by measurements of the drift velocity of electrons in H_2-Ne mixtures. *Australian Journal of Physics* **41,** 573 (1988).

140. Schmidt, B, Berkhan, K, Gtz, B & Mller, M. New experimental techniques in the study of electron swarms in gases and their impact on the determination of low energy electron scattering cross sections. *Physica Scripta* **1994,** 30 (1994).

141. Morrison, M. A., Saha, B. C., Crompton, R. W. & Petrovic, Z. L. Near-threshold rotational and vibrational excitation of H_2 by electron impact - Theory and experiment. *Australian Journal of Physics* **40,** 239–281 (1987).

142. Nesbet, R. K. Energy-modified adiabatic approximation for scattering theory. *Phys. Rev. A* **19,** 551–556 (Feb. 1979).

143. Crompton, R. W. & Morrison, M. A. Analyses of recent experimental and theoretical determinations of e-H_2 vibrational excitation cross sections: assessing a long-standing controversy. *Australian Journal of Physics* **46,** 203 (1993).

144. Brunger, M. J. & Buckman, S. J. Electronmolecule scattering cross-sections. I. Experimental techniques and data for diatomic molecules. *Physics Reports* **357,** 215–458. ISSN: 0370-1573 (2002).

145. Astashkevich, S. A. & Lavrov, B. P. Lifetimes of Vibro-Rotational Levels in Excited Electronic States of Diatomic Hydrogen Isotopologues. *Journal of Physical and Chemical Reference Data* **44,** 023105 (2015).

146. Sartori, C. S., da Paixão, F. J. & Lima, M. A. P. Superelastic cross sections in e^--H_2 scattering. *Phys. Rev. A* **55,** 3243–3246 (Apr. 1997).

147. Joshipura, K. N., Kothari, H. N., Shelat, F. A., Bhowmik, P. & Mason, N. J. Electron scattering with metastable H_2^* ($c\,^3\Pi_u$) molecules: ionization and other total cross sections. *Journal of Physics B: Atomic, Molecular and Optical Physics* **43,** 135207 (2010).

148. Scarlett, L. H., Tapley, J. K., Fursa, D. V., Zammit, M. C., Savage, J. S. & Bray, I. Electron-impact dissociation of molecular hydrogen into neutral fragments. *The European Physical Journal D* **72,** 34. ISSN: 1434-6079 (Feb. 2018).

149. Tapley, J. K., Scarlett, L. H., Savage, J. S., Zammit, M. C., Fursa, D. V. & Bray, I. Vibrationally resolved electron-impact excitation cross sections for singlet states of molecular hydrogen. *Journal of Physics B: Atomic, Molecular and Optical Physics* **51,** 144007 (2018).

150. Tapley, J. K., Scarlett, L. H., Savage, J. S., Zammit, M. C., Fursa, D. V. & Bray, I. To be published.

151. Zammit, M. C., Savage, J. S., Colgan, J., Fursa, D. V., Kilcrease, D. P., Bray, I., Fontes, C. J., Hakel, P. & Timmermans, E. State-resolved Photodissociation and Radiative Association Data for the Molecular Hydrogen Ion. *The Astrophysical Journal* **851,** 64 (2017).

152. Schneider, B. I., Segura, J., Gil, A., Guan, X. & Bartschat, K. A new Fortran 90 program to compute regular and irregular associated Legendre functions. *Computer Physics Communications* **181,** 2091–2097. ISSN: 0010-4655 (2010).

153. *NIST Digital Library of Mathematical Functions* http://dlmf.nist.gov/, Release 1.0.17 of 2017-12-22. F. W. J. Olver, A. B. Olde Daalhuis, D. W. Lozier, B. I. Schneider, R. F. Boisvert, C. W. Clark, B. R. Miller and B. V. Saunders, eds.

154. Rose, M. *Elementary Theory of Angular Momentum* ISBN: 9780486684802 (Dover, 1995).

155. Bethe, H. Zur Theorie des Durchgangs schneller Korpuskularstrahlen durch Materie. *Annalen der Physik* **397,** 325–400.